HYBRID ESTIMATION FOR CONTROL AND PLANNING

A Dissertation

Presented to the Faculty of the Graduate School

of Cornell University

in Partial Fulfillment of the Requirements for the Degree of

Doctor of Philosophy

by

Paul Guillermo Otanez Maldonado

January 2008

HYBRID ESTIMATION FOR CONTROL AND PLANNING

Paul Guillermo Otanez Maldonado, Ph.D.

Cornell University 2008

Hybrid or switched models are often used in engineering to analyze complex behavior. The hybrid paradigm can be used to design systems that utilize the relationship between discrete and continuous variables. This dissertation presents three examples in which hybrid principles are implemented in order to: 1) reduce the number of models required to establish hard bounds on the state estimate of smooth nonlinear systems, 2) enable the exchange of low-level information between vehicles using movements instead of radio-communication, and 3) improve the cooperative reconnaissance performance of two autonomous aerial vehicles in a leader/follower configuration under strict communication constraints.

First, the problem of establishing hard bounds on the state estimate of a nonlinear system using a switching piecewise linear hybrid estimator is considered. Within an operating region, the proposed hybrid/switched estimator uses a variant of the Extended Set-Membership Filter to select piecewise linear models based on minimizing uncertainty. A priori selection of the base piecewise linear models is achieved by optimizing the placement of operating points over the operating region.

Second, vehicle mode detection in a cooperative environment while minimizing communication is investigated. The behavior of a vehicle is described using a finite number of operating modes. Each mode is defined by a model which describes the vehicle's dynamics as well as a perturbation signature based on Gold codes. A locally most powerful detector is derived based on detection theory in which the test statistic is a function of the Kalman Filter innovations. In order to facilitate real-time implemen-

tation, a suboptimal detector that requires less computations is also developed. Monte Carlo simulations of a linear and a nonlinear system are presented and the detection performance of the locally most powerful and the suboptimal detectors are compared.

Finally, the cooperative reconnaissance performance of two unmanned aerial vehicles (leader/follower) in uncertain environments while minimizing communication is investigated. To enable cooperative reconnaissance, the follower estimates the operating mode of the leader vehicle by using video camera measurements. The performance of the overall system is gauged using two metrics: 1) by the length of time required for the two vehicles to collect a certain level of information, and 2) by the amount of information collected in a time interval. Monte Carlo simulations of the system are compared to a decentralized system in which there is no cooperation and a centralized system with full communication.

BIOGRAPHICAL SKETCH

Paul Otanez was born in Quito, Ecuador. He received the B.S. degree in mechanical and aerospace engineering from Cornell University, Ithaca, NY, in 2000, the M.S. degree in mechanical engineering from the University of Michigan, Ann Arbor, in 2002, and M.S. degree from the Cornell University Sibley School of Mechanical and Aerospace Engineering in 2005. He has held summer internship positions at the Dell Computer Corporation Shock and Vibrations Laboratory and the General Electric Global Research Center, Automation and Control Laboratory. His research interests include nonlinear estimation theory, cooperative estimation, control, and planning of autonomous aerial and underwater systems, and networked control systems. He currently holds a research position in the Powertrain Systems Research Laboratory at the General Motors Technical Center in Warren, MI.

To my parents Guillermo and María del Pilar.

ACKNOWLEDGEMENTS

My thanks and appreciation go to my advisor Professor Mark Campbell for his patience, guidance and support throughout the time it took to conduct this research and write this dissertation. His knowledge and vision as well as the sincere respect he has for all his students made it a pleasure to work with him. I would also like to thank Professor Mark Psiaki for giving me the chance to get a taste of research during my undergraduate career at Cornell University. This experience motivated me to pursue a career in research. As a member of the my dissertation committee Professor Psiaki's many insights and attention to detail also helped me improve the quality of this work. My thanks must also go to Professor Hod Lipson for being part of my dissertation committee and generously giving his time and expertise. I would also like to thank Professor Ephrahim Garcia for agreeing to serve as a proxy.

It is my pleasure to acknowledge Ramu Chandra, Atif Chaudry, Terry McLoughlin, Jarurat Ousingsawat, Eelco Scholte, and Darren Zanon for the many research related discussions in the old controls graduate office Upson 139 and more recently Upson 245. In addition, I would also like to thank Benjamin Lee and Tuhin Sahai for the numerous academic and not so academic discussions over the last few years.

My sincere gratitude also goes to Professor Dawn Tilbury and Doctor James Moyne for their words of encouragement and guidance while writing my M.S. thesis on networked control at the University of Michigan, Ann Arbor.

This work and all my accomplishments are dedicated to my parents. Their understanding, support, and hard work made it possible for me to pursue a career in a field that I truly enjoy. I owe everything I have ever achieved to them. I would also like to thank my uncle Ivan and aunt Ivonne who have always cheered me on and helped me to pursue my undergraduate studies at Cornell University.

One last word of gratitude goes to Rochelle whose support, enthusiasm and patience helped me immensely during the writing of this dissertation.

This work was supported by the DARPA Software Enabled Control program administered through AFRL at Wright Patterson AFB and the Embedded & Hybrid Systems (EHS) program at the National Science Foundation.

TABLE OF CONTENTS

LIST OF TABLES

LIST OF FIGURES

CHAPTER 1

INTRODUCTION

In this dissertation, estimation methods are derived for systems in which it is beneficial to use multiple models. The systems studied include: 1) smooth nonlinear systems with unknown-but-bounded uncertainties, and 2) multiple vehicle systems used in cooperative reconnaissance in uncertain environments. Hybrid/switched estimation methods are derived and tested on these systems.

Chapter 2 investigates the problem of establishing hard bounds on the state estimate of a smooth nonlinear system using a switching piecewise linear hybrid estimator based on set-membership. The basis of set-membership estimation is to assume hard bounds on the noise, which allows hard bounds on the state estimate to be developed. Set-membership estimation recursively computes an output set in which no point is more likely to be the actual state than any other point, but does guarantee that the actual state lies within this set. The linear set-membership filter, first derived in [1], is extended in [2] for dynamic nonlinear systems to formulate the extended set-membership filter (ESMF). Within an operating region, the proposed hybrid/switched estimator uses a switched version of the ESMF to select piecewise linear models based on minimizing uncertainty. A priori selection of the base piecewise linear models is achieved by optimizing the placement of operating points over the operating region. The algorithm calculates the minimum number of models (and their locations) necessary within an operation region to guarantee a certain level of uncertainty. Several methods of switching models are also investigated. The algorithm is implemented on a complex high performance aircraft model to demonstrate its function and benefits.

In Chapter 3, vehicle mode detection in a cooperative environment while minimizing communication is investigated. The behavior of a vehicle is described using a finite number of operating modes. Each mode is defined by a model which describes the

vehicle's dynamics as well as a perturbation signature based on Gold codes which is embedded in the trajectory of the system. The perturbations are designed such that there are the small enough not to affect the performance of the vehicle, yet large enough to be detected in the presence of noise by another vehicle. A locally most powerful detector is derived based on detection theory in which the test statistic is a function of the Kalman Filter innovations. A suboptimal detector that requires less computations is also developed. Monte Carlo simulations of a linear and a nonlinear system are presented and the detection performance of the locally most powerful and the suboptimal detectors are compared.

Chapter 4 describes the cooperative reconnaissance performance of two unmanned aerial vehicles (leader/follower) in uncertain environments while minimizing communication. The goal is to evaluate whether it is possible to implement cooperative reconnaissance using perturbation signatures in the absence of direct radio communication between the vehicles. To enable cooperative reconnaissance the first vehicle, or the leader, uses mode perturbation signatures to encode information about its current target. A video camera is used by the second vehicle, or follower, to observe the motion of the leader. The suboptimal detector developed in Chapter 3 is used by the follower to detect the leader's operating mode as a way to estimate information about the leader's current target. The mode estimate is then used by the follower to evaluate whether cooperation would improve performance. The performance of the overall system (leader and follower) is gauged using two metrics: 1) by the length of time required for the two vehicles to collect a certain level of information, and 2) by the amount of information collected in a time interval. Monte Carlo simulations of the system are compared to a decentralized system in which there is no cooperation and a centralized system with full communication.

CHAPTER 2

SWITCHED LINEAR ESTIMATOR FOR SMOOTH NONLINEAR SYSTEMS

2.1 Introduction

The study of hybrid systems is attractive because of its wide applicability to complex systems. Although the term *hybrid system* is used for a wide range of systems, it can loosely be defined as a system in which there is interaction of discrete (in value) and continuous dynamics. Hybrid systems arise in various engineering applications such as automotive power-train systems, intelligent vehicle systems, and air traffic management [3, 4, 5]. A more specific definition of a hybrid system is a system described by a set of ordinary differential equations with discontinuities [6]. These models can be used to represent nonlinearities such as saturation, hysteresis, switches, relays, and dead zones. Control laws such as rule-based control, programmable logic control, and gain scheduling are piecewise linear by nature and fit naturally into the hybrid framework.

A hybrid framework poses a challenge to estimation theory as estimators must use measurements to recover information not only about the continuous state (sometimes referred as the base-state), but also about the discrete state (sometimes referred to as the modal state). The Interacting Multiple Model (IMM) estimator fuses N models to efficiently compute a high quality state estimate. Fusion is based on computing the probability of the modes based on their residuals; the mode with the smaller residual is weighted more in the estimate [7]. Other stochastic multiple model estimators are presented in [8, 9, 10]. Biased estimates calculated by the Extended Kalman Filter (EKF) in problems with incorrect noise assumptions led to the development of the Polymorphic Estimator (PME) derived in Ref. [11]. As an alternative, the Gaussian Wavelet Estimator (GWE) is derived in Ref. [12], which finds a finite dimensional Gaussian wavelet approximation to the unnormalized density function of the hybrid state. In Ref. [13],

the author proves that a switching observer with asymptotically stable error dynamics can be constructed under the assumptions of compactness and Lyapunov detectability. The usefulness of the approach is somewhat limited as it is difficult to design each of the observers using the Lyapunov direct method. There exists a rich literature addressing estimators for hybrid systems and the above summary is not exhaustive.

This paper develops a piecewise linear, hybrid bounded estimator designed for a large family of systems (including continuous nonlinear); the output is a set of bounds on the state estimate that are guaranteed even through model switching. System nonlinearities are addressed by implementing a set of estimators designed for linear models, each over a particular operating range. Each individual continuous estimator is designed in a context similar to the Extended Set-Membership Filter (ESMF) [2]: where the effects from higher order uncertainty of the nonlinear system are integrated directly into the estimation framework. In contrast, stochastic filters such as the Extended Kalman Filter (EKF) and Sigma Point Filter (SPF) [14] address nonlinearities directly: the EKF linearizes the dynamics while the SPF propagates finite points through the nonlinear dynamics. But both approaches ignore higher order terms of the nonlinearities. By ignoring these higher order terms, the error covariance is not an accurate measurement of the bound on the state estimate. Therefore, many of these estimators are incompatible with current robust and hybrid control techniques that require bounded uncertainty information in their formulations in order to guarantee closed loop stability and performance. The proposed hybrid observer can be integrated with control in the following ways: 1) by finding the largest bound across the operating region and models and using it as a constant uncertainty bound, or 2) in model predictive control where the uncertainty bounds constrain the optimization [15]. Unique aspects of this work include: 1) a hybrid switching methodology that directly minimizes the estimation uncertainty while also guaranteeing bounds, 2) a model selection process which finds the number and loca-

tion (state) of each model/estimator which minimizes the states estimation uncertainty, and 3) theoretically guaranteeing boundedness of the estimator for a particular class of systems.

The paper is presented as follows. Section 2.2 describes the ESMF and how its hard bounds on the state are obtained. The derivation of the piecewise linear hybrid estimator is derived in Section 2.3, based in part on the ESMF steps. Model selection methods and conditions that guarantee the boundedness of the state estimate are also presented. The *a priori* selection of piecewise linear models for use with the hybrid estimator is discussed in Section 2.4. Finally an aircraft example is presented in Section 2.6 to illustrate the function and benefits of the proposed techniques.

2.2 The Extended Set-Membership Filter

The basis of set-membership estimation is to assume hard bounds on the noise, which allows hard bounds on the state estimate to be developed. In contrast, the Kalman Filter (or Extended Kalman Filter for nonlinear systems) assumes noise sources are stochastic, and then recursively calculates the highest probability state estimate and covariance [16]. Set-membership estimation recursively computes an output set in which no point is more likely to be the actual state than any other point, but does guarantee that the actual state lies within this set. In the literature, set-membership methods have been derived using polytope and ellipsoidal methods. Ellipsoid methods require less information to represent the uncertainty as compared to polytope methods, and are perhaps more intuitive because of their analogy to the covariance in stochastic estimation. The ellipsoidal set method, as developed by Schweppe for linear systems [17], is extended in [2] for dynamic nonlinear systems to formulate the extended set-membership filter (ESMF). The ESMF is chosen as a basis for a piecewise linear hybrid estimator in this paper because it is well suited for on-line usage, does not make any assumptions on noise

statistics (except that they are bounded), and allows boundedness of the uncertainty to be verified, even for smooth nonlinear systems.

Consider the discrete nonlinear state-space system:

$$\mathbf{x_{k+1}} = f(\mathbf{x_k}) + \mathbf{w_k} \tag{2.1}$$

$$\mathbf{y_{k+1}} = h(\mathbf{x_{k+1}}) + \mathbf{v_{k+1}} \tag{2.2}$$

where $\mathbf{x_k} \in \mathbb{R}^n$ is the state vector, $\mathbf{w_k} \in \mathbb{R}^n$ is the disturbance, $\mathbf{y_{k+1}} \in \mathbb{R}^{n_y}$ is the measurement, $\mathbf{v_{k+1}} \in \mathbb{R}^{n_y}$ is the sensor noise. Note that adding a disturbance, sensor noise, or control input which does not enter Equations (2.1-2.2) linearly is a straightforward extension to the subsequent developments, but if left out for convenience.

The initial state, $\mathbf{x_0}$, process noise, and sensor noise are assumed to be bounded by ellipsoids.

$$\mathbf{x_0} \in \Omega(\hat{\mathbf{x}}_\mathbf{0}, \Sigma_{0,0}), \tag{2.3}$$

$$\mathbf{w_k} \in \Omega(\mathbf{0}, Q_k), \tag{2.4}$$

$$\mathbf{v_{k+1}} \in \Omega(\mathbf{0}, R_{k+1}), \tag{2.5}$$

where an ellipsoidal constraint of the form

$$[\mathbf{x} - \hat{\mathbf{x}}]^T P^{-1} [\mathbf{x} - \hat{\mathbf{x}}] \leq 1 \tag{2.6}$$

is represented by the notation $\mathbf{x} \in \Omega(\hat{\mathbf{x}}, P)$.

Linearizing Equation (2.1) about the current state estimate, $\hat{\mathbf{x}}_\mathbf{k}$, yields

$$\mathbf{x_{k+1}} = f(\hat{\mathbf{x}}_\mathbf{k}) + \left.\frac{\partial f(\mathbf{x_k})}{\partial \mathbf{x}}\right|_{\mathbf{x_k}=\hat{\mathbf{x}}_\mathbf{k}} (\mathbf{x_k} - \hat{\mathbf{x}}_\mathbf{k}) + O(\mathbf{x_k}^2) + \mathbf{w_k}. \tag{2.7}$$

Even though Equation (2.6) only defines a set that contains $\mathbf{x}$, if a point estimate is needed the center of the ellipsoidal set can be used as it minimizes the error between the true value and $\hat{\mathbf{x}}$. The ESMF [2] combines the higher order terms and the process noise into one bound such that Equation (2.7) can be rewritten as

$$\mathbf{x_{k+1}} = f(\hat{\mathbf{x}}_\mathbf{k}) + \left.\frac{\partial f(\mathbf{x_k})}{\partial \mathbf{x}}\right|_{\mathbf{x_k}=\hat{\mathbf{x}}_\mathbf{k}} (\mathbf{x_k} - \hat{\mathbf{x}}_\mathbf{k}) + \hat{\mathbf{w}}_\mathbf{k} \tag{2.8}$$

where $\hat{\mathbf{w}}_{\mathbf{k}}$ is a new noise term that bounds both the original noise and the linearization remainder, $\hat{\mathbf{w}}_{\mathbf{k}} \in \Omega(0, \hat{Q}_k)$. The procedure to combine the process and measurement noise with the linearization remainder utilizes interval mathematics for bounding, and is described in detail in [2]. Considering the scalar case for simplicity, Equation (2.7) can be rewritten as

$$x_{k+1} = f(x_k)|_{x_k=\hat{x}_k} + \left.\frac{\partial f(x_k)}{\partial x}\right|_{x_k=\hat{x}_k} (x_k - \hat{x}_k) + \ldots + \left.\frac{f(x_k)^{n_r}}{n_r!}\right|_{x_k=\hat{x}_k} (x_k - \hat{x}_k)^{n_r} + \mathcal{R}_{n_r}(x_k - \hat{x}_k, X_k) + w_k \quad (2.9)$$

where $\mathcal{R}_{n_r}$ is a remainder term, and f^{n_r} the $(n_r)^{th}$ derivative. Following Taylor's Theorem [18], the Lagrange remainder is written as

$$\mathcal{R}_{n_r}(x_k, \hat{x}_k, X_k) = \frac{f^{(n_r+1)}(X_k)}{(n_r+1)!} (x_k - \hat{x}_k)^{n_r+1}. \quad (2.10)$$

The term X_k can take on any value over an interval that includes the state x_k. Therefore, Equation (2.10) can be bounded by simply defining the interval X_k and evaluating $\mathcal{R}_{n_r}(x_k - \hat{x}_k, X_k)$ using interval mathematics [2]. The ESMF considers $n_r = 1$, the first order dynamics used for prediction and update steps and the second order terms used to define the Lagrange remainder, and therefore the uncertainty.

Given the initial conditions ($\Omega(\hat{\mathbf{x}}_{\mathbf{0}}, \Sigma_{0,0})$), the extended noise bound calculated at each time step, $\hat{\mathbf{w}}_{\mathbf{k}} \in \Omega(\mathbf{0}, \hat{Q}_{k,k})$, and the system dynamics in Equation (2.1), the predicted state ellipsoid, $\Omega(\mathbf{x}_{\mathbf{k+1,k}}, \Sigma_{k+1,k})$, can be estimated recursively by applying a linear set-membership filter at each time step [17]. Note that starting at time k the subscripts (k,k), $(k+1,k)$, and $(k+1,k+1)$ are used to denote the elements used in the prediction step, the update step, and final estimate at time $k+1$. A similar procedure is applied to the measurement update using the output in Equation (2.2), the extended sensor noise bounds $\hat{\mathbf{v}}_{\mathbf{k+1}} \in \Omega(\mathbf{0}, R_{k+1})$, to yield the updated state ellipsoid, $\Omega(\hat{\mathbf{x}}, \Sigma_{k+1,k+1})$.

A summary of the ESMF is given in Equations (2.12-2.17). The prediction step, Equations (2.12-2.13), is physically the addition of two ellipsoids: 1) the augmented

noise ellipsoid $\Omega(0, \hat{Q}_{k,k})$ and 2) the state uncertainty ellipsoid $\Omega(\hat{\mathbf{x}}_{\mathbf{k},\mathbf{k}}, \Sigma_{k,k})$ rotated and scaled by the linearized dynamics, A_k^T and A_k. The update step, Equations (2.14-2.17), is the intersection of two sets: 1) the predicted state ellipsoid $\Omega(\hat{\mathbf{x}}_{\mathbf{k+1},\mathbf{k}}, \Sigma_{k+1,k})$ and 2) the set described by the output equation $\Omega(\mathbf{y}_{\mathbf{k+1}}, \hat{R}_k)$. The actual state, $\mathbf{x}_{\mathbf{k}}$, is then bounded by $\Omega(\hat{\mathbf{x}}_{\mathbf{k+1},\mathbf{k+1}}, \Sigma_{k+1,k+1})$, or

$$\left[\mathbf{x}_{\mathbf{k+1}} - \hat{\mathbf{x}}_{\mathbf{k+1},\mathbf{k+1}}\right]^T \Sigma_{k+1,k+1}^{-1} \left[\mathbf{x}_{\mathbf{k+1}} - \hat{\mathbf{x}}_{\mathbf{k+1},\mathbf{k+1}}\right] \leq 1. \tag{2.11}$$

2.3 Bounded Hybrid Estimator

A hybrid system, or more specifically a switched dynamical system, can be described by an ordinary differential equation of the form:

$$\dot{\mathbf{x}}(t) = f_i(\mathbf{x}(t), \mathbf{u}(t), \mathbf{w}(t)), \;\; \mathbf{y}(t) = h_i(\mathbf{x}(t), \mathbf{u}(t), \mathbf{v}(t))$$

where $\mathbf{x}(t) \in \mathbb{R}^n$ is the state and $f_i(\cdot)$, $h_i(\cdot)$ for $i \in 1, \ldots, N$, are continuous vector functions that describe the behavior and output of the system under N conditions. This hybrid model is used to more accurately describe systems in which a single vector function is not sufficient. Switching between the individual models is done for control reasons, such as to maintain stability or improve robustness. The work here focuses on switching an estimator based on the estimation uncertainty.

2.3.1 Derivation

The proposed hybrid estimator uses a single active estimator as the one that minimizes a measure of the set that contains the state estimate (equivalently this measure can be referred to as a measure of the uncertainty bound). This is defined generally to be $J(\cdot) : \mathbb{R}^n \times \mathbb{R}^n \rightarrow \mathbb{R}$. The switching law is then given as

$$J_{i^*}^* = \min_i \left[J_1(\cdot), \ldots, J_N(\cdot)\right] \tag{2.19}$$

Prediction step

$$\hat{\mathbf{x}}_{\mathbf{k+1},\mathbf{k}} = f(\hat{\mathbf{x}}_{\mathbf{k},\mathbf{k}}) \tag{2.12}$$

$$\Sigma_{k+1,k} = A_k \frac{\Sigma_{k,k}}{1-\beta_k} A_k^T + \frac{\hat{Q}_{k,k}}{\beta_k} \tag{2.13}$$

Update step

$$\hat{\mathbf{x}}_{\mathbf{k+1},\mathbf{k+1}} = \hat{\mathbf{x}}_{\mathbf{k+1},\mathbf{k}} + \frac{\Sigma_{k+1,k}}{1-\rho_{k+1}} C_{k+1}^T \left[C_{k+1} \frac{\Sigma_{k+1,k}}{1-\rho_{k+1}} C_{k+1}^T + \frac{\hat{R}_{k+1}}{\rho_{k+1}} \right]^{-1} \left[\mathbf{y}_{\mathbf{k+1}} - h(\hat{\mathbf{x}}_{\mathbf{k+1},\mathbf{k}}) \right] \tag{2.14}$$

$$\bar{\Sigma}_{k+1,k+1} = \frac{\Sigma_{k+1,k}}{1-\rho_{k+1}} - \frac{\Sigma_{k+1,k}}{1-\rho_{k+1}} C_{k+1}^T \left[C_{k+1} \frac{\Sigma_{k+1,k}}{1-\rho_{k+1}} C_{k+1}^T + \frac{\hat{R}_{k+1}}{\rho_{k+1}} \right]^{-1} C_{k+1} \frac{\Sigma_{k+1,k}}{1-\rho_{k+1}} \tag{2.15}$$

$$\delta_{k+1} = \left[\mathbf{y}_{\mathbf{k+1}} - h(\hat{\mathbf{x}}_{\mathbf{k+1},\mathbf{k}}) \right]^T \left[C_{k+1} \frac{\Sigma_{k+1,k}}{1-\rho_{k+1}} C_{k+1}^T + \frac{\hat{R}_{k+1}}{\rho_{k+1}} \right]^{-1} \left[\mathbf{y}_{\mathbf{k+1}} - h(\hat{\mathbf{x}}_{\mathbf{k+1},\mathbf{k}}) \right] \tag{2.16}$$

$$\Sigma_{k+1,k+1} = (1-\delta_{k+1}) \bar{\Sigma}_{k+1,k+1} \tag{2.17}$$

$$A_k = \left. \frac{\partial f(\mathbf{x_k})}{\partial \mathbf{x}} \right|_{\mathbf{x_k}=\hat{\mathbf{x}}_{\mathbf{k},\mathbf{k}}}, \quad C_{k+1} = \left. \frac{\partial h(\mathbf{x_k})}{\partial \mathbf{x}} \right|_{\mathbf{x_k}=\hat{\mathbf{x}}_{\mathbf{k},\mathbf{k}}} \tag{2.18}$$

---

based on evaluating $J(\cdot)$ for each of the N filters. This enables the hybrid estimator to minimize and bound uncertainty across the operating regions and transitions.

For the proposed hybrid estimator formulation, the nonlinear dynamics are linearized about N *operating points*, $\bar{\mathbf{x}}_\mathbf{i}$, for $i \in [1,\ldots,N]$, not the current state estimate, $\hat{\mathbf{x}}_\mathbf{k}$, as in the ESMF. Linearizing f_i and h_i in Equation (2.19) about the i^{th} operating point, $\bar{\mathbf{x}}_\mathbf{i}$, results in the i^{th} model, Φ_i, composed of the matrices (A_i, B_i, C_i, D_i). This allows the

estimator to remain linear over a particular operating range, but with varying process and sensor noise bounds. Thus, this switched estimator, as compared to the ESMF, has the advantage of being piecewise linear which is helpful for analysis and control design. Although for estimation the cost of model switching is not high, it is advantageous to minimize the number of operating points around which controllers must be designed and tuned. The disadvantage for estimation and control of having a *minimal* set of operating points is that there is a larger uncertainty because the system does not always operate very close to the operating points.

The expansion of the true state dynamics about the i^{th} operating point analogous to Equation (2.9) for the one-state case using a Lagrange remainder is

$$x_{k+1} = f(x_k)|_{x_k=\bar{x}_i} + \left.\frac{\partial f(x_k)}{\partial x}\right|_{x_k=\bar{x}_i} (x_k - \bar{x}_i) + \mathcal{R}_k\left(x_k - \bar{x}_i, \overline{X}_{k,k}\right) + w_k \tag{2.20}$$

where $\mathcal{R}_k$ is again the Lagrange remainder, and is written as

$$\mathcal{R}_k\left(x_k - \bar{x}_i, \overline{X}_{k,k}\right) = (x_k - \bar{x}_i)^T \frac{1}{2} \frac{\partial^2 f(\overline{X}_{k,k})}{\partial x} (x_k - \bar{x}_i), \tag{2.21}$$

for x_k, $\bar{x}_i \in \overline{X}_{k,k}$ and the subscript k,k is used to denote the value of a variable used in the prediction step of the estimator.

To maintain the piecewise linear characteristics of the estimator, the prediction step of the hybrid estimator, (analogous to Equation (2.12) for the ESMF) must be modified to rely on a linear model to calculate $\hat{\mathbf{x}}_{\mathbf{k+1,k}}$. The linear prediction step for the estimator that functions near the i^{th} operating point has the following form:

$$\hat{x}_{k+1} = f(x_k)|_{x_k=\bar{x}_i} + \left.\frac{\partial f(x_k)}{\partial x}\right|_{x_k=\bar{x}_i} (\hat{x}_k - \bar{x}_i). \tag{2.22}$$

Equation (2.22) differs from the ESMF prediction step as the current state estimate is passed through the nonlinear dynamics in the latter. The error dynamics are found by subtracting Equation (2.22) from Equation (2.20):

$$x_{k+1} - \hat{x}_{k+1} = \left.\frac{\partial f(x_k)}{\partial x}\right|_{x_k=\bar{x}_i} (x_k - \hat{x}_k) + \mathcal{R}_k\left(x_k - \bar{x}_i, \overline{X}_{k,k}\right) + w_k. \tag{2.23}$$

The term $\mathcal{R}_k\left(x_k-\bar{x}_i,\overline{X}_{k,k}\right)$ can be bounded by an interval such that, $\mathcal{R}_k \in \overline{X}_{\mathcal{R}_k}$, by defining $\overline{X}_{k,k}$ and evaluating $\mathcal{R}_k\left(x_k-\bar{x}_i,\overline{X}_{k,k}\right)$ using interval mathematics. For the scalar case this is,

$$\overline{X}_{\mathcal{R}_k}=\left(\overline{X}_{k,k}-\bar{x}_i\right)^T\frac{1}{2}\frac{\partial^2 f(\overline{X}_{k,k})}{\partial x}\left(\overline{X}_{k,k}-\bar{x}_i\right). \tag{2.24}$$

The expression for the general multi-state case is shown in Equation (2.32). In order to guarantee that the higher order terms are bounded, the hybrid estimator requires that the system be twice differentiable and smooth over all states and inputs.

The state interval is found by finding the extrema of the current state ellipsoid $\Omega\left(\hat{\mathbf{x}}_{\mathbf{k},\mathbf{k}},\Sigma_{k,k}\right)$:

$$[X_{k,k}]^j=\left[[\hat{x}_{k,k}]^j-\sqrt{[\Sigma_{k,k}]^{j,j}},\ \ [\hat{x}_{k,k}]^j+\sqrt{[\Sigma_{k,k}]^{j,j}}\right] \tag{2.25}$$

where the superscripts j denotes the j^{th} state and j,j denotes the (j^{th}-j^{th}) element of $\Sigma_{k,k}$. In contrast to the ESMF, the interval $\overline{\mathbf{X}}_{\mathbf{k},\mathbf{k}}$ in the hybrid formulation must explicitly include the current operating point to guarantee that $\mathcal{R}_k \in \overline{X}_{\mathcal{R}_k}$ bounds the linearization error:

$$\overline{\mathbf{X}}_{\mathbf{k},\mathbf{k}}=\mathbf{X}_{\mathbf{k},\mathbf{k}}\cup\left[\overline{\mathbf{x}}_{\mathbf{i}},\overline{\mathbf{x}}_{\mathbf{i}}\right], \tag{2.26}$$

where $\left[\overline{\mathbf{x}}_{\mathbf{i}},\overline{\mathbf{x}}_{\mathbf{i}}\right]$ is equivalent to a degenerate interval.

The interval of the remaining term is found by using the interval defined in Equation (2.26) and evaluating Equation (2.24) using interval mathematics. While there are many bounding ellipsoids available, a unique closed form can be found by minimizing the volume of the ellipsoid. If the volume is minimized, the closed form solution of the outer bounded ellipsoid is written as [2]

$$\left[\overline{Q}_{k,k}\right]_{\mathcal{R}_k}^{j,l}=2\left(\frac{\left[\overline{X}_{\mathcal{R}_k,+}\right]^j-\left[\overline{X}_{\mathcal{R}_k,-}\right]^j}{2}\right)^2,\ \text{ if }\ j=l,\ \ 0\ \text{ otherwise,} \tag{2.27}$$

for $j,\ \ l\in[1,\ldots,n]$ where $\left[\overline{X}_{\mathcal{R}_k,\pm}\right]^j$ represents the j^{th} element extrema of the interval in Equation (2.24) (see Ref. [19] for a derivation). The combined process noise bound,

$\hat{Q}_{k,k}$, is found by adding the ellipsoid bounding the linearization remainder, Equation (2.27), and the ellipsoid bounding the process noise, Q_k, or $\hat{Q}_{k,k} = \Omega_s(\overline{Q}_{k,k}, Q_k, \beta_Q)$, where β_Q is a scalar, $0 < \beta_Q < 1$. Note that $\Omega_s(\cdot,\cdot,\cdot)$ denotes the addition of two ellipsoids. A similar approach can be used for the update step.

A summary of the hybrid ESMF is given in Equations (2.31-2.52). The prediction step, Equations (2.39-2.40), is physically the addition of two ellipsoids: 1) the augmented noise ellipsoid $\Omega(0, \hat{Q}_{k,k})$ and 2) the state uncertainty ellipsoid $\Omega(\hat{\mathbf{x}}_{\mathbf{k},\mathbf{k}},, \Sigma_{k,k})$ rotated and scaled by the linearized dynamics, A_k^T and A_k. The update step, Equations (2.49-2.52), is the intersection of two sets: 1) the predicted state ellipsoid,

$$\Omega\left(\hat{\mathbf{x}}_{\mathbf{k+1},\mathbf{k}}, \Sigma_{k+1,k}\right), \tag{2.28}$$

and 2) the set described by the output equation

$$\Omega(\mathbf{y}_{\mathbf{k+1}}, \hat{R}_k). \tag{2.29}$$

The actual state, $\mathbf{x}_\mathbf{k}$, is then bounded by $\Omega(\hat{\mathbf{x}}_{\mathbf{k+1},\mathbf{k+1}}, \Sigma_{k+1,k+1})$, or

$$\left[\mathbf{x}_{\mathbf{k+1}} - \hat{\mathbf{x}}_{\mathbf{k+1},\mathbf{k+1}}\right]^T \Sigma_{k+1,k+1}^{-1} \left[\mathbf{x}_{\mathbf{k+1}} - \hat{\mathbf{x}}_{\mathbf{k+1},\mathbf{k+1}}\right] \leq 1. \tag{2.30}$$

When the initial state, noise, and higher order terms are bounded the δ_{k+1} term in Equation (2.51) has to be < 1. In the hybrid ESMF formulation, as the system moves away from an operating point a $\delta_{k+1} > 1$ means that the ellipsoid defined in Equation (2.37) is not correctly bounding the higher order terms suggesting that the continuity and smoothness assumptions on the system are invalid. The scalar parameters β_k and ρ_{k+1} in Equations (2.40), (2.49) are defined strictly between 0 and 1 can be optimized to minimize a metric on the size of the resulting set (the reader is referred to [2] for a more detailed discussion).

The switched ESMF algorithm can be summarized by the following steps performed on each of the operating points, $\overline{\mathbf{x}}_\mathbf{i}$, for $i \in [1, \ldots, N]$:

1. Calculate the Jacobian, Equation (2.31), evaluated at, $\bar{\mathbf{x}}_\mathbf{i}$.
2. Evaluate the Hessian, Equation (2.32).
3. Find the state interval, $\mathbf{X}_{\mathbf{k},\mathbf{k}}$ Equation (2.32), bound by computing the extrema of the current state ellipsoid, $\Omega\left(\hat{\mathbf{x}}_{\mathbf{k},\mathbf{k}}, \Sigma_{k,k}\right)$, Equation (2.34).
4. Find the union of the state interval, $\mathbf{X}_{\mathbf{k},\mathbf{k}}$, and the degenerate interval containing $\bar{\mathbf{x}}_\mathbf{i}$, Equation(2.35).
5. Evaluate the Lagrange Remainder, Equation (2.36), using interval mathematics.
6. Compute the ellipsoid, $\hat{Q}_{k,k}$, that bounds the Lagrange Remainder, Equation (2.37).
7. Find the ellipsoid that bounds the addition of the process noise ellipsoid, Q_k, and the Lagrange Remainder ellipsoid $\hat{Q}_{k,k}$.
8. Calculate the predicted state ellipsoid, Equations (2.39-2.40).
9. Using the state prediction $\hat{\mathbf{x}}_{\mathbf{k+1},\mathbf{k}}$, repeat steps 1-7 for the output dynamics, $h(\cdot)$, to calculate the ellipsoid that bounds the measurement noise ellipsoid, R_{k+1}, and the bounding ellipsoid of the Lagrange Remainder of output dynamics $\overline{R}_{k+1}$.
10. Calculate the updated state ellipsoid, $\Omega\left(\hat{\mathbf{x}}_{\mathbf{k+1},\mathbf{k+1}}, \Sigma_{k+1,k+1}\right)$, Equations (2.49-2.52).

Switched ESMF Prediction Step:

$$A_i = \left.\frac{\partial f(\mathbf{x_k})}{\partial \mathbf{x}}\right|_{\mathbf{x_k}=\bar{\mathbf{x}}_\mathbf{i}}, \tag{2.31}$$

$$H_{f^j} = \frac{\partial^2 f^j(\cdot)}{\partial \mathbf{x}^2}, \tag{2.32}$$

$$[X_{k,k}]^j = \left[[\hat{x}_{k,k}]^j_-, [\hat{x}_{k,k}]^j_+\right], \tag{2.33}$$

$$= \left[[\hat{x}_{k,k}]^j - \sqrt{[\Sigma_{k,k}]^{j,j}},\ [\hat{x}_{k,k}]^j + \sqrt{[\Sigma_{k,k}]^{j,j}}\right], \tag{2.34}$$

$$\overline{\mathbf{X}}_{\mathbf{k},\mathbf{k}} = \mathbf{X}_{\mathbf{k},\mathbf{k}} \cup [\bar{\mathbf{x}}_\mathbf{i}, \bar{\mathbf{x}}_\mathbf{i}], \tag{2.35}$$

$$\overline{\mathbf{X}}_{\mathcal{R}_\mathbf{k}} = \frac{1}{2} diag\left(\overline{\mathbf{X}}_{\mathbf{k},\mathbf{k}} - \overline{\mathbf{x}}_\mathbf{i}\right)^T \begin{bmatrix} H_{f^1}(\overline{\mathbf{X}}_{\mathbf{k},\mathbf{k}}) \\ \vdots \\ H_{f^n}(\overline{\mathbf{X}}_{\mathbf{k},\mathbf{k}}) \end{bmatrix} \left(\overline{\mathbf{X}}_{\mathbf{k},\mathbf{k}} - \overline{\mathbf{x}}_\mathbf{i}\right), \tag{2.36}$$

$$\left[\overline{Q}_{k,k}\right]^{j,l}_{\mathcal{R}_k} = 2\left(\frac{\left[\overline{X}_{\mathcal{R}_k,+}\right]^j - \left[\overline{X}_{\mathcal{R}_k,-}\right]^j}{2}\right)^2, \tag{2.37}$$

if $j = l$, 0 otherwise.

$$\hat{Q}_{k,k} = \Omega_s(\overline{Q}_{k,k}, Q_k, \beta_Q), \tag{2.38}$$

$$\hat{\mathbf{x}}_{\mathbf{k+1},\mathbf{k}} = f(\overline{\mathbf{x}}_\mathbf{i}) + A_i(\hat{\mathbf{x}}_\mathbf{k} - \overline{\mathbf{x}}_\mathbf{i}), \tag{2.39}$$

$$\Sigma_{k+1,k} = A_i \frac{\Sigma_{k,k}}{1-\beta_k} A_i^T + \frac{\hat{Q}_{k,k}}{\beta_k}, \tag{2.40}$$

Switched ESMF Update Step:

$$C_i = \left.\frac{\partial h(\mathbf{x}_\mathbf{k})}{\partial \mathbf{x}}\right|_{\mathbf{x}_\mathbf{k}=\overline{\mathbf{x}}_\mathbf{i}}. \tag{2.41}$$

$$H_{h^j} = \frac{\partial^2 h^j(\cdot)}{\partial \mathbf{x}^2}, \tag{2.42}$$

$$[X_{k+1,k}]^j = \left[[\hat{x}_{k+1,k}]^j_-, [\hat{x}_{k+1,k}]^j_+\right], \tag{2.43}$$

$$= \left[[\hat{x}_{k+1,k}]^j - \sqrt{[\Sigma_{k+1,k}]^{j,j}},\ [\hat{x}_{k+1,k}]^j + \sqrt{[\Sigma_{k+1,k}]^{j,j}}\right], \tag{2.44}$$

$$\overline{\mathbf{X}}_{\mathbf{k+1},\mathbf{k}} = \mathbf{X}_{\mathbf{k+1},\mathbf{k}} \cup \left[\overline{\mathbf{x}}_\mathbf{i}, \overline{\mathbf{x}}_\mathbf{i}\right], \tag{2.45}$$

$$\overline{\mathbf{X}}_{\mathcal{R}_{\mathbf{k+1}}} = \frac{1}{2} diag\left(\overline{\mathbf{X}}_{\mathbf{k+1},\mathbf{k}} - \overline{\mathbf{x}}_\mathbf{i}\right)^T \begin{bmatrix} H_{h^1}(\overline{\mathbf{X}}_{\mathbf{k+1},\mathbf{k}}) \\ \vdots \\ H_{h^n}(\overline{\mathbf{X}}_{\mathbf{k+1},\mathbf{k}}) \end{bmatrix} \left(\overline{\mathbf{X}}_{\mathbf{k+1},\mathbf{k}} - \overline{\mathbf{x}}_\mathbf{i}\right) \tag{2.46}$$

$$\left[\overline{R}_{k+1}\right]^{j,l}_{\mathcal{R}_{k+1}} = 2\left(\frac{\left[\overline{X}_{\mathcal{R}_{k+1},+}\right]^j - \left[\overline{X}_{\mathcal{R}_{k+1},-}\right]^j}{2}\right)^2, \tag{2.47}$$

if $j = l$, 0 otherwise.

$$\hat{R}_{k+1} = \Omega_s(\overline{R}_{k+1}, R_{k+1}, \beta_R), \tag{2.48}$$

$$\hat{\mathbf{x}}_{\mathbf{k+1},\mathbf{k+1}} = \hat{\mathbf{x}}_{\mathbf{k+1},\mathbf{k}} + \frac{\Sigma_{k+1,k}}{1-\rho_{k+1}} C_i^T \left[C_i \frac{\Sigma_{k+1,k}}{1-\rho_{k+1}} C_i^T + \frac{\hat{R}_{k+1}}{\rho_{k+1}} \right]^{-1} \left[\mathbf{y_{k+1}} - \left(h(\bar{\mathbf{x}}_\mathbf{i}) + C_i(\hat{\mathbf{x}}_{\mathbf{k+1},\mathbf{k}} - \bar{\mathbf{x}}_\mathbf{i}) \right) \right], \quad (2.49)$$

$$\bar{\Sigma}_{k+1,k+1} = \frac{\Sigma_{k+1,k}}{1-\rho_{k+1}} - \frac{\Sigma_{k+1,k}}{1-\rho_{k+1}} C_i^T \left[C_i \frac{\Sigma_{k+1,k}}{1-\rho_{k+1}} C_i^T + \frac{\hat{R}_{k+1}}{\rho_{k+1}} \right]^{-1} C_i \frac{\Sigma_{k+1,k}}{1-\rho_{k+1}}, \quad (2.50)$$

$$\delta_{k+1} = \left[\mathbf{y_{k+1}} - \left(h(\bar{\mathbf{x}}_\mathbf{i}) + C_i(\hat{\mathbf{x}}_{\mathbf{k+1},\mathbf{k}} - \bar{\mathbf{x}}_\mathbf{i}) \right) \right]^T \left[C_i \frac{\Sigma_{k+1,k}}{1-\rho_{k+1}} C_i^T + \frac{\hat{R}_{k+1}}{\rho_{k+1}} \right]^{-1} \left[\mathbf{y_{k+1}} - \left(h(\bar{\mathbf{x}}_\mathbf{i}) + C_i(\hat{\mathbf{x}}_{\mathbf{k+1},\mathbf{k}} - \bar{\mathbf{x}}_\mathbf{i}) \right) \right], \quad (2.51)$$

$$\Sigma_{k+1,k+1} = (1-\delta_{k+1})\bar{\Sigma}_{k+1,k+1}. \quad (2.52)$$

2.3.2 Piecewise Linear Estimator Selection

It is proposed here to switch estimators based on the size of the uncertainty, while maintaining boundedness in the uncertainty through the mode transitions. There are several approaches to this, such as using the actual state uncertainty, the higher order term uncertainty, or using a normalized version of these. Part of the study here is to evaluate and compare metrics.

Each of the i estimators develop a bound of the state in the form of an ellipsoid, $\Omega\left(\hat{\mathbf{x}}_{\mathbf{k},\mathbf{k}}, \Sigma_{k,k}\right)$. The true state is guaranteed to lie within this ellipsoid for all i estimators; the quality of the estimate can be assessed by evaluating the size of the uncertainty bound. In the ESMF, the size of the bound is influenced by the measurement, the process and measurement noise, and the higher order term uncertainty. In the hybrid formulation of the ESMF, the linearization remainder inherently increases as the system moves away from the operating points. The quality of the estimate is evaluated by comparing (in terms of a scalar metric) the "size" of the uncertainty ellipsoids, $\Omega\left(\hat{\mathbf{x}}_{\mathbf{k},\mathbf{k}}, \Sigma_{k,k}\right)$. The advantage of this metric is that it is the "true" evaluation of the estimator performance. Metrics that could be used include the trace, determinant (volume), and maximum eigen

value of $\Sigma_{k,k}$ (largest dimension). In practice, the trace is often used for this purpose because of its speed of computation. An alternative metric can be developed for estimator selection based on the bound on the linearization remainder, such as $\Omega\left(\mathbf{0}, \hat{Q}_{k,k}\right)$ or $\Omega\left(\mathbf{0}, \hat{R}_k\right)$. The advantage of this metric is that it isolates the influence of the linearization remainder on the size of the uncertainty, which is the primary difference between the estimators. Because these metrics do not consider the measurement, $\mathbf{y_{k+1}}$, the metrics immediately react to fluctuations in the linearization error.

In addition to using the uncertainty for estimator selection, based on $\Sigma_{k,k}$, $\hat{Q}_{k,k}$, and $\hat{R}_k$, a scaling can be used to change the relative magnitude of elements of the matrices. Consider the scaling matrix of the following form:

$$S_{(\cdot)} = S \cdot (\cdot) \cdot S^T, \tag{2.53}$$

where s^j scales elements of the matrix $(\cdot)$. $S = diag\left(s^1, \ldots, s^n\right)$. As an example, consider $\mathcal{X}^{j,-}$, $\mathcal{X}^{j,+}$ which denote the minimum and maximum values respectively that the j^{th} element of the state achieves in the operating range $\mathcal{X}$. In cases where the relative magnitude of the state variables is not equal, the scaling s_i can be defined as follows:

$$s^j = \frac{1}{\sqrt{\mathcal{X}^{j,+} - \mathcal{X}^{j,-}}}. \tag{2.54}$$

Let $J_i = f(\cdot)$ denote the evaluation of an uncertainty metric corresponding to the i^{th} model where $f(\cdot)$ could be the trace, determinant, or maximum eigenvalue of $\Sigma_{k,k}$, $\hat{Q}_{k,k}$, $\hat{R}_k$, or $S_{(\cdot)}$.

The proposed bounded hybrid estimator is modelled as a hybrid automaton. Each node, q_i, in the graph represents the model currently used. Let $J_i(\cdot)$ denote the evaluation of an uncertainty metric corresponding to the i^{th} model. Portions of all filters must evolve in order to evaluate $J_i(\cdot)$ at each time step. At each time step, the state estimate and state uncertainty are calculated by using only the i^{th} model that is associated with the i^{th} node. In stricter mathematical terms, let $Q = \{q_1, q_2, \ldots, q_i, \ldots, q_n\}$ be the set

of discrete states and define the discrete variable $\overline{q} \in Q$. The current state estimate and uncertainty remain in the domain of q_i, where the domain is defined as follows:

$$Dom(q_i) = \left\{ J_i(\cdot) \in \mathbb{R} \mid J_i(\cdot) = \min_i [J_1(\cdot), \ldots, J_N(\cdot)] \right\}, \tag{2.55}$$

as long as the uncertainty metric for the i^{th} estimator is the minimum. Equation (2.55) states that the current model (node on the graph) is active as long as the scalar metric, $J_i(\cdot)$, is the smallest among all models. Otherwise, the guards dictate which other model is selected to compute the next step of the estimator.

To prevent unnecessary sensitivity in the model transitions, "memory" can be imparted onto the expression of Equation (2.55) by counting the number of times that the minimum uncertainty metric associated with the i^{*th} estimator does not correspond to the current discrete state, q_i. At every step, if $i^* \neq i$ then a counter is increased, $\eta = \eta + 1$. Equation (2.55) can be rewritten to include this memory term in the following way:

$$Dom(q_i) = \left\{ J_i(\cdot) \in \mathbb{R} \mid J_i(\cdot) = \min_i [J_1(\cdot), \ldots, J_N(\cdot)] \text{ OR } \eta < \mathrm{L} \right\}, \tag{2.56}$$

where L is length of the memory. This is done in order to minimize the effects of noise in switching, and to retard a model switch until there is enough information to warrant a transition. The difference between Equation (2.55) and Equation (2.56) is that in the latter the scalar uncertainty metric for a model must be the smallest for L steps before a switch occurs. The next model is selected by evaluating a guard for i^{th} node that has the following form:

$$G(q_i, q_{i+1}) = \left\{ J_i(\cdot) \in \mathbb{R} \mid J_{i+1} = \min_i [J_1(\cdot), \ldots, J_N(\cdot)] \right\}. \tag{2.57}$$

The guard allows the transition from q_i to q_{i+1} if the metric for the $(i+1)^{th}$ estimator is the minimum. If a transition occurs then the estimate and state ellipsoid of the $(i+1)^{th}$ estimator is selected to be the active estimator. After a transition, the continuous state remains the same, but the counter is reset, $\eta = 0$.

2.3.3 Stability Analysis

For real time implementation, it is important to understand the stability characteristics of an estimator. For the hybrid estimator, analysis shows if nonlinear observability is maintained both the state ellipsoid and the error dynamics (error between the center of the ellipsoid and the true state) are bounded. This issue is further discussed in the Appendix A.

2.3.4 Numerical Example

In order to gain insight into how the hybrid observer functions, it is applied to the relative motion of one aircraft with respect to another,

$$\begin{aligned} x_{r,k+1} &= x_{r,k} + T[-v_{0,k} + v_{1,k}\cos\psi_{r,k} + \omega_0 y_{r,k}] &= f^1 \\ y_{r,k+1} &= y_{r,k} + T[v_{1,k}\sin\psi_{r,k} - \omega_0 x_{r,k}] &= f^2 \\ \psi_{r,k+1} &= \psi_{r,k} + T[\omega_1 - \omega_0] &= f^3 \end{aligned} \tag{2.58}$$

where $(x_r, y_r, \psi_r) \subset \mathcal{X} = [0,20] \times [0,20] \times [0, \frac{\pi}{2}]$, is the relative position and orientation of aircraft 1 with respect to aircraft 0 and v_i and ω_i are the linear and angular velocities of each aircraft, $\omega_0 = \omega_1 = 0$. The control input is the linear velocity of aircraft 0, $u_k = v_{0,k} = 0$, the disturbance is the linear velocity of aircraft 1, $d_k = v_{1,k} = 10$, and $T = 0.01$ is the sampling time. The sensor output is:

$$\mathbf{y_{k+1}} = \begin{bmatrix} x_{r,k+1} \\ \\ y_{r,k+1} \end{bmatrix} + \mathbf{v_{k+1}}. \tag{2.59}$$

The trajectory for the system is shown in Figure 2.1.

Since the purpose of the switched piecewise linear observer is to minimize the number of models necessary for accurate estimation, it would be impossible to guarantee accuracy without defining an operating region, $\mathcal{X}$, in which the system is expected to

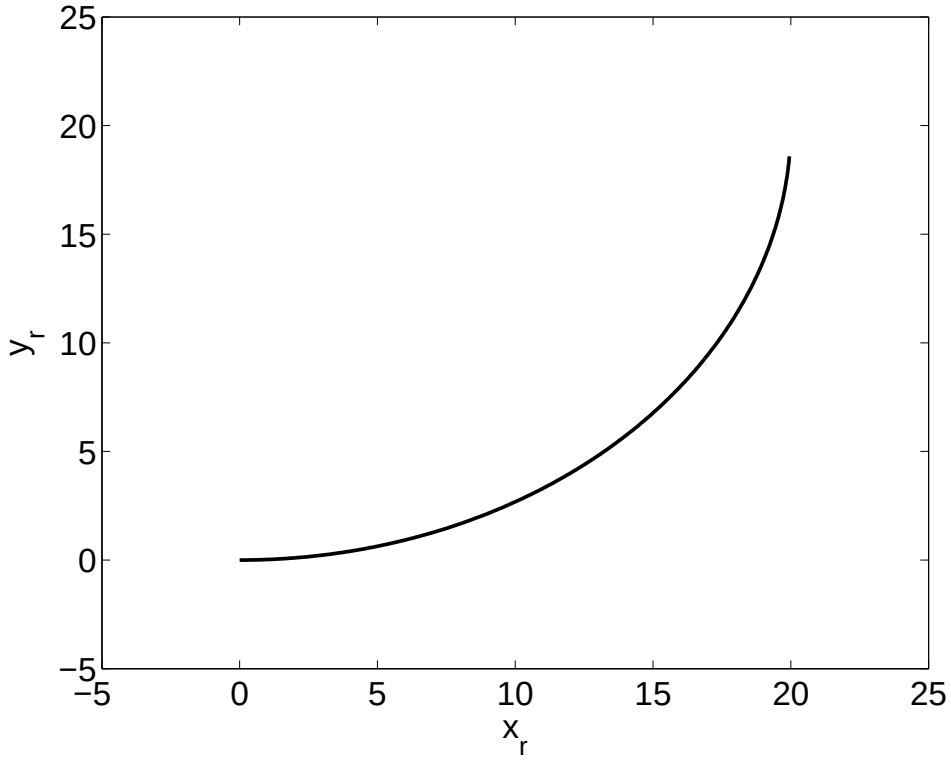

Figure 2.1: Relative motion of plane 1 with initial conditions $[0, 0, 0]^T$.

operate. This requirement is not overly restrictive as in estimation and tracking applications a priori information about the speed and agility of the system is used to define prediction models and to tune noise parameters.

For the case of three operating points, $N = 3$, Figure 2.2 shows the state ellipsoid uncertainty metric, $tr\left(\Sigma_{k,k}\right)$. The dashed horizontal lines in Figure 2.2 show the location of the operating points, $\bar{\mathbf{x}}_\mathbf{i}$, for each of the three models. As the system evolves in time the value of the linearization remainder and uncertainty metrics change for the three models. Model switches which are shown by the vertical dashed lines in the figure. The figure shows that for $t < 1$, when the state is near the initial condition, the estimator implemented with the first operating point, $\bar{\mathbf{x}}_\mathbf{3} = [0,0,0]$, has a smaller uncertainty (as measured by $tr(\Sigma_{k,k})$) than the other two estimators. As the system moves towards $\psi_r \rightarrow \frac{\pi}{4}$ radians, the uncertainty of the estimator using the model defined around the

second operating point, $\bar{\mathbf{x}}_{\mathbf{2}} = [0, 0, 0.82]$, decreases because the linearization remainder for this estimator becomes smaller. The same can be said as $\psi_r \rightarrow \frac{\pi}{2}$ for the estimator using the third model around the operating point, $\bar{\mathbf{x}}_{\mathbf{3}} = [0, 0, 1.35]$.

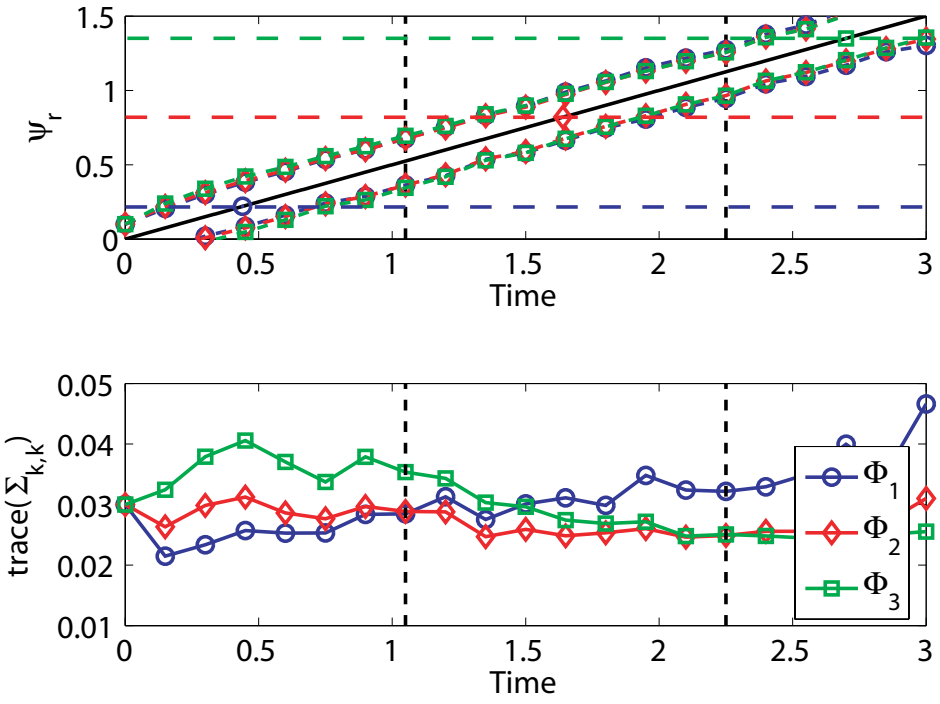

Figure 2.2: Estimate and bounds on the orientation $\psi_{r,k}$ for estimators run with constant plant models $\overline{\psi}_{1,2,3} = 0.22$, 0.82, and 1.35 radians and the trace of the uncertainty for systems with these models. In the upper figure the location of the operating points is shown by horizontal dashed lines. Model switches are marked by vertical dashed lines in the upper and lower plot.

Figure 2.3 compares two types of switching criteria: the full state uncertainty, or $tr(\Sigma_{k,k})$, and the bounded remainder bound, or $tr(\hat{Q}_{k,k})$. As the heading changes from 0 to $\frac{\pi}{2}$, each of the metrics selects which estimator (model and operating point) is more appropriate. As seen in Figure 2.3, switching between models using $\left(\Sigma_{k,k}\right)$ occur later, but is relatively similar in profile to the other two switching metrics. The vertical dashed line in this figure marks the time at which a switch first occurs for estimators based on using $\hat{Q}_{k,k}$ for model selection. Switching occurs earlier compared to the switching pro-

file found using $tr(\Sigma_{k,k})$. The effects of the linearization are somewhat masked in the $tr(\Sigma_{k,k})$ cost by the sensor update, which is why the switch times are delayed. However, $tr(\hat{Q}_{k,k})$ is more sensitive to noise as some jittering is observed in the transition from model 1 to model 2 ($0.8 < t1.2$ sec)compared to the $\left(\Sigma_{k,k}\right)$ switching profile. The sensitivity of using $tr(\hat{Q}_{k,k})$ is also caused by not using the update portion of the estimator when evaluating the switching logic. For the entire switching trajectory, $0.0 < t < 3.0$ sec, switching based on $tr(\hat{Q}_{k,k})$ results in a total of 10 mode changes. Figure 2.3 also shows the results of the hybrid estimator using the bounded remainder as the switching metric and a memory of $L = 3$, which is designed to counteract the sensitivity near the model switching. In this case, the number of intermediate switches are reduced from 10 in the case of $L = 1$ to 3 in the case $L = 3$.

2.4 A Priori Selection of the Base Piecewise Linear Models and Operating Points

The size of the uncertainty in the hybrid estimator, as defined by any of the metrics in Section 2.3.2, is a function of the number of operating points N as well as their location, $\bar{\mathbf{x}}_\mathbf{i}$. Thus, the designer can select either the number of individual estimators N or the size of uncertainty (Section 2.3.2) of the bounded hybrid estimator prior to implementation.

A procedure is developed here to find the location of N operating points used in the hybrid estimator by minimizing the system uncertainty. Inside the operating range $\mathcal{X}$, N operating points are defined as $\bar{\mathbf{x}}_\mathbf{i}$ for $i = \{1,...,N\}$ As mentioned in Section 2.3.4, to minimize the number of plant models used in estimation it is necessary to define an operating region in which the system is expected to operate. If such operating region, $\mathcal{X}$, is not known a priori or becomes invalid, then the estimation accuracy of the switched linear estimator is not guaranteed and other estimation methods should be considered.

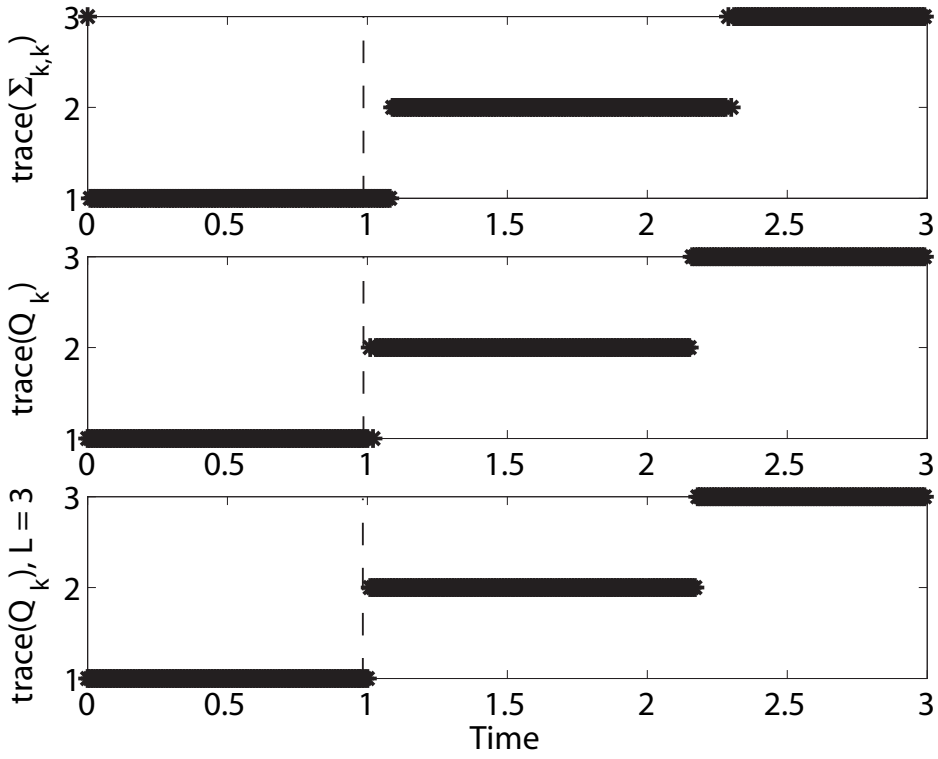

Figure 2.3: Constant plant models $\overline{\Psi}_{1,2,3} = 0.22$, 0.82, and 1.35 chosen by considering the trace of the state ellipsoid and the trace of combined process noise ellipsoid. Model switching with memory, $L = 3$, is shown in the lower plot. The vertical dashed lines show the time at which a switch from the first to second model occurs based on using the $tr(\hat{Q}_{k,k})$ uncertainty metric.

Based on the dynamics in Equation (2.1), a Hessian-like term for j^{th} component of $f(\mathbf{x_k})$ and the i^{th} operating point is (with the subscript k dropped for clarity):

$$H_i^j(\mathbf{x}, \overline{\mathbf{x}}_\mathbf{i}) = (\mathbf{x} - \overline{\mathbf{x}}_\mathbf{i})^T \left. \frac{\partial^2 f^j(\mathbf{x})}{\partial \mathbf{x}^2} \right|_{\mathbf{x}=\overline{\mathbf{x}}_\mathbf{i}} (\mathbf{x} - \overline{\mathbf{x}}_\mathbf{i}). \tag{2.60}$$

This Hessian-like term is proportional to the size of the linearization remainder as described in Equation (2.21). The goal is to place the N operating points, $\overline{\mathbf{x}}_\mathbf{i}$, such that the term in Equation (2.60) is minimized throughout the operating range defined by $\mathcal{X}$. Said another way, the location of the operating points should be chosen such that the maximum uncertainty achieved by the set of N operating points is minimized.

Consider the following cost which defines the maximum value of the Hessian-like

term (Equation (2.60)) over the operating range for the i^{th} operating point:

$$J_i^*(\mathbf{x}_\mathbf{i}^*, \overline{\mathbf{x}}_\mathbf{i}) = \max_{\mathbf{x}\in\mathcal{X}} \; J\left(S \cdot diag\left[H_1^j(\mathbf{x}, \overline{\mathbf{x}}_\mathbf{i}), \ldots, H_N^j(\mathbf{x}, \overline{\mathbf{x}}_\mathbf{i})\right] \cdot S^T\right), \tag{2.61}$$

where the state that denotes this maximum is defined as $\mathbf{x}_\mathbf{i}^*$, and S is a scaling matrix, and $J(\cdot)$ is an uncertainty metric (both defined in Section 2.3.2). Note that optimization must be used to evaluate 2.61 as the value of $\mathbf{x} \in \mathcal{X}$ must be varied to find the maximum values of the terms $H_1^j, \ldots, H_N^j$.

Using the cost given in Equation (2.61) as the basis, the following optimization is defined to find the operating points,

$$J_{MODEL}^* = \min_{\overline{\mathbf{x}}_\mathbf{i}\in\mathcal{X}} \left\{ \max_i \left(J_1^*[\mathbf{x}_\mathbf{1}^*, \overline{\mathbf{x}}_\mathbf{1}], \ldots, J_N^*[\mathbf{x}_\mathbf{N}^*, \overline{\mathbf{x}}_\mathbf{N}]\right) \right\}. \tag{2.62}$$

The inner maximization in Equation (2.62) selects the worst case uncertainty (largest remainder bound in $\mathcal{X}$) among the N operating points, while the outer minimization attempts to minimize the worst case uncertainty by changing the location of the operating points, $[\overline{\mathbf{x}}_\mathbf{1}, \ldots, \overline{\mathbf{x}}_\mathbf{N}]$. The same optimization procedure can be defined for the output equation of the system.

The optimization defined in Equation (2.62) focuses on minimizing the worst case higher order terms of the system dynamics (Equation (2.39), which obviously affects the prediction step). A similar optimization of course can be performed for the higher order terms of the output (Equation (2.49), which obviously affects the update step). A procedure is developed here based on the steady state uncertainty, which then combines the effects of the higher order uncertainty from both the system dynamics and output. The approach here is to use the Bersekas formulation of the set-membership filter [20] as opposed to the Schweppe formulation presented in Section 2.2, because the state uncertainty matrix $\Sigma_{k,k}$ does not depend on the observation and will converge to a steady state value, i.e. $\lim_{k\to\infty} \Sigma_{k,k} = \Sigma_{ss}$ [20]. It is noted that both approaches are outer bounding

and related. The Bertsekas formulation differs in how the state matrix is propagated,

$$\Sigma_{k,k} = \left[(1-\rho_{k+1}) \overline{\Sigma}_{k,k}^{-1} + \rho_{k+1} C_{k+1}^T \hat{R}_{k+1}^{-1} C_{k+1} \right]^{-1} \tag{2.63}$$

$$\delta_k = (1-\beta_{k-1})(1-\rho_k)\delta_{k-1} + (z_k - C_k A_{k-1} \hat{x}_{k-1})^T \tag{2.64}$$

with the initial condition, $\delta_0 = 0$. In the Bertsekas based ESMF, Equations (2.50,2.51) are replaced by Equations (2.63,2.64) respectively. The actual state $\mathbf{x_k}$ is bounded by $\Omega(\hat{\mathbf{x}}_{\mathbf{k+1,k+1}}, (1-\delta_{k+1})\Sigma_{k+1,k+1}^{-1})$.

The model selection process is proposed as follows. Define a diagonal matrix, Σ_{max}, which defines a maximum allowable ellipsoid uncertainty bound in the state estimate. The procedure to find the location and minimum number of N operating points to satisfy the uncertainty described by Σ_{max} is the following:

Choose Σ_{max} based on a desired level of uncertainty, and $N = 0$:

1. Solve the steady state linear SMF, Equations (2.40,2.50,2.63,2.64), with no round-off uncertainty, or $\hat{Q}_{k,k} = Q$, to find the smallest steady state uncertainty, $\Sigma_{ss} = \lim_{k\to\infty} \Sigma_{k,k}$. For $j \in [1,\ldots,n]$, if $\Sigma_{max}^{j,j} > [\Sigma_{ss}]^{j,j} \ \forall j$ then go on to step 2; else redefine Σ_{max} because the current Σ_{max} is infeasible.

2. Add one operating point within $\mathcal{X}$, for a total $N = N+1$ operating points .

3. Solve the nonlinear minimax optimization problem, Equation (2.62), for N operating points, $[\overline{\mathbf{x}}_\mathbf{1}, \ldots, \overline{\mathbf{x}}_\mathbf{N}]$, and the maximum higher order term uncertainty, J_{MODEL}^*.

4. Find the process noise bound, $\hat{Q}_{ss}$, by adding maximum roundoff uncertainty for N operating points, $\overline{Q}_{max}^N$ and original process noise, $\hat{Q}_{ss} = \Omega_s\left(\overline{Q}_{max}^N, Q, \beta_Q\right)$. It should be noted that the k subscript has been dropped from the process noise ellipsoid as for this algorithm it must be constant or the *maximum* (worst case) value of the noise ellipsoid must be considered. To compute $\overline{Q}_{max}^N$, define the

interval $[\overline{X}]^j = \left[[x_i^*]^j \pm \sqrt{[\Sigma_{max}]^{j,j}}\right]$, evaluate $\overline{Q}_{k,k}$ using a bounding method similar to Equations (2.32,2.37). By replacing $\hat{Q}_{k,k}$ with $\hat{Q}_{ss}$ in Equations (2.40,2.50, 2.63,2.64), find the steady state uncertainty, Σ_{ss}^N.

5. If $[\Sigma_{ss}^N]^{j,j} > \Sigma_{max}^{j,j}$ for any j, then go to step 2, else the location $\overline{\mathbf{x}}_\mathbf{i}$ and number N of operating points that meet the desired uncertainty Σ_{max} has been found.

Referring back to the system presented in Equation (2.58), the nonlinear minimax optimization problem, Equation (2.62), relates the location and number of the operating points with a given level of uncertainty. The cost function is in general nonconvex due to the structure of the objective function; therefore convergence to a global minimum is not guaranteed [21]. Sequential quadratic programming is used to minimize Equation (2.62) in MATLAB. The algorithm is initialized by selecting F points from a uniform distribution spanning $\mathcal{X}$. The insert of Figure 2.4 shows the cost, $J_{MODEL}^*(\cdot)/(Tv_1)$, (Equation (2.62) for $N = 3$ normalized by Tv_1) for $F = 1000$ initial starting points. For comparison purposes, an exhaustive search over $\mathcal{X}$ yields the "smallest" uncertainty cost to be $J_{MODEL}^*(\cdot)/(Tv_1) = 0.006$. Figure 2.4 also presents the percentage of optimized solutions that converge to a given percentage threshold of $J_{MODEL}^*(\cdot)/(Tv_1)$. The extreme nonlinear nature of the optimization makes it very difficult to find optimal solutions, and as shown in Figure 2.4, the algorithm indeed does find suboptimal solutions. The points below the dashed line in the inset figure are the points that are within 10% of the $J_{MODEL}^*(\cdot)/(Tv_1)$ found from the exhaustive search. However, Figure 2.4 suggests that, for a desired solution to be within 10% of $J_{MODEL}^*(\cdot)/(Tv_1)$, the algorithm can be solved p times and $\frac{p}{2}$ of the solutions will be within the bound. Figure 2.5 shows the $tr\left(\Sigma_{k,k}\right)$ cost for $N = 2,3,5$ operating points. Comparing these curves, the uncertainty metric decreases quickly with N. While indirect, the *a priori* model selection process attempts to minimize the peaks shown in Figure 2.5. As more operating points are added, the uncertainty of the system decreases and approaches the uncertainty of the full ESMF.

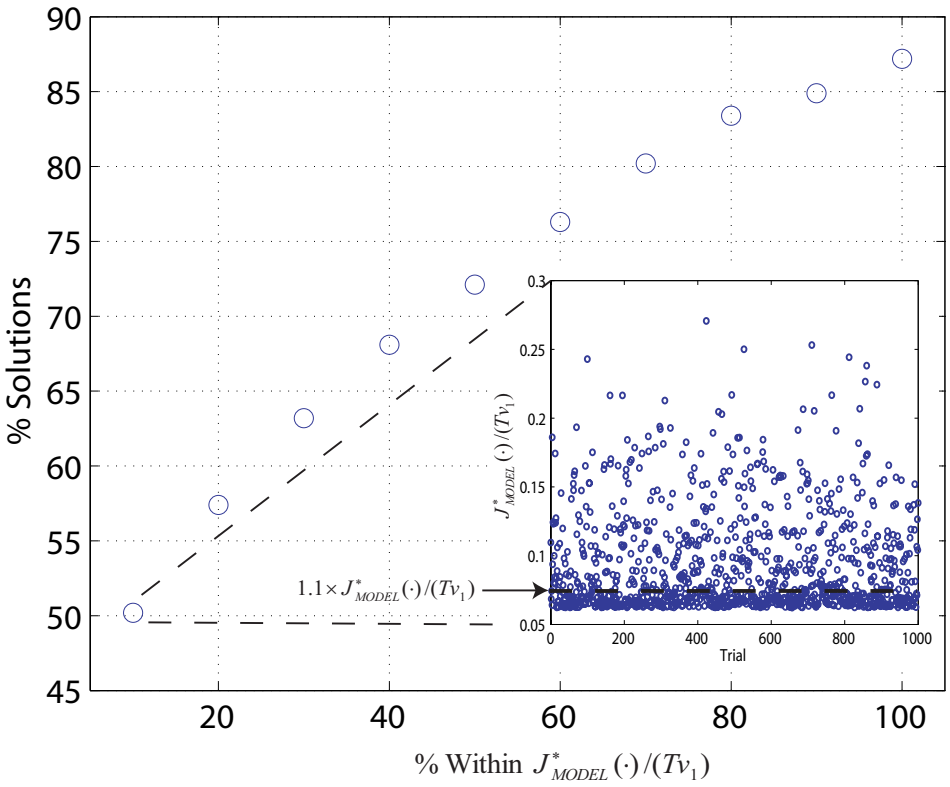

Figure 2.4: Percentage of solutions that are within a percentage of the minimum value of the objective function for the example in Equation (2.58).

2.5 Algorithm Summary

The implementation of the linear switched estimator is shown in Figure 2.6 is divided in two parts: 1) the off-line optimization to find the number and location of operating points, and 2) the on-line model selection and estimation. Optimizing the cost function defined in Equation (2.62) must be done off-line as finding a solution (even if suboptimal) is computationally expensive. The set of operating points is found using the procedure proposed in 2.4 and the set becomes an input to the on-line portion of the algorithm. The lower part of Figure 2.6 shows the on-line linear switched estimator algorithm that has as inputs the set of operating points found off-line as well as the current: 1) state estimate, $\hat{\mathbf{x}}_{\mathbf{k},\mathbf{k}}$, 2) state ellipsoid, $\hat{\Sigma}_{k,k}$, 3) discrete state (model with the least

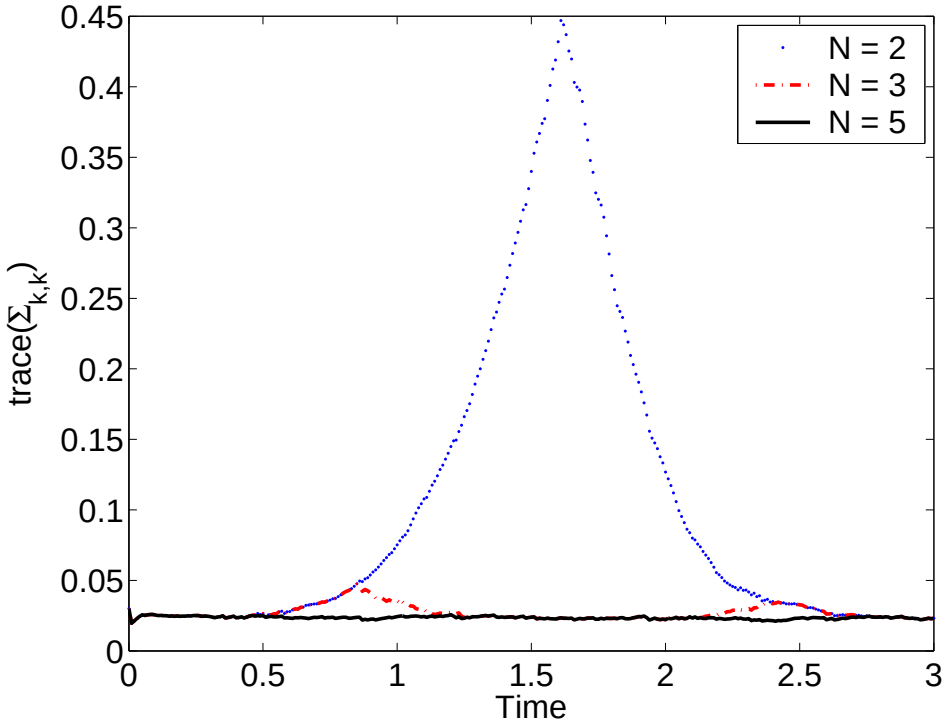

Figure 2.5: The bound on $\psi_{r,k}$ for two, three, and five operating models for the example in Equation (2.58).

uncertainty), $\hat{q}_k$, 4) the control input, u_k, and 5) measurement, $\mathbf{y_{k+1}}$. The linear switched estimator then bounds the higher orders terms for the N models, Equations (2.32-2.38). The N models are then propagated for one step, Equations (2.39-2.40), and the resulting uncertainty is evaluated using any of the metrics proposed in 2.3.2. The model with the least uncertainty is selected and the estimate and state ellipsoid at time $k+1$ is then calculated.

2.6 High Performance Aircraft Simulation Example

To evaluate the proposed hybrid estimator and its design tools, an aircraft example is used that considers the longitudinal dynamics of a high-performance F-16-like aircraft. The longitudinal nonlinear dynamics of a high performance F-16-like model are consid-

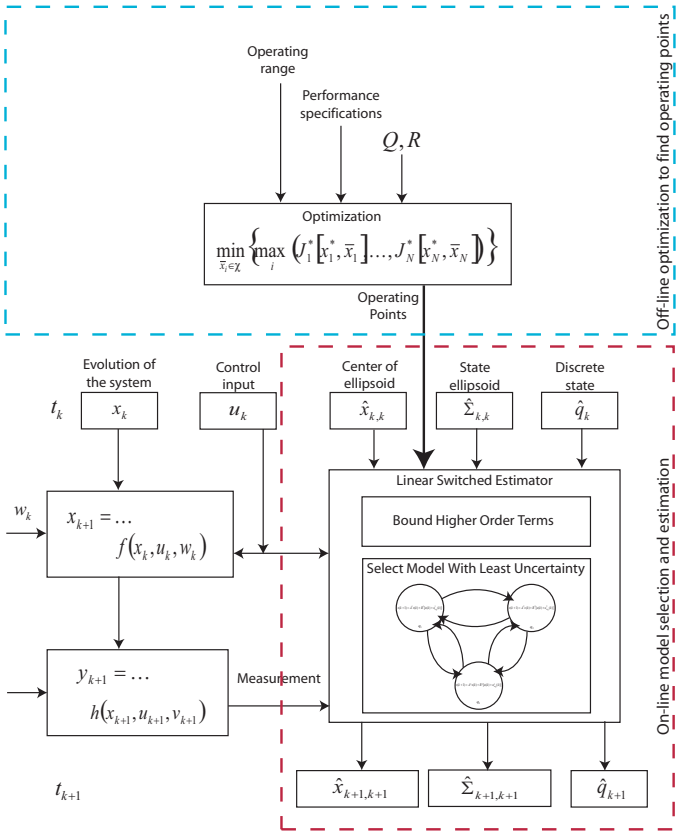

Figure 2.6: The cycle of the linear switched estimator. The off-line optimization used to find the number and location of operating points is shown in the upper portion and the on-line model selection and estimation process is shown in the lower portion of the figure.

ered here because the uncertainty is multi-dimensional and a function of four variables. Also, there is a large body of work in gain scheduled control for aircraft that could be utilized by this switched linear estimator concept.

The nonlinear continuous dynamics of the aircraft are given by:

$$\begin{array}{rcll} \dot{x}_p & = & V\cos(\theta-\alpha) & = f^1 \\ \dot{h} & = & V\sin(\theta-\alpha) & = f^2 \\ \dot{\theta} & = & q & = f^3 \\ \dot{V} & = & -g\sin(\theta-\alpha)+\frac{(T+F_x)\cos\alpha+F_z\sin\alpha}{m} & = f^4 \\ \dot{\alpha} & = & q+\frac{g}{V}\cos(\theta-\alpha)+\frac{F_z\cos\alpha-(T+F_x)\sin\alpha}{mV} & = f^5 \\ \dot{q} & = & \frac{1}{J_{AC}}\left[\overline{Q}S\overline{c}\left(C_m+\frac{2\overline{c}}{V}C_{mq}q\right)+F_z\left(x_{ac}-x_{cg}\right)\right] & = f^6 \end{array} \tag{2.65}$$

where the state is $\mathbf{x} = [x_p \;\; h \;\; \theta \;\; V \;\; \alpha \;\; q]^T$, which includes the aircraft's relative position, altitude, pitch, speed, angle of attack, and pitch rate [22]. The two control actuators are the thrust, T, and elevator deflection angle, δ_e. The aeroforces F_x and F_z are assumed to have the following form: $F_x = \widetilde{Q}\widetilde{S}\left(C_x+\frac{\bar{c}}{2V}C_{xq}q\right)$, $F_z = \widetilde{Q}\widetilde{S}\left(C_z+\frac{\bar{c}}{2V}C_{zq}q\right)$, where $\widetilde{S}$ is the wing area, $\bar{c}$ is the chord length, J_{AC} is the moment of inertia, x_{ac} is the aerodynamic center, x_{cg} is the center of gravity. The dynamic pressure, $\widetilde{Q}(V,h)$, is obtained from a look-up table based on altitude, and C_m, C_{mq}, C_z, C_{zq}, C_x, and C_{xq} are stability derivatives and are functions of the angle of attack and elevator deflection angle.

The Hessians, $H_{f^j} = \frac{\partial^2 f^j(\cdot)}{\partial \mathbf{x}^2}$, are obtained analytically by using the nonlinear equations of motion and are found to have the following variable dependence: $H_{f^1}(\theta,V,\alpha)$, $H_{f^2}(\theta,V,\alpha)$, $H_{f^3}=0$, $H_{f^4}(\theta,V,\alpha,q)$, $H_{f^5}(\theta,V,\alpha,q)$, and $H_{f^6}(V,q)$.

The sensor and process noise for the system has the following form: $\eta = g(\underline{\eta})$, where $\underline{\eta} \sim \mathcal{N}(0,\sigma^2)$ and $g(\cdot)$ is a transformation function that passes only values within $\pm\sigma$ of the mean. The result is a mixed random variable, η, that does not violate the assumptions of the ESMF because $\eta_k \in \Omega(0,\sigma^2)$ for all k. The output measurements are composed of the following, which are typical for aircraft, $y = [x_p \;\; h \;\; \theta \;\; V \;\; \alpha \;\; q]^T + v$. The parameters for this simulation are as follows: $T = 0.01$, $Q_k = 0.01I$ where I is the identify matrix $\in \mathbb{R}^{6,6}$, $R_k = \text{diag}(10,10,0.075,1,0.075,0.075)$, $\Sigma_{max}(3,3) < 10^\circ$, $\Sigma_{max}(5,5) < 10^\circ$.

For this example, the simulation parameters are listed in Table 2.1.

Table 2.1: Longitudinal Dynamics of a High Performance Aircraft System Parameters.

Parameter	Value
T	0.01
Q_k	diag(0.01,0.01,0.01,0.01,0.01,0.01)
R_k	diag(10,10,0.075,1,0.075,0.075)
$\Sigma_{max}(3,3)$	$< 10^\circ$
$\Sigma_{max}(5,5)$	$< 10^\circ$

Selection of Operating Points: The operating region, $\mathcal{X}$, is defined by the following inequalities: $-24^\circ \leq \theta \leq 24^\circ$, 400 ft/sec $\leq V \leq 650$ ft/sec, $-24^\circ \leq \alpha \leq 24^\circ$, $-20^\circ/sec \leq q \leq 20^\circ/sec$. As mentioned in 2.4, if the system is not in the operating region, $\mathbf{x} \in \mathcal{X}$, then the accuracy of the switched linear estimator is not guaranteed and other estimation methods must be considered.

The trajectory that the aircraft follows consists of three pieces: 1) flying at a constant altitude and speed, 2) performing a climbing maneuver, and 3) settling to a constant altitude and speed flight; the altitude and speed for this trajectory are shown in Figure 2.7(a),(b). If a trim condition is defined as aircraft motion where $\dot{\theta} = q = \dot{\alpha} = 0$, then the three sections of the trajectory in this example are ideal trim conditions. Three LQR controllers at each of the three trim conditions are implemented to allow the aircraft to follow the desired trajectory. It is noted that the number and location of the operating points are calculated to minimize the uncertainty within the operating region and are independent of the particular trajectory the system follows.

The design specifications require that the uncertainty for the pitch and angle of attack are less than 10.0°, resulting in the matrix: $\Sigma_{max} = diag(\kappa, \kappa, 10^2, \kappa, 10^2, \kappa)$, where $\kappa = 1 \times 10^6$ because these states are not part of the design.

1. The first step of the design procedure described in 2.4 solves the ESMF equations with roundoff error, $\overline{Q}_{k,k} = 0$ and $\hat{Q}_{k,k} = Q$, to determine whether the design specifications can be met in this system. Equations (2.40,2.50,2.63,2.64) yield the

following steady-state uncertainty ellipsoid,

$\Sigma_{ss} = diag\left(3.6^2,\ 3.6^2,\ 9.3^2,\ 1.1^2,\ 9.3^2,\ 9.3^2\right)$. Examining Σ_{ss} shows that the uncertainty in θ and α satisfy the design requirements, or $[\Sigma_{ss}]^{j,j} < \Sigma_{max}^{j,j}$ for $j = [3,5]$. Therefore it is not necessary to redefine the specifications, Σ_{max}, or to reconfigure the system (such as sensor changes).

2. Add one operating point within $\mathcal{X}$, $N = N + 1$.

3. The solution of a nonlinear minimax optimization problem, Equation (2.62), is required using N operating points. For this example, sequential quadratic programming was implemented in MATLAB and initialized at 1000 different points randomly selected within $\mathcal{X}$. The value of the objective function, $J^*_{MODEL}(\cdot)$ in Equation (2.62), decreases as operating points are added as shown in Table 2.2.

4. For $N = 1$, substituting $\overline{Q}^1_{max}$ into Equation (2.40) and solving Equations (2.50), (2.63), (2.64) reveals that the uncertainty for θ is $\sqrt{[\Sigma^1_{ss}]^{3,3}} = 9.61^\circ$ and for α is $\sqrt{[\Sigma^1_{ss}]^{5,5}} = 10.92^\circ$.

5. Because the uncertainty in α violates the design specification, $[\Sigma^1_{ss}]^{5,5} > \Sigma^{5,5}_{max}$, the procedure iterates back to step 2 with additional operating points added. Table 2.2 shows that $N = 3$ operating points must be used in order to satisfy the specification $\left[\Sigma^N_{ss}\right]^{5,5} < \Sigma^{5,5}_{max}$. The operating points found from optimization which guarantee that the design specifications are met are: $\bar{\mathbf{x}}_\mathbf{1} = [0,\ 0,\ 24.0,\ 538,\ 14.1,\ 0.0]^T$, $\bar{\mathbf{x}}_\mathbf{2} = [0,\ 0,\ 22.9,\ 450,\ 19.2,\ 13.8]^T$, $\bar{\mathbf{x}}_\mathbf{3} = [0,\ 0,\ 24.0,\ 568,\ 0.5,\ 5.1]^T$. The units for the variables in the operating points are feet, feet, degrees, feet/sec, degrees, and degrees/sec respectively. For this example, the operating points that minimize the uncertainty in Equation (2.62) are particularly dominated by the aircraft velocities of 538, 450, and 568 feet/sec. It can be shown that the $\bar{\mathbf{x}}_\mathbf{1}$ and $\bar{\mathbf{x}}_\mathbf{2}$ operating points are not at or near a trim condition because $q \neq 0$. The third operating point, $\bar{\mathbf{x}}_\mathbf{3}$ is close to a trim condition of level flight at a speed of 568

Table 2.2: Longitudinal Dynamics of a High Performance Aircraft Design Iteration.

N	$\bar{\mathbf{x}}_\mathbf{i}$	$J^*_{MODEL}(\cdot)$	$\Sigma^{N,3,3}_{min}$	$\Sigma^{N,3,3}_{min} < \Sigma^{3,3}_{max} = 10^2$	$\Sigma^{N,5,5}_{min}$	$\Sigma^{N,5,5}_{min} < \Sigma^{5,5}_{max} = 10^2$
1	$[0,0,20,580,12.5,6.9]^T$	8.19×10^{15}	9.61	Yes	10.92	No
2	$[0,0,20,542,12.2,12.6]^T$, $[0,0,20,600,10.3,9.2]^T$	5.88×10^6	9.51	Yes	10.06	No
3	$[0,0,24,538,14.1,20.0]^T$, $[0,0,23,450,19.2,13.8]^T$, $[0,0,24,568,0.5,5.1]^T$	5.41×10^5	9.45	Yes	9.82	Yes

feet/sec. Because the uncertainty minimization (Equation (2.62)) did not constraint $q = 0$, it is not surprising that resultant vectors are not trim conditions. Following the notation defined in Section 2.3, each piecewise linear model is defined by the operating points, $\Phi_1(\bar{\mathbf{x}}_\mathbf{1})$,$\Phi_2(\bar{\mathbf{x}}_\mathbf{2})$, $\Phi_3(\bar{\mathbf{x}}_\mathbf{3})$. The iterations to meet the design requirements are summarized in Table 2.2.

Implementation and Evaluation of the Hybrid Estimator:

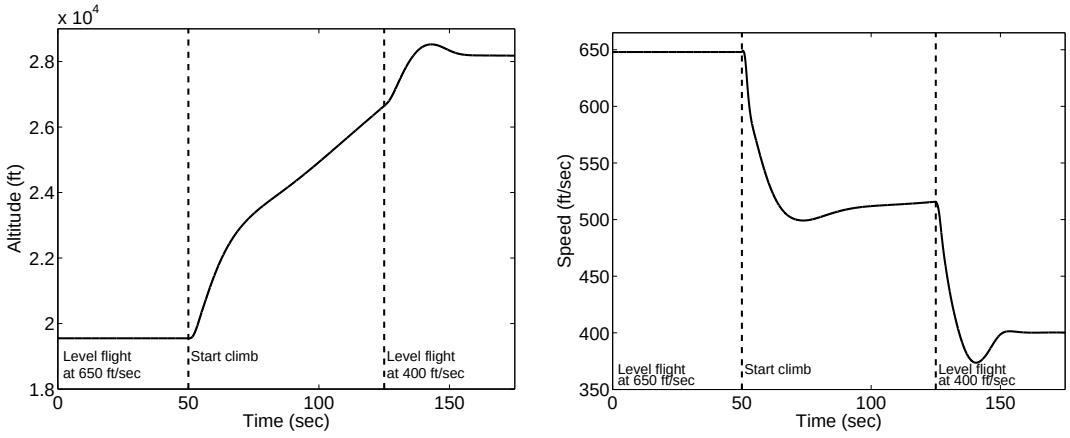

(a) (b)

Figure 2.7: Altitude and speed of the F-16 considered in Section 2.6.

The first metric used for model selection in the hybrid estimator is $tr(\Sigma_{k,k})$. Figure 2.9(a) shows the estimators selected as the aircraft completes its maneuvers. For $t < 50$,

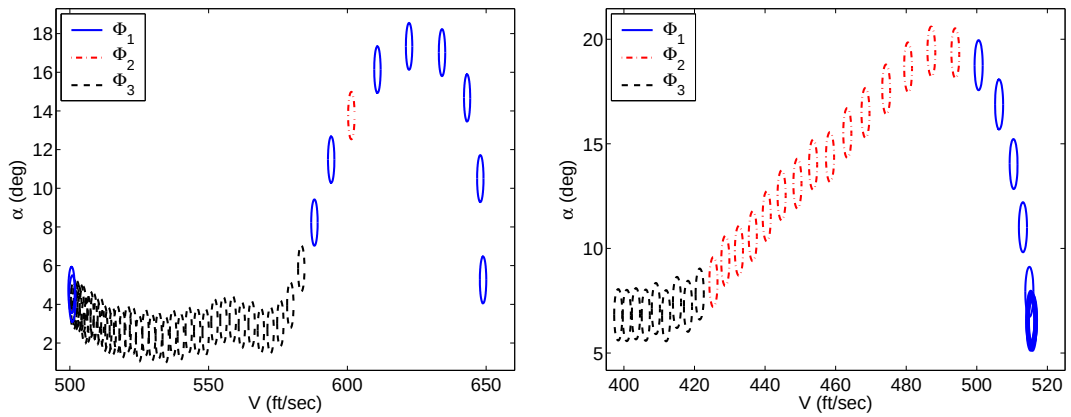

Figure 2.8: System trajectory for V and α and the bounding ellipsoids for the transitions from level flight at 650 ft/sec to climb (50 sec $< t <$ 70 sec) and climb to level-flight (120 sec $< t <$ 135 sec). The ellipsoid line type corresponds to the model used.

the uncertainty is dominated by the velocity V and the third estimator is selected. When the aircraft switches to a steady climb maneuver ($t > 50$), the uncertainty is dominated by both V and α. Interestingly, after a few intermediate estimator switches the first estimator is selected. When the aircraft levels off towards level flight ($t > 125$), the uncertainty is dominated by V only. Again, several switches occur and the estimator settles to the first estimator.

Also shown is a close-up of the time where the aircraft transitions from a constant speed, altitude to a steady climb maneuver. The close-up shows that the hybrid ESMF switches between estimator 2 and 1 several times. There are several factors that contribute to this behavior. First, the presence of random measurement noise can force a model switch. Second, the base hybrid estimator operating points found from minimizing the uncertainty in the range $\mathcal{X}$ and are not necessarily trim conditions. In fact, it appears that estimator 2 is only used as a transition between the other two estimators. During the transition from level-flight and climbing, it is not surprising that the hybrid ESMF switches between estimators. Figure 2.8 shows in detail the evolution of two important states α, V, and their projected ellipsoid uncertainties. In Figure 2.8(a), the

system starts its climbing maneuver at $t = 50$ seconds and 650 ft/sec and slows down to 500 ft/sec at $t = 70$ seconds. The transition from climbing to level-flight (120 seconds $< t <$ 135 seconds) is shown in Figure 2.8(b).

For controller design and implementation minimizing model switching is much more important than it is for estimation. It is advantageous for control if the linear switched estimator reduces the number of model switches as that minimizes the complexity associated with guaranteeing performance during a controller switch. In order to evaluate the effects of the hybrid estimator implementation on switching, the switching metrics are varied to include different functions, parameters, and scaling. The use of $tr(\cdot)$ and max[eig$(\cdot)$] did not affect the performance of the hybrid estimator appreciable, and both resulted in over 100 switches in the hybrid estimator. Scaling was implemented in the model switching guard, Equation (2.57), to evaluate how a balanced set of uncertainty affects model switching. If the diagonal elements of $\hat{Q}_{k,k}$ are normalized by the following transformation:

$S_1 = diag(0.0071,\ 0.0071,\ 1.545,\ 0.039,\ 0.0071,\ 1.693)$, the number of estimator switches increased dramatically. This is a result of increased sensitivity of the x, h states and their sensor noise, in the estimator switching. However, if the scaling S_2 was changed so that the element corresponding to α was dominant, $S_2 = \left(1 \times 10^{-10}\right)\mathbf{I}$, where $\mathbf{I}$ is the identity matrix, $\mathbf{I} \in \mathbb{R}^{5,5}$, then the number of switches is reduced significantly. A summary of the effects of the metrics implemented and scaling on model switching and the 2-norm of the sum of the residuals, $||\hat{\mathbf{x}}_{\mathbf{k},\mathbf{k}} - \mathbf{x}_{\mathbf{k},\mathbf{true}}||^2$, is presented in Table 2.3. The $trace\left(\Sigma_{k,k}\right)$ metric has the best performance based on the sum of the residuals. However, as expected, the ESMF performs the best at the expense of linearizing the system dynamics at each step. It should be noted that the linear switched estimator finds the optimal location and number of operating points off-line and therefore it is computationally cheaper to implement on-line that the ESMF. Table 2.3 also

Table 2.3: Number of model switches for the longitudinal dynamics example using several metrics and scaling.

Metric	Number of Switches	$\sum \|\|\hat{\mathbf{x}} - \mathbf{x_{true}}\|\|^2$
$trace(\Sigma_{k,k})$	71	9.62×10^3
max [eig($\Sigma_{k,k}$)]	159	3.11×10^4
$trace(\hat{Q}_k)$	122	2.18×10^4
max [eig($\hat{Q}_{k,k}$)]	105	4.32×10^4
$trace(S_1 \hat{Q}_{k,k} S_1^T)$	662	5.54×10^4
$trace(S_2 \hat{Q}_{k,k} S_2^T)$	7	6.44×10^4
ESMF	17501	3.66×10^3

lists the sum of the residuals for each of the elements of the state for the same metrics and scaling. The sum of the residuals for the first, second, and fourth elements are largest since their relative magnitude is much larger than the other elements.

Another remedy for minimizing the number of estimator switches is to change the switching logic to include a memory of L discrete steps; said another way, the estimator must be selected for L straight instances before an estimator switch is allowed. The insert of Figure 2.9(b) shows that by restricting a switch to occur after 5 steps ($L = 5$), the intermittent selection of estimators observed in the insert of Figure 2.9(a) is eliminated. The number of switches for memory sizes of $L = 0, 5, 15$ are $71, 23, 15$ respectively. The 2-norm of the residuals, $||\hat{\mathbf{x}}_{\mathbf{k},\mathbf{k}} - \mathbf{x}_{\mathbf{k},\mathbf{true}}||^2$, is about $\sim 9.62x10^3$ for all memories. By increasing L to as little as 5 steps the number of switches is reduced dramatically at little expense in terms of accuracy. At the expense of using more models (17501 switches), the ESMF performance is the best ($||\hat{\mathbf{x}}_{\mathbf{k},\mathbf{k}} - \mathbf{x}_{\mathbf{k},\mathbf{true}}||^2 = 0.17x10^4$) . This shows that imparting memory onto the hybrid estimator does not significantly change its performance. The importance of minimizing switching depends on the application of the estimator; for closed-loop control, where stability and performance are the driving issues, the number of model switches can be important and therefore a metric and scaling that minimizes switching should be selected.

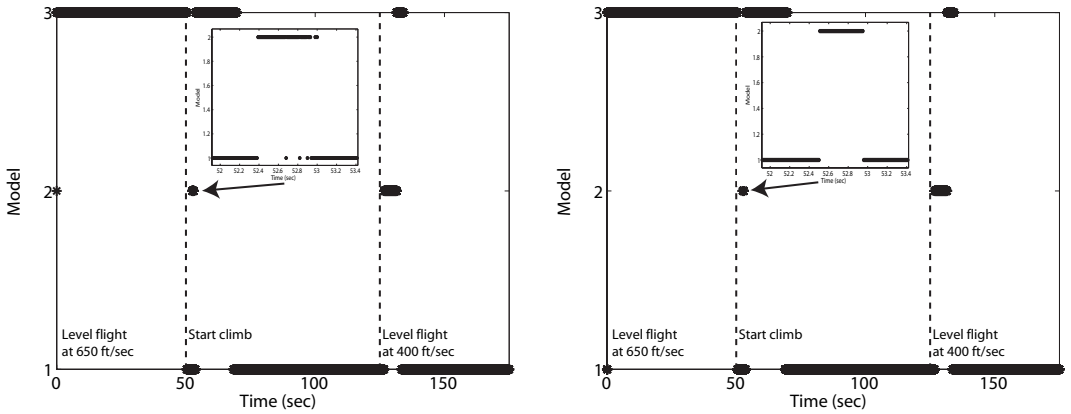

Figure 2.9: Models selected for the aircraft longitudinal dynamics example using the $tr(\Sigma_{k,k})$ as a switching metric (left). Model selection using the $tr(\Sigma_{k,k})$ as a switching metric and by using a memory of $L = 5$ in the switching logic (right).

2.7 Conclusion

A switching piecewise linear switched (or hybrid) estimator that guarantees a bound on the state uncertainty was developed. The hybrid estimator bounds the uncertainty from higher order terms of the nonlinear dynamics, thus allowing the use of a piecewise linear estimator and guaranteed bounds even as the estimators switch. In order to guarantee that the higher order terms are bounded, the system must be twice differentiable and smooth for all states and inputs in the operating range. Several switching metrics were examined. Although minimizing model switching is advantageous in estimation, it is even more beneficial in control as it reduces the number of times that complications associated with controller switching must be addressed. Estimator model switching based on the linearization uncertainty was quick to react, but sensitive. Switching based on the state uncertainty was less sensitive and had a similar profile, but slightly delayed in time. Imparting memory on the hybrid estimator reduced switching, but did not significantly affect performance. The estimation error of the hybrid estimator, defined as the difference between the center of the ellipsoidal set and the true value, is bounded if

the nonlinear system is observable and the linearization remainder is bounded. An approach to determining the minimum number and location of operating points required to guarantee a desired level of uncertainty was presented. Implementation of the switched piecewise linear observer requires a priori knowledge of a region in which the system is expected to operate (if this assumption is violated the accuracy of the algorithm cannot be guaranteed). This requirement is not overly restrictive as a priori information about the speed and agility of a system is often used in estimation and tracking to define models and to tune noise parameters. The successful implementation of the proposed linear switched estimator depends on adequately finding "good" operating points in the operating region. This is accomplished by solving an optimization problem and selecting an appropriate switching metric. The examples presented can be adequately solved by using sequential quadratic programming algorithms, initialized at different points within the operating region. If the optimization converges to a local minimum, the linear switched estimator still functions well, albeit at reduced performance because the uncertainty bound is more conservative.

CHAPTER 3

HYBRID MODE DETECTION USING PERTURBATION SIGNATURES FOR MULTI-VEHICLE SYSTEMS

3.1 Introduction

The use of unmanned vehicles, such as aerial and underwater vehicles [23], [24], [25], is attractive in civilian and military applications where the environment is too dangerous and/or it is too expensive to use a human operator. "Swarms" of small versions of these vehicles are now being envisioned because of the ability to build strong, robust small scale electronics and smart sensors, economies of scale, and robustness that accompanies large numbers. Implementation of swarms, or "active networks" is non-trivial, and involves a coordinated effort to address control, sensing of the environment, distributed and collaborative processing, and decision making [26], [27], [28], [29].

Cooperative control approaches, such as those addressed in Refs. [30] and [31], have been shown to work well in a variety of missions such as cooperative reconnaissance and coordinated strikes. Creating and maintaining an intra-vehicle communication network is critical to the end performance and robustness of the cooperative nature of these teams of vehicles. Cooperative control algorithms for these teams of vehicles acting in the presence of a communication network must be robust to communication failures, outages, or blackouts, and must also scale well with the numbers of vehicles. The work here focuses on non-traditional means of enabling inter-vehicle communications for the problem of cooperative control,where partner vehicles are considered part of the environment. The goal is to improve collaborative performance using minimal communications. Applications where this work would be enabling include: 1) stealth like missions, where communications are forbidden, 2) multi-vehicle systems where communications are "expensive" (i.e. power), such that short broadcasts or multi-hop are

required, 3) multi-vehicle networked systems where faults have occurred, 4) and active sensor networks with actions that are decided locally, but global behavior is desired.

More specifically, this paper investigates the problem of locally estimating (on each vehicle) the behavior of the environment, with specific focus on partner vehicles, in order to improve performance and decision making. Partner vehicles are described with behaviors defined by a finite number of operating modes. For example, in the case of cooperative reconnaissance, the partner vehicle's operating modes could include: 1) search an area, 2) identify a target, and 3) locate a target. This mode-based behavior of each vehicle is modelled as a hybrid system [32]. A hybrid estimation/mode detection algorithm is used to determine the current operating mode of each partner vehicle from sensor measurements, thus enabling vehicles to probabilistically know what their partner vehicles are doing even with no communications.

Because of the wide applicability of hybrid systems, the problem of state (sometimes referred to as the base-state) and mode (sometimes referred to as the modal state) estimation in hybrid systems has been addressed in the literature. The Interacting Multiple Model (IMM) estimator developed in Ref. [7] fuses the estimates from N models in order to efficiently compute a high quality state estimate. The fusion process is based on computing a probability of each estimator using their innovations or residuals. Each estimate is then weighted into the final estimate using these residuals. In Ref. [8], the IMM was modified to include measurements of the operating mode. For nonlinear systems which have unknown but bounded uncertainties, a hybrid estimator is derived in Ref. [33]. Mode switching occurs based on a metric to minimize the uncertainty in the state estimate.

In contrast to the previously described estimators, Ref. [34] proposes a moving-horizon estimation (MHE) algorithm for hybrid systems modeled in the mixed logic dynamical form. The implementation of MHE relies on solving a mixed-integer quadratic

program as a function of a set of penalties which can be used to improve the estimate in the presence of noise.

This paper develops two schemes to detect the mode of a partner vehicle whose behavior is modelled as a hybrid system. Each mode of the hybrid system not only includes a model that describes the vehicle's dynamics, but also includes a unique motion-based signature. These mode signatures are designed as Gold Codes, which are a type of pseudorandom noise with the desireable properties in signal processing: 1) they are unique and can be differentiated from random noise, 2) they have large auto-correlation peaks, and 3) they have small cross-correlation peaks. The correlation properties of the signatures are used in this work for synchronization and for mode detection. Two mode detection algorithms are derived based on: 1) an optimal detector which uses detection and estimation theory, and 2) a suboptimal approximation that requires less computations. Both methods are derived and simulations are used to show the benefits and limitations of each.

The paper is presented as follows. Section 3.2 describes the logistics of using motion-based signatures to transmit information between vehicles. In Section 3.3, detection and estimation theory are used to derive an optimal mode detector under the presence of measurement Gaussian noise. The probability of false alarm given a threshold is also derived. Due to the high computational cost of the optimal detector, a suboptimal detector is then derived in Section 3.4. The performance of both detectors are tested in two examples using Monte Carlo methods, first in a linear model in which a Kalman Filter (KF) is used for estimation, Section 3.6, and then in a two-dimensional example with nonlinear radar-like output equations in which the Sigma Point Filter (SPF) is used, Section 3.7. Both examples include detailed descriptions of how the model-based estimators are tuned.

3.2 Mode Estimation Method

The motivation for assigning a unique signature to each of the i modes is to facilitate mode estimation and thus enable the exchange of vehicle information in the absence of a formal communication system. By knowing which mode a partner vehicle is operating in, a higher quality of cooperation can be realized. Figure 3.1 shows each component of this mode estimation process for a two vehicle system. The method presented here applies to more than two vehicles. The first vehicle transfers information by choosing a corresponding operating mode, i, which is then encoded into a mode perturbation signature, z^i_{sig}. The scalar mode perturbation signature is transformed by the controller into a vehicle perturbed reference, $\mathbf{r}^i_{\text{sig}}$, and combined with the nominal vehicle reference, $\mathbf{r}$, to define the total reference, $\bar{\mathbf{r}}^i$. The controller calculates the total control input $\bar{\mathbf{u}}^i_{\text{sig}}$ as a function of its vehicle state estimate, $\hat{\mathbf{x}}$, and $\bar{\mathbf{r}}^i_{\text{sig}}$. The total control input drives the nonlinear vehicle dynamics, and its response, $\bar{\mathbf{y}}$, is fed into a vehicle state estimator for use by the first vehicle for its controller.

A mode detection method is used on the second vehicle to detect the operating mode of the first vehicle. The mode detector block uses the measurements of the second vehicle's monitoring sensors, denoted as $\mathbf{y}$, and the stored mode perturbation signatures replica, $\tilde{z}^{i,\tau}_{\text{sig}}$, to detect the mode which was transmitted by the first vehicle, $\hat{i}$. The mode estimate $\hat{i}$ is used by the planner on the second vehicle to modify the behavior of the second vehicle in order to maximize a performance metric. In this section, the logistics of transmitting information through vehicle dynamics are explained.

3.2.1 Signature Generation

Consider a rectangular pulse composed of m_ρ points defined at T time intervals and chip duration $T_c = m_\rho T$ with value ρ^0 or ρ^1 corresponding to the 0 or 1 respectively

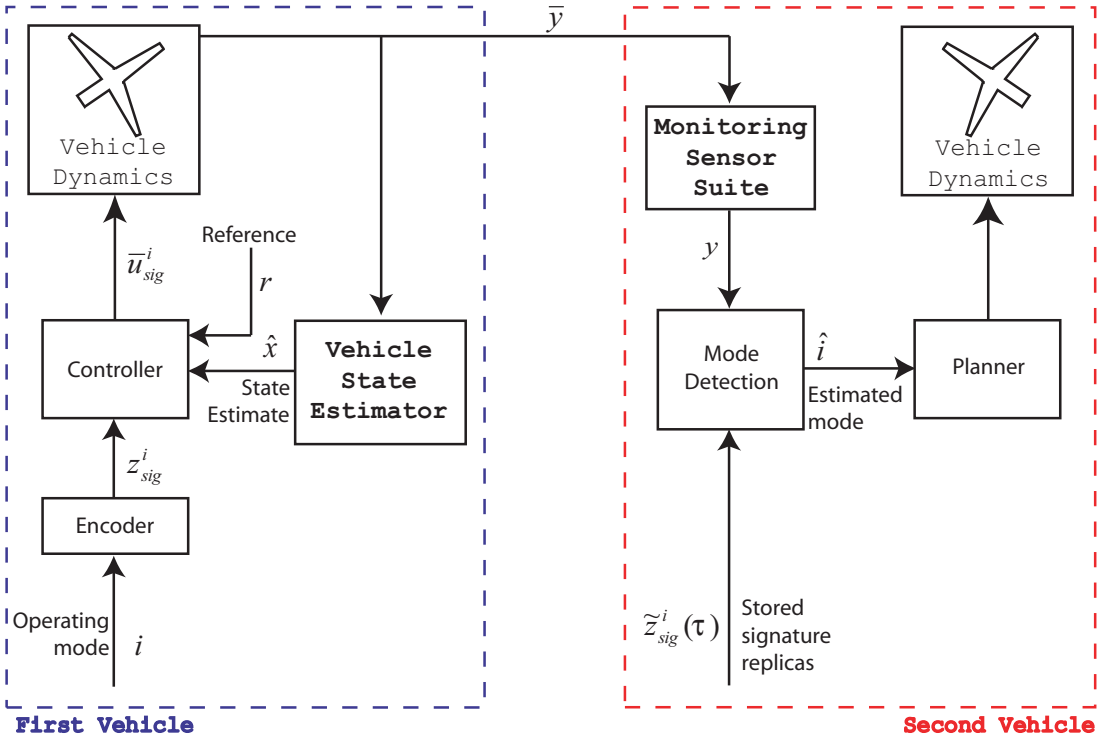

Figure 3.1: A block diagram of how information is exchanged via movements between two vehicles.

(other values could be used). Let the sequence of such n_ρ nonoverlapping rectangular chips (or pulses) for the i^{th} signature be defined as

$$p^i = \left[b_{i,1}, b_{i,2}, \ldots, b_{i,n_\rho}\right] \tag{3.1}$$

where $p^i \in \mathbb{R}^{n_\rho}$ and $b_{(\cdot)} \in \left[\rho^0, \rho^1\right]$. For example, consider a sequence p^i of $n_\rho = 6$ where $b_{i,1} = 1$, $b_{i,2} = 0$, $b_{i,3} = 1$, $b_{i,4} = 1$, $b_{i,5} = 1$, and $b_{i,6} = 1$ in which this bit pattern is infinitely repeated. If each rectangular pulse $(b_{i,1}, b_{i,2}, b_{i,3}, b_{i,4}, b_{i,5}, b_{i,6})$ is composed of $m_\rho = 1$ points then for the first six time samples Table 3.1 lists the time index k, the sample times occurring every T seconds, the first six bits of the sequence p^i, and the sequence delayed by $\tau = 1$.

The i^{th} mode perturbation signature, z^i_{sig}, is formally defined at time k as the product

Table 3.1: The relationship between the time index k, the sample times, the sequence p^i, and p^i delayed by $\tau = 1$.

Quantity	Sequence					
k	1	2	3	4	5	6
Sample Times	t_1	t_2	t_3	t_4	t_5	t_6
p^i	1	0	1	1	1	1
$p^i[\tau = 1]$	1	1	0	1	1	1

of the chip sequence p^i and a sinusoidal carrier:

$$z^i_{\text{sig},k} = p^i_k \cos\left[2\pi f_c t_k + \theta_k\right], \tag{3.2}$$

where f_c, the carrier frequency, and θ is the carrier phase. By combining n_ρ chips, a mode signature, z^i_{sig} is defined. As an example, consider bipolar-phase shift keying (BPSK), where the 0 chip (*off*) is represented by $\rho^0 = -1$, while the 1 bit (*on*) is $\rho^1 = 1$. For a system with three operating modes, $N = 2$, the corresponding mode signatures with $f_c = 1$ Hz and $\theta = 0$ is multiplied by scaling factor, $a_{\text{sig}} = 0.1$ and is shown in Figure 3.2. This signature formulation scales well because more chips can be added to the signature sequence, Equation (3.2), as the number of modes increases.

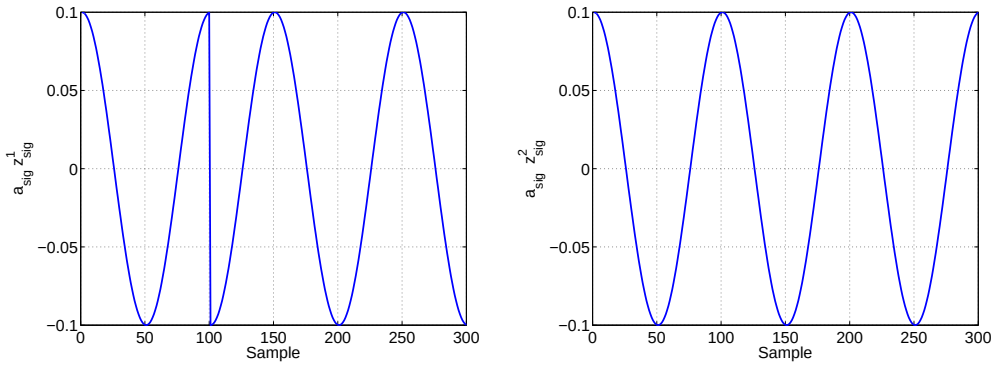

$a_{\text{sig}} z^1_{\text{sig}} = \left[\rho^1, \rho^0, \rho^0\right]$ $\qquad$ $a_{\text{sig}} z^2_{\text{sig}} = \left[\rho^1, \rho^1, \rho^1\right]$

Figure 3.2: Mode signatures for a system with $N = 2$ modes using bipolar-phase shift keying.

Pseudonrandom noise (PRN) is a known sequence of bits that, when added to a base signal, results in a signal which has statistical properties similar to noise [35]. An observer could recover the base signal only through correlation with a known sequence which is an exact replica of the original PRN. Certain PRN sequences have desirable properties, particularly in auto and cross-correlation. The discrete time cross-correlation function for any two sequences d_s and e_s is defined as follows:

$$S[\tau_d] = \sum_{k=1}^{T_p} d_{s,k} e_{s,k}[\tau_d], \tag{3.3}$$

where T_p is the number of samples in a period of the sequences and τ_d is a delay. Maximal length sequences or *m*-sequences are a special type of periodic PRN sequences with useful properties in communications [36]. In the late 1960's, Gold published the construction of two preferred pair *m*-sequences [35], yielding a family of sequences called Gold Codes. Ref. [37] presents a thorough discussion of the special properties of PRN sequences such as *m*-sequences and Gold Codes, a summary of the implementation of PRN sequences in communications and navigation, and a large bibliography.

Applying Equation (3.3) to two signals with Gold Codes encoded into the carrier can be used to determine: 1) how well the two signals are correlated, and 2) if there exists a delay between the signals. Because of their favorable properties, Gold codes are used in communications applications such as in Code Division Multiple Access (CDMA) systems [38, 36]. For these reasons, Gold Codes are chosen to define the mode signatures in this paper.

The signature estimate at time k is given as:

$$\hat{z}^i_{\text{sig},k} = z^i_{\text{sig},k} + e_k, \tag{3.4}$$

where $z^i_{\text{sig},k}$ is the transmitted signature and e_k is the error in the estimate. Because each mode perturbation signature z^i_{sig} is defined using the observed vehicle's internal time clock, the observing vehicle must determine if there a clock offset, τ, with its stored

mode signature replica, $\tilde{z}_{\text{sig}}$. This problem is also encountered in the global positioning system (GPS) where the signal traveling time is determined by the time shift required for a match between the received code from the satellite and the receiver replica [38, 16]. To determine the clock offset, a correlation test (similar to Equation (3.3)) is performed on $\tilde{z}^i_{\text{sig}}$ (embedded on the vehicle position) and the expected signature time shifted by the clock offset, $\tilde{z}_{\text{sig}}(\tau)$, stored on the vehicle. To find the delay, τ is varied over a range, $\tau \in \Gamma = \left[0, \ldots, n_\rho T_c\right]$, which is used so that all possible delays can be tested. The range Γ is divided into $\overline{b}$ equally-sized intervals or cells. Each cell, defined by the discrete time offset $\tau[m] = m\frac{n_\rho T_c}{b}$ for $m \in \left\{0, \ldots, \overline{b}-1\right\}$, is equally probable of being the correct delay. The value of m which maximizes $S(\tau_m[m])$, Equation (3.3), is the estimated clock offset or delay and is denoted as $\hat{\tau}$.

To illustrate the concept of a correlation test, Figure 3.3(a) shows that the vehicle signature, z_{sig}, and the expected signature replica, $\tilde{z}_{\text{sig}}(\tau = 0)$, are not in phase (only the first 1.5 seconds of the signals is shown). Figure 3.3(b) shows a plot of the correlation $S(\tau[m])$ for $m \in [1, \ldots, 31]$. The maximum of the correlation $S(\tau[m])$ yields the best estimate of the delay, which is shown to be $\hat{m} = 14$ in Figure 3.3(b). Thus, the estimated clock offset is then given as $\hat{\tau} = 14\frac{n_\rho T_c}{\overline{b}}$.

In summary, for a direct-sequence system with phase modulation, the mode perturbation signature with scaling factor a_{sig} received is modeled as:

$$a_{\text{sig},k} z^i_{\text{sig},k} = a_{\text{sig},k} p^i_k[\tau] \cos\left[2\pi f_c t_k + 2\pi f_{d,k} + \theta_k\right], \tag{3.5}$$

where at time k p^i_k is the i^{th} spreading waveform (Gold code with $\rho^0 = -1$ and $\rho^1 = 1$) with phase τ, f_c is the carrier frequency, and θ_k is the random carrier phase. The variables τ and f_d are the code phase delay and carrier frequency offset, respectively, which must be estimated at the receiver. Equation (3.5) is the signal model that would be used at the vehicle observing (receiving) the mode perturbation signature. Gold code phases are designed so that they coincide with chip boundaries. The Gold Code phase

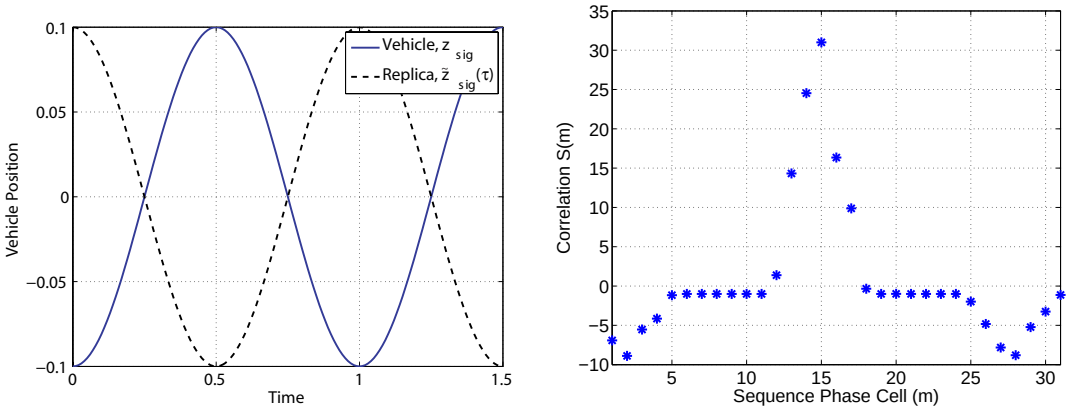

(a) Part of the signature and replica.

(b) Correlation of z_{sig} and $z_{\text{sig}}(\tau)$.

Figure 3.3: The clock offset between the vehicle and expected signature and the time shift correlation.

is discretized and defined as $\tau = mT_c$. The variable m is an integer since by design, the transmitter will only transmit the code phase delays which are integer multiples of the chip duration. The frequency offset, f_d, may be due to a Doppler shift, or to a drift or an instability in the transmitter's oscillator.

3.2.2 Controller

Each mode, denoted the i^{th} mode, is correlated with a signature; there are N modes or mode perturbation signatures defined. The approach here is to express the signature using favorable signal processing properties, and then use this signature as an input to the vehicle system dynamics as shown in Figure 3.1. Therefore, each vehicle can be thought of as a system with a plant and controller with a nominal and perturbed referenced command input. To begin, consider at time k a nominal reference input signal, $\mathbf{r}_k$, and a small perturbation to the signal, $\mathbf{r}^i_{\text{sig},k}$. The total reference signal with the perturbation, $\bar{\mathbf{r}}^i_k$, is then

$$\bar{\mathbf{r}}^i_k = \mathbf{r}_k + \mathbf{r}^i_{\text{sig},k}. \tag{3.6}$$

In physical terms, this nominal reference $\mathbf{r}_k$ is typically the required vehicle state trajectory for the vehicle to complete its task. Let $t_z^r(\cdot)$ denote the mapping from the scalar signature to the reference:

$$\mathbf{r}_{\text{sig}}^i = a_{\text{sig}} t_z^r\left(z_{\text{sig}}^i\right). \tag{3.7}$$

The function $t_z^r(\cdot)$ maps the scalar signature z_{sig}^i to the physical reference coordinates, $\mathbf{r}_k$, to form $\mathbf{r}_{\text{sig}}^i$. If elements in the reference vector have a differential relationship with the scalar mapping of z_{sig}^i, then $t_z^r(\cdot)$ must preserve the relationship when building $\mathbf{r}_{\text{sig}}^i$. For example, if the reference vector is composed of one dimensional position, x_p and its derivative, $\bar{\mathbf{r}}_k = \begin{bmatrix} r_x, & \dot{r}_{\dot{x}_p} \end{bmatrix}$, then the mapping is:

$$\begin{aligned} \bar{\mathbf{r}}_k^i &= \mathbf{r}_k + a_{\text{sig}} t_z^r\left(z_{\text{sig}}^i\right), & (3.8) \\ &= \begin{bmatrix} r_{x_p} \\ \dot{r}_{x_p} \end{bmatrix} + a_{\text{sig}} \begin{bmatrix} \int z_{\text{sig}}^i dt \\ z_{\text{sig}}^i \end{bmatrix}. & (3.9) \end{aligned}$$

Another example to consider is an aircraft where the reference vector includes the altitude. In this case $t_z^r(\cdot)$ would a rotational matrix which maps the states of the aircraft to the altitude.

The reference perturbation, $\mathbf{r}_{\text{sig}}^i$, must be small enough so that the performance of the vehicle is not compromised, yet large enough to be detected in the presence of process and measurement noise. Ideally, the reference perturbations ($\mathbf{r}_{\text{sig}}^i$, $i \in [1,\ldots,N]$) are designed to also be uncorrelated with each other to also aid in the mode detection schemes.

A feedback controller is required to assure that the vehicle tracks the desired total reference $\bar{\mathbf{r}}_k^i$. In the absence of a perturbation signature, the nominal controller is a function of the state and nominal reference,

$$\mathbf{u}_k = c\left(\mathbf{x}_k, \mathbf{r}_k\right), \tag{3.10}$$

and is designed such that the state $\mathbf{x}_k$ tracks the nominal reference $\mathbf{r}_k$. The controller in Equation (3.10) typically represents any linear or nonlinear controller which minimizes

the tracking error, $||\mathbf{r}_k - \mathbf{x}_k||$, in the presence of noise and disturbances. For the vehicle to follow the total reference, $\bar{\mathbf{r}}^i_{\text{sig}}$, the total control input $\bar{\mathbf{u}}^i_k$ becomes:

$$\bar{\mathbf{u}}^i_k = c\left(\mathbf{x}_k, \mathbf{r}_k + \mathbf{r}^i_{\text{sig},k}\right). \tag{3.11}$$

3.2.3 Hybrid Model

The behavior of a vehicle in a team of vehicles is defined by a finite set of N operating modes. The system is described using a hybrid automaton as shown in Figure 3.4. Each node in the automaton, q_i, corresponds to one of the N operating modes. The vehicle dynamics and state evolution for the i^{th} mode are governed by:

$$\mathbf{x}_{k+1} = f^i\left(\mathbf{x}_k, \bar{\mathbf{u}}^i_k, z^i_{\text{sig},k}, \mathbf{w}_k\right) \tag{3.12}$$

$$\mathbf{y}_k = h^i\left(\mathbf{x}_k, \bar{\mathbf{u}}^i_k, z^i_{\text{sig},k}, \mathbf{v}_k\right), \tag{3.13}$$

where at time k, $\mathbf{x}_k \in \mathbb{R}^{n_x}$ is the state, $\mathbf{y}_k \in \mathbb{R}^{n_y}$ the measurement, $\bar{\mathbf{u}}_k \in \mathbb{R}^{n_u}$ the control input from Equation (3.11), and $z^i_{\text{sig},k} \in \mathbb{R}$ is a scalar signature which represents the i^{th} mode. The process noise $\mathbf{w}_k$ and sensor noise $\mathbf{v}_k$ are zero-mean white Gaussian signals with covariances,

$$E\left[\mathbf{w}_k \mathbf{w}_k^T\right] = Q_k, \tag{3.14}$$

$$E\left[\mathbf{v}_k \mathbf{v}_k^T\right] = R_k. \tag{3.15}$$

In contrast to most hybrid system formulations, the state evolution governed by mode i is not only influenced by the control input $\mathbf{u}_k$, process noise $\mathbf{w}_k$, but also by the perturbation signature, z^i_{sig}.

3.3 The Locally Most Powerful Mode Detector

Having described how a vehicle embeds a mode perturbation signature in its trajectory to transmit information, it is necessary to formulate an optimal method for mode

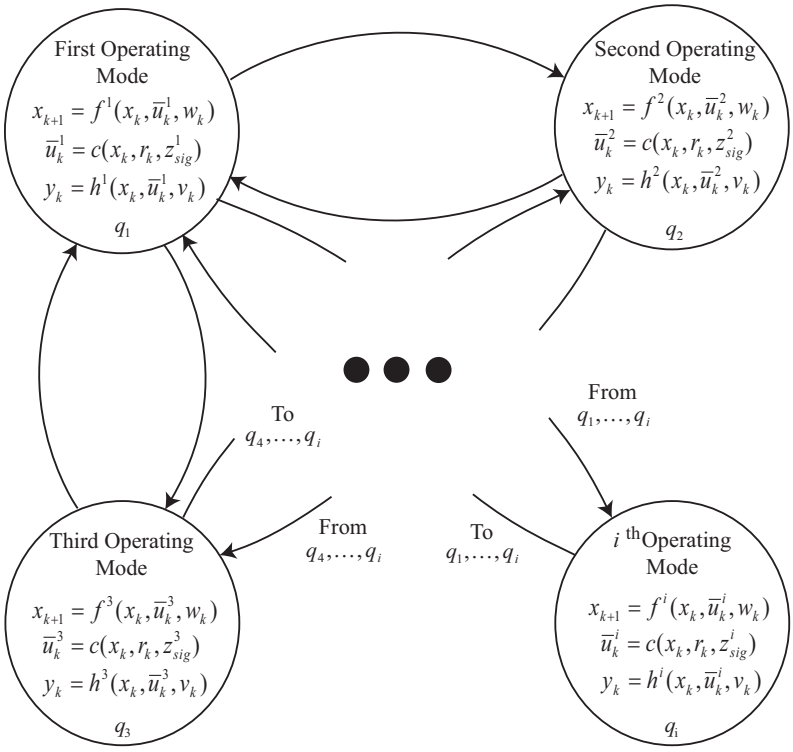

Figure 3.4: Hybrid automaton with N nodes corresponding to the operating modes or behaviors of each vehicle.

detection. In this section, a locally most powerful mode detector is derived. An optimal test statistic is derived which is based on detection theory that consists of solely correlating the measured movements of the vehicle with mode perturbation signature replicas. However, it is advantageous to derive an equivalent mode detection test statistic which integrates a model-based estimator used to handle noisy measurements. The results in this section show that the sum of the innovations of the model-based estimator is an equivalent way to evaluate the locally most powerful mode detector.

Consider a signal detection problem which has two hypotheses:

$$H_0 : \mathbf{y} = \mathbf{n}, \tag{3.16}$$

$$H_1 : \mathbf{y} = a_{\text{sig}}\mathbf{z}_{\text{sig}}^{i,\tau,\theta,f_c} + \mathbf{n}, \tag{3.17}$$

where $\mathbf{y} \in \mathbb{R}^{n_m}$ is a vector containing n_m scalar measurements and $\mathbf{n} \in \mathbb{R}^{n_m}$ is zero-mean Gaussian noise, with covariance $P \in \mathbb{R}^{n_m \times n_m}$. The variable $\mathbf{z}_{\text{sig}}^{i,\tau,\theta,f_c}$ is a stacked vector of n_m scalar signatures $z_{\text{sig}}^{i,\tau,\theta,f_c}$, or

$$\mathbf{z}_{\text{sig}}^{i,\tau,\theta,f_c} = \begin{bmatrix} z_{\text{sig},1}^{i,\tau,\theta,f_c} \\ z_{\text{sig},2}^{i,\tau,\theta,f_c} \\ \vdots \\ z_{\text{sig},n_m}^{i,\tau,\theta,f_c} \end{bmatrix}, \tag{3.18}$$

where

$$z_{\text{sig,k}}^{i,\tau,\theta,f_c} = p_k^i[\tau]\cos[2\pi f_c t_k + \theta_k]. \tag{3.19}$$

Given the measurements $\mathbf{y}$, the hypothesis H_0 represents the belief that there was no signal present, while the hypothesis H_1 represents the belief that a signal was present. The term $\mathbf{z}_{\text{sig}}^{i,\tau,\theta,f_c} \in \mathbb{R}^{n_m}$ defines the mode perturbation history for the i^{th} mode, as a function of the Gold Code with phase τ, carrier sinusoid phase θ, and carrier frequency f_c. The frequency offset term, f_d, is omitted from $\mathbf{z}_{\text{sig}}^{i,\tau,\theta,f_c}$ without loss of generality. The parameter a_{sig} is the unknown scalar amplitude of the mode perturbation history. The

measurement probability density functions, or likelihoods, under both hypotheses are written as:

$$p(\mathbf{y}|H_0) = \frac{1}{2\pi^{\frac{n_m}{2}}|P|^{\frac{1}{2}}} \exp\left[-\frac{1}{2}\mathbf{y}^T P^{-1}\mathbf{y}\right], \tag{3.20}$$

$$p(\mathbf{y}|H_1) = \frac{1}{2\pi^{\frac{n_m}{2}}|P|^{\frac{1}{2}}} \exp\left[-\frac{1}{2}\left(\mathbf{y} - a_{\text{sig}}\mathbf{z}_{\text{sig}}^{i,\tau,\theta,f_c}\right)^T P^{-1}\left(\mathbf{y} - a_{\text{sig}}\mathbf{z}_{\text{sig}}^{i,\tau,\theta,f_c}\right)\right] \tag{3.21}$$

The corresponding Newman-Pearson hypothesis test statistic [39] for evaluating whether to accept H_1 (a signature is present) is then written as a likelihood ratio:

$$\lambda(\mathbf{y}) = \frac{p(\mathbf{y}|H_1)}{p(\mathbf{y}|H_0)} \geq \lambda_{\text{thresh}}, \tag{3.22}$$

where λ_{thresh} is a threshold that if exceeded, determines whether hypothesis H_1 should be accepted. It is noted that λ_{thresh} can be chosen as to minimize a probability of false alarm.

It is desirable to remove the dependence of $p(\mathbf{y}|H_1)$, Equation (3.21), on the carrier phase θ, since it would simplify the formulation and reduce the number of computations required in the evaluation of the detection test statistic. A random carrier phase delay θ is assumed in this formulation, and can be modeled as a uniformly distributed random variable from 0 to 2π radians. This represents the belief that all phases are equally likely to occur. The marginal probability density for the probability density function, Equation (3.21), can be computed to remove its dependency on the carrier phase delay:

$$p_\theta(\mathbf{y}|H_1) = \int_0^{2\pi} \frac{1}{2\pi} p(\mathbf{y}|H_1)\, d\theta. \tag{3.23}$$

The likelihood ratio is reformulated by substituting Equation (3.23) into Equation (3.22) which results in:

$$\lambda_\theta(\mathbf{y}) = \frac{p_\theta(\mathbf{y}|H_1)}{p(\mathbf{y}|H_0)}. \tag{3.24}$$

By expanding the terms in Equation (3.24) and the moving the terms corresponding to $p(\mathbf{y}|H_0)$ inside the integral, the Newman-Pearson hypothesis test statistic can then be

rewritten as:

$$\lambda_\theta(\mathbf{y}) = c_\lambda \int_0^{2\pi} \exp\left\{ -\frac{1}{2}\left[\mathbf{y} - a_{\text{sig}}\mathbf{z}_{\text{sig}}^{i,\tau,\theta,f_c}\right]^T P^{-1}\left[\mathbf{y} - a_{\text{sig}}\mathbf{z}_{\text{sig}}^{i,\tau,\theta,f_c}\right] + \frac{1}{2}\mathbf{y}^T P^{-1}\mathbf{y}\right\} d\theta, \tag{3.25}$$

and furthered simplified to:

$$\lambda_\theta(\mathbf{y}) = c_\lambda \int_0^{2\pi} \exp\left\{ a_{\text{sig}}\mathbf{y}^T P^{-1}\mathbf{z}_{\text{sig}}^{i,\tau,\theta,f_c} - \frac{1}{2}a_{\text{sig}}^2\left(\mathbf{z}_{\text{sig}}^{i,\tau,\theta,f_c}\right)^T P^{-1}\mathbf{z}_{\text{sig}}^{i,\tau,\theta,f_c}\right\} d\theta. \tag{3.26}$$

where $c_\lambda = \frac{1}{2\pi}$.

Because a_{sig} is unknown and must be estimated, a Neyman-Pearson locally most powerful test statistic is formulated. First, in hypothesis H_1 it is assumed that a_{sig} is known. Equation (3.26) is used to derive a Neyman-Pearson locally most powerful test in the limit of small, but known a_{sig}. The locally most powerful (LMP) test is derived by expanding Equation (3.26) into a Taylor series around a_{sig} that yields:

$$\lambda_\theta(\mathbf{y}) \approx \lambda_\theta(\mathbf{y})|_{a_{\text{sig}}=0} + \left.\frac{\partial\lambda_\theta(\mathbf{y})}{\partial a_{\text{sig}}}\right|_{a_{\text{sig}}=0} a_{\text{sig}} + \frac{1}{2}\left.\frac{\partial^2\lambda_\theta(\mathbf{y})}{\partial a_{\text{sig}}^2}\right|_{a_{\text{sig}}=0} a_{\text{sig}}^2. \tag{3.27}$$

The locally most powerful tests consists of taking the limit of small, but known a_{sig}. The LMP theory shows that this limits minimizes the probability of missed detection for a given probability of false alarm for all small a_{sig} [39]. The first term in the Taylor series in Equation (3.27) is a constant, or:

$$\begin{aligned} \lambda_\theta(\mathbf{y})|_{a_{\text{sig}}=0} &= c_\lambda \int_0^{2\pi} d\theta & (3.28)\\ &= c_\lambda 2\pi & (3.29)\\ &= c_{\lambda_0}. & (3.30) \end{aligned}$$

Evaluating the second term of the series in Equation (3.27) requires differentiating the likelihood ratio, Equation (3.26), with respect to a_{sig},

$$\frac{\partial\lambda_\theta(\mathbf{y})}{\partial a_{\text{sig}}} = c_\lambda \int_0^{2\pi} \left(\mathbf{y}^T P^{-1}\mathbf{z}_{\text{sig}}^{i,\tau,\theta,f_c} - a_{\text{sig}}\left(\mathbf{z}_{\text{sig}}^{i,\tau,\theta,f_c}\right)^T P^{-1}\mathbf{z}_{\text{sig}}^{i,\tau,\theta,f_c}\right) \exp\left\{ a_{\text{sig}}\mathbf{y}^T P^{-1}\mathbf{z}_{\text{sig}}^{i,\tau,\theta,f_c} - \frac{1}{2}a_{\text{sig}}^2\left(\mathbf{z}_{\text{sig}}^{i,\tau,\theta,f_c}\right)^T P^{-1}\mathbf{z}_{\text{sig}}^{i,\tau,\theta,f_c}\right\} d\theta. \tag{3.31}$$

The substitution of $a_{\text{sig}} = 0$ into Equation (3.31) yields:

$$\left.\frac{\partial \lambda_{\theta}(\mathbf{y})}{\partial a_{\text{sig}}}\right|_{a_{\text{sig}}=0} = c_{\lambda} \int_{0}^{2\pi} \mathbf{y}^{T} P^{-1} \mathbf{z}_{\text{sig}}^{i,\tau,\theta,f_c} d\theta. \tag{3.32}$$

In order to compute the integral with respect to θ, it is necessary to expand the expression for the mode perturbation signature, $z_{\text{sig}}^{i,\tau,\theta,f_c}$. At time k, the discrete time version of the mode perturbation signature in Equation (3.2) has the form:

$$z_{\text{sig},k}^{i,\tau,\theta,f_c} = p_k^i(\tau)\cos\left[2\pi f_c t_k - \theta_k\right], \tag{3.33}$$

where the unknown carrier phase delay, θ_k, is subtracted to simplify the derivation. Using trigonometric identities Equation (3.33) can be written as:

$$z_{\text{sig},k}^{i,\tau,\theta,f_c} = p_k^i(\tau)\left\{\cos\left[2\pi f_c t_k\right]\cos\left[\theta_k\right]\right\} + p_k^i(\tau)\left\{\sin\left[2\pi f_c t_k\right]\sin\left[\theta_k\right]\right\}, \tag{3.34}$$

or to simplify the notation:

$$z_{\text{sig},k}^{i,\tau,\theta,f_c} = z_{\cos,k}^{i,\tau,f_c}\cos\left[\theta_k\right] + z_{\sin,k}^{i,\tau,f_c}\sin\left[\theta_k\right], \tag{3.35}$$

where

$$z_{\cos,k}^{i,\tau,f_c} = p_k^i(\tau)\cos\left[2\pi f_c t_k\right], \tag{3.36}$$

$$z_{\sin,k}^{i,\tau,f_c} = p_k^i(\tau)\sin\left[2\pi f_c t_k\right]. \tag{3.37}$$

Substituting Equation (3.35) into Equation (3.32) and computing the integral with respect to θ results in:

$$\left.\frac{\partial \lambda(\mathbf{y})}{\partial a_{\text{sig}}}\right|_{a_{\text{sig}}=0} = 0. \tag{3.38}$$

Therefore no useful locally most powerful detector is found from the second term since it vanishes for small a_{sig}.

Moving onto the third term in the series, the likelihood ratio, Equation (3.26), can be differentiated with respect to a_{sig}. The differentiation of Equation (3.26) twice with

respect to a_{sig} yields:

$$\frac{\partial^2 \lambda_\theta(\mathbf{y})}{\partial a_{\text{sig}}^2} = c_\lambda \int_0^{2\pi} \left\{ -\left(\mathbf{z}_{\text{sig}}^{i,\tau,\theta,f_c}\right)^T P^{-1} \mathbf{z}_{\text{sig}}^{i,\tau,\theta,f_c} + \left(\mathbf{y}^T P^{-1} \mathbf{z}_{\text{sig}}^{i,\tau,\theta,f_c} - a_{\text{sig}} \left(\mathbf{z}_{\text{sig}}^{i,\tau,\theta,f_c}\right)^T P^{-1} \mathbf{z}_{\text{sig}}^{i,\tau,\theta,f_c}\right) \left(\mathbf{y}^T P^{-1} \mathbf{z}_{\text{sig}}^{i,\tau,\theta,f_c} - a_{\text{sig}} \left(\mathbf{z}_{\text{sig}}^{i,\tau,\theta,f_c}\right)^T P^{-1} \mathbf{z}_{\text{sig}}^{i,\tau,\theta,f_c}\right) \right\} \exp\left\{ a_{\text{sig}} \mathbf{y}^T P^{-1} \mathbf{z}_{\text{sig}}^{i,\tau,\theta,f_c} - \frac{1}{2} a_{\text{sig}}^2 \left(\mathbf{z}_{\text{sig}}^{i,\tau,\theta,f_c}\right)^T P^{-1} \mathbf{z}_{\text{sig}}^{i,\tau,\theta,f_c} \right\} d\theta, \quad (3.39)$$

The substitution of $a_{\text{sig}} = 0$ into Equation (3.39) yields:

$$\left.\frac{\partial^2 \lambda_\theta(\mathbf{y})}{\partial a_{\text{sig}}^2}\right|_{a_{\text{sig}}=0} = c_\lambda \int_0^{2\pi} \left\{ -\left(\mathbf{z}_{\text{sig}}^{i,\tau,\theta,f_c}\right)^T P^{-1} \mathbf{z}_{\text{sig}}^{i,\tau,\theta,f_c} + \left(\mathbf{y}^T P^{-1} \mathbf{z}_{\text{sig}}^{i,\tau,\theta,f_c}\right)^2 \right\} d\theta. \quad (3.40)$$

For clarity, the terms inside the integrals are computed separately. The first term is derived by realizing that $\left(\mathbf{z}_{\cos}^{i,\tau,f_c}\right)^T P^{-1} \mathbf{z}_{\cos}^{i,\tau,f_c} \approx \left(\mathbf{z}_{\sin}^{i,\tau,f_c}\right)^T P^{-1} \mathbf{z}_{\sin}^{i,\tau,f_c}$ for a diagonal P (uncorrelated noise), and a long time interval, and then computing the integral over θ yielding:

$$-\int_0^{2\pi} \left(\mathbf{z}_{\text{sig}}^{i,\tau,\theta,f_c}\right)^T P^{-1} \mathbf{z}_{\text{sig}}^{i,\tau,\theta,f_c} = -2 \int_0^{2\pi} \left(\mathbf{z}_{\cos}^{i,\tau,f_c}\right)^T P^{-1} \mathbf{z}_{\cos}^{i,\tau,f_c} d\theta, \quad (3.41)$$

$$= c_{z^T P^{-1} z}. \quad (3.42)$$

The second term is computed by substituting the signature definition in Equation (3.35) into Equation (3.40) and computing the integral over θ yielding:

$$\int_0^{2\pi} \left(\mathbf{y}^T P^{-1} \mathbf{z}_{\text{sig}}^{i,\tau,\theta,f_c}\right)^2 d\theta = \int_0^{2\pi} \left(\mathbf{y}^T P^{-1} \left\{ \mathbf{z}_{\cos,k}^{i,\tau,f_c} \cos[\theta_k] + \mathbf{z}_{\sin,k}^{i,\tau,f_c} \sin[\theta_k] \right\}\right)^2 d\theta \quad (3.43)\text{–}(3.44)$$

$$= \pi \left(\mathbf{y}^T P^{-1} \mathbf{z}_{\cos}^{i,\tau,f_c}\right)^2 + \pi \left(\mathbf{y}^T P^{-1} \mathbf{z}_{\sin}^{i,\tau,f_c}\right)^2. \quad (3.45)$$

Substituting the two terms, Equations (3.42) and (3.45), into Equation (3.40) results in:

$$\left.\frac{\partial^2 \lambda_\theta(\mathbf{y})}{\partial a_{\text{sig}}^2}\right|_{a_{\text{sig}}=0} = c_\lambda \left\{ c_{z^T P^{-1} z} + \pi \left(\mathbf{y}^T P^{-1} \mathbf{z}_{\cos}^{i,\tau,f_c}\right)^2 + \pi \left(\mathbf{y}^T P^{-1} \mathbf{z}_{\sin}^{i,\tau,f_c}\right)^2 \right\}. \quad (3.46)$$

Finally by substituting Equations (3.42) and (3.46) into Equation (3.27) results in the following definition of the LMP test statistic:

$$\lambda_{\mathrm{LMP}}(\mathbf{y}) \approx c_{\lambda_0} + \frac{1}{2} c_{\lambda} \left\{ c_{z^T P^{-1} z} + \pi \left(\mathbf{y}^T P^{-1} \mathbf{z}_{\cos}^{i,\tau,f_c} \right)^2 + \pi \left(\mathbf{y}^T P^{-1} \mathbf{z}_{\sin}^{i,\tau,f_c} \right)^2 \right\} a_{\mathrm{sig}}^2. \quad (3.47)$$

As stated in Equation (3.22), $\lambda_{\mathrm{LMP}}(\mathbf{y})$ can be compared to $\lambda_{\mathrm{thresh}}$ to determine the acceptance of hypothesis H_1.

$$c_{\lambda_0} + \frac{1}{2} c_{\lambda} \left\{ c_{z^T P^{-1} z} + \pi \left(\mathbf{y}^T P^{-1} \mathbf{z}_{\cos}^{i,\tau,f_c} \right)^2 + \pi \left(\mathbf{y}^T P^{-1} \mathbf{z}_{\sin}^{i,\tau,f_c} \right)^2 \right\} a_{\mathrm{sig}}^2 \geq \lambda_{thresh} \quad (3.48)$$

The inequality in Equation (3.48) can be manipulated to yield the following:

$$\left(\mathbf{y}^T P^{-1} \mathbf{z}_{\cos}^{i,\tau,f_c} \right)^2 + \left(\mathbf{y}^T P^{-1} \mathbf{z}_{\sin}^{i,\tau,f_c} \right)^2 \geq \frac{1}{\pi} \left(2 \frac{\lambda_{thresh} - c_{\lambda_0}}{c_{\lambda} a_{\mathrm{sig}}^2} - c_{z^T P^{-1} z} \right), \quad (3.49)$$

or

$$\overline{\lambda}_{\mathrm{LMP}} \geq \overline{\lambda}_{\mathrm{LMP,tresh}}. \quad (3.50)$$

The left-hand side of the inequality can be evaluated independent of a_{sig}.

The test statistic in Equation (3.50) indicates, to a particular level of probability of false alarm, a signal is present. In the proposed application more information is required, namely that the correct signal has been detected. Because the signatures vary over i, τ, f_c,

$$\overline{\lambda}_{\mathrm{LMP}}^{i,\tau,f_c}(\mathbf{y}) = \left(\mathbf{y}^T P^{-1} \mathbf{z}_{\cos}^{i,\tau,f_c} \right)^2 + \left(\mathbf{y}^T P^{-1} \mathbf{z}_{\sin}^{i,\tau,f_c} \right)^2, \quad (3.51)$$

The approach is to use $\overline{\lambda}_{\mathrm{LMP}}^{i,\tau,f_c}$ both as a signal detector and as an optimization tool over i, τ, f_c, or

$$\begin{aligned} \overline{\lambda}_{\mathrm{LMP}}^{*} &= \max_{i,\tau,f_c} \left\{ \overline{\lambda}_{\mathrm{LMP}}^{i,\tau,f_c} \right\} & (3.52) \\ &= \max_{i,\tau,f_c} \left\{ \left(\mathbf{y}^T P^{-1} \mathbf{z}_{\cos}^{i,\tau,f_c} \right)^2 + \left(\mathbf{y}^T P^{-1} \mathbf{z}_{\sin}^{i,\tau,f_c} \right)^2 \right\} & (3.53) \\ &= \max_{i,\tau,f_c} \left\{ \eta_{\mathrm{LMP,cos}}^{i,\tau,f_c} + \eta_{\mathrm{LMP,sin}}^{i,\tau,f_c} \right\} & (3.54) \end{aligned}$$

where $\eta_{\mathrm{LMP,cos}}^{i,\tau,f_c}$ and $\eta_{\mathrm{LMP,sin}}^{i,\tau,f_c}$ are the square of the correlations between the measurements $\mathbf{y}$ and the mode perturbation signatures with in-phase and quadrature carriers.

Equation (3.53) consists of correlating the measurements, $\mathbf{y}$, with in-phase ($\mathbf{z}_{\cos}^{i,\tau,f_c}$) and quadrature ($\mathbf{z}_{\sin}^{i,\tau,f_c}$) replicas of the mode perturbation signature, squaring the results, and finally summing them. The test statistic in Equation (3.54) is a function of the i^{th} mode, Gold Code phase τ, and frequency f_c, but it is not a function of the carrier phase delay θ. These parameters are estimated by maximizing $\overline{\lambda}_{\text{LMP}}^{i,\tau,f_c}$, or

$$\hat{i},\hat{\tau},\hat{f}_c = \arg\max \overline{\lambda}_{\text{LMP}}^{i,\tau,f_c}. \tag{3.55}$$

The LMP statistic in Equation (3.54) was developed by assuming that a_{sig} is known. But in practice, a_{sig} is estimated. Thus, the terms on the right-hand side of Equation (3.54) must be related to the estimator.

Consider the alternate hypothesis,

$$H_{1,\cos} : \mathbf{y} = a_{\text{sig}}\mathbf{z}_{\cos}^{i,\tau,f_c} + \mathbf{n}, \tag{3.56}$$

where Equation (3.56) differs from H_1, Equation (3.17), by the fact that the mode perturbation signature is expressed in terms of the in-phase ($\mathbf{z}_{\cos}^{i,\tau,f_c}$) signature replica. The likelihood for $H_{1,\cos}$ is written as:

$$p\left(\mathbf{y}|H_{1,\cos}\right) = \frac{1}{2\pi^{\frac{n_m}{2}}\left|P\right|^{\frac{1}{2}}} \exp\left[-\frac{1}{2}\left(\mathbf{y}-a_{\text{sig}}\mathbf{z}_{\cos}^{i,\tau,f_c}\right)^T P^{-1}\left(\mathbf{y}-a_{\text{sig}}\mathbf{z}_{\cos}^{i,\tau,f_c}\right)\right]. \tag{3.57}$$

Assuming that the hypothesis $H_{1,\cos}$ is satisfied, an estimate of a_{sig} can be found by maximizing the likelihood $p\left(\mathbf{y}|H_{1,\cos}\right)$ given in Equation (3.57) or:

$$\hat{a}_{\text{sig}} = \arg\max_{a_{\text{sig}}} p\left(\mathbf{y}|H_{1,\cos}\right) = \max_{a_{\text{sig}}}\left\{\frac{1}{2\pi^{\frac{n_m}{2}}\left|P\right|^{\frac{1}{2}}} \exp\left[-\frac{1}{2}\left(\mathbf{y}-a_{\text{sig}}\mathbf{z}_{\cos}^{i,\tau,f_c}\right)^T P^{-1}\left(\mathbf{y}-a_{\text{sig}}\mathbf{z}_{\cos}^{i,\tau,f_c}\right)\right]\right\}. \tag{3.58}$$

Define $\mathcal{L}$ as the log likelihood, or

$$\mathcal{L}\left[\mathbf{y}|H_{1,\cos}\right] = -\log\left[p\left(\mathbf{y}|H_{1,\cos}\right)\right]. \tag{3.59}$$

Because the natural logarithm function is monotonically increasing, it can be used to simplify Equation (3.58):

$$\begin{aligned}
\mathcal{L}^*\left[\mathbf{y}|H_{1,\cos}\right] &= \min_{a_{\text{sig}}} \mathcal{L}\left[\mathbf{y}|H_{1,\cos}\right] && (3.60)\\
&= \min_{a_{\text{sig}}} \left[c_{\log} - \frac{1}{2}\left(\mathbf{y} - a_{\text{sig}}\mathbf{z}_{\cos}^{i,\tau,f_c}\right)^T P^{-1}\left(\mathbf{y} - a_{\text{sig}}\mathbf{z}_{\cos}^{i,\tau,f_c}\right)\right] && (3.61)\\
&= \min_{a_{\text{sig}}} \left[-\frac{1}{2}\left(\mathbf{y} - a_{\text{sig}}\mathbf{z}_{\cos}^{i,\tau,f_c}\right)^T P^{-1}\left(\mathbf{y} - a_{\text{sig}}\mathbf{z}_{\cos}^{i,\tau,f_c}\right)\right], && (3.62)
\end{aligned}$$

where $c_{\log} = \log\left(2\pi^{-\frac{m}{2}}|P|^{-\frac{1}{2}}\right)$ is a constant and can be removed from the optimization in Equation (3.61) with no loss in generality.

The optimal maximum likelihood estimate of a_{sig} can be found by differentiating Equation (3.62) with respect to a_{sig}, setting the result to zero, and solving for a_{sig}:

$$\frac{\mathcal{L}\left[\mathbf{y}|H_{1,\cos}\right]}{\partial a_{\text{sig}}} = 0 = \mathbf{y}^T P^{-1}\mathbf{z}_{\cos}^{i,\tau,f_c} - a_{\text{sig}}\left(\mathbf{z}_{\cos}^{i,\tau,f_c}\right)^T P^{-1}\mathbf{z}_{\cos}^{i,\tau,f_c}, \tag{3.63}$$

$$\hat{a}_{\text{sig},H_{1,\cos}} = \frac{\mathbf{y}^T P^{-1}\mathbf{z}_{\cos}^{i,\tau,f_c}}{\left(\mathbf{z}_{\cos}^{i,\tau,f_c}\right)^T P^{-1}\mathbf{z}_{\cos}^{i,\tau,f_c}}. \tag{3.64}$$

Substituting Equation (3.64) into Equation (3.62) results in:

$$\overline{\mathcal{L}}^*\left[\mathbf{y}|H_{1,\cos},\hat{a}_{\text{sig}}\right] = \frac{1}{2}\left(\mathbf{y}^T P^{-1}\mathbf{y} - \frac{\left[\mathbf{y}^T P^{-1}\mathbf{z}_{\cos}^{i,\tau,f_c}\right]^2}{(\mathbf{z}_{\cos}^{i,\tau,f_c})^T P^{-1}\mathbf{z}_{\cos}^{i,\tau,f_c}}\right), \tag{3.65}$$

where $\overline{\mathcal{L}}^*\left[\mathbf{y}|H_{1,\cos},\hat{a}_{\text{sig}}\right]$ is defined as the likelihood when the optimal value of the estimate of a_{sig} is used.

Equation (3.65) is very similar to $\eta_{\text{LMP},\cos}^{i,\tau,f_c}$ in Equation (3.54). as a LMP test statistic similar to Equation (3.54) to determine the transmitted signal parameters. Noting that the $\mathbf{y}^T P^{-1}\mathbf{y}$ term in Equation (3.65) is not a function of a_{sig} or the optimization variables i, τ, and f_c, and

$$c_{\text{sig}}^{i,\tau,f_c} = \left(z_{\text{sig},\cos}^{i,\tau,f_c}\right)^T P^{-1} z_{\text{sig},\cos}^{i,\tau,f_c} \tag{3.66}$$

is known, the in-phase test statistic can be written as:

$$\eta_{\text{LMP,cos}}^{i,\tau,f_c} = \left\{-\overline{\mathcal{L}}\left[\mathbf{y}|H_{1,\cos},\hat{a}_{\text{sig}}\right]+\mathcal{L}\left[\mathbf{y}|H_0\right]\right\}c_{\text{sig}}^{i,\tau,f_c}, \tag{3.67}$$

$$= \left\{-\frac{1}{2}\left(\mathbf{y}^T P^{-1}\mathbf{y}-\frac{\left[\mathbf{y}^T P^{-1}\mathbf{z}_{\cos}^{i,\tau,f_c}\right]^2}{(\mathbf{z}_{\cos}^{i,\tau,f_c})^T P^{-1}\mathbf{z}_{\cos}^{i,\tau,f_c}}\right)+\frac{1}{2}\mathbf{y}^T P^{-1}\mathbf{y}\right\}c_{\text{sig}}^{i,\tau,f_c}, \tag{3.68}$$

$$= \frac{1}{2}\left[\mathbf{y}^T P^{-1}\mathbf{z}_{\cos}^{i,\tau,f_c}\right]^2. \tag{3.69}$$

where $\mathcal{L}\left[\mathbf{y}|H_0\right]$ is the likelihood for H_0 or $a_{\text{sig}}=0$. Note that adding $\mathcal{L}\left[\mathbf{y}|H_0\right]$ to the negative value of $\overline{\mathcal{L}}\left[\mathbf{y}|H_{1,\cos},\hat{a}_{\text{sig}}\right]$, does not modify the solution to the optimization problem over i, τ, and f_c.

Consider another hypothesis,

$$H_{1,\text{sin}}:\mathbf{y}=a_{\text{sig}}\mathbf{z}_{\text{sin}}^{i,\tau,f_c}+\mathbf{n}, \tag{3.70}$$

where Equation (3.70) differs from H_1, Equation (3.17), by the fact that the mode perturbation signature is expressed in terms of the quadrature ($\mathbf{z}_{\text{sin}}^{i,\tau,f_c}$) signature replica. The likelihood for $H_{1,\text{sin}}$ is written as:

$$p\left(\mathbf{y}|H_{1,\text{sin}}\right)=\frac{1}{2\pi^{\frac{nm}{2}}|P|^{\frac{1}{2}}}\exp\left[-\frac{1}{2}\left(\mathbf{y}-a_{\text{sig}}\mathbf{z}_{\text{sin}}^{i,\tau,f_c}\right)^T P^{-1}\left(\mathbf{y}-a_{\text{sig}}\mathbf{z}_{\text{sin}}^{i,\tau,f_c}\right)\right]. \tag{3.71}$$

Define the optimization of the likelihood for hypothesis, $H_{1,\text{sin}}$, as:

$$\mathcal{L}^*\left[\mathbf{y}|H_{1,\text{sin}}\right]=\min_{a_{\text{sig}}}\mathcal{L}\left[\mathbf{y}|H_{1,\text{sin}}\right]. \tag{3.72}$$

In the same way as shown in Equation(3.63), the optimal maximum likelihood estimate of a_{sig} is

$$\hat{a}_{\text{sig},H_{1,\text{sin}}}=\frac{\mathbf{y}^T P^{-1}\mathbf{z}_{\text{sin}}^{i,\tau,f_c}}{\left(\mathbf{z}_{\text{sin}}^{i,\tau,f_c}\right)^T P^{-1}\mathbf{z}_{\text{sin}}^{i,\tau,f_c}}. \tag{3.73}$$

Substituting $\hat{a}_{\text{sig},H_{1,\text{sin}}}$ into Equation (3.72) results in:

$$\overline{\mathcal{L}}^*\left[\mathbf{y}|H_{1,\text{sin}},\hat{a}_{\text{sig}}\right]=\frac{1}{2}\left(\mathbf{y}^T P^{-1}\mathbf{y}-\frac{\left[\mathbf{y}^T P^{-1}\mathbf{z}_{\text{sin}}^{i,\tau,f_c}\right]^2}{(\mathbf{z}_{\text{sin}}^{i,\tau,f_c})^T P^{-1}\mathbf{z}_{\text{sin}}^{i,\tau,f_c}}\right). \tag{3.74}$$

As was done in Equation (3.67), a $\mathcal{L}[\mathbf{y}|H_0]$ term is added to Equation (3.74) multiplied by -1 in order to remove the $\mathbf{y}^T P^{-1}\mathbf{y}$ term:

$$\eta_{\text{LMP,sin}}^{i,\tau,f_c} = \left\{-\overline{\mathcal{L}}\left[\mathbf{y}|H_{1,\text{sin}},\hat{a}_{\text{sig}}\right] + \mathcal{L}\left[\mathbf{y}|H_0\right]\right\} c_{\text{sin}}^{i,\tau,f_c}, \tag{3.75}$$

where for a large interval

$$\begin{aligned}\left(z_{\text{sig,sin}}^{i,\tau,f_c}\right)^T P^{-1} z_{\text{sig,sin}}^{i,\tau,f_c} &\approx \left(z_{\text{sig,cos}}^{i,\tau,f_c}\right)^T P^{-1} z_{\text{sig,cos}}^{i,\tau,f_c} &(3.76)\\ &\approx c_{\text{sig}}^{i,\tau,f_c}. &(3.77)\end{aligned}$$

Equation (3.75) simplifies to:

$$\begin{aligned}\eta_{\text{LMP,sin}}^{i,\tau,f_c} &= \left\{-\frac{1}{2}\left(\mathbf{y}^T P^{-1}\mathbf{y} - \frac{\left[\mathbf{y}^T P^{-1}\mathbf{z}_{\text{sin}}^{i,\tau,f_c}\right]^2}{(\mathbf{z}_{\text{sin}}^{i,\tau,f_c})^T P^{-1}\mathbf{z}_{\text{sin}}^{i,\tau,f_c}}\right) + \frac{1}{2}\mathbf{y}^T P^{-1}\mathbf{y}\right\} c_{\text{sig}}^{i,\tau,f_c} &(3.78)\\ &= \frac{1}{2}\left[\mathbf{y}^T P^{-1}\mathbf{z}_{\text{sin}}^{i,\tau,f_c}\right]^2. &(3.79)\end{aligned}$$

Substituting Equations (3.67) and (3.75) into Equation (3.54) produces the following optimization:

$$\begin{aligned}\hat{i},\hat{\tau},\hat{f}_c &= \arg\max_{i,\tau,f_c}\left[\eta_{\text{LMP,cos}}^{i,\tau,f_c} + \eta_{\text{LMP,sin}}^{i,\tau,f_c}\right], &(3.80)\\ &= \arg\max_{i,\tau,f_c}\left\{2\cdot\mathcal{L}\left[\mathbf{y}|H_0\right] - \mathcal{L}\left[\mathbf{y}|H_{1,cos},\hat{a}_{\text{sig}}\right] - \mathcal{L}\left[\mathbf{y}|H_{1,sin},\hat{a}_{\text{sig}}\right]\right\} c_{\text{sig}}^{i,\tau,f_c} &(3.81)\\ &= \arg\max_{i,\tau,f_c}\left\{2\cdot\mathcal{L}\left[\mathbf{y}|H_0\right] - \mathcal{L}\left[\mathbf{y}|H_{1,cos},\hat{a}_{\text{sig}}\right] - \mathcal{L}\left[\mathbf{y}|H_{1,sin},\hat{a}_{\text{sig}}\right]\right\} &(3.82)\end{aligned}$$

where the constant $c_{\text{sig}}^{i,\tau,f_c}$ is removed from Equation (3.81) as it is inconsequential to the optimization.

With the proposed optimization of the test statistic in Equation (3.54), the likelihoods in Equations (3.69) and (3.79) are now related to the KF which is used to recursively estimate $\hat{a}_{\text{sig}}$.

It is proposed that the amplitude of the perturbation signature, a_{sig}, is estimated from noisy measurements using a model-based estimator. Consider the discrete time linear system:

$$\mathbf{x}_{k+1} = A_k\mathbf{x}_k + B_u\mathbf{u}_k + \mathbf{w}_k^x, \tag{3.83}$$

where $\mathbf{x}_k \in \mathbb{R}^{n_x}$ is the system state, $\mathbf{u}_k \in \mathbb{R}^{n_u}$ is the control input and $\mathbf{w}_k^x \in \mathbb{R}^{n_x}$ is zero-mean Gaussian process noise with covariance Q_k . Consider a full-state feedback control law with gain K based on

$$\mathbf{u}_k = K\left(-\mathbf{x}_k + \overline{\mathbf{r}}_k^i\right), \tag{3.84}$$

where the objective of the controller is to make the system track a reference (that includes a mode perturbation signature or Gold Code), $\overline{\mathbf{r}}_k^i \in \mathbb{R}^{n_x}$ using a linear full-state feedback controller. By substituting the expression for the total reference, Equation (3.6), into Equation (3.84), the following expression that includes the amplitude of the perturbation signature is derived:

$$\mathbf{u}_k = K\left(-\mathbf{x}_k + \mathbf{r}_k + a_{\text{sig}} t_z^r\left(z_{\text{sig}}^{i,\tau,f_c}\right)\right). \tag{3.85}$$

The evolution of the nominal reference is expressed by the following expression:

$$\mathbf{r}_{k+1} = A_r \mathbf{r}_k + \mathbf{w}_k^r, \tag{3.86}$$

where $A_r \in \mathbb{R}^{n_x, n_x}$ and $\mathbf{w}_k^r$ is zero-mean Gaussian process noise with covariance Q_k^r. Stacking $\mathbf{x}_k$, $\mathbf{r}_k$, and a_{sig} into a vector, the following system is derived:

$$\begin{bmatrix} \mathbf{x}_{k+1} \\ \mathbf{r}_{k+1} \\ a_{\text{sig},k+1} \end{bmatrix} = \begin{bmatrix} A_k - B_u K & B_u K & B_u K t_z^r\left(z_{\text{sig}}^{i,\tau,f_c}\right) \\ \mathbf{0} & A_r & \mathbf{0} \\ \mathbf{0} & \mathbf{0} & 1 \end{bmatrix} \begin{bmatrix} \mathbf{x}_k \\ \mathbf{r}_k \\ a_{\text{sig},k} \end{bmatrix} + \overline{\mathbf{w}}_{\mathbf{k}}, \tag{3.87}$$

where $\mathbf{0}$ are matrices of zeros of appropriate dimensions and $\overline{\mathbf{w}}_k = \begin{bmatrix} \mathbf{w}_k^x & \mathbf{w}_k^r & w_k^a \end{bmatrix}^T$ is a stacked vector containing the process noise for the state, the reference, as well as the process noise perturbing the amplitude of the perturbation signature, w_k^a. Let $\overline{\mathbf{x}}_k = \begin{bmatrix} \mathbf{x}_k & \mathbf{r}_k & a_{\text{sig}} \end{bmatrix}^T$ be the stacked state vector used in Equation (3.87). The measurement output equation is defined as:

$$\mathbf{y}_k = \begin{bmatrix} C & \mathbf{0} & 0 \end{bmatrix} \begin{bmatrix} \mathbf{x}_k \\ \mathbf{r}_k \\ a_{\text{sig},k} \end{bmatrix} + \mathbf{v}_k, \tag{3.88}$$

where $\mathbf{v}_k$ is zero-mean Gaussian noise with covariance R_k.

Consider a KF implemented to estimate the augmented state vector, $\overline{\mathbf{x}}_k$, of Equation (3.87) given the noisy measurements, Equation (3.88). The KF computes the minimum mean square error estimate of $\overline{\mathbf{x}}_k$ which is the mean of $\overline{\mathbf{x}}_k$ conditioned on all the measurements up to $\mathbf{y}_k$, or

$$\hat{\overline{\mathbf{x}}}_k = \mathrm{E}\left[\overline{\mathbf{x}}_k | \mathbf{Y}^k\right], \tag{3.89}$$

where

$$\mathbf{Y}^k = \left\{\mathbf{y}_j\right\}_{j=1}^{k}, \tag{3.90}$$

is the sequence of measurements available at time k. Also define the KF innovation, ν_{k+1}, as:

$$\begin{aligned} \nu_{k+1} &= \mathbf{y}_{k+1} - \mathrm{E}\left[\mathbf{y}_{k+1} | \mathbf{Y}^k\right] && (3.91)\\ &= \mathbf{y}_{k+1} - C \cdot \mathrm{E}\left[\overline{\mathbf{x}}_{k+1} | \mathbf{Y}^k\right] && (3.92)\\ &= \mathbf{y}_{k+1} - \hat{\mathbf{y}}_{k+1} && (3.93) \end{aligned}$$

The next step is to relate the KF estimate of the system from Equation (3.87) to the LMP detector. The form of the LMP in Equation (3.54) is related to the KF by considering the negative log likelihood cost conditioned on measurements up to sample k. The joint probability distribution of the measurements (Equation (3.90)) up to k conditioned on the hypothesis $H_{\{\cdot\}}$, where $H_{\{\cdot\}}$ is either H_0 (the signal is absent), $H_{1,\cos}$ (the in-phase component of the signal is present), or $H_{1,\sin}$ (the quadrature component of the signal is present), can be written as:

$$p\left[\mathbf{Y}^k | H_{\{\cdot\}}\right] = p\left[\mathbf{y}_k, \mathbf{Y}^{k-1} | H_{\{\cdot\}}\right] \tag{3.94}$$

The distribution can be furthered simplified using Bayes' Rule:

$$\begin{aligned} p\left[\mathbf{Y}^k | H_{\{\cdot\}}\right] &= p\left[\mathbf{y}_k | \mathbf{Y}^{k-1}, H_{\{\cdot\}}\right] p\left[\mathbf{Y}^{k-1} | H_{\{\cdot\}}\right] && (3.95)\\ &= \prod_{j=1}^{k} p\left[\mathbf{y}_j | \mathbf{Y}^{j-1}, H_{\{\cdot\}}\right]. && (3.96) \end{aligned}$$

Although not shown explicitly, $p\left[\mathbf{Y^k}|H_{\{\cdot\}}\right]$ is conditioned not only on the hypothesis $H_{\{\cdot\}}$, but also on the system model and the a priori information about $\mathbf{x_0}$. Because a KF is used to estimate the augmented state, $\overline{\mathbf{x}}_k$, the distributions in Equation (3.96) are Gaussian, or

$$\begin{aligned} p\left[\mathbf{y}_j|\mathbf{Y}^{j-1},H_{\{\cdot\}}\right] &= \mathcal{N}\left[\mathbf{y}_j-\hat{\mathbf{y}}_j;0,S_j|H_{\{\cdot\}}\right] && (3.97)\\ &= p\left[\nu_i|H_{\{\cdot\}}\right], && (3.98)\end{aligned}$$

where $\nu_j=\mathbf{y}_j-\hat{\mathbf{y}}_j$ is the estimator's innovation at sample j, and S_j is its covariance. Substituting Equation (3.98) into Equation (3.96) equals:

$$p\left[\mathbf{Y}^k|H_{\{\cdot\}}\right]=\prod_{j=1}^{k}p\left[\nu_j|H_{\{\cdot\}}\right] \tag{3.99}$$

Since $p\left[\mathbf{Y}^k|H_{\{\cdot\}}\right]$ is conditioned on the system model, Equation (3.99), is actually the likelihood of the measurement sequence. In other words, $p\left[\mathbf{Y}^k|H_{\{\cdot\}}\right]$, Equation (3.99), is equivalent to the likelihood function derived in Equation (3.65) or Equation (3.74). The negative log likelihood function, Equation (3.99), is also related to the Kalman Filter innovations:

$$\begin{aligned} \mathcal{L}_{KF}\left(\mathbf{Y}^k|H_{\{\cdot\}}\right) &= -\log p\left[\mathbf{Y}^k|H_{\{\cdot\}}\right], && (3.100)\\ &= -\log\prod_{j=1}^{k}p\left[\nu_j|H_{\{\cdot\}}\right], && (3.101)\\ &= \left[\frac{1}{2}\sum_{j=0}^{k}\nu_j^T S_j^{-1}\nu_j\right]_{H_{\{\cdot\}}}. && (3.102)\end{aligned}$$

The log likelihood function for the KF for each hypothesis is the sum of the innovations up through sample k conditioned on the hypothesis $H_{\{\cdot\}}$ [16]. Since $\mathcal{L}\left(\mathbf{Y}^k|H_{\{\cdot\}}\right)$ is the likelihood function of the KF, the following substitutions can be made:

$$\begin{aligned} \mathcal{L}\left[\mathbf{y}|H_0\right] &= \mathcal{L}_{KF}\left(\mathbf{Y}^k|H_0\right) && (3.103)\\ \mathcal{L}\left[\mathbf{y}|H_{1,\cos},\hat{a}_{\text{sig}}\right] &= \mathcal{L}_{KF}\left(\mathbf{Y}^k|H_{1,\cos}\right) && (3.104)\\ \mathcal{L}\left[\mathbf{y}|H_{1,\sin},\hat{a}_{\text{sig}}\right] &= \mathcal{L}_{KF}\left(\mathbf{Y}^k|H_{1,\sin}\right) && (3.105)\end{aligned}$$

in Equations (3.67) and (3.75). Equations (3.103), (3.104), and (3.105) can be rewritten in terms of the KF innovations Equation (3.102) yielding:

$$\mathcal{L}\left[\mathbf{y}|H_0\right] = \left[\frac{1}{2}\sum_{j=0}^{k}\nu_j^T S_j^{-1}\nu_j\right]_{H_0} \tag{3.106}$$

$$\mathcal{L}\left[\mathbf{y}|H_{1,\cos},\hat{a}_{\text{sig}}\right] = \left[\frac{1}{2}\sum_{j=0}^{k}\nu_j^T S_j^{-1}\nu_j\right]_{H_{1,\cos}} \tag{3.107}$$

$$\mathcal{L}\left[\mathbf{y}|H_{1,\sin},\hat{a}_{\text{sig}}\right] = \left[\frac{1}{2}\sum_{j=0}^{k}\nu_j^T S_j^{-1}\nu_j\right]_{H_{1,\sin}} \tag{3.108}$$

It is now possible to relate the KF innovations to the original LMP statistic in Equation (3.51) and the associated optimization problem in Equation (3.54). Equations (3.106), (3.107), and (3.108), can be substituted into Equation (3.82) to rewrite the signal detection optimization problem over i, τ, and f_c in terms of the KF innovations:

$$\hat{i},\hat{\tau},\hat{f}_c = \max_{i,\tau,f_c}\left\{2\cdot\left[\frac{1}{2}\sum_{j=0}^{k}\nu_j^T S_j^{-1}\nu_j\right]_{H_0} - \left[\frac{1}{2}\sum_{j=0}^{k}\nu_j^T S_j^{-1}\nu_j\right]_{H_{1,\cos}} - \left[\frac{1}{2}\sum_{j=0}^{k}\nu_j^T S_j^{-1}\nu_j\right]_{H_{1,\sin}}\right\}. \tag{3.109}$$

In summary, for each i^{th} mode, τ Gold Code phase, and f_c carrier frequency, the locally most powerful test statistic in Equation (3.109) requires the evaluation of:

1. A KF under hypothesis H_0 that assumes no perturbation signature is present, $a_{\text{sig}} = 0$.
2. A KF under the hypothesis, $H_{1,\cos}$, that there is a perturbation signature present, with an in-phase carrier, $\cos(\cdot)$, that has the form $t_z^r\left(z_{\cos}^{i,\tau,f_c}\right)$.
3. A KF under the hypothesis, $H_{1,\cos}$, that there is a perturbation signature present, with a quadrature carrier, $\sin(\cdot)$, that has the form $t_z^r\left(z_{\sin}^{i,\tau,f_c}\right)$.

The values of i, τ, and f_c which maximize Equation (3.109) are declared under the LMP test as the detected parameters.

3.4 Suboptimal Detector

The optimal detector derived in Section 3.3 has two significant disadvantages: 1) the complexity of the model-based estimator (the magnitude of the perturbation signature must estimated), and 2) the computational cost. Although the Neyman-Pearson Lemma guarantees the optimally of the LMP for linear systems [39], a suboptimal detector might be more feasible for real-time implementation by providing comparable performance with less computations. The suboptimal detector uses a model-based estimator to reconstruct, from noisy measurements, the full reference $\left[\bar{\mathbf{r}}^i = \mathbf{r} + a_{\text{sig}} t_z^r \left(z_{\text{sig}^i}\right)\right]$. The estimate is then correlated with replicas of the mode perturbation signatures, as a function of i, τ, f_c and f_d. If the total reference is a vector, then only the component in which the mode perturbation signature was embedded is correlated with the signature replica. This suboptimal method, referred to as the Suboptimal Cascading Approach (SCA), detects a particular mode based on signal correlation in contrast to the LMP, which uses a KF's innovations.

In the SCA, a lower order model-based estimator (compared to the estimator for the LMP on Equation (3.87) is required to reconstruct the combined reference signal. Consider the linear discrete time system in Equation (3.83) and the corresponding linear full state feedback controller, $\mathbf{u}_k^i = K\left(-\mathbf{x}_k + \bar{\mathbf{r}}_k^i\right)$, where $\mathbf{x}_k$ and $\bar{\mathbf{r}}_k^i$ are stacked into a state vector yielding the following augmented state space model:

$$\begin{bmatrix} \mathbf{x}_{k+1} \\ \bar{\mathbf{r}}_{k+1}^i \end{bmatrix} = \begin{bmatrix} A_k - B_u K & B_u K \\ \mathbf{0} & \overline{A}_r \end{bmatrix} \begin{bmatrix} \mathbf{x}_k \\ \bar{\mathbf{r}}_k^i \end{bmatrix} + \overline{\mathbf{w}}_{\mathbf{k}}^{\mathbf{SCA}}, \tag{3.110}$$

where $\overline{\mathbf{w}}_k^{SCA} = \left[\mathbf{w}_k^x \;\; \mathbf{w}_k^{\bar{r},i}\right]^T$. The estimate of the total reference at time k is denoted as $\hat{\bar{\mathbf{r}}}_k^i$. The augmented system equations for the LMP, Equation (3.87) and the SCA, Equation (3.110), differ in that the SCA does not require the direct estimation of the signature amplitude, a_{sig}, thus reducing the dimension of the state vector.

The test statistic for the SCA relies on calculating the correlation of one the components of the KF estimated total reference of the KF, $\hat{\bar{r}}^{i,j}$ and the mode perturbation signature. The term $\hat{\bar{r}}^{i,j}$ is written to emphasize that if the total reference is a vector, only the j^{th} component will be used in the test statistic. Define $\hat{\bar{\mathbf{r}}}^{i,j}$ as the stacked vector of n_m scalar $\hat{\bar{r}}^{i,j}$ (typically over a block of time), or

$$\hat{\bar{\mathbf{r}}}^{i,j} = \begin{bmatrix} \hat{\bar{r}}_1^{i,j} \\ \hat{\bar{r}}_2^{i,j} \\ \vdots \\ \hat{\bar{r}}_{n_m}^{i,j} \end{bmatrix}. \tag{3.111}$$

Having calculated an estimate of the total reference, results for detection under carrier phase uncertainty or noncoherent detection are applied. The optimal noncoherent detector correlates a set of measurements with in-phase and quadrate Gold Code replicas [39], [40], [41]. For the SCA the optimal noncoherent detector test statistic for the i^{th} mode, correlates $\hat{\bar{\mathbf{r}}}^{i,j}$ with the in-phase and quadrature components of the perturbation signature replicas,

$$\lambda_{SCA} = \left(\left[\hat{\bar{\mathbf{r}}}^{i,j} \right]^T P^{-1} \mathbf{z}_{\sin}^{i,\tau,f_c} \right)^2 + \left(\left[\hat{\bar{\mathbf{r}}}^{i,j} \right]^T P^{-1} \mathbf{z}_{\cos}^{i,\tau,f_c} \right)^2. \tag{3.112}$$

In similar form to the LMP test statistic, Equation (3.112) replaces the measurements $\mathbf{y}_k$ with $\hat{\bar{\mathbf{r}}}^{i,j}$.

In this application, the detector is used to optimize over the unknown i, τ, and f_c to find the optimal value of the SCA test statistic, or

$$\hat{i}, \hat{\tau}, \hat{f}_c = \arg \max_{i,\tau,f_c} \lambda_{SCA}. \tag{3.113}$$

It should be noted that the SCA test statistic does not consider the optimality of the KF estimate.

The motivation for a suboptimal SCA detector is to reduce the complexity and the computational cost of the LMP detector. The SCA simplifies the detector by relying on

Table 3.2: Computational cost per sample comparison between the optimal detector (LMP) and a suboptimal formulation (SCA). This table assumes that the dimension of the augmented state is larger than the dimension of the output vector of the augmented system.

	Optimal Detector	Suboptimal Detector
Kalman Filter Cost	$n_{\text{sig}} \cdot n_\tau \cdot n_F \cdot (2n_x+1)^3$	$(2n_x)^3$
Correlations	0	$n_{\text{sig}} \cdot n_\tau \cdot n_F$
Total Computational Cost	$3n_{\text{sig}} \cdot n_\tau \cdot n_F \cdot (2n_x+1)^3$	$n_{\text{sig}} \cdot n_\tau \cdot n_F + (2n_x)^3$

a lower order KF and on discrete time correlation calculation for detection. In general, the computational cost of the KF is approximately proportional to the cube of the larger dimension between the state vector or measurement vector, $\max(n_x, n_y)$[16]. Let n_{sig}, n_τ, and n_F denote the number of mode signatures, mode signature phases, and sinusoidal carrier frequency offsets that compose the detection search space. The LMP requires the KF to estimate an augmented vector, $\begin{bmatrix}\mathbf{x}_k & \mathbf{r}_k & a_{\text{sig}}\end{bmatrix}^T \in \mathbb{R}^{2n_x+1}$, which is composed of the state, reference, plus the mode signature amplitude. However, three KFs must be run for each condition in the search space (for hypotheses: H_0, $H_{1,\cos}$, and $H_{1,\sin}$). Therefore, the computational cost for the LMP is: $3n_{\text{sig}} \cdot n_\tau \cdot n_F \cdot (2n_x+1)^3$ which scale as $n_{\text{sig}} \cdot n_\tau \cdot n_F \cdot n_x^3$. In contrast to the LMP, the SCA only requires one computation of the KF with an augmented state vector of dimension $\begin{bmatrix}\mathbf{x}_k & \mathbf{r}_k\end{bmatrix}^T \in \mathbb{R}^{2n_x}$ and $n_{\text{sig}} \cdot n_\tau \cdot n_F$ correlation computations. This analysis shows that the computational cost reduction of the SCA is proportional to $n_{\text{sig}} \cdot n_\tau \cdot n_F$ and thus makes its implementation more feasible in real-time. Table 3.2 summarizes the computational cost for the LMP and SCA.

3.5 Probability of False Alarm

The derived test statistic in Equation (3.49) can be used to calculate the false alarm probability based on a detection threshold, $\overline{\lambda}_{\text{LMP,thresh}}$. As shown in Equation (3.49),

the test statistic is a function of the observations, $\mathbf{y}$, and the in-phase and quadrature components of the mode perturbation signature. As defined in Equation (3.50), $\overline{\lambda}_{\text{LMP}}$, is the value of the test statistic,

$$\overline{\lambda}_{\text{LMP}} = \left(\mathbf{y}^T P^{-1} \mathbf{z}_{\cos}^{i,\tau,f_c}\right)^2 + \left(\mathbf{y}^T P^{-1} \mathbf{z}_{\sin}^{i,\tau,f_c}\right)^2. \tag{3.114}$$

If $\beta_{\cos}$, $\beta_{\sin}$ are defined as the correlation of the measurements and the in-phase and quadrature components of the mode perturbation signatures, then Equation (3.114) can be written as:

$$\overline{\lambda}_{\text{LMP}} = \beta_{\cos}^2 + \beta_{\sin}^2. \tag{3.115}$$

It should be noted that $\overline{\lambda}_{\text{LMP}}$ is a random variable as it depends on the measurements. A signal is declared present if:

$$\overline{\lambda}_{\text{LMP}} > \overline{\lambda}_{\text{LMP,thresh}}. \tag{3.116}$$

The probability of false alarm is the cumulative distribution of $\overline{\lambda}_{\text{LMP}}$ under hypothesis H_0 evaluated from $\overline{\lambda}_{\text{LMP,thresh}}$ to infinity and written as:

$$P_F = \int_{\overline{\lambda}_{\text{LMP,thresh}}}^{\infty} p_{\overline{\lambda}_{\text{LMP}}}\left(\overline{\lambda}_{\text{LMP}} \middle| H_0\right) d\overline{\lambda}_{\text{LMP}}, \tag{3.117}$$

where $p_{\overline{\lambda}_{\text{LMP}}}$ is the probability distribution of the test statistic.

The probability distribution for $\overline{\lambda}_{\text{LMP}}$ is found by deriving the probability distributions of the its components. Because $\beta_{\cos}$ is a linear transformation of the zero-mean Gaussian vector $\mathbf{y}$ with covariance P under hypothesis H_0, then $\beta_{\cos}$ is also Gaussian [42]. Therefore, only the first two moments of $\beta_{\cos}$ need to be calculated. The expectation of $\beta_{\cos}$ is:

$$\begin{aligned} \text{E}\left[\beta_{\cos}\right] &= \text{E}\left[\mathbf{y}^T P^{-1} \mathbf{z}_{\cos}^{i,\tau,f_c}\right], & (3.118)\\ &= \text{E}\left[\mathbf{y}^T P^{-1}\right] \mathbf{z}_{\cos}^{i,\tau,f_c}, & (3.119)\\ &= 0, & (3.120) \end{aligned}$$

where in Equation (3.119) the linearity of the expectation operator, $\mathrm{E}[\cdot]$, is used and Equation (3.120) is zero because the noise elements have a Gaussian distribution with zero mean. The covariance of $\beta_{\cos}$ defined as $P_{\beta_{\cos}}$ is:

$$
\begin{aligned}
P_{\beta_{\cos}} &= \mathrm{E}\left[\left(\mathbf{y}^T P^{-1}\mathbf{z}_{\cos}^{i,\tau,f_c} - \mathrm{E}[\beta_{\cos}]\right)\left(\mathbf{y}^T P^{-1}\mathbf{z}_{\cos}^{i,\tau,f_c} - \mathrm{E}[\beta_{\cos}]\right)^T\right] && (3.121)\\
&= \mathrm{E}\left[\left(\mathbf{y}^T P^{-1}\mathbf{z}_{\cos}^{i,\tau,f_c}\right)\left(\mathbf{y}^T P^{-1}\mathbf{z}_{\cos}^{i,\tau,f_c}\right)^T\right]. && (3.122)\\
&= \mathrm{E}\left[\left(\mathbf{z}_{\cos}^{i,\tau,f_c} P^{-1}\mathbf{y}\right)\left(\mathbf{y}^T P^{-1}\mathbf{z}_{\cos}^{i,\tau,f_c}\right)\right], && (3.123)
\end{aligned}
$$

where the expression in Equation (3.123) is derived because the scalar $\beta_{\cos}$ is equal to its transpose and by substituting the following expression:

$$
\left(\mathbf{y}^T P^{-1}\mathbf{z}_{\cos}^{i,\tau,f_c}\right)^T = \left(\mathbf{z}_{\cos}^{i,\tau,f_c}\right)^T P^{-1}\mathbf{y}. \tag{3.124}
$$

By substituting the definition of the hypothesis H_0, Equation (3.16), into Equation (3.122), the covariance $P_{\cos}$ is then calculated:

$$
\begin{aligned}
P_{\beta_{\cos}} &= \mathrm{E}\left[\left(\mathbf{z}_{\cos}^{i,\tau,f_c} P^{-1}\mathbf{n}\right)\left(\mathbf{n}^T P^{-1}\mathbf{z}_{\cos}^{i,\tau,f_c}\right)\right] && (3.125)\\
&= \left(\mathbf{z}_{\cos}^{i,\tau,f_c}\right)^T P^{-1}\mathrm{E}\left[\mathbf{n}\mathbf{n}^T\right] P^{-1}\mathbf{z}_{\cos}^{i,\tau,f_c} && (3.126)\\
&= \left(\mathbf{z}_{\cos}^{i,\tau,f_c}\right)^T P^{-1}\mathbf{z}_{\cos}^{i,\tau,f_c}. && (3.127)
\end{aligned}
$$

Therefore $\beta_{\cos}$ has a zero-mean Gaussian distribution with covariance $P_{\beta_{\cos}}$. The same analysis yields that other component of the test statistic, $\beta_{\sin}$, has a zero-mean Gaussian distribution with covariance,

$$
P_{\beta_{\sin}} = \left(\mathbf{z}_{\sin}^{i,\tau,f_c}\right)^T P^{-1}\mathbf{z}_{\sin}^{i,\tau,f_c}. \tag{3.128}
$$

Using Equation (3.77) it can be shown that

$$
P_{\beta_{\cos}} \approx P_{\beta_{\sin}}, \tag{3.129}
$$

therefore $\beta_{\cos}$ and $\beta_{\sin}$ both have zero-mean Gaussian distributions with covariance $P_{\beta_{\cos}}$.

The probability distribution of the sum of the squares of two Gaussian distributed random variables, $\beta_{\cos}$ and $\beta_{\sin}$, with mean of zero, and covariance of $P_{\beta_{\cos}}$ is a chi-squared distribution [40]. The chi-squared distribution of $\overline{\lambda}_{\text{LMP}}$ is:

$$p_{\overline{\lambda}_{\text{LMP}}}\left(\overline{\lambda}_{\text{LMP}}\right) = \frac{1}{2P_{\beta_{\cos}}} \exp\left(-\frac{\overline{\lambda}_{\text{LMP}}}{2P_{\beta_{\cos}}}\right). \tag{3.130}$$

To compute the probability of false alarm, Equation (3.130) is substituted into Equation (3.134) resulting in:

$$\begin{aligned} P_F &= \int_{\overline{\lambda}_{\text{LMP,thresh}}}^{\infty} \frac{1}{2P_{\beta_{\cos}}} \exp\left(-\frac{\overline{\lambda}_{\text{LMP}}}{2P_{\beta_{\cos}}}\right) d\overline{\lambda}_{\text{LMP}} && (3.131)\\ &= -\exp\left(-\frac{\overline{\lambda}_{\text{LMP}}}{2P_{\beta_{\cos}}}\right)\Bigg|_{\overline{\lambda}_{\text{LMP,thresh}}}^{\infty} && (3.132)\\ &= 0 - \left[-\exp\left(-\frac{\overline{\lambda}_{\text{LMP,thresh}}}{2P_{\beta_{\cos}}}\right)\right] && (3.133)\\ &= \exp\left(\frac{\overline{\lambda}_{\text{LMP,thresh}}}{2P_{\beta_{\cos}}}\right). && (3.134) \end{aligned}$$

The threshold necessary to detect the presence of a signal to a probability of false alarm, α_{LMP}, is derived from Equation (3.134) by substituting Equation (3.127) and solving for $\overline{\lambda}_{\text{LMP,thresh}}$ yielding:

$$\overline{\lambda}_{\text{LMP,thresh}} = -2\left(\mathbf{z}_{\cos}^{i,\tau,f_c}\right)^T P^{-1} \mathbf{z}_{\cos}^{i,\tau,f_c} \log \alpha_{\text{LMP}}. \tag{3.135}$$

3.6 Linear Numerical Example

The mode detection methodology, including mode detection based on the Neyman-Pearson locally most powerful statistic (LMP) and the sub-optimal approach (SCA) are numerically evaluated in this section using a two-state linear system with linear output equations. The goal is to test the performance of both detection methods and gain insights into the tuning the corresponding model-based state estimators. Because of its

Table 3.3: Simulation parameters for the Monte Carlo runs.

Parameter	Value
K	$\begin{bmatrix} 30 & 8.0 \end{bmatrix}$
T	0.01

optimality for linear systems with Gaussian noise and well known equations, the discrete time Kalman Filter is used for state estimation. Since its publication by Rudolph Kalman in [43], the KF has been applied to estimation problems in various fields that include tracking, navigation, physics, and economics. The reader interested in a more detailed derivation and explanation of the KF is referred to the following references [16], [44], [45].

3.6.1 Two State Linear Model with Linear Output Equations

The dynamics of motion in one dimension are modeled using a linear point mass model to describe the motion in an inertial plane, resulting in:

$$\mathbf{x}_{k+1} = A_k \mathbf{x}_k + B_u u_k + \mathbf{w}_k, \tag{3.136}$$

$$\mathbf{x}_{k+1} = \begin{bmatrix} 1 & T \\ 0 & 1 \end{bmatrix} \mathbf{x}_k + \begin{bmatrix} 0 \\ T \end{bmatrix} u_k + \mathbf{w}_k, \tag{3.137}$$

where the state, $\mathbf{x}_k = [x_k, \dot{x}_k] \in \mathbb{R}^2$, contains the position and velocity of the vehicle in the x direction, $\mathbf{w}_k$ is zero-mean Gaussian process noise with covariance Q, and T is the sampling time. The controller in Equation (3.11) is a full state feedback controller, given as

$$u_k = K\left(-\mathbf{x}_k + \bar{\mathbf{r}}_k\right), \tag{3.138}$$

is used for tracking the reference $\bar{\mathbf{r}}_k$, Equation (3.6). Constants used in the model and the controller are shown in Table 3.3.

Table 3.4: Operating modes and corresponding mode signatures with $n_\rho = 31$.

Mode	Behavior	Signature
1	A	[11000010101110010110110000011011]
2	B	[11001000010111011101110011101 00]
3	C	[10101101101100101111011101 01010]

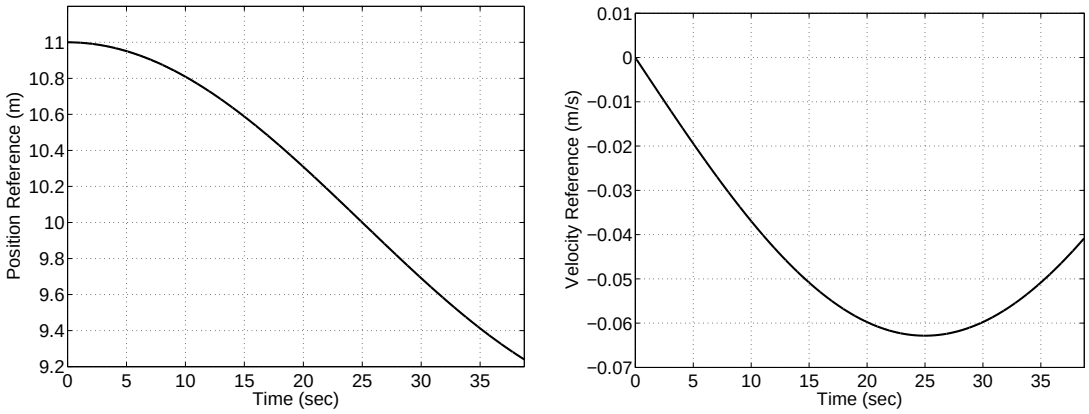

(a) (b)

Figure 3.5: Position reference of amplitude equal to 1 meter and frequency 0.01 Hz. The corresponding velocity reference is also shown.

The position trajectory of the simplified vehicle motion, is described by three operating modes: 1) behavior A, 2) behavior B, and 3) behavior C. These modes are defined with the signatures (Gold Codes) shown in Table 3.4 [36]. Since the mode perturbation signature is embedded in the position reference, its derivative must be embedded in the tracking reference. Therefore, the function which maps from the scalar mode perturbation signature z^i_{sig} to the perturbation reference $\mathbf{r}^i_{\text{sig}}$ has the following form:

$$\mathbf{r}^i_{\text{sig},k} = a_{\text{sig}} t^r_z \left(z^i_{\text{sig},k} \right), \tag{3.139}$$

$$= a_{\text{sig}} \begin{bmatrix} z^i_{\text{sig},k} \\ \frac{d}{dt} z^i_{\text{sig},k} \end{bmatrix}. \tag{3.140}$$

The nominal reference, $\mathbf{r_k}$, for the vehicle is shown in Figure 3.5. Figure 3.6 shows the combined reference composed of the addition of the nominal reference and the mode

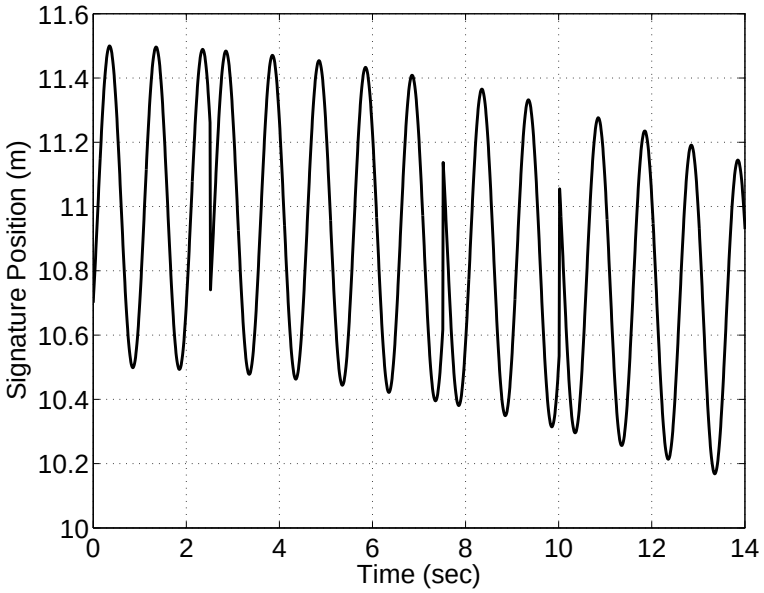

Figure 3.6: The combined position reference composed of the position reference and the mode perturbation signature.

perturbation signature. The closed-loop response of the two-state linear system to a combined position reference is shown in Figure 3.7.

The output equation is scalar with the form:

$$y_k = C\mathbf{x}_k + v_k = \begin{bmatrix} 1 & 0 \end{bmatrix} \mathbf{x}_k + v_k, \tag{3.141}$$

where v_k is zero-mean Gaussian noise with covariance R_k.

3.6.2 Estimator Setup

In the LMP, the KF uses replicas of the perturbation signatures as known inputs and estimates the system's nominal reference, $\hat{\mathbf{r}}_k$, and perturbation signature amplitude, $\hat{a}_{\text{sig}}$. The system has a full-state feedback controller gain, K, and the control input has the form:

$$u_k = K\left(\mathbf{r}_k + a_{\text{sig}} t_z^r\left(z_{\text{sig},k}^{i,\tau}\right) - \mathbf{x}_k\right). \tag{3.142}$$

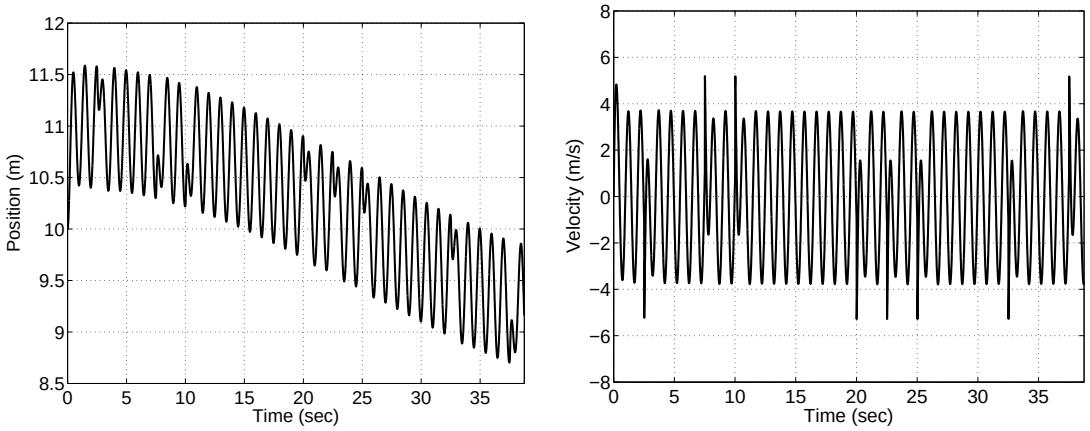

(a) (b)

Figure 3.7: The response of the two state linear model to the combined position reference shown in Figure 3.6.

The carrier frequency of the carrier f_c is known and therefore dropped from the notation, while the frequency offset f_d is not considered here as its uncertainty is small for the system in this example.

An augmented state is defined for use with the estimation model,

$$\begin{bmatrix} \mathbf{x}_{k+1} \\ \mathbf{r_{k+1}} \\ a_{\text{sig},k+1} \end{bmatrix} = \begin{bmatrix} A_k - B_u K & B_u K & B_u K t_z^r \left(z_{\text{sig},k}^{i,\tau} \right) \\ \mathbf{0} & A_r & \mathbf{0} \\ \mathbf{0} & \mathbf{0} & 1 \end{bmatrix} \begin{bmatrix} \mathbf{x_k} \\ \mathbf{r_k} \\ a_{\text{sig},k} \end{bmatrix} + \overline{\mathbf{w}}_{\mathbf{k}}. \tag{3.143}$$

where $\overline{\mathbf{w}}_{\mathbf{k}}$ is the process noise for the augmented with covariance $\overline{Q}_k$. The matrix A_r will be used for tuning the estimator.

The output equation of the system is linear and has the position as the sole measurement:

$$y_k = \begin{bmatrix} 1 & 0 & \mathbf{0} & 0 \end{bmatrix} \begin{bmatrix} \mathbf{x_k} \\ \mathbf{r_k} \\ a_{\text{sig}} \end{bmatrix} + v_k, \tag{3.144}$$

where v_k is zero-mean Gaussian noise with covariance R.

The SCA KF formulation is similar and the only difference is that it is not necessary

to estimate a_{sig}. The SCA augmented system has the form shown in Equation (3.110), or

$$\begin{bmatrix} \mathbf{x}_{k+1} \\ \overline{\mathbf{r}}^{i}_{k+1} \end{bmatrix} = \begin{bmatrix} A_k - B_u K & B_u K \\ \mathbf{0} & \overline{A}_r \end{bmatrix} \begin{bmatrix} \mathbf{x}_k \\ \overline{\mathbf{r}}^{i}_{k} \end{bmatrix} + \overline{\mathbf{w}}^{\mathbf{SCA}}_{\mathbf{k}}, \tag{3.145}$$

where the matrix $\overline{A}_r$ will be determined in the next section.

3.6.3 Estimator Tuning

The effectiveness of the mode detection methods proposed in this chapter rely significantly on the performance of the KF. In mode detection, great care must be given to tuning the process and noise covariances of the KF in order to not only minimize the effects of noise disturbances, but also to aid in detection. In this section, the KF tuning procedure for the augmented systems formulated in Section 3.6.2 is summarized and the resulting estimates are used for mode detection using the LMP and the SCA detection algorithms.

Kalman Filter Tuning for the LMP Test Statistic

Consider the two-state linear model, Equation (3.87), that has as a nominal reference of the form:

$$r_k = a_r \cos\left[2\pi f_r t_k\right], \tag{3.146}$$

where a_r is the sinusoid amplitude and $f_r = 0.1$ Hz is its frequency. The mode perturbation signature associated with behavior B (see Table 3.4) has magnitude, a_{sig}. Initially to better understand the behavior of the estimator, both the process and measurement noise are set to small values $\left(Q = R = 10^{-5}\right)$. In Equation (3.143), $\mathbf{r}_k$ is modeled as a second order Markov process. The corresponding A_r is::

$$A_r = \begin{bmatrix} 1 & T \\ 0 & 1 \end{bmatrix}, \tag{3.147}$$

where T is the sampling time. As $T \to 0$ the model for $\mathbf{r}_k$ becomes a random walk. Expanding the second order Markov process model yields the following equations for the elements of $\mathbf{r}_k$,

$$r_{k+1} = r_k + T\dot{r}_k, \tag{3.148}$$

$$\dot{r}_{k+1} = \dot{r}_k + Tw_k. \tag{3.149}$$

However, the second term in the right side of Equation (3.149) implies that the acceleration of the reference can change instantaneously and could violate a physical or modeling constraint. To impart memory into the integration of the acceleration, a $(-\omega_r \dot{r}_k)$ term can be added to Equation (3.149) such that it becomes:

$$\dot{r}_{k+1} = \dot{r}_k + T\left(w_k - \omega_r \dot{r}_k\right), \tag{3.150}$$

where $\omega_r \in \mathbb{R}^{0,+}$ delays the integration of the acceleration. Figure 3.8 shows the velocity reference ($a_r = 1.0$, $f_r = 0.01$ Hz) as well as four KF estimates corresponding to different values of ω_r. The covariance matrices for the process and measurement noise are:

$$\overline{Q}_k = \text{diag}\left(\left[10^{-2},\ 10^{+1},\ 10^{-1},\ 10^{+1}\right]\right), \tag{3.151}$$

and

$$R_k = 10^{-5}. \tag{3.152}$$

Progressing from Figure 3.8(a) to (b), (c), and (d) it is observed that increasing ω_r decreases the amplitude of the estimated velocity reference sinusoid. This makes sense as ω_r was introduced in order to slow the integration of the reference velocity term. The value of ω_r can be used in tuning to control the magnitude of the KF's estimate of the velocity reference.

Tuning the elements of the diagonal process covariance matrix, $\overline{Q}_k$, is critical for the optimal performance of the KF. The parameters used for this example are shown in Table 3.5. Using an estimation horizon less than one Gold Code period can be problem-

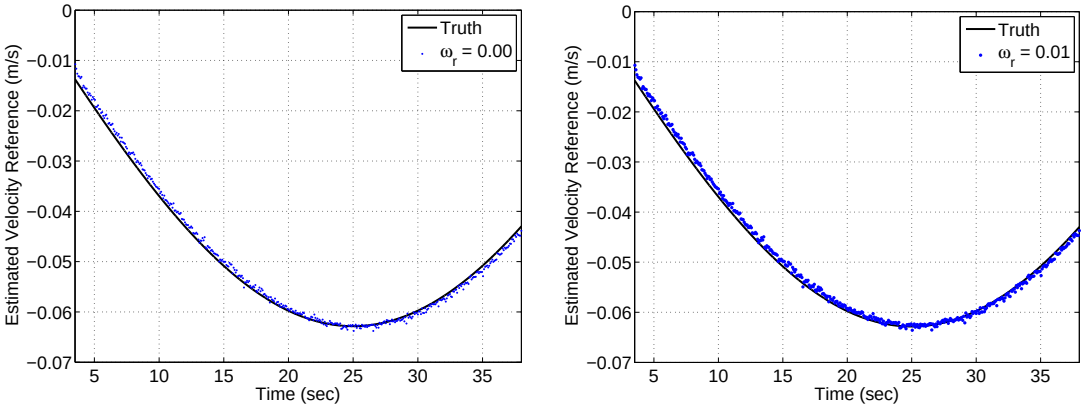

(a) $\omega_r = 0.00$

(b) $\omega_r = 0.01$

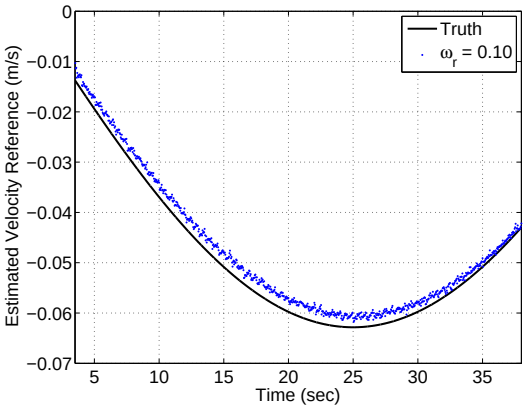

(c) $\omega_r = 0.10$

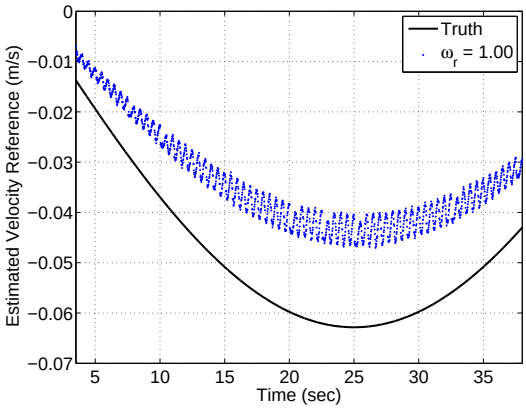

(d) $\omega_r = 1.00$

Figure 3.8: The effects of increasing the memory term, ω_r, in the estimation of the velocity reference.

Table 3.5: Simulation parameters for a 1-D Kalman Filter example with a linear output equation.

Parameter	Value
Perturbation Mode	Behavior B
Gold Code Period	77.5 seconds
Estimation Horizon	38.8 seconds
Cold Code Phase	8
Carrier Frequency	1 Hz
Carrier Phase	0 degrees
Bit Length	2.5 seconds
a_r	1.0 meter
a_{sig}	0.5 meters
f_r	0.10 Hertz
Sampling Time, T	0.01 seconds
Measurement Noise	$1x10^{-5}$ meters^2
ω_r	0

atic as the auto and cross correlation properties of the sequences are not fully exploited. However, in this investigation it is essential to minimize the time (or number of measurements) needed to make a decision, thus justifying the need to explore the performance of the approach with small time horizons. Figure 3.9 shows KF estimates for different values of the element in the process noise covariance matrix corresponding to the velocity reference, denoted as $\overline{Q}_{\dot{r}}$. In Figure 3.9, the accuracy in the estimate is shown to decrease with a decrease in $\overline{Q}_{\dot{r}}$. Although a larger process noise covariance element improves accuracy, it also produces an inevitable larger initial estimation error transient (see Figure 3.10). However, since the estimation horizons considered in this investigation extend well beyond the initial transients the effects of the initial estimation error transient are inconsequential as they are shared by all test statistics.

In the estimate of a constant perturbation signature amplitude, a_{sig}, the corresponding process noise covariance element, denoted as $\overline{Q}_{a_{\text{sig}}}$, determines the estimate's settling time. Figure 3.11 shows how different values of the perturbation signature amplitude

process noise element, $\overline{Q}_{a_{\text{sig}}}$, affect the settling time of the estimate. It should be noted that a priori statistical information about the state, P_0, also influences the settling time of the estimate. Given that for these numerical studies the truth model was available, the P_0 used was common to all simulations and had the value 10^{-2} along its diagonal given th. When using real data, various techniques can be used to correctly initialize the estimator [16] or use the information form of the KF in defining P_0 is not necessary. Define the sum of squares of the estimation errors (SSE) defined as

$$\text{SSE} = \sum_{k=1}^{k_{\max}} \left(\hat{\upsilon}_k - \upsilon_k\right)^T \left(\hat{\upsilon}_k - \upsilon_k\right), \tag{3.153}$$

where k is a time index, $k_{\max}$ is the number of samples considered, υ_k is the truth value for the variable, and $\hat{\upsilon}_k$ is the estimate of the variable. For this example, the SSE, Equation (3.153), is calculated for the state element corresponding to a_{sig} and for three values of the associated process noise covariance element of: 10^{-2}, 1, and 10^2 and $k_{\max} = 250$. Simulation studies show that the optimal value of the SSE is found process noise covariance element is $\overline{Q}_{a_{\text{sig}}} = 1.0$. as this value yields the best tradeoff between settling time and insensitivity to noise. Similar tradeoffs between faster response and increased sensitivity to error were observed in the tuning of the other estimated signals. Equations (3.154) and (3.155) show the process noise covariances found to result in the best estimates for the KFs the corresponding to the hypotheses that no signal is present, $\overline{Q}_k^{H_0}$, and a mode perturbation signature is present, $\overline{Q}_k^{H_1}$.

$$\overline{Q}_k^{H_0} = \text{diag}\left(\left[10^{-3},\ 10^{+2},\ 10^{-1},\ 10^{+1}\right]\right). \tag{3.154}$$

$$\overline{Q}_k^{H_1} = \text{diag}\left(\left[10^{-3},\ 10^{+2},\ 10^{-1},\ 10^{+1},\ 10^{0}\right]\right). \tag{3.155}$$

It is important to analyze how the LMP test statistic, Equation (3.51), reacts to increased noise intensity and its effect on mode detection. In the evaluation of the LMP test statistic the simulation parameters from Table 3.6 are used. Figure 3.12 shows the evaluation of the LMP test statistic as a function of mode behavior and Gold Code phase.

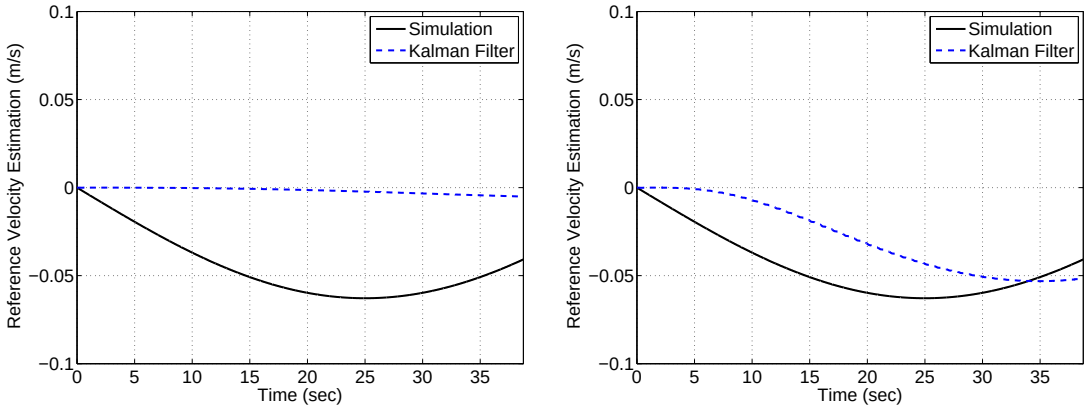

(a) $\overline{Q}_{\dot{r}} = 10^{-5}$ (b) $\overline{Q}_{\dot{r}} = 10^{-3}$

(c) $\overline{Q}_{\dot{r}} = 10^{-1}$ (d) $\overline{Q}_{\dot{r}} = 10^{+1}$

Figure 3.9: Estimating the derivative of the position reference by tuning the process noise covariance.

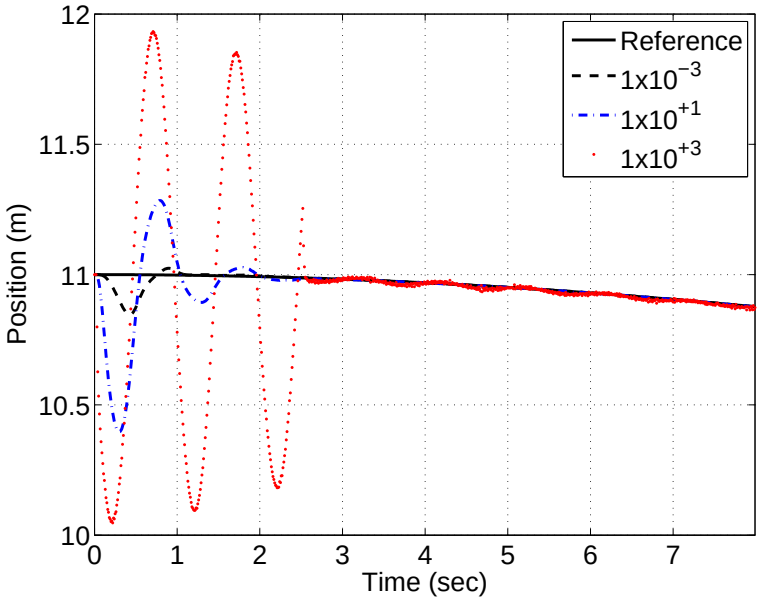

Figure 3.10: Effects of increasing the $\overline{Q}_r$ element of process noise covariance matrix and its effects on the initial estimation error for the position reference.

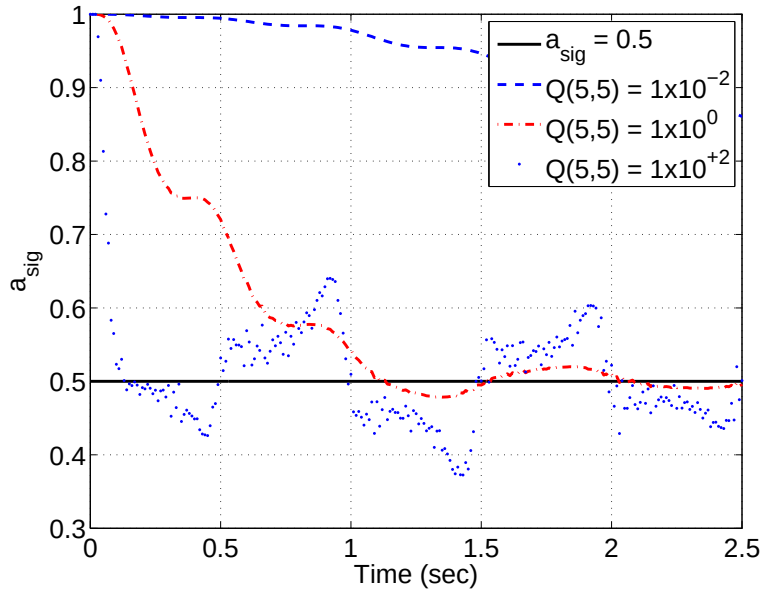

Figure 3.11: Estimation of the perturbation signature magnitude, a_{sig}.

As mentioned earlier, because Doppler effects are unlikely in this type of system, frequency offsets are not considered. In this investigation, the amplitude-to-noise ratio (ANR) is defined as:

$$\text{ANR} = \frac{a_{\text{sig}}^2}{2R_{\max}}, \tag{3.156}$$

where $R_{\max}$ is maximum element of the measurement noise covariance matrix, or

$$R_{\max} = \max_{l} R(l,l), \tag{3.157}$$

for $l = 1, \ldots, n_y$. The relationship between the ANR and the signal-to-noise ratio (SNR) commonly used in detection is:

$$\text{SNR} = \text{ANR} \times k_{\max}, \tag{3.158}$$

where as defined previously $k_{\max}$ is the number of samples considered [39]. The ANR was defined independent of the number of samples in order to isolate its influence on the performance of the algorithm. Equation (3.158) clearly shows that either the ANR or SNR can be easily computed from the other. In Figure 3.12, the evaluation of the LMP test statistic for the three different amplitude-to-noise ratios expressed in decibels ($10\log(\cdot)$) is: 1) 94.3, 2) 48.3, and 3) 25.3 are shown. In Figure 3.12(a), the test statistic correctly detects the mode and phase, while Figures 3.12(b) and (c) show that the increased noise level leads to incorrect detections.

The measurement noise covariance matrix can be tuned to reduce the effects of measurement noise and increase the detection parameter separation in the LMP. The term detection parameter separation refers to the difference in value that exists when the test statistic is calculated for the correct and incorrect parameters (mode or Gold Code and Gold Code phase). In this one dimensional example, increasing the KF measurement noise covariance leads to the estimator which behaves as a low-pass filter by reducing the Kalman Gain [46]. Figure 3.13 shows the evaluation of the LMP test statistic when the KF measurement noise covariance is $R = c_r \cdot R_0$ where $c_r = \left[1, 10^2, 10^4\right]$ and R_0 is

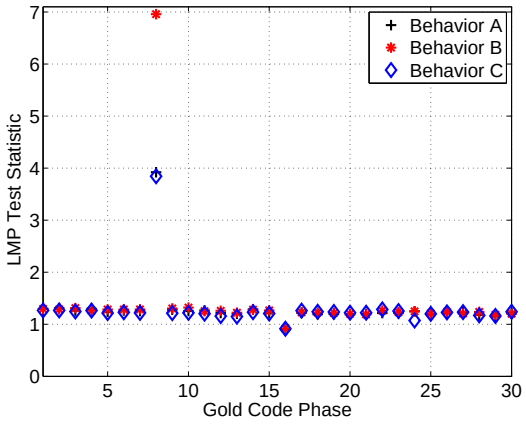

(a) ANR = 94.3

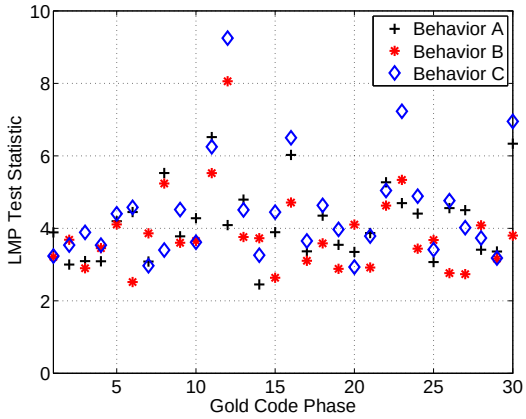

(b) ANR = 48.3

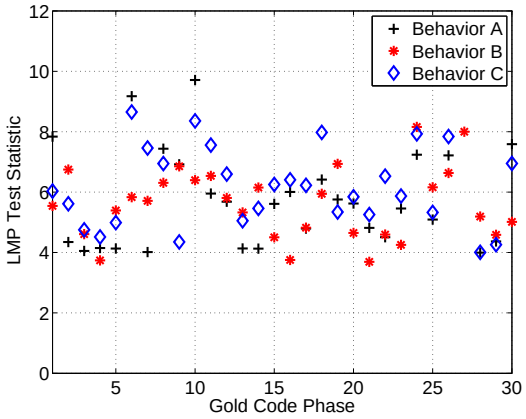

(c) ANR = 25.3

Figure 3.12: The effects of measurement noise on the LMP test statistic, $\overline{\lambda}^{i,\tau}_{\text{LMP}}$. Each row depicts the evaluation of the test statistic for the three amplitude-to-noise ratios in decibels: 1) 94.3, 2) 48.3, and 3) 25.3. The truth mode and Gold Code phase are Behavior B at a phase of 8. The frequency of the position reference is 0.10 Hertz.

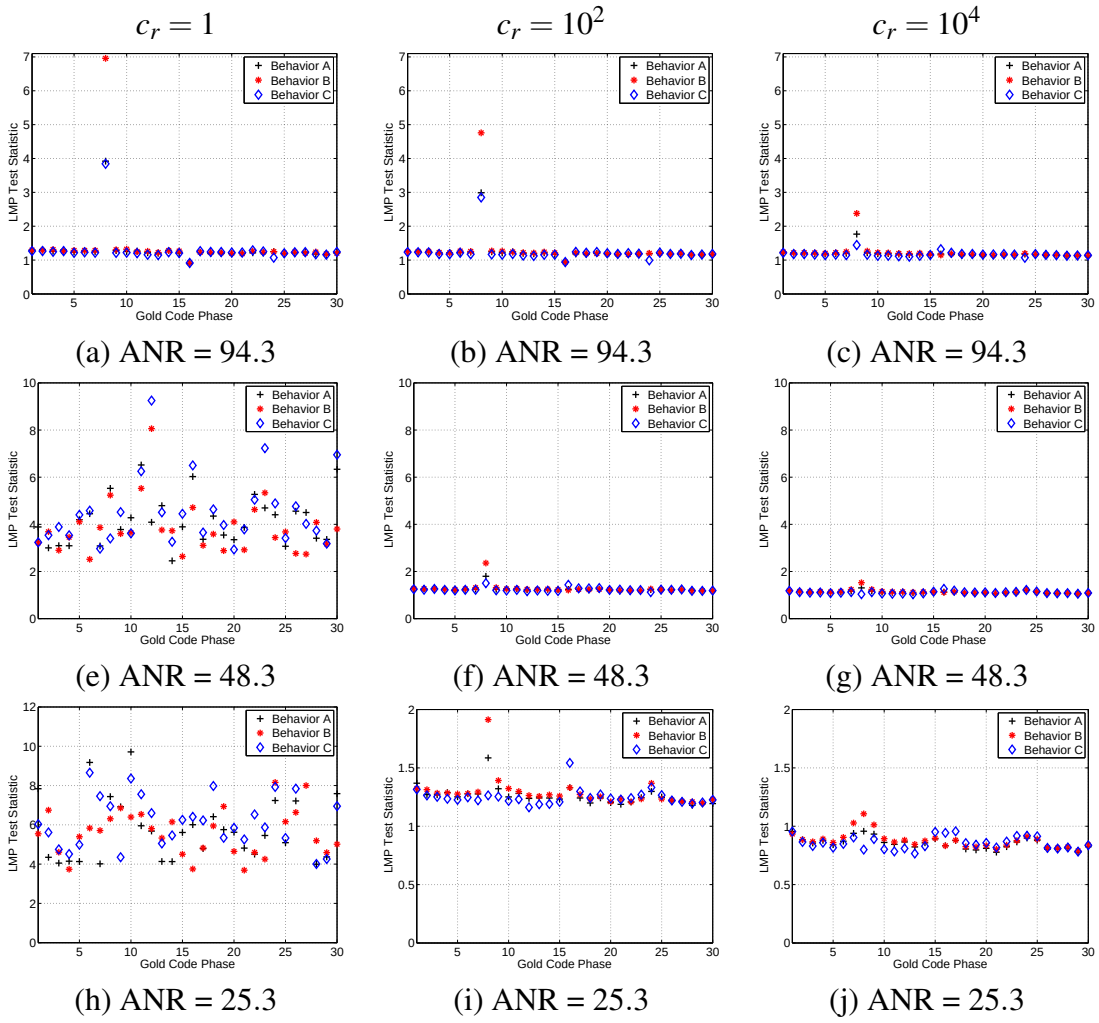

Figure 3.13: Multiplying the process noise covariance of the KF by factor of 10^0, 10^2, and 10^4 and and its effect on the LMP test statistic, $\overline{\lambda}^{i,\tau}_{\text{LMP}}$. Each row depicts the evaluation of the test statistic for the three amplitude-to-noise ratios in decibels: 1) 94.3, 2) 48.3, and 3) 25.3 (from the top). The columns correspond to the LMP evaluation in which the KF measurement noise covariance is multiplied by $c_r = \left[1, 10^2, 10^4\right]$. The frequency of the position reference is 0.10 Hertz.

Table 3.6: Simulation parameters used to analyze the LMP test statistic for a 1-D Kalman Filter example with a linear output equation.

Parameter	Value
Perturbation Mode	Behavior B
Gold Code Period	77.5 seconds
Cold Code Phase	8
Carrier Frequency	1 Hz
Carrier Phase	2.9 radians
Bit Length	2.5 seconds
a_r	1.0 meter
a_{sig}	0.5 meters
f_r	0.10 Hz
Estimation Horizon	38.8 seconds
Sampling Time, T	0.01 seconds
ω_r	0

the covariance matrix for each ANR value. The figures shows that decreasing the bandwidth of the estimator reduces the value of the LMP test statistic for signals with the incorrect parameters. For the figures with ANR of 48.3 and 25.3, it can be seen that if the measurement noise covariance is not multiplied by a factor detection is not possible. For the parameters in this example, an ANR ≤ 48.3 requires that the KF measurement covariance is increased by a factor of $c_r = 10^2$ for robust detection parameter separation. Increasing the measurement noise covariance allows the detector to perform better by reducing the test statistic value for the incorrect parameters. However, Figure 3.13(c) shows that as the KF measurement noise covariance increases, the value of the LMP test statistic reduces for the signal with the correct parameters. For this example, the best tradeoff is found when KF measurement noise covariance is multiplied by a factor of 10^2 as shown in Figure 3.13. As expected, the noise disturbance rejection achieved by lowering the bandwidth of the estimator can also be seen in the state estimate. Figure 3.14 compares the estimation of a_{sig} when the KF measurement covariance matrix is multiplied by a factor of $c_r = 0$ and $c_r = 10^2$. Similar results are observed in the esti-

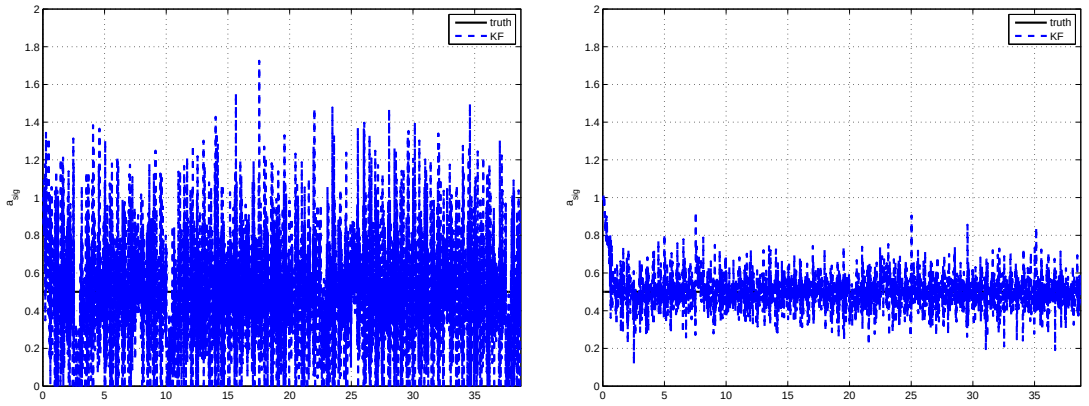

(a) $c_r = 0$ (b) $c_r = 10^2$

Figure 3.14: The estimate of the mode perturbation signature amplitude and the effects of using different values in the measurement covariance in the KF. The position reference has a frequency of $f_r = 0.10$ Hz and the measurement noise is $R = 10^{-3}$. The KF estimate of the magnitude of the mode perturbation signature is shown with a measurement noise covariance that is equal to the one used in the truth-model (left) and a measurement noise covariance that is $c_r \cdot R$ or $10^2 \cdot R$ (right).

mates of the other state variables. Although, Figures 3.12 and 3.13 consider the effects of measurement noise for a position reference of 0.10 Hz, simulations at references frequencies of 0.01 and 1.00 Hertz shared similar characteristics. It should be noted that the ω_r factor described previously could also be used to reduce the effects of noise on the estimates. Simulation studies, however, showed that multiplying the KF measurement noise covariance by a factor of $c_r = 10^2$ was a more effective way to reduce the effects of noise and increase detection parameter separation (the difference between the value of the test statistic for correct and incorrect signal parameters).

Kalman Filter Tuning for the SCA Test Statistic

The procedure of tuning the KF for use for detection based on correlation is similar to the one presented for the LMP. It should be noted that the KF used for correlation-based detection is trying to estimate the summation of the position reference and the mode perturbation signature. As discussed for the LMP, the elements in the process

noise covariance matrix define the tradeoff between speed of response and sensitivity to noise. Simulation of the linear system in Equation (3.137) and parameters summarized in Table 3.5 showed that for position reference frequencies between 0.01 and 1.0 Hz, the following KF process covariance matrix produced the best results:

$$Q_k = \text{diag}\left(\left[10^{-1}, 10^{+3}, 10^{+1}, 10^{+6}\right]\right). \tag{3.159}$$

One advantage of the detection based on correlation approach is that the matrix in Equation (3.159) has one less element to tune compared to the KF used for the LMP test statistic. By having to estimate the summation of the position reference and the mode perturbation signature, the terms corresponding to the position and velocity references in the KF process covariance matrix are larger. This is unavoidable as the KF must react quickly to bit changes in the embedded mode perturbation signature. Simulation studies were also done to determine if adding pseudo measurement noise improved the performance of the detector. However, it was found that adding pseudo measurement noise did not improve the performance of the detector (it did not hurt performance either).

3.6.4 Monte Carlo Simulations

This section compares the results for the optimal detection method (the LMP presented in Section 3.3) and a suboptimal test statistic (the SCA presented in Section 3.4) using Monte Carlo methods. Simulations were repeated for at least a total of 31 trials with Gaussian process and measurement noise in order to obtain meaningful simulation statistics. In order to incorporate realistic maneuvers, the system tracked sinusoidal references with $a_r = 10$ at three frequencies: 1) 0.01 Hz, 2) 0.10 Hz, and 3) 1.00 Hz. Four amplitude-to-noise ratios in decibels were also considered: 1) 2.2, 2) 25.3, 3) 48.3, and 4) 94.3. The performance of the detector was measured by considering the percentage of times the correct parameter (i and τ) were detected. The correct mode detection percentage results with error bars can be found in Appendix C.

Figure 3.15 shows the performance of the LMP detector, Equation (3.109), with the system tracking a reference of 0.01 Hz. As would be expected, the performance of the detector improves as the estimation horizon and ANR increase. It can be seen that even for $ANR = 1.58$ acceptable performance of about 80% can be achieved if the estimation horizon is extended beyond 40 seconds. Figure 3.16 shows how increasing the frequency of the tracking reference to 0.10 Hz affects detection. The percentage performance is primarily not effected by this increase in the reference frequency in areas of large estimation horizon (> 40 seconds) and ANR (> 48.3). Most of the degradation in performance occurs for low ANRs. However, a tracking reference with frequency of 1.00 Hz deteriorates the performance of the detector. This effect is evident when Figure 3.17 is compared to Figures 3.15 and 3.16. For this condition, the nominal reference and the mode perturbation signature share the same frequency ($f_c = f_r = 1.0$ Hz) decreasing the performance of the LMP detector, Equation (3.109). However, as Figure 3.17 shows that a detection rate higher than 90% is attainable if the estimation horizon is large (> 60 seconds) and the ANR is large (≥ 94.3). Figures 3.15, 3.16, and 3.17 have sufficient information to select an estimation horizon and ANR and predict a rate of correct parameter detection.

Consider now the performance of the SCA detector, Equation (3.113). The same conditions in terms of the mode perturbation signature amplitude, the tracking reference frequency, and the ANR were simulated using the SCA. Figures 3.18, 3.19, and 3.20 show the same trend as seen with the LMP test statistic in terms of estimation horizon and ANR. However when compared to the LMP, there is a significant drop in performance seen in Figure 3.20 for a tracking reference of 1.00 Hz.

Insight is gained by evaluating the separation between the values of the SCA detector statistic, Equation (3.113), for the correct and the incorrect modes and Gold Code phases. Figure 3.21 shows the evaluation of the SCA detector for the three mode per-

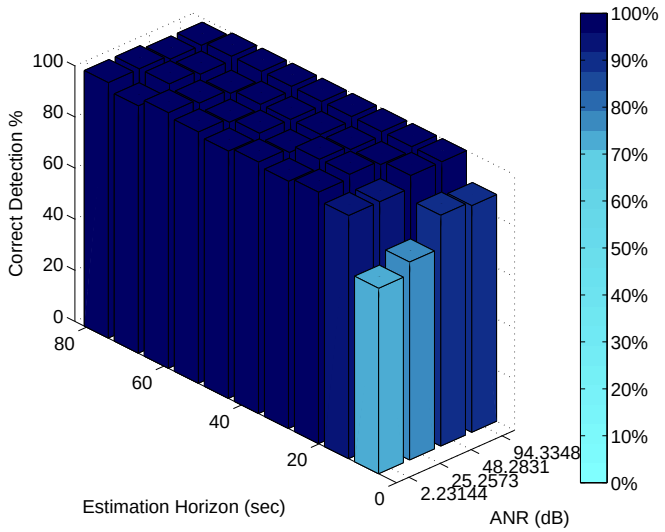

Figure 3.15: Correct mode detection percentage for the LMP detector, Equation (3.109), with a mode perturbation signature amplitude of $a_{\text{sig}} = 0.5$ tracking a reference with frequency of 0.01 Hz.

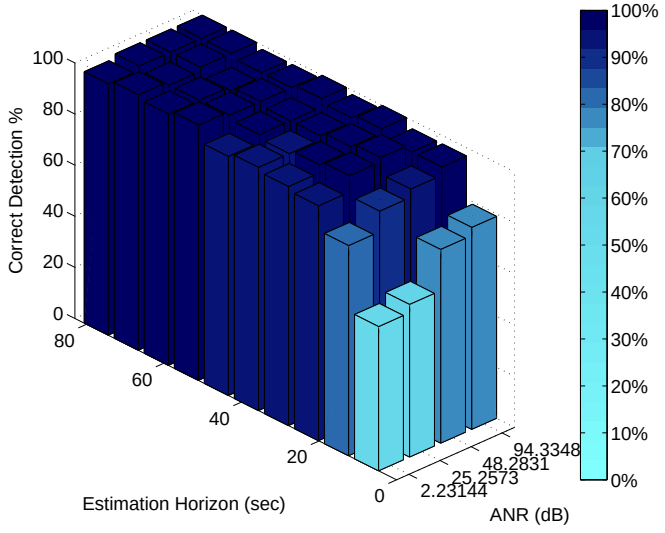

Figure 3.16: Correct mode detection percentage for the LMP detector, Equation (3.109), with a mode perturbation signature amplitude of $a_{\text{sig}} = 0.5$ tracking a reference with frequency of 0.10 Hz.

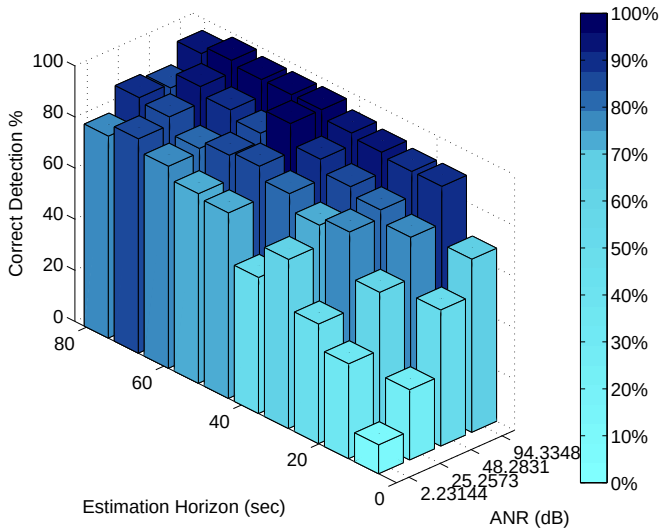

Figure 3.17: Correct mode detection percentage for the LMP detector, Equation (3.109), with a mode perturbation signature amplitude of $a_{\text{sig}} = 0.5$ tracking a reference with frequency of 1.00 Hz.

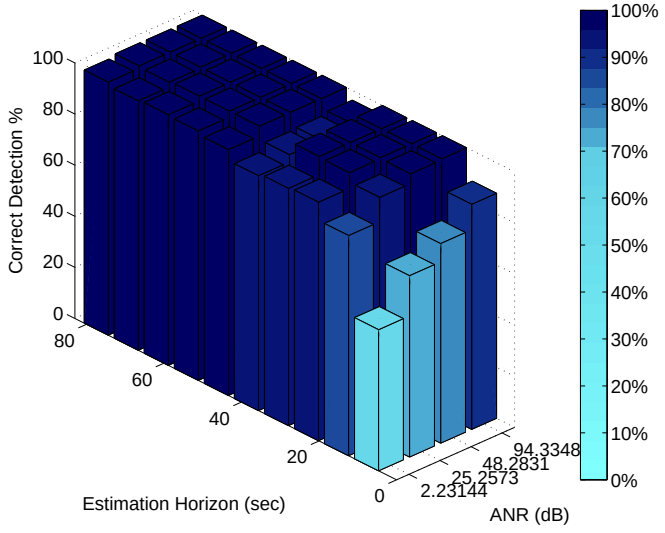

Figure 3.18: Correct mode detection percentage for the SCA detector, Equation (3.113), with a mode perturbation signature amplitude of $a_{\text{sig}} = 0.5$ tracking a reference with frequency of 0.01 Hz.

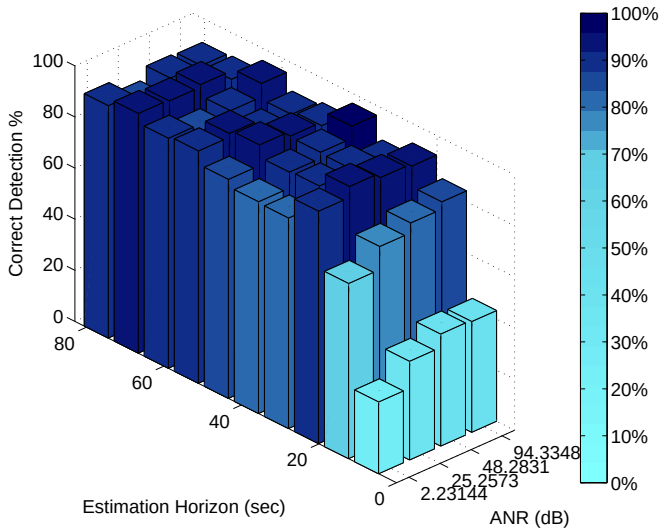

Figure 3.19: Correct mode detection percentage for the SCA detector, Equation (3.113), with a mode perturbation signature amplitude of $a_{\text{sig}} = 0.5$ tracking a reference with frequency of 0.10 Hz.

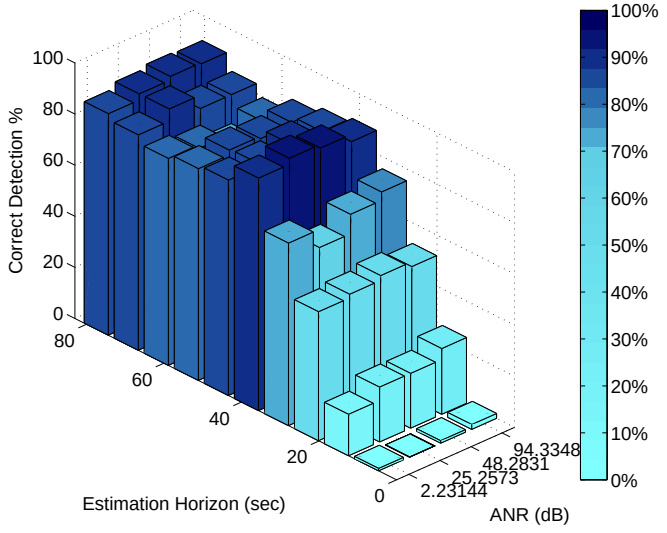

Figure 3.20: Correct mode detection percentage for the SCA detector, Equation (3.113), with a mode perturbation signature amplitude of $a_{\text{sig}} = 0.5$ tracking a reference with frequency of 1.00 Hz.

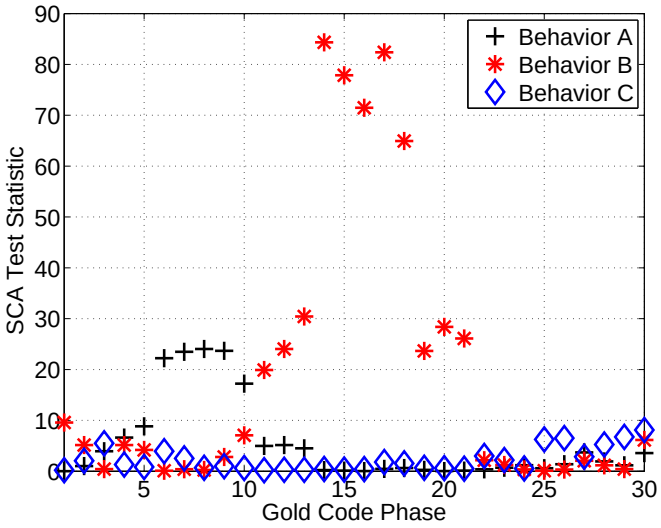

Figure 3.21: The evaluation of the SCA detector, Equation (3.113), for the three modes and Gold Code phases with an estimation horizon of 50 seconds. The frequency of the tracking reference is equal to 0.10 Hz and the ANR is 48.3.

turbation signatures and Gold Code phases under an estimation horizon of 50 seconds. In the simulation, the ANR and tracking reference frequency were equal to 48.3 and 0.10 Hz respectively. The parameters used to generate the truth-model for this example were: 1) Behavior B, and 2) Gold Code phase of 14. It can be seen that the figure lacks a single peak significantly separated from the other evaluations. However, for Behavior B there is a cluster of points around the truth value. If the estimation horizon increased, the SCA detector would detect more energy at the correct parameters and Figure 3.21 would resemble the LMP detector evaluations shown in Figure 3.12(a).

However, since in this investigation it is more important to detect the correct mode behavior, i, rather than the correct Gold Code phase, τ, the detection requirements can be relaxed. The dependence of the SCA detector on the Gold Code phase can be removed by summing the energy detected at each Gold Code phase. The reformulated SCA detector for the i^{th} mode is then:

$$\overline{\lambda}_{\text{SCA}}^{i,f_c} = \sum_{\tau=0}^{N_\tau} \left[\left(\left[\hat{\bar{\mathbf{r}}}^{i,j} \right]^T P^{-1} \mathbf{z}_{\text{sig}}^{\sin,\mathbf{i},\tau,\mathbf{f_c}} \right)^2 + \left(\left[\hat{\bar{\mathbf{r}}}^{i,j} \right]^T P^{-1} \mathbf{z}_{\text{sig}}^{\cos,\mathbf{i},\tau,\mathbf{f_c}} \right)^2 \right], \tag{3.160}$$

where N_τ is the number of phases in the Gold Code. The modified SCA detector then chooses the largest $\overline{\lambda}_{\text{SCA}}^{i,f_c}$, or

$$\hat{i}, \hat{f}_c = \arg\max_{i,f_c} \overline{\lambda}_{\text{SCA}}^{i,f_c}. \tag{3.161}$$

The Gold Code phase is still part of the parameter search space as the evaluation of the modified SCA test statistic, $\overline{\lambda}_{\text{SCA}}^{i,f_c}$, is dependent on the energy at each Gold Code phase.

The conditions of the Monte Carlo simulations are then simulated using the modified SCA detector, Equation (3.161), and shown in Figure 3.22, 3.23, and 3.24. It is to be tested whether the correct detection percentage would increase if the requirement of detecting the correct Gold Code phase is relaxed. Comparing Figures 3.23 and 3.24 with Figures 3.18 and 3.19 it is apparent that the performance of the detector has improved dramatically. However, for a tracking reference with a frequency of 1.00 Hz (Figure 3.24) the modified SCA detector, Equation (3.161), improved for small estimation horizons, it could not match percentages greater than 80% seen in Figure 3.20. Simulation data showed that a reference frequency of 1.00 Hz significantly reduced the parameter separation, thus making the modified SCA detector ineffective. At a tracking reference frequency of 1.00 Hz, the performance of the LMP detector, Equation (3.109), (Figure 3.15) was better. The Monte Carlo simulations suggest that the modified SCA detector is effective for tracking references with a frequency less than 1.00 Hz.

Relaxing the Gold Code phase detection requirement was investigated for the LMP test statistic, however Monte Carlo simulations showed that the performance of the detector did not improve. This can be explained by looking at difference in the test statistic evaluation for the LMP (Figure 3.12(a)) and the SCA (Figure 3.21). As shown in Figure 3.12(a) in the LMP there is a clear peak at the correct mode and Gold Code phase. If a test statistic similar to $\overline{\lambda}_{\text{SCA}}^{i,f_c}$ was used for this linear example, it would not improve the parameter separation of the peak at the correct parameters since the statistic is already robust.

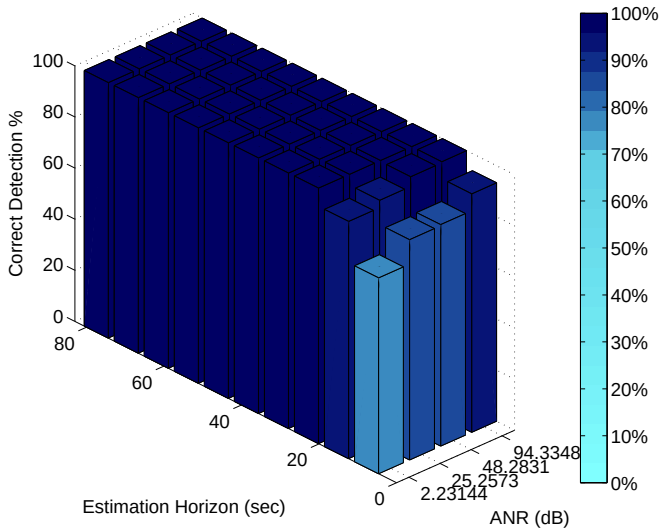

Figure 3.22: Correct mode detection percentage for the modified SCA test statistic, Equation (3.160), with a mode perturbation signature amplitude of $a_{\text{sig}} = 0.5$ tracking a reference with frequency of 0.01 Hz.

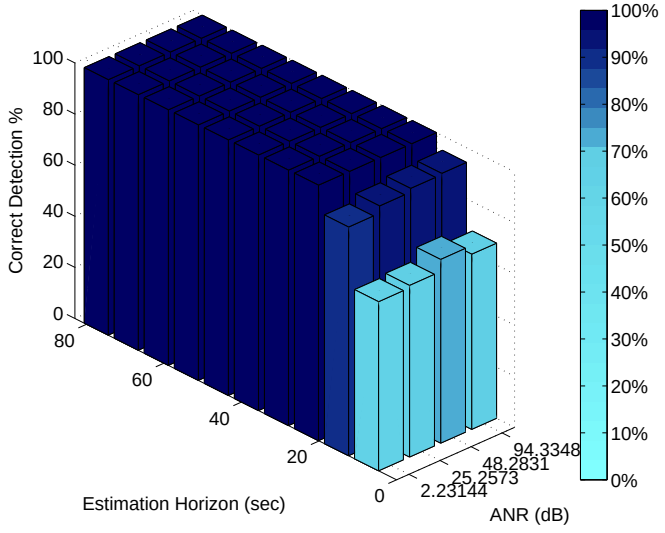

Figure 3.23: Correct mode detection percentage for the modified SCA test statistic, Equation (3.160), with a mode perturbation signature amplitude of $a_{\text{sig}} = 0.5$ tracking a reference with frequency of 0.10 Hz.

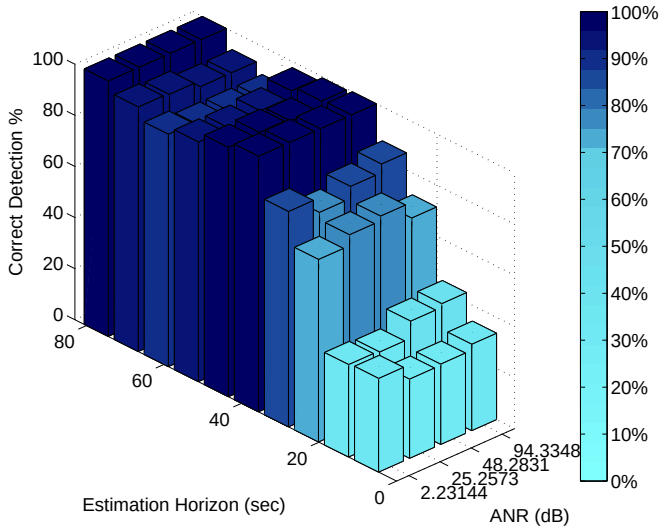

Figure 3.24: Correct mode detection percentage for the modified SCA test statistic, Equation (3.160), with a mode perturbation signature amplitude of $a_{\text{sig}} = 0.5$ tracking a reference with frequency of 1.00 Hz.

The probability of false alarm derived in Section 3.5 was calculated for LMP in order to compare it to the simulation correct detection percentage. Figure 3.25 shows the value of the test statistic under the following conditions: 1) estimation horizon of 4 seconds and ANR = 2.2, and 2) estimation horizon of 80 seconds and ANR = 94.3. As can be seen in the Figure 3.25(a), at this small estimation horizon and ANR, the probability of false alarm must be increased to 40% for 98% of the samples points to have a value greater than the threshold. However, if the estimation horizon and ANR are increased as shown in Figure 3.25(b) then a probability of false alarm of only 10% is needed for all points to be above the threshold. As expected for higher estimation horizons and ANRs the value of the test statistic is higher which enables for a lower probability of false alarm to be selected.

The results of the Monte Carlo simulations in this section showed the tradeoff between the estimation horizon, the ANR, and the performance of the LMP and SCA detector. The data showed that the performance of both detectors suffered as the tracking

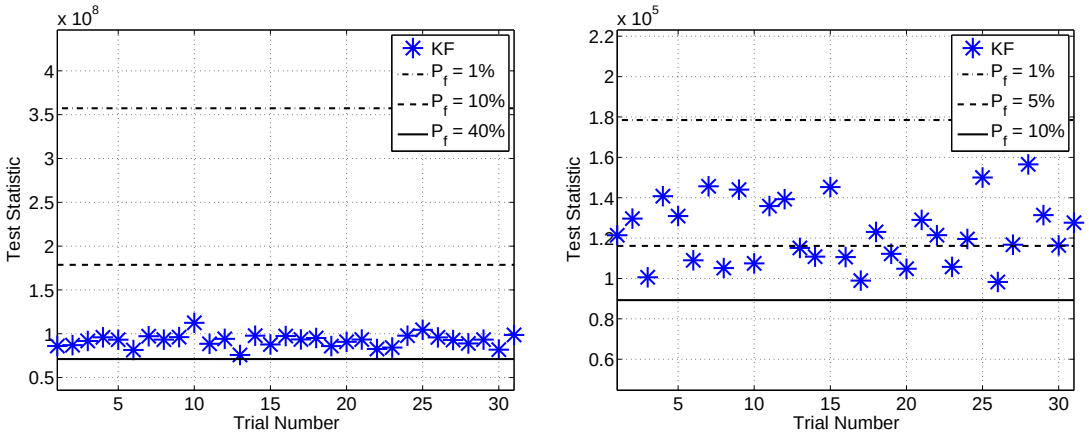

(a) (b)

Figure 3.25: The probability of false alarm as derived in Section 3.5 calculated for the LMP.

reference frequency increased. For a tracking reference frequency of 1.00 Hz, the performance of the LMP was significantly better than the SCA. Simulation results showed that for a tracking frequency of less than 1.00 Hz the SCA detector yielded results similar to the LMP detector. The performance of the SCA detector can be further improved by relaxing the Gold Code phase detection requirement by summing up the energy at the Gold Code phases for each mode, Equation (3.161).

3.7 Nonlinear Numerical Example

The performance of the LMP and SCA detectors for a simple linear model with a linear output equation was evaluated in Section 3.6. In this section, the LMP and SCA detectors are applied to a more complex linear model with nonlinear radar output equations. It is of interest to investigate how the nonlinearities of the measurement equations affect the relationship between the estimation horizon, ANR, and resulting performance. Another factor to evaluate is how sensitive is the larger order estimator required by the LMP.

The nonlinear radar measurements proposed in this investigation require the use of a nonlinear estimator. For accuracy and for numerical stability, the square-root implementation of the Sigma Point Filter (SPF) is chosen [47]. The SPF or Unscented Kalman Filter consists of using the system model to sample specific points which can be used to numerically reconstruct the probability distribution of the state. Some excellent references that present derivations and explanations of the SPF include: [48], [49], and [50].

3.7.1 Four State Linear Model with Nonlinear Radar-Like Equations

Motion in two dimensions is described by the following linear discrete time model:

$$\mathbf{x}_{k+1} = A_k \mathbf{x}_k + B_k \overline{\mathbf{u}}_k^i, \tag{3.162}$$

$$\mathbf{x_{k+1}} = \begin{bmatrix} 1 & T & 0 & 0 \\ 0 & 1 & 0 & 0 \\ 0 & 0 & 1 & T \\ 0 & 0 & 0 & 1 \end{bmatrix} \mathbf{x_k} + \begin{bmatrix} 0 & 0 \\ T & 0 \\ 0 & 0 \\ 0 & T \end{bmatrix} \overline{\mathbf{u}}_k^i + \mathbf{w}_k, \tag{3.163}$$

where the state, $\mathbf{x}_k$ is composed of the position and velocity along the x-axis and the position and its derivative along the y-axis, or $\mathbf{x}_k = [x_k \;\; \dot{x}_k \;\; y_k \;\; \dot{y}_k]^T \in \mathbb{R}^4$. The control input has components for each axis, $\overline{\mathbf{u}}_k^i = \begin{bmatrix} u_k^{x,i} & u_k^{y,i} \end{bmatrix}^T \in \mathbb{R}^2$, and is calculated using full-state feedback:

$$\overline{\mathbf{u}}_k^i = K\left(-\mathbf{x}_k + \overline{\mathbf{r}}_k^i\right), \tag{3.164}$$

where $\mathbf{r}_k^i = \mathbf{r}_k + a_{\text{sig}} t_z^r \left(z_{\text{sig}}^i\right)$ is the total reference for the i^{th} mode. The variable $\mathbf{w}_k \in \mathbb{R}^4$ is zero-mean white Gaussian noise with covariance Q_k.

The nonlinear output equations are composed of radar-like measurements: the range, κ_k, and an angle, χ_k, relative to the x-axis, as shown in Figure 3.26. The nonlinear

measurement equations are the following:

$$\mathbf{y}_k = h\left(\mathbf{x_k}, \mathbf{v_k}\right), \tag{3.165}$$

$$\begin{bmatrix} \kappa_k \\ \chi_k \end{bmatrix} = \begin{bmatrix} \sqrt{x_k^2 + y_k^2} \\ \tan^{-1}\left(\frac{y_k}{x_k}\right) \end{bmatrix} + \mathbf{v}_k, \tag{3.166}$$

where $\mathbf{v}_k$ is zero-mean white Gaussian measurement noise with covariance R_k.

3.7.2 Estimator Setup

In this example, the setup of the estimator is similar to the one described in Section 3.6.2, the only differences coming from the fact that motion in the y-axis must be considered. The augmented state equations are defined as follows:

$$\begin{bmatrix} \mathbf{x}_{k+1} \\ \mathbf{r}_{k+1} \\ \mathbf{a}_{\text{sig},k+1} \end{bmatrix} = \begin{bmatrix} A_k - B_u K & B_u K & B_u K t_z^r\left(z_{\text{sig}}^{i,\tau}\right) \\ \mathbf{0} & A_r & \mathbf{0} \\ \mathbf{0} & \mathbf{0} & I \end{bmatrix} \begin{bmatrix} \mathbf{x_k} \\ \mathbf{r}_k \\ \mathbf{a}_{\text{sig},k} \end{bmatrix} + \overline{\mathbf{w}}_k. \tag{3.167}$$

where $\overline{\mathbf{w}}_\mathbf{k}$ is zero-mean Gaussian process noise for the augmented system with covariance $\overline{Q}_k$. The matrix A_r has the form:

$$A_r = \begin{bmatrix} 1 & T & 0 & 0 \\ 0 & 1 & 0 & 0 \\ 0 & 0 & 1 & T \\ 0 & 0 & 0 & 1 \end{bmatrix}, \tag{3.168}$$

and the vector of mode perturbation amplitudes is:

$$\mathbf{a}_{\text{sig}} = \begin{bmatrix} a_{\text{sig}}^x \\ a_{\text{sig}}^y \end{bmatrix}. \tag{3.169}$$

The function $t_z^r(\cdot)$ computes the mode perturbation reference by mapping the scalar mode perturbation signature to the position reference and also computing its derivative

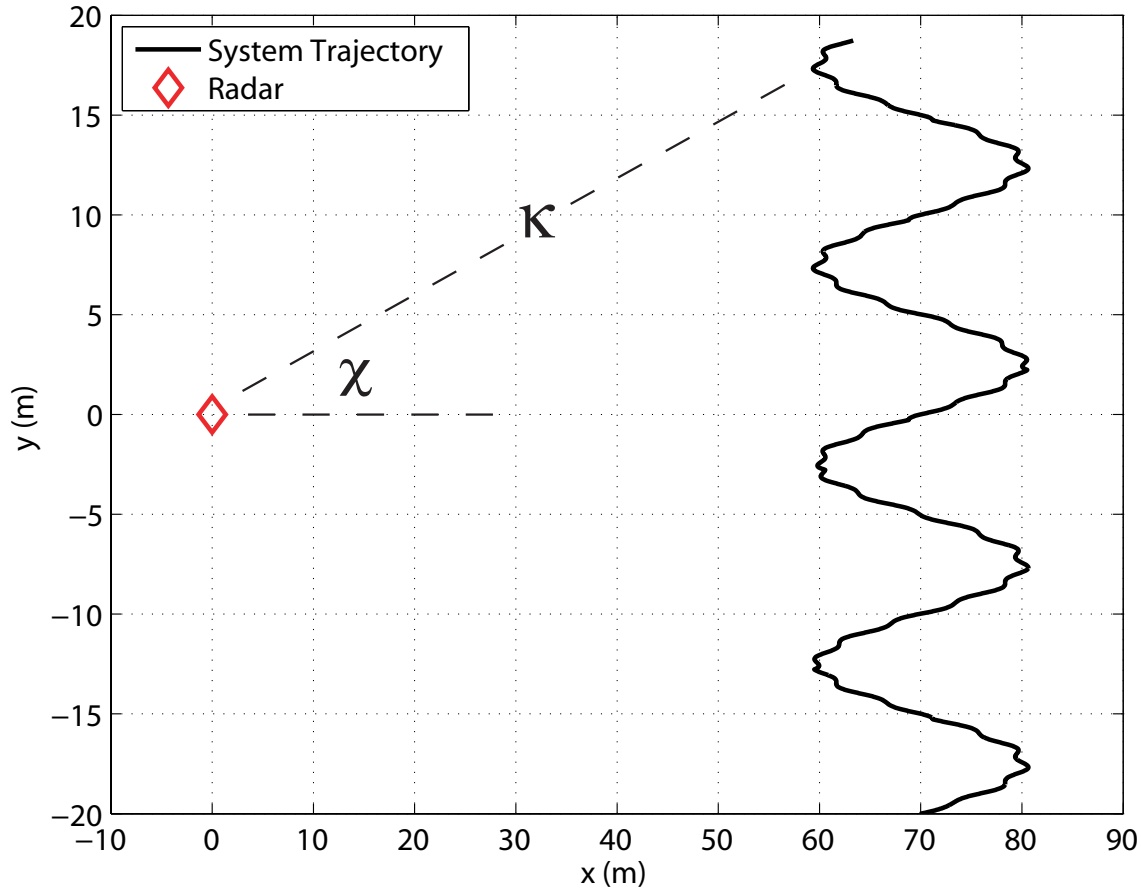

Figure 3.26: Trajectory of the system with initial position $[70, -20]$ (the initial speed for both directions is zero) with a mode perturbation signature frequency of 0.10 Hz and ANR of 94.3 dB. The red diamond symbolizes the location of the radar that takes range, κ_k, and angle measurements, χ_k, of the system. The mode perturbation signature can be seen embedded in the sinusoidal trajectory of the vehicle. The frequency of the mode perturbation signature is faster than the frequency of the reference, therefore the ripples observed in the figure are caused by the mode perturbation signature.

(see Equation (3.140)). The function $t_z^r(\cdot)$ maps the mode perturbation signature to the reference in the following way:

$$t_z^r\left(z_{\text{sig},k}^{i,\tau}\right) = T_z^r \begin{bmatrix} z_{\text{sig},k}^{i,\tau} & 0 \\ 0 & \frac{d}{dt} z_{\text{sig},k}^{i,\tau} \end{bmatrix}. \tag{3.170}$$

The matrix T_z^r maps the elements of the scalar perturbation signature and its derivative accordingly,

$$T_z^r = \begin{bmatrix} 1 & 0 \\ 0 & 1 \\ 1 & 0 \\ 0 & 1 \end{bmatrix}. \tag{3.171}$$

For the SCA estimator setup, it is not necessary to estimate the mode perturbation signature amplitudes for either direction. The SCA augmented system has the form:

$$\begin{bmatrix} \mathbf{x}_{k+1} \\ \bar{\mathbf{r}}_{k+1}^i \end{bmatrix} = \begin{bmatrix} A_k - B_u K & B_u K \\ \mathbf{0} & A_r \end{bmatrix} \begin{bmatrix} \mathbf{x_k} \\ \bar{\mathbf{r}}_k^i \end{bmatrix} + \overline{\mathbf{w}}_k^{\text{SCA}}, \tag{3.172}$$

where $\overline{\mathbf{w}}_k^{\text{SCA}}$ is zero-mean Gaussian process noise for the SCA augmented system.

The nonlinear output equations of the system have the same form as in Equation (3.166) where the range, κ_k, and the angle, χ_k, are the measurements.

3.7.3 Estimator Tuning

As in the linear case, Section 3.6, the performance of either detector is neccessarily dependent on the performance of the model-based estimator. Tuning the underlying estimator is more challenging for this example as the model is of larger dimension and the measurement equations are nonlinear. In this section, the strategy used to tune the SPF is summarized.

Sigma Point Filter Tuning for the LMP

Tuning the SPF for the system was challenging because small changes in the process and measurement covariance matrices affected the performance of both the estimator and the subsequent mode detector. Although there is not a single best way to tune the estimator, simulation studies showed that it is most effective to start by tuning the estimator to minimize the error in the velocity elements of the reference in both the x and y directions and then to continue with the other elements. Therefore, the corresponding elements in the process covariance matrix were tuned until the accuracy of the reference velocity estimate was maximized. As seen in Section 3.6, increasing the process covariance element for the velocity element improved the accuracy of the estimate, but increased its sensitivity to noise. As the elements corresponding to the reference velocity were tuned, the reference position elements of the process covariance matrix was also adjusted. Once tuning produced acceptable estimates of the reference and mode perturbation signature amplitude , it was found that the SPF was slightly less sensitive to variations in the process covariance elements corresponding to the position and velocity in the x and y direction.

For the LMP detector, the process covariance matrices found to produce the best estimates for the SPF in terms of maximizing the value of the test statistic for the correct parameters under hypothesis H_0 were the following:

$$\overline{Q}_k^{H_0} = \text{diag}\left(\left[10^{-1}, 10^{-3}, 10^{-1}, 10^{-3}, 10^{-1}, 10^{+4}, 10^{-1}, 10^{+4}\right]\right), \tag{3.173}$$

where $\overline{Q}_k^{H_0}$ is the process noise covariance matrix of the SPF for the hypothesis that no signal is present, H_0, and

$$\overline{Q}_k^{H_1} = \text{diag}\left(\left[10^{-1}, 10^{+2}, 10^{-1}, 10^{+1}, 10^{-2}, 10^{+2}, 10^{+2}, 10^{+3}, 10^{-1}, 10^{0}\right]\right), \tag{3.174}$$

where $\overline{Q}_k^{H_1}$ is the process noise covariance matrix of the SPF for the hypothesis that a signal is present, H_1, either with a cosine or sine carrier.

Monte Carlo simulations showed that multiplying the covariance matrix by a factor, $R = c_r \cdot R_0$, (as described in Section 3.6.3) hurt the performance of the LMP detector. Also, imparting memory in the integration of the position reference, as described in Equation (3.150), did not improve performance and therefore ω_r was set to zero.

Sigma Point Filter Tuning for the SCA

A similar procedure as the one described for the LMP was used to tune the covariance matrices of the SPF for the SCA test statistic. The process covariance matrix that was found to produce the best performance for the SCA test statistic was:

$$Q_k = \text{diag}\left(\left[10^{-1}, 10^{-3}, 10^{-1}, 10^{-3}, 10^{+0}, 10^{+6}, 10^{+0}, 10^{+6}\right]\right). \tag{3.175}$$

The elements corresponding to the reference in Equation (3.175) are larger than the same elements in Equation (3.174) for the LMP because the estimator for the SCA must estimate $\bar{\mathbf{r}}^i$ which is a fast varying signal as opposed to the estimate for the LMP which estimates the nominal reference, $\mathbf{r}$, and a_{sig} which is a constant. The larger magnitude of these elements in the SCA suggests that the estimator for the SCA would be more sensitive to noise. The performance of the SPF for the SCA for this nonlinear example did not improve if the measurement covariance matrix of the KF was multiplied by a factor, $R = c_r \cdot R_0$, (as described in Section 3.6.3) or if memory was imparted, as shown in Equation (3.150), in the position reference integration $(\omega_r \neq 0)$.

3.7.4 Monte Carlo Simulations

This section compares the results for the optimal detection method (the LMP presented in Section 3.3) and the suboptimal test statistic (the SCA presented in Section 3.4 and modified in Section 3.6.4) using Monte Carlo methods. In the simulations, the radar sensor was located at the origin of an $x-y$ coordinate system while the motion

of the vehicle started at the coordinates $(70, -20)$ with an initial speed of zero for both directions. The trajectory of the vehicle tracking a reference with amplitude $a_r = 10$ and frequency of $f_r = 0.01$ Hz and mode perturbation signature amplitude of $a_{\text{sig}} = 0.5$ was previously shown in Figure 3.26. As with the linear numerical example in Section 3.6, the simulations were repeated for a total of 31 trials with Gaussian process and measurement noise. In order to incorporate realistic maneuvers, the system tracked sinusoidal references at three frequencies: 1) 0.01 Hz, 2) 0.10 Hz, and 3) 1.00 Hz. Since in this example there are two measurements the measurement noise covariance used in the simulation was:

$$R_k = c_R \times \text{diag}\left([0.5, 0.0305]\right), \tag{3.176}$$

where $c_R = \left[10^{-5}, 10^{-3}, 10^{-2}, 10^{-1}\right]$ is a factor that scales the measurement noise. Using the definition of ANR, Equations (3.156-3.157), the ratio is computed for the element of largest element in R_k, 0.5, resulting in the following ANRs in dB: 1) 9.2, 2) 32.2, 3) 55.2, and 4) 101.3. If the ANR was computed based on the other element of R_k the values would be: 1) 37.1, 2) 60.2, 3) 83.2, and 4) 129.2. The performance of the detector was measured by considering the percentage of correct parameter detections (the i^{th} mode and Gold Code phase τ) for at least 62 trials. More trials were conducted until the standard error (standard deviation of the samples) was below 12%. The correct mode detection percentage results with error bars can be found in Appendix C.

The Monte Carlo simulations results in Figure 3.27 show that the performance of the LMP detector, Equation (3.109), dropped off significantly for ANRs of less than 101.3. Figure 3.27 shows the simulation results, for a ANR= 101.3 the relationship between the estimation horizon and the performance is similar to the one seen in the simpler one dimensional numerical example, Section 3.6. However, the performance does not smoothly decrease for smaller ANRs as the performance degrades quickly when the ANR is lowered to 55.2.

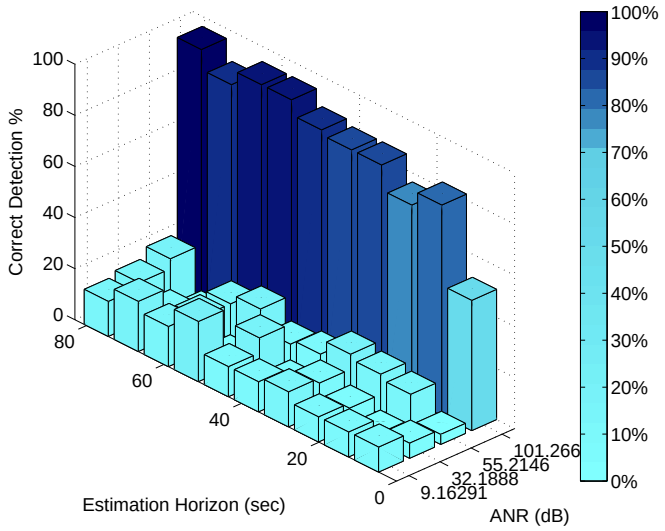

Figure 3.27: Correct mode detection percentage for the LMP detector for the nonlinear simulation example with a mode perturbation signature amplitude of $a_{\text{sig}} = 0.5$ tracking a reference with frequency of 0.01 Hz.

It is of interest to determine whether the performance of the algorithm is more sensitive to measurement noise in one of the measurement variables. Figure 3.28 shows the LMP test statistic evaluated when the two dimensional linear model, Equation (3.163), is used with nonlinear radar measurement equations. Figure 3.28(a) shows the test statistic evaluated with the measurement noise covariance defined in Equation (3.176) when $c_R = 10^{-5}$. The corresponding ANRs for the range and angle are 101.3 and 129.2 respectively. The evaluation of the test statistic in Figure 3.28(a) shows that the algorithm is able to detect the correct signature parameters (Gold A, Gold Code phase 17). Figure 3.28(c) shows the evaluation of the test statistic as the measurement noise increases ($c_R = 10^{-3}$, ANR: $\kappa = 55.2$ and $\chi = 83.2$). As it is evident from Figure 3.28(c), the algorithm is not able to detect the correct mode signature parameters at this measurement noise level. However, it is not clear if the algorithm is more sensitive to measurement noise in one of the variables. Figure 3.28(b) shows the evaluation of the test statistic for ANRs of: $\kappa = 101.3$ and $\chi = 83.2$. In this case the ANR for the range has been

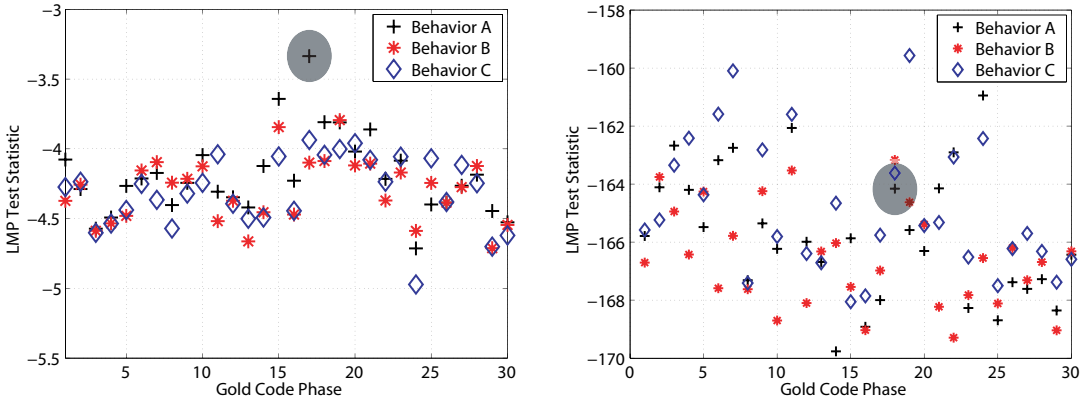

(a) ANR: $\kappa = 101.3$, $\chi = 129.2$

(b) ANR: $\kappa = 101.3$, $\chi = 83.2$

(c) ANR: $\kappa = 55.2$, $\chi = 83.2$

(d) ANR: $\kappa = 55.2$, $\chi = 129.2$

Figure 3.28: The evaluation of the LMP detector as a function of Gold Code phase for the 2D model, Section 3.7, with nonlinear radar measurements. The ANRs in decibels for both the range, κ, and the angle, χ, are also shown. The estimation horizon for the plots was 80 seconds.The parameters of the mode perturbation signature simulated in the truth-model were: Behavior A and Gold Code phase 17. The test statistics as computed by the algorithm at the truth-model parameters are shown inside a gray circle.

kept constant while the ANR for the angle has decreased when compared to the noise levels for Figure 3.28(a). Figure 3.28(d) also shows the evaluation of the test statistic for different noise levels. When compared to Figure 3.28(a), the ANR for the range has decreased while the ANR for the angle is kept constant. The value of the ANRs for Figure 3.28(d) are: $\kappa = 55.2$ and $\chi = 129.2$. The evaluation of the test statistic shows that the algorithm is able to detect the correct signatures parameters in Figure 3.28(d), but not in Figure 3.28(b). These results propose that the algorithm when applied to the model in Equation (3.163) with nonlinear output measurements is much more sensitive to the noise level of the angle measurement than the range measurement.

The LMP formulation requires the SPF to have two extra states as the mode perturbation signatures magnitudes in the x and y directions must be estimated. However, simulation studies for the SPF when the mode perturbation signature amplitudes were not estimated did not yield significantly better results in terms of the percentage of times that the algorithm detects the correct signature parameters. These studies along with the data shown in Figure 3.28 suggest that the increased noise in the angle measurement explains why the LMP detector's performance decreases for lower ANRs. In the simulation studies presented in this chapter, the noise for both variables is changed simultaneously using the definition of the measurement noise covariance in Equation (3.176). The ANR for both measurements variables decreases as c_R increases. For this nonlinear example the performance of the estimator, in this case the SPF, plays a more significant factor in the performance of the detector because the estimation problem is harder.

Although the Neyman-Pearson Lemma guarantees the optimality of the LMP detector [39], the analysis presented in Section 3.3 does not consider several factors that can affect detection. As shown in Figure 3.28, the nonlinearity of the output equation plays a significant factor in the performance of the detector, yet it is not considered in the LMP analysis. Since minimizing the time to detect the signal parameters is essential in this

application, it is necessary to attempt detection for estimation horizons that are less than one Gold Code period. By using less than a complete Gold Code period for detection, it is not possible to fully utilize the favorable cross-correlation properties of Gold Codes. Another factor to consider is that in any set of Gold Codes, there is inevitably some cross-correlation. The limitations of the LMP analysis motivate relaxing the detection requirements by modifying the detectors. As was done for the modified SCA detector, Equation (3.161), consider summing up the energy at each Gold Code phase for each of the i^{th} Gold Codes, or

$$\hat{i}, \hat{f}_c = \arg\max_{i, f_c} \left\{ \sum_{\tau=0}^{N_\tau} \max \bar{\lambda}_{\text{LMP}}^{i,\tau,f_c} \right\}. \tag{3.177}$$

The LMP detector in Equation (3.177) effectively averages the energy over all Gold Codes phases. Another variation to the LMP detector is to relax the detection requirements. In the simulation studies, it was required for the detector to correctly detect both the mode $\hat{i}$ and corresponding Gold Code phase $\hat{\tau}$ in order to declare a correct detection. However, in this application it is most important to detect the mode $\hat{i}$, while detecting $\hat{\tau}$ is not essential. This detector, referred to as the relaxed LMP detector, has the form:

$$\hat{i}, \hat{\tau}, \hat{f}_c, = \arg\max_{i, \tau, f_c} \bar{\lambda}_{\text{LMP}}^{i,\tau,f_c}, \tag{3.178}$$

where the optimization is still performed over τ, however when evaluating the detection performance only the estimates of $\hat{i}$ and $\hat{f}_c$ are compared to the truth values. Said another way, the detector is said to have detected the correct signal parameters if $\hat{i} = i$ and $\hat{f}c = f_c$, even if $\hat{\tau} \neq \tau$. Figures 3.29 and 3.30 plot the percentage of correct detection over 31 trials as a function of the estimation horizon and ANR. Figures 3.29 and 3.30 demonstrate that by modifying the LMP detector, the detection performance improves. In particular, the LMP detector based on Equation (3.177) achieves the best performance. Figures 3.31, 3.32, and 3.33 show the detection performance for the three variations of the LMP detector for a reference frequency of 0.10 Hz. Finally Figures 3.34, 3.35, and 3.36 show the detection performance for a reference frequency of 1.00

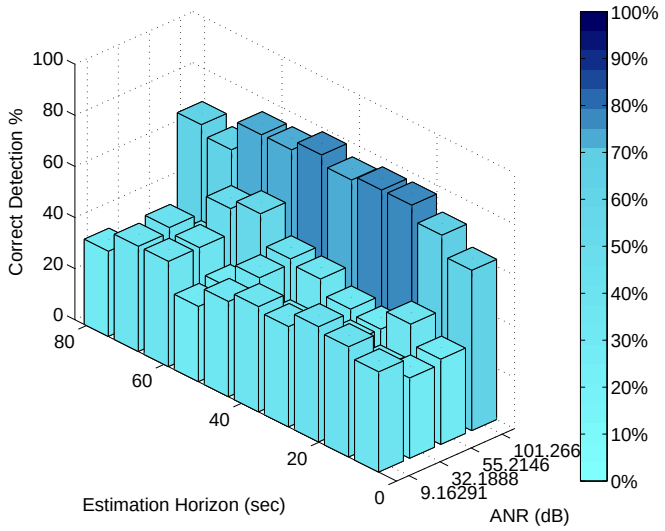

Figure 3.29: Correct mode detection percentage for the modified LMP detector, Equation (3.177), for the nonlinear simulation example with a mode perturbation signature amplitude of $a_{\text{sig}} = 0.5$ tracking a reference with frequency of 0.01 Hz.

Hz. As the frequency of the reference increases, the detection performance of the LMP detectors degrades. The modifications to the LMP, Equation (3.177) and (3.178), do improve the detection performance, however an increasing reference frequency inevitably reduces detection performance. Under both reference frequencies, the LMP detector based on summation, Equation (3.177), is able to achieve the best performance.

In contrast to the LMP detector, Figure 3.37 shows that the SCA detector is more robust to smaller ANRs, although its overall correct detection percentage is lower. For a tracking reference frequency of 0.10 Hz, the same trend is observed in Figures 3.31 and 3.39 where the LMP test statistic exhibits a significant dropoff in performance for smaller ANRs while the SCA test statistic does not. However, for a high ANR (≈ 101.3) the data does show that the LMP test statistic outperforms the SCA test statistic.

Consider relaxing the detection requirements, so that similar to the modified LMP

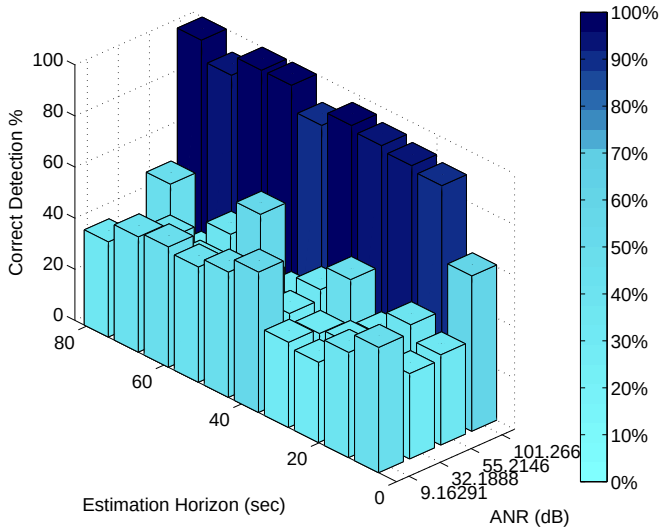

Figure 3.30: Correct mode detection percentage for the modified LMP detector based on only estimating i, Equation (3.178), for the nonlinear simulation example with a mode perturbation signature amplitude of $a_{\text{sig}} = 0.5$ tracking a reference with frequency of 0.01 Hz.

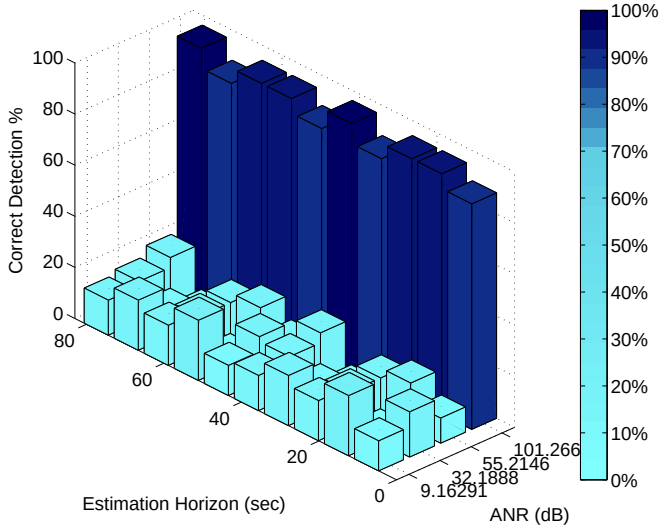

Figure 3.31: Correct mode detection percentage for the LMP test statistic for the nonlinear simulation example with a mode perturbation signature amplitude of $a_{\text{sig}} = 0.5$ tracking a reference with frequency of 0.10 Hz.

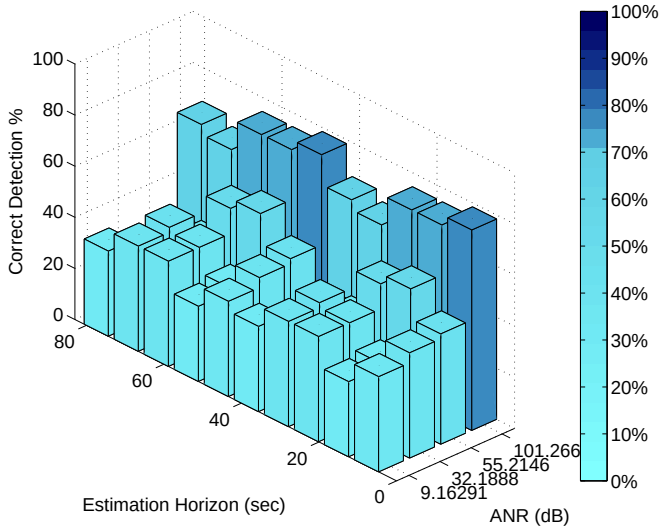

Figure 3.32: Correct mode detection percentage for the modified LMP detector, Equation (3.177), for the nonlinear simulation example with a mode perturbation signature amplitude of $a_{\text{sig}} = 0.5$ tracking a reference with frequency of 0.10 Hz.

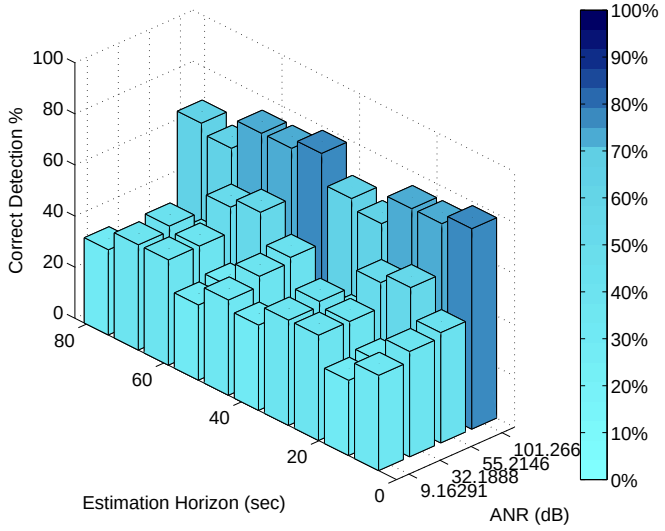

Figure 3.33: Correct mode detection percentage for the modified LMP detector based on only estimating i, Equation (3.178), for the nonlinear simulation example with a mode perturbation signature amplitude of $a_{\text{sig}} = 0.5$ tracking a reference with frequency of 0.10 Hz.

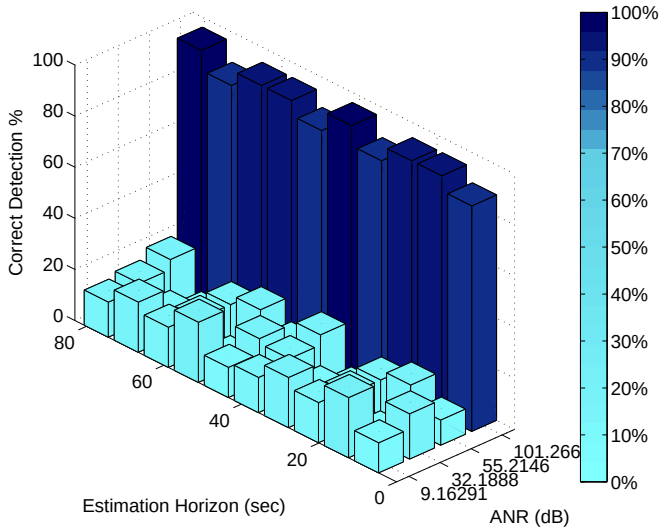

Figure 3.34: Correct mode detection percentage for the LMP detector for the nonlinear simulation example with a mode perturbation signature amplitude of $a_{\text{sig}} = 0.5$ tracking a reference with frequency of 1.00 Hz.

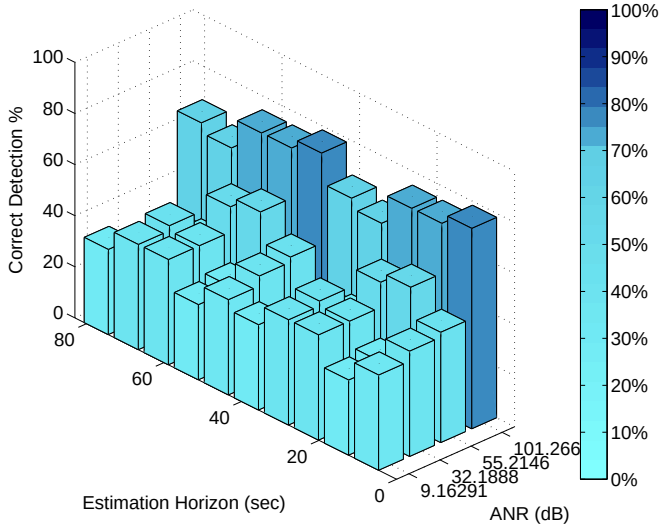

Figure 3.35: Correct mode detection percentage for the modified LMP detector, Equation (3.177), for the nonlinear simulation example with a mode perturbation signature amplitude of $a_{\text{sig}} = 0.5$ tracking a reference with frequency of 1.00 Hz.

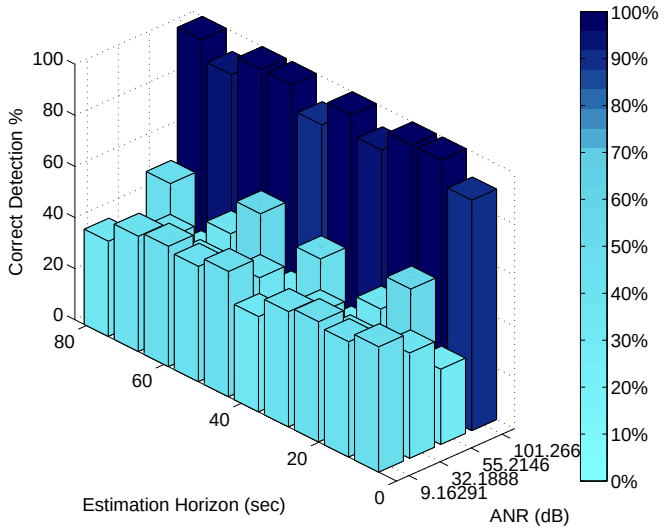

Figure 3.36: Correct mode detection percentage for the modified LMP detector based on only estimating i, Equation (3.178), for the nonlinear simulation example with a mode perturbation signature amplitude of $a_{\text{sig}} = 0.5$ tracking a reference with frequency of 1.00 Hz.

detector in Equation (3.178), the SCA detector is not required to correctly estimate $\hat{i}$, or

$$\hat{i}, \hat{\tau} \hat{f}_c = \arg \max_{i, \tau, f_c} \overline{\lambda}_{\text{SCA}}. \tag{3.179}$$

Figures 3.37 and 3.38 plot the percentage of correct detections for 62 trials for the SCA detector that averages the energy over τ, Equation (3.160), and the SCA detector that is not required to correctly estimate $\hat{\tau}$, Equation (3.179). Figure 3.38 shows that by only estimating $\hat{i}$, Equation (3.179), the detection performance improves significantly compared to the SCA detector in Equation (3.160). For reference frequencies of 0.10 and 1.00 Hz, Figure 3.37, 3.38, 3.39, 3.40, 3.41, and 3.42 show that both SCA detectors produce very similar results. It can be concluded the SCA detector in Equation (3.179) produces better detection results for a reference frequency of 0.01, but for reference frequencies of 0.10 and 1.00 Hz the performance of both SCA detectors is comparable. It should be noted that the performance of the LMP detector is better than either SCA detector at high ANRs.

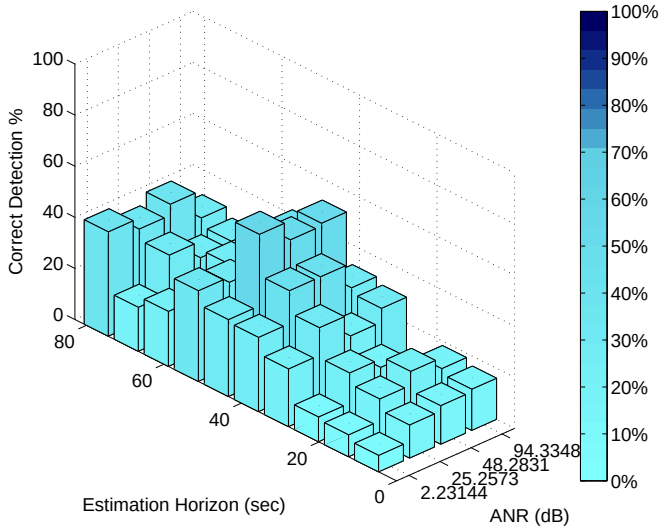

Figure 3.37: Correct mode detection percentage for the modified SCA detector, Equation (3.160), for the nonlinear simulation example with a mode perturbation signature amplitude of $a_{\text{sig}} = 0.5$ and tracking a reference with frequency of 0.01 Hz.

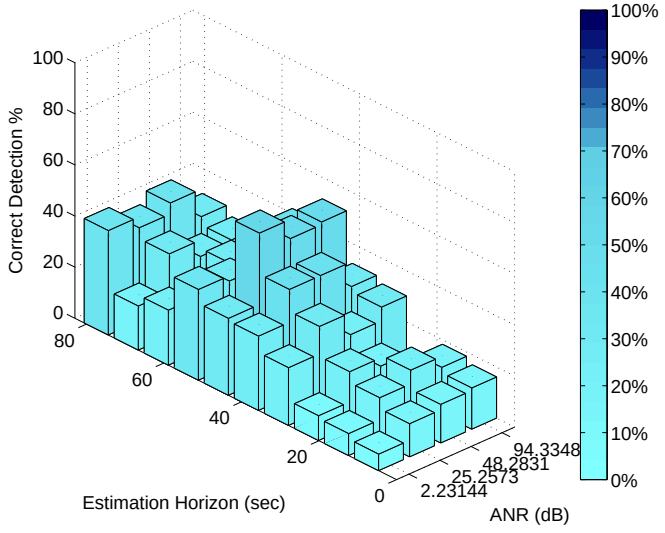

Figure 3.38: Correct mode detection percentage for the modified SCA detector based on only estimating $\hat{i}$, Equation (3.179), for the nonlinear simulation example with a mode perturbation signature amplitude of $a_{\text{sig}} = 0.5$ and tracking a reference with frequency of 0.01 Hz.

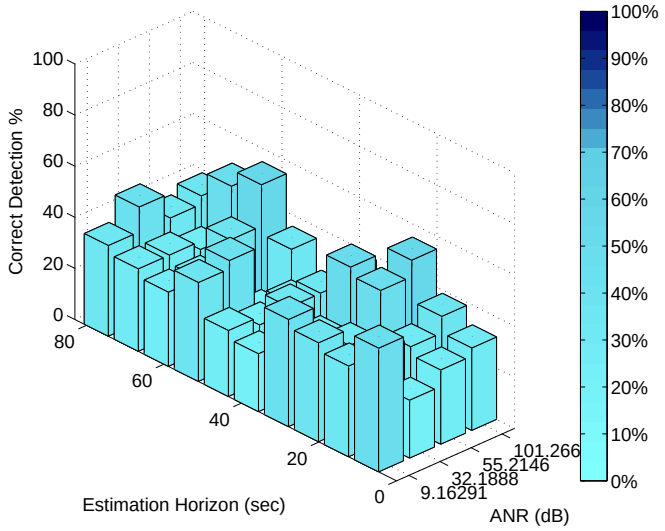

Figure 3.39: Correct mode detection percentage for the modified SCA detector, Equation (3.160), for the nonlinear simulation example with a mode perturbation signature amplitude of $a_{\text{sig}} = 0.5$ tracking a reference with frequency of 0.10 Hz.

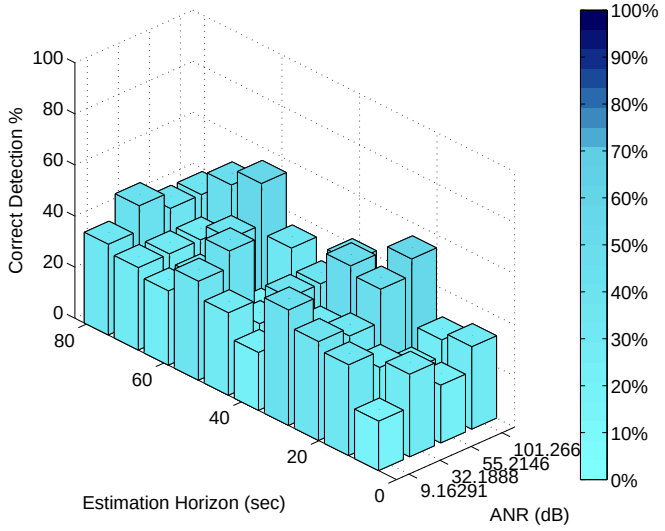

Figure 3.40: Correct mode detection percentage for the modified SCA detector based on only estimating $\hat{i}$, Equation (3.179), for the nonlinear simulation example with a mode perturbation signature amplitude of $a_{\text{sig}} = 0.5$ and tracking a reference with frequency of 0.10 Hz.

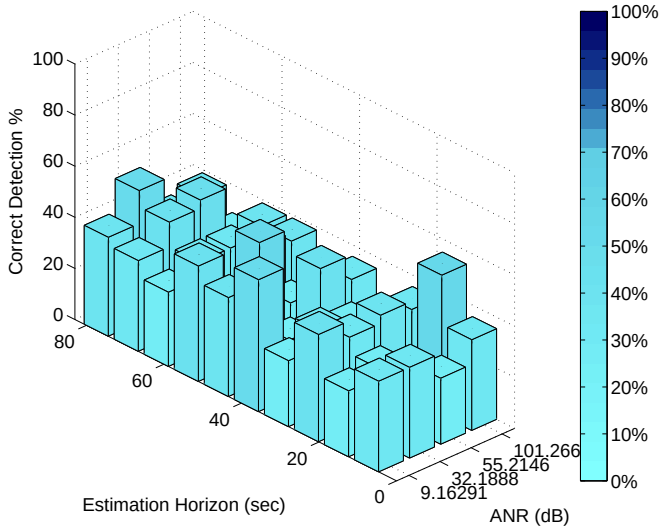

Figure 3.41: Correct mode detection percentage for the modified SCA detector, Equation (3.160), for the nonlinear simulation example with a mode perturbation signature amplitude of $a_{\text{sig}} = 0.5$ tracking a reference with frequency of 1.00 Hz.

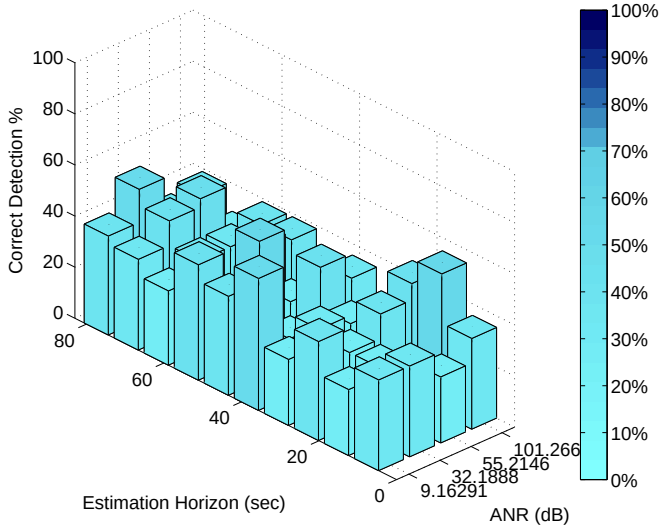

Figure 3.42: Correct mode detection percentage for the modified SCA detector based on only estimating $\hat{i}$, Equation (3.179), for the nonlinear simulation example with a mode perturbation signature amplitude of $a_{\text{sig}} = 0.5$ and tracking a reference with frequency of 1.00 Hz.

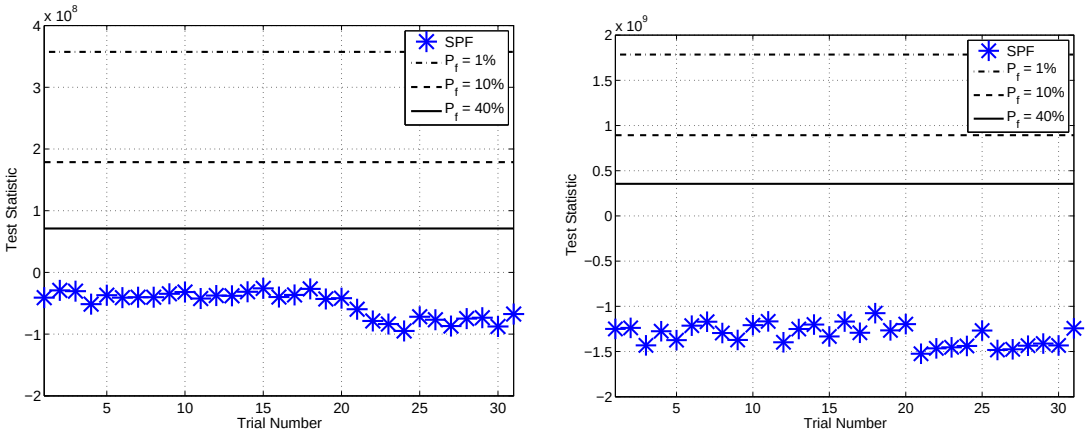

(a) (b)

Figure 3.43: The probability of false alarm as derived in Section 3.5 calculated for the LMP.

The probability of false alarm derived in Section 3.5 was calculated for LMP in order to compare it to the simulation correct detection percentage. Figure 3.43 shows the value of the test statistic under the following conditions: 1) estimation horizon of 4 seconds and ANR = 9.2, and 2) estimation horizon of 80 seconds and ANR = 101.3. As can be seen in the Figure 3.43(a), at this small estimation horizon and ANR, even a probability of false alarm of 40% does not yield any points that are above the threshold. When the estimation horizon and ANR are increased as shown in Figure 3.43(b), the simulation samples are still not above the threshold corresponding to a probability of false alarm of 40%. As the simulation results in this section have shown, it is very difficult for the algorithm to detect the correct signature parameters. The results shown in Figure 3.43 show that the inferior performance of the algorithm compared to the linear example also leads to lower values of the test statistic. However, it should be emphasized that the optimization problem for mode detection, Equation (3.109), relies on the values of the test statistic as a function of the mode signature parameters. Said another way, the algorithm finds the signature parameters that maximize the test statistic regardless of the absolute value of the test statistic.

The Monte Carlo simulation studies in this section explored the robustness of the LMP and SCA detectors with nonlinear output equations to different levels of ANRs and their relationship to the estimation horizon. Two modifications to the detectors were also considered: 1) summing the energy for the i^{th} mode each Gold Code phase, and 2) only requiring the detector to estimate $\hat{i}$ correctly. Although the LMP detector formulation requires that the SPF estimate an extra two states (compared to the SCA test statistic), this was not the major factor in limiting its performance. The results showed that for a reference frequency of 0.01 Hz, the decreasing the ANR for the angle measurement below 129.2 dB limited the ability of the LMP detector to maintain acceptable parameter separation. In contrast, the SCA detector showed a more consistent performance for the ANRs and estimation horizons tested. However, simulation results for both detectors showed that the detection performance (measured as the percentage of times the correct signal parameters were detected) for a tracking reference frequency of 1.00 Hz had detection percentage below 50% suggesting that neither detector should be used under the conditions tested.

3.8 Summary and Conclusion

The problem of receiving information using movements instead of direct radio communication was investigated. A hybrid system model was formulated under the assumption that the behavior can be described by a finite set of operating modes. Each mode consists of a model that describes the vehicle's dynamics as well as a mode perturbation signature. The signatures were designed as Gold codes since they are differentiable from noise and have favorable correlation properties. A locally most powerful detector (LMP) was presented that uses principles from detection and estimation theory to derive an optimal test statistic. In order to minimize computations and to facilitate real-time implementation a suboptimal detector (SCA) was also formulated. Monte Carlo simu-

lations of a one dimensional linear model and a more complicated two-dimensional example with nonlinear radar measurements were presented. For the simulations studies, the KF and the SPF were the model-based estimators used for the linear and nonlinear examples respectively. A detailed summary of how the process and measurement covariance matrices of the estimators were tuned to maximize the performance of the detector was also presented.

Monte Carlo simulations showed the detection performance, defined as the percentage of times the correct mode perturbation signature parameters are detected, is a function of the estimation horizon (number of measurements used to compute the test statistic) and the ANR. In the linear example, the LMP is shown to outperform the SCA for similar estimation horizons and ANRs. The data also shows that for the linear case, the performance of the LMP is significantly more robust to a tracking reference frequency of 1.00 Hz. However, there is a tradeoff to the superior performance of the LMP as the formulation requires a factor of $n_{\text{sig}} \cdot n_{\tau} \cdot n_F$ more computations than the SCA.

The example with nonlinear radar measurements shows different results for the LMP and SCA compared to the linear case. By computing the evaluation of LMP detector for the same two dimensional linear model with nonlinear output equations, it is shown that the signature detection algorithm is much more sensitive to changes in the measurement noise level of the angle measurement. The evaluation of the test statistic for different range and angle ANRs showed that for angle ANRs lower than 129.2, the mode perturbation detection parameter separation (the difference in the value of the test statistic for the correct and incorrect singature parameters) is lost in the LMP. In other words for an angle measurement ANR $<$ 129.2, the LMP detector has difficulties detecting the correct signal parameters. This causes a drastic drop off in performance for smaller ANRs. Analysis showed that this is not caused by the larger order state in the estimator (compared to the SCA), but rather by how the noise in the angle measurement

affects the LMP. The SCA did not exhibit a drastic detection performance degradation for angle ANRs < 129.2. However, the detection performance of both detectors for a reference frequency of 1.00 Hz was marginal (the percentage of times that the correct signal parameters were detected was below 50%) for the conditions considered.

The two detectors derived are able to detect the transmitted mode and their performance is dependent on the estimation horizon, ANR, and the frequency of the tracking reference. The results for the linear and nonlinear should be used as a reference to design for a desired detection performance. Numerical studies showed that for the nonlinear case, the SCA test statistic achieves results that are in the same range as the much more computationally costly LMP test statistic. For lower ANRs, the simulations show that SCA test statistic performs better than the LMP test statistic. The inferior performance of the LMP detector for low ANRs can be attributed to characteristics of the problem that were not considered in the analysis. These unmodeled characteristics include the nonlinearities of the measurement equation and the cross-correlation between Gold Codes which is exacerbated by the short estimation horizons.

CHAPTER 4

HYBRID COOPERATIVE RECONNAISSANCE WITH LIMITED COMMUNICATION USING THE SEASCAN UAV

4.1 Introduction

The advantages of unmanned vehicles are well documented and include: significant weight savings, low risk for human operators, and potential for superior coordination [51]. Aerial, ground, and underwater unmanned vehicles, are also an alternative for civilian and military applications where the environment is too dangerous and/or too expensive to use a human operator. "Swarms" of smaller versions of these vehicles are now being envisioned because of the advantages of building small scale electronics and integrating smart sensor and software technologies on board, economies of scale, and robustness. However, creating and maintaining a communication network (intra-vehicle) would not scale well with the numbers of vehicles. The work here focuses on the problem of cooperative reconnaissance and planning with strict radio communication constraints often encountered in stealth like reconnaissance missions in enemy territory.

Inherent to cooperative missions without communication is the need of each vehicle to estimate the behavior of its environment in order to improve its performance and decision making. This environment includes partner vehicles whose behavior is critical to the cooperative missions. The work here assumes the vehicle behavior can be described using a finite number of operating modes. In principle, optimal control can be used for cooperative reconnaissance and planning [52], however high computational costs and numerical problems make it challenging for real-time implementation. Reduction of the complexity of the mission is achieved by quantizing the behavior of partner vehicles into finite operating modes, which could also be used for intra-vehicle communication.

In contrast to Ref. [53], where vehicle maneuvers are quantized into motion primitives, the approach here is to associate the reconnaissance operating mode to the vehicle's targets. This paper presents a two vehicle, leader/follower, configuration, although more complex configurations when more vehicles are present can be realized. Assuming the behavior of each vehicle is described by a finite set of operating modes, then the environment can be modelled using a hybrid automaton. A hybrid system can loosely be defined as a system in which there is an interaction of discrete (the operating modes) and continuous dynamics (the vehicle's state) [32]. A detection scheme must then be used to determine the current operating mode of the hybrid system from measurements of the environment.

The problem of state (sometimes referred to as the base-state) and mode (sometimes referred to as the modal state) estimation in hybrid systems has been addressed in literature. The marginal performance of the Extended Kalman Filter (EKF) in certain tracking/recognition problems led to the development of the interacting multiple model (IMM) estimator [7]. The IMM estimator developed in fuses N models to efficiently compute a high quality state estimate. Fusion is based on computing the probability of the modes based on their residuals; the mode with the smaller residual is weighted more in the estimate. For smooth nonlinear systems that have unknown but bounded uncertainties, Ref. [54] derives in an estimator in which mode switching occurs based on metrics to minimize the uncertainty in the state estimate. In contrast to the previously mentioned estimators, Ref. [34] proposes a moving-horizon estimation (MHE) algorithm for hybrid systems modelled in the mixed logic dynamical form. The implementation of MHE relies on solving a mixed-integer quadratic program that depends on initial penalties, which improve the estimate in the presence of noise. In Ref. [55], the authors propose defining operating modes using the system dynamics as well as perturbation signatures. When these signatures are chosen such that they have favorable

cross-correlation properties, the estimates can be correlated with the signatures, thus enabling mode estimation. The use of mode perturbation signatures is further developed and a a Neyman-Pearson most locally powerful detector is derived in Chapter 3 of this dissertation.

This paper investigates the use of mode perturbation signatures to achieve cooperative reconnaissance and planning with limited communication between two SeaScan unmanned aerial vehicles (UAVs) searching a random enemy environment. The cooperative reconnaissance performance of the system (leader/follower) under strict communication constraints is tested in two ways: 1) by measuring the length of time it takes for the vehicles to collect information from an area, and 2) by the amount of information collected in a fixed time interval. The mode perturbation signature method proposed in [55] and furthered developed in Chapter 3 of this dissertation is implemented to correlate reconnaissance operating modes with Gold codes. A correlation based test is then used to detect the mode of operation. Monte Carlo simulations are used to analyze the cooperative reconnaissance performance of the vehicles using perturbation signatures. The performance of the system is compared to a decentralized system in which there is no cooperation and a centralized system with full communication.

The paper is presented as follows. Section 4.2 defines the cooperative reconnaissance and the two ways to gauge performance based on the time to complete the mission and the information collected. The nonlinear model, control, sensor suite, estimation, and mode perturbations for the SeaScan UAV are described in Section 4.3. In Section 4.4, the mode detection algorithm used to detect reconnaissance operating modes is developed. Finally, Section 4.5 presents Monte Carlo simulation results for the cooperative reconnaissance and planning of two vehicles in random environments.

4.2 Problem Statement

The proposed cooperative reconnaissance problem consists of assigning two unmanned aerial vehicles the task of searching an area containing ($2M$) target points. One of the vehicles is named the leader while the other is the follower. Initially, each vehicle is assigned a set of M target points. Each vehicle proceeds by flying to each target point, and orbits about the point with radius, R, until a level of information, I_{thresh}, is collected or a time constraint is met, T_{thresh}. When the vehicle reaches the target point, in addition to locating the target, it also identifies the target as: 1) empty, 2) an adversary, or 3) an obstacle. Then while orbiting the target, the UAV communicates the identification information back to the other vehicle by the means of a mode perturbation signature or trajectory perturbation. The three possible identities of the target points are associated with three operating modes. Figure 4.1 shows a search area with three targets and the trajectory the leader would follow to collect information about Target 1.

Both vehicles are equipped with sensors which can locate and identify targets. The localization sensor has an associated uncertainty, such that it is beneficial to cooperate. The identification sensor is assumed to be instantaneous once the vehicle begin orbiting the target point. One of the vehicles, the leader, flies over its assigned set of target points collecting information. If a target is identified as an adversary, the leader notifies the second vehicle by using to the corresponding mode signature. As the vehicles traverse the target field, the follower monitors the movements of the leader. If a switch by the leader to a mode signaling the presence of an adversary is sensed, the follower evaluates a cost function in order to decide whether to leave its current target and fly to collect information about the leader's target. This cost is influenced by factors such as location, detection time, and rate of cooperative information collection, the combination of which could make vehicle collaboration necessary or unnecessary. Two metrics are used to evaluate switching to cooperation. The first metric looks to minimize the time

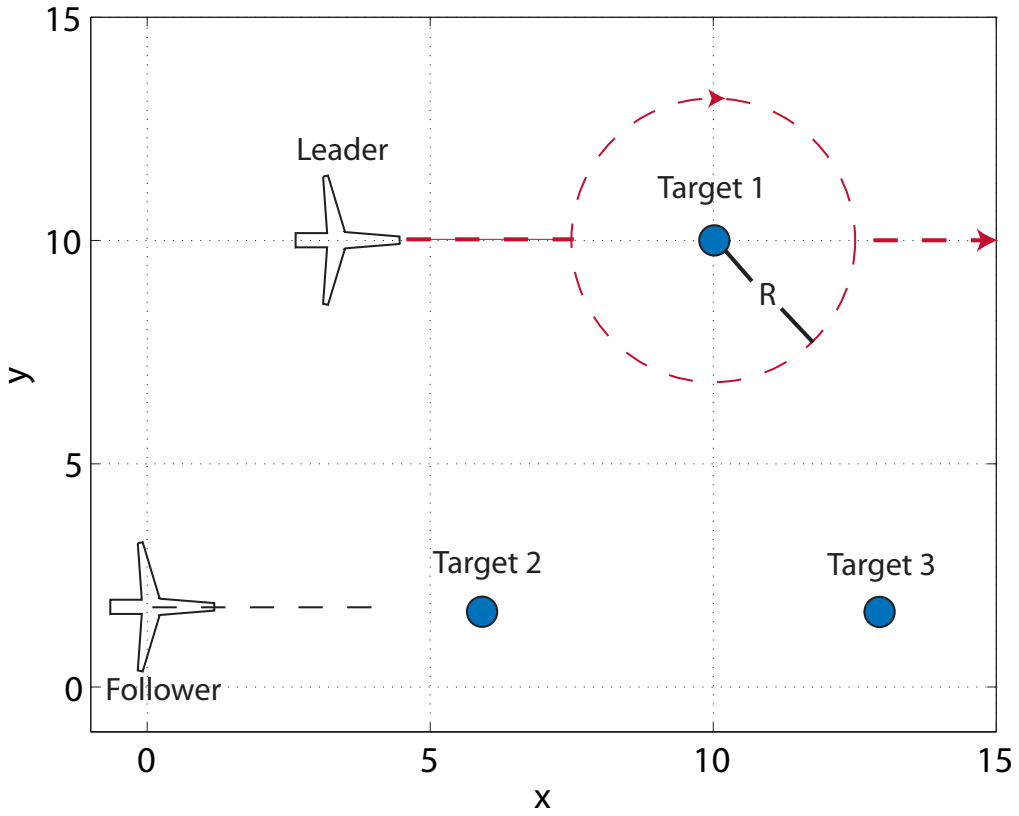

Figure 4.1: Search area with three targets and the trajectory of the leader to collect information about Target 1.

necessary to collect a certain level of information. The second metric, aims to maximize the amount of information collected in a fixed time interval. Once enough information is collected or a time constraint is met, the follower returns to its assigned targets. The follower continues to monitor the movements of the leader, and evaluates whether cooperation would improve mission performance.

4.2.1 Information Collection and Cost

The mission objective for the cooperating vehicles is to collect information while orbiting about and sensing a target.

In this work, a simplified cost metric for information is desired in order to study the

effect of the mode signature approach on cooperating vehicles. Emphasis here is on the time constant of the information collection, i.e. how fast a vehicle or group of vehicles can collect information. Consider a scalar continuous time, random walk model for the target location,

$$\dot{x} = Ax + w, \tag{4.1}$$

$$\dot{x} = w, \tag{4.2}$$

where $x \in \mathbb{R}$ is the target state and $w \in \mathbb{R}$ is a zero-mean white noise process with intensity Q. The sensor measurement from the UAV is given as:

$$y = C_1 x + v, \tag{4.3}$$

where $v \in \mathbb{R}$ is a zero-mean white noise process with intensity R_1. The continuous time information filter, which can be used to estimate the information collected about the target state x is written as:

$$\dot{Y} = -2AY - Y^2 Q + C_1^T R_1^{-1} C_1, \tag{4.4}$$

where Y is the information collected. It can be seen from Equation (4.2) that $A = 0$, and thus Equation (4.4) is equal to:

$$\dot{Y} = -Y^2 Q + C_1^T R_1^{-1} C_1. \tag{4.5}$$

Assuming no a priori information, $Y(0) = 0$, solving for $Y(t)$ then yields;

$$Y(t) = \left[\sqrt{C_1^T R_1^{-1} C_1}\sqrt{Q^{-1}}\right] \tanh\left[\sqrt{C_1^T R_1^{-1} C_1}\sqrt{Q}t\right]. \tag{4.6}$$

Note that the information starts at time $t = 0$ and $Y(0) = 0$, and then increases to a steady-state, $Y(t \to \infty) = \left[\sqrt{C_1^T R_1^{-1} C_1}\sqrt{Q^{-1}}\right]$. Associated with this information collection is a time constant. Equation (4.6) can be fitted with an exponential function yielding:

$$\begin{aligned} Y(t) &\approx \left[\sqrt{C_1^T R_1^{-1} C_1}\sqrt{Q^{-1}}\right]\left(1 - \exp\left[-1.5\sqrt{C_1^T R_1^{-1} C_1}\sqrt{Q}t\right]\right) && (4.7) \\ &\approx I_0\left(1 - \exp\left[-\lambda t\right]\right), && (4.8) \end{aligned}$$

where λ is the information collection time constant when a single vehicle collects information about the target.

In the event that there is cooperation, Equation (4.3) must be modified to account for two measurements, or

$$\mathbf{y} = \begin{bmatrix} C_1 \\ C_2 \end{bmatrix} x + \overline{\mathbf{v}}, \tag{4.9}$$

$$= \overline{C}x + \overline{\mathbf{v}}, \tag{4.10}$$

where $\overline{\mathbf{v}} \in \mathbb{R}^2$ is a zero-mean white noise process with intensity $\overline{R} \in \mathbb{R}^2$. The matrix $\overline{R}$ has the form:

$$\overline{R} = \begin{bmatrix} R_1 & 0 \\ 0 & R_2 \end{bmatrix}, \tag{4.11}$$

where R_1 and R_2 are the noise intensities for the first and second vehicle's measurement noise. Since $A = 0$, Equation (4.5) can be rewritten for cooperation scenario yielding:

$$\dot{Y} = -Y^2 Q + \overline{C}^T \overline{R}^{-1} \overline{C}, \tag{4.12}$$

As for the single vehicle case, if the assumption is made that there is no a priori information, $Y(0) = 0$, solving for $Y(t)$ then yields:

$$Y(t) = \left[\sqrt{\overline{C}^T \overline{R}^{-1} \overline{C}} \sqrt{Q^{-1}} \right] \tanh \left[\sqrt{\overline{C}^T \overline{R}^{-1} \overline{C}} \sqrt{Q} t \right]. \tag{4.13}$$

Equation (4.13) can be fitted with an exponential function yielding:

$$Y(t) \approx I_0^c \left(1 - \exp\left[-\lambda^c t\right]\right), \tag{4.14}$$

where

$$I_0^c = \sqrt{\overline{C}^T \overline{R}^{-1} \overline{C}} \sqrt{Q^{-1}}, \tag{4.15}$$

and the time constant for cooperation is:

$$\lambda^c = 1.5 \sqrt{\overline{C}^T \overline{R}^{-1} \overline{C}} \sqrt{Q}. \tag{4.16}$$

The ratio of the time constants for the single and two vehicle case is:

$$\frac{\lambda_c}{\lambda} = \frac{1.5\sqrt{\overline{C}^T \overline{R}^{-1} \overline{C}}\sqrt{Q}}{1.5\sqrt{C_1^T R_1^{-1} C_1}\sqrt{Q}} \tag{4.17}$$

$$= \sqrt{\frac{C_1^2 R_1^{-1} + C_2^2 R_2^{-1}}{C_1^2 R_1^{-1}}} \tag{4.18}$$

In the event that the white-noise intensity for the process noise in Equation (4.3) is equal for both the single and two vehicle cases, the measurement noise intensities in Equation (4.9) are equal $R_1 = R_2$, and $C_1 = C_2$ (the measurement is related to the state in the same way), the ratio between λ and λ^c and I_0, I_0^c is:

$$\frac{I_0^c}{I_0} = \frac{\lambda^c}{\lambda} = \sqrt{2}. \tag{4.19}$$

In this investigation, the collection of information for a single vehicle is modeled using an exponential function of the form:

$$I_i = I_0 \left(1 - \exp\left[-\lambda_i t_i\right]\right), \tag{4.20}$$

where I_i is the information for the i^{th} target, I_0 is a constant, and λ_i is the information collection time constant. If two vehicles are cooperatively collecting information about the i^{th} target, the information collection model is:

$$I_i = I_0^c \left(1 - \exp\left[-\lambda_i^c t_i\right]\right), \tag{4.21}$$

where I_0^c and λ_i^c are the respective constants for cooperation. The information curves, defined by Equation (4.20) for the case of collecting information with one ($I_0 = 1$, $\lambda = 1$) or two ($I_0^c = 1$, $\lambda^c = 1.5$) vehicles respectively are shown in Figure 4.2. The advantage of collecting information cooperatively is shown as the information curve for the two vehicles has a steeper slope.

When the leader identifies the presence of an adversary, the follower must detect this through the use of detection theory, and then decide whether collecting information cooperatively will improve the mission objectives (information or time) through

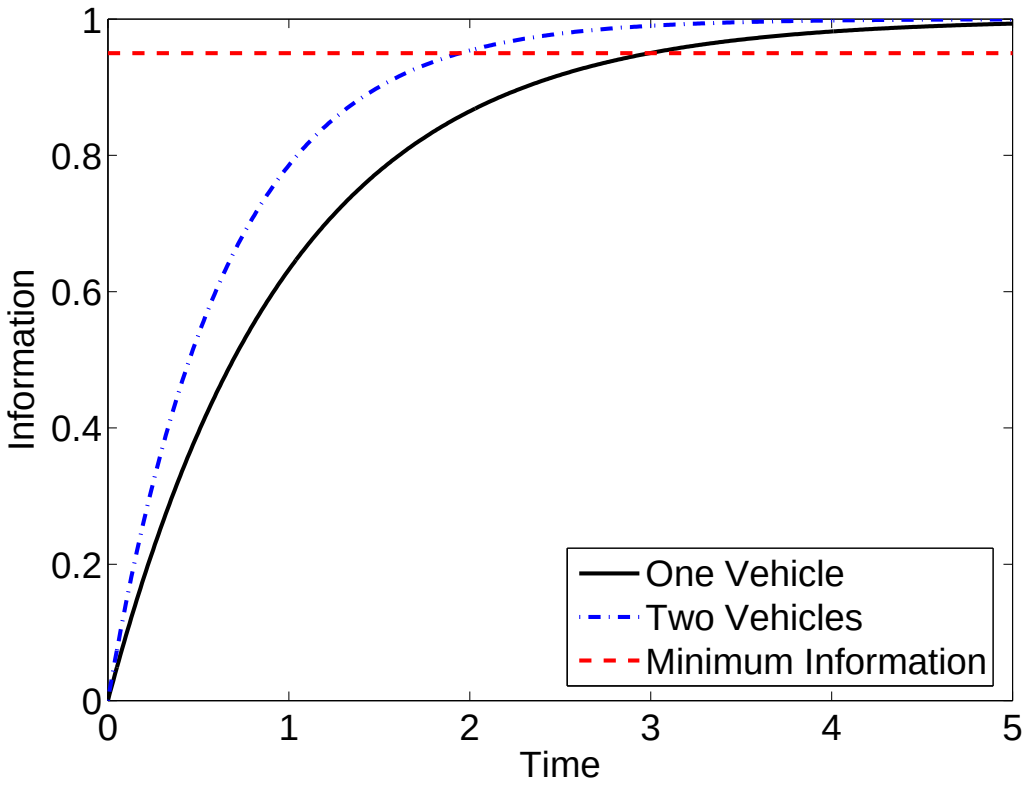

Figure 4.2: Information curves when one and two vehicles collect information about a target. The dashed line represents the desired amount of information for the target.

cooperation. A mission cost function is defined by: 1) maximizing the amount of information given a time constraint, or 2) minimizing the mission time given an amount of information is collected.

4.2.2 Minimize Mission Time Given Information Constraints

Consider the case where the goal is to minimize the total mission time given enough information is collected about each of the targets. First, consider the cost function when there is no cooperation, J^{nc}, between the leader and the follower. The cost function is composed of the time it would take the leader, $J^{\text{nc}}_{t,l}$ and the follower, $J^{\text{nc}}_{t,f}$, to complete collecting information about their assigned targets:

$$J^{\text{nc}}_{t} = \min\left(J^{\text{nc}}_{t,l} + J^{\text{nc}}_{t,f}\right), \tag{4.22}$$

such that

$$I_0\left(1 - \exp\left[-\lambda_i t_i\right]\right) > I_{\min,i}, \tag{4.23}$$

where I^{i}_{min}, $i \in [1,\ldots,2M]$ is the minimum amount of information that must be collected for the i^{th} target. Of the total $2M$ targets, the leader is assigned the first M targets yielding a cost with the form:

$$J^{\text{nc}}_{t,l} = \sum_{i=1}^{M} t_i + \sum_{j=1}^{M-1} t^{j,j+1}, \tag{4.24}$$

where t_i is the time spent collecting information about the i^{th} target and $t^{i,j}$ is the travel time between targets i and j. Similarly, given that the follower is assigned targets $M+1$ to $2M$, the cost function for the follower vehicle without cooperation is:

$$J^{\text{nc}}_{t,f} = \sum_{i=M+1}^{2M} t_i + \sum_{j=M+1}^{2M-1} t^{j,j+1}. \tag{4.25}$$

In the absence of cooperation and for known target point locations, all terms in Equations (4.24) and (4.25) are known and can be calculated a priori. Therefore, the total cost for

no cooperation is:

$$J_t^{\text{nc}} = \sum_{i=1}^{M} t_i + \sum_{j=1}^{M-1} t^{j,j+1} + \sum_{i=M+1}^{2M} t_i + \sum_{j=M+1}^{2M-1} t^{j,j+1}. \tag{4.26}$$

It should be noted that the order in which each vehicle visits its targets is predetermined. In other words, optimizing the target assignment is not part of the investigation.

Define the target point p as a a target in the list of targets assigned to the leader, or $p \in [1,\ldots,M]$, while target point r is a target in the list of targets assigned to the follower, $r \in [M+1,\ldots,2M]$. In the event that the follower detects that the leader is orbiting about target point p, and that target point is an adversary, the cost in Equation (4.22) must be reevaluated continuously as the mission proceeds in order to decide whether the cooperation cost, $J_t^{\text{c}} = J_{t,f}^{\text{c}} + J_{t,l}^{\text{c}}$, would improve the mission cost without cooperation, J_t^{nc}, i.e. $J_t^{\text{c}} < J_t^{\text{nc}}$. Given that target point p is an adversary and the follower is currently orbiting about target point r, the the cooperation cost for the remainder of the mission must be computed. The cost for the follower vehicle would be identical to the cost shown in Equation (4.25), however extra terms are necessary to account for the travel time between target points r and p. Denote the travel time from target point r to p as $t^{r,p}$, and the time spent cooperatively collecting information about target point p as t_p^{c}. Therefore, the time cost for the follower is the sum of the cost, $J_{t,f}^{\text{nc}}$, of going through all its assigned targets ($M+1$ through $2M$), the travel time to and from the leader's target ($t^{r,p}$), and the time spent cooperatively collecting information about target point p (t_p^{c}), or:

$$J_{t,f}^{\text{c}} = J_{t,f}^{\text{nc}} + 2t^{r,p} + t_p^{\text{c}}. \tag{4.27}$$

The cost in Equation (4.27) is valid under the assumption that if an adversary is detected, the follower will immediately leave its current target and cooperate with the leader. The information collected at target point p is equal to the sum of the information collected by the leader before the follower arrives, $I_p^{\text{c},-}$, and the information collected by both

vehicles cooperatively, $I_p^{c,+}$,

$$I_p^c = I_p^{c,-} + I_p^{c,+}. \tag{4.28}$$

Because the target information is transmitted through the leader's movements, the follower requires time to collect measurements (estimation horizon) for mode detection, denoted as a detection delay, t_{det}. Therefore, the time until the follower arrives at target point p is:

$$t_{\text{det}} + t^{r,p}. \tag{4.29}$$

By using Equation (4.29), the information that the leader collects before the follower arrives is:

$$I_p^{c,-} = I_0 \left(1 - \exp\left[-\lambda_p \left(t_{\text{det}} + t^{r,p}\right)\right]\right). \tag{4.30}$$

Once the follower arrives, both vehicles orbit about target point p collecting information cooperatively. The information constraint, Equation (4.23), must still be met before the leader can move its next target. The information constraint at target point p takes the form:

$$I^{c,-} + \left(I_0^c - I^{c,-}\right)\left(1 - \exp\left[-\lambda_p^c t_p^c\right]\right) > I_{\min,p}, \tag{4.31}$$

where I_0^c is the information constant for cooperation at target point p (see Equation (4.21)). Under cooperation, the total time spent by the leader at target point p is:

$$J_{t,l}^c \Big| p = t_{\text{det}} + t^{r,p} + t_p^c. \tag{4.32}$$

Finally, the updated total time cost for the leader when cooperating at target point p is the sum of the time cost from target 1 to $p-1$, the time cost at target point p, and the time cost from target $p+1$ to M:

$$\begin{aligned} J_{t,l}^c &= J_{t,l}^{nc}\Big|_1^{p-1} + J_{t,l}^c \Big| p + J_{t,f}^{nc}\Big|_{p+1}^{M} && (4.33) \\ &= J_{t,l}^{nc}\Big|_1^{p-1} + t_{\text{det}} + t^{r,p} + t_p^c + J_{t,f}^{nc}\Big|_{p+1}^{M}. && (4.34) \end{aligned}$$

Using Equation (4.27) and (4.34), the updated total time cost of the mission when the vehicles cooperate at target point p is:

$$\begin{aligned} J_t^{\mathrm{c}} &= J_{t,l}^{\mathrm{c}} + J_{t,f}^{\mathrm{c}} && (4.35) \\ &= J_{t,l}^{\mathrm{nc}}\Big|_1^{p-1} + t_{\mathrm{det}} + t^{r,p} + t_p^{\mathrm{c}} + J_{t,f}^{\mathrm{nc}}\Big|_{p+1}^{M} + J_{t,f}^{\mathrm{nc}} + 2t^{r,p} + t_p^{\mathrm{c}}. && (4.36) \end{aligned}$$

Information about target point p is collected cooperatively if

$$J_t^{\mathrm{c}} < J_t^{\mathrm{nc}}. \tag{4.37}$$

Since both sides of the inequality in Equation (4.37) share common elements, the inequality can be simplified yielding:

$$t_{\mathrm{det}} + 3t^{r,p} + 2t_p^{\mathrm{c}} < t_p, \tag{4.38}$$

where t_p is the time leader would need to spend orbiting about target point p without cooperation before meeting the information constraint $I_{\min,p}$.

4.2.3 Maximizing Information Given a Time Constraint

In the case where the objective is to maximize the amount of information collected given a time constraint without cooperation, the cost function is written as follows:

$$J_I^{\mathrm{nc}} = \left(J_{I,l}^{\mathrm{nc}} + J_{I,f}^{\mathrm{nc}}\right), \tag{4.39}$$

where

$$J_{I,l}^{\mathrm{nc}} = \max_{t_i} \left\{ \sum_{i=1}^{M} I_i \left(1 - \exp\left[-\lambda_i t_i\right]\right) \right\}, \tag{4.40}$$

such that

$$T = \sum_{i=1}^{M} t_i + \sum_{j=1}^{M-1} t^{j,j+1}. \tag{4.41}$$

The optimization problem in Equations (4.40) and (4.41) is solved analytically by solving for t_M in Equation (4.41), substituting the result into Equation (4.40), and setting

$\frac{\partial J_{I,l}^{\text{nc}}}{\partial t_i} = 0$. The optimal values of t_i are:

$$[t_1 \dots t_{M-1}]^T = (\lambda_M U + diag([\lambda_1 \dots \lambda_{M-1}]))^{-1} \begin{bmatrix} \ln \frac{I_1 \lambda_1}{I_M \lambda_M} + \lambda_M \overline{T} \\ \vdots \\ \ln \frac{I_i \lambda_i}{I_M \lambda_M} + \lambda_M \overline{T} \\ \ln \frac{I_{M-1} \lambda_{M-1}}{I_M} \lambda_M \overline{T} \end{bmatrix}, \tag{4.42}$$

where $U \in \mathbb{R}^{(M-1)\times(M-1)}$ is a matrix whose elements are all 1's and

$$\overline{T} = T - \sum_{j=1}^{M-1} t^{j,j+1}. \tag{4.43}$$

For the leader, define the current optimal value of the cost, $J_{I,l}^*$, and time schedule, $\mathbf{t}_l^*$, from the solution of the optimization problem in Equations (4.40) and (4.41). $\mathbf{t}_l^*$ is stacked vector that contains optimal times for the leader to spend at each target, or:

$$\mathbf{t}_l^* = \begin{bmatrix} t_{1,l}^* \\ t_{2,l}^* \\ \dots \\ t_{M,l}^* \end{bmatrix}. \tag{4.44}$$

The same approach is implemented with the information cost of the follower, $J_{I,f}^{\text{nc}}$. The optimization problem for the follower is:

$$J_{I,f}^{\text{nc}} = \max_{t_i} \left\{ \sum_{i=M+1}^{2M} I_i \left(1 - \exp\left[-\lambda_i t_i\right]\right) \right\}, \tag{4.45}$$

such that

$$T = \sum_{i=M+1}^{2M} t_i + \sum_{j=M+1}^{2M-1} t^{j,j+1}. \tag{4.46}$$

For the follower, denote the optimal value of the cost as $J_{I,f}^*$, and the optimal time schedule as $\mathbf{t}_f^* = \left[t_{M+1,f}^*, \dots, t_{2M,f}^*\right]^T$. The current optimal total mission cost is then:

$$J_I^* = J_{I,l}^* + J_{I,f}^*. \tag{4.47}$$

If the leader declares that an adversary was found, then in a similar way as was done with the case of minimizing mission time given information constraints, Section 4.2.2, the follower evaluates whether cooperation would improve the mission cost. The information cost for cooperation for the leader at target point p is the sum of the information before, $I_p^{c,-}$, and after, $I_p^{c,+}$, the follower arrives, or:

$$J_{I,l}^{c}\Big| p = I_p^{c,-} + I_p^{c,+}. \tag{4.48}$$

The information collected before the follower arrives is a function of the detection time, t_{det}, and the travel time from target points r to p:

$$I_p^{c,-} = I_0 \left(1 - \exp\left[-\lambda_p \left(t_{\text{det}} + t^{r,p}\right)\right]\right). \tag{4.49}$$

The information collected during cooperation at target point p is:

$$I_p^{c,+} = \left(I_0^{c} - I_p^{c,-}\right)\left(1 - \exp\left[\lambda_p^{c} t_p^{c}\right]\right), \tag{4.50}$$

where t_p^{c} is the time the two vehicles collect information cooperatively. Having calculated the cost for cooperation at the p^{th} target point, the cost for the remainder of the mission must be re-evaluated because: 1) the travel time to fly to and from the leader's adversary target must be considered in the cost function, and 2) the time saved by cooperation can be reallocated to improve the overall mission cost. Said another way, each time cooperation takes place the optimization problem in Equation (4.40) must be recomputed for both the leader and the follower. For the leader, the time schedule and associated cost will be recalculated from target points p after the follower arrives to target point M. The leader's cost function for cooperation used for optimization from target point p is:

$$J_{I,l}^{c}\Big|_{p}^{M} = \left(I_p - I_p^{c,+}\right)\left(1 - \exp\left[-\lambda_p^{c} t_p^{c}\right]\right) + \sum_{i=p+1}^{M} I_i \left(1 - \exp\left[-\lambda_i t_i\right]\right), \tag{4.51}$$

where the first term in the right side of Equation (4.51) represents the information that the leader and follower would collect cooperatively and the summation represents the

information that would be collected in the remainder of the mission. It should be noted that the term $I_p^{c,-}$, is not included in Equation (4.51) since this term is a function of t_{det} and $t^{r,p}$ and cannot be optimized.

The updated time constraint is:

$$\widetilde{T}_l = T_l + t_{\text{det}} + t^{r,p} + t_p^c + \sum_{i=p+1}^{M} t_i + \sum_{j=p}^{M-1} t^{j,j+1}, \tag{4.52}$$

where T_l represents the time spent by the leader before reaching target point p. Equation (4.42) is used to solve the new optimization problem for the leader (Equations (4.51)-(4.52)) and calculate the new cost $J_{I,l}^{new}$ and time schedule $\mathbf{t}_l^{\text{new}} = \left[t_p^{\text{new}}, \ldots, t_M^{\text{new}}\right]^T$. The updated total information mission cost for the leader is then:

$$J_{I,l}^{\text{c,new}} = J_{I,l}^{*}\big|_1^p + I_p^{\text{c},-} + J_{I,l}^{\text{new}}, \tag{4.53}$$

where $J_{I,l}^{*}\Big|_1^p$ is the information cost of the leader before reaching target point p.

The time schedule and information cost must also be updated for the follower to account for cooperation. If the follower is orbiting about target point r, the information cost is a function of the time it has spent collecting information before flying to target point p, t_r^-, as well as the time spent after returning from target point p, t_r^+. It should be noted that it is possible for the optimization to yield a value of $t_r^+ = 0$ in which case the follower would proceed to its next target. The information cost for the follower at target point r is:

$$J_{t,f}^{\text{nc}}\Big| r = I_r^- + I_r^+, \tag{4.54}$$

where

$$I_r^- = I_0\left(1 - \exp\left[-\lambda t_r^-\right]\right), \tag{4.55}$$

$$I_r^+ = \left(I_0 - I_r^-\right)\left(1 - \exp\left[-\lambda t_r^+\right]\right) \tag{4.56}$$

The cost function that will be used to compute a new time schedule for the follower is:

$$J_{I,f}^{\text{c}}\Big|_r^{2M} = \left(I_r^+ - I_r^-\right)\left(1 - \exp\left[-\lambda_r t_r^+\right]\right) + \sum_{i=r+1}^{2M} I_i\left(1 - \exp\left[-\lambda_i t_i\right]\right). \tag{4.57}$$

The updated time constraint for the follower is:

$$\widetilde{T}_f = T_f + t_r^- + 2t_{r,p} + t_p^c + t_r^+ + \sum_{i=r+1}^{2M} t_i + \sum_{j=r+1}^{2M} t^{j,j+1}, \tag{4.58}$$

where T_f represents the time spent by the follower before reaching target point r. Analytically solving the updated optimization problem for the leader in Equations (4.57)-(4.58) yields the updated information cost $J_{I,f}^{\text{new}}$ and the associated time schedule $\mathbf{t}_f^{\text{new}} = \left[t_{r^*}, \ldots, t_{2M}^{\text{new}}\right]^T$. The updated total information mission cost for the follower is then:

$$J_{I,f}^{\text{c,new}} = J_{I,f}^* \big|_{M+1}^{r} + I_r^- + J_{I,f}^{\text{new}}, \tag{4.59}$$

where $J_{I,f}^* \Big|_{M+1}^{r}$ is the information collected by the follower before reaching target point r. Having calculated the updated information cost for both the leader and follower, it is now possible to evaluate the total mission information cost:

$$J_I^{\text{new}} = J_{I,l}^{\text{c,new}} + J_{I,f}^{\text{c,new}}. \tag{4.60}$$

The follower flies to collect information about the leader's target point if cooperation would improve the total information mission cost. If $J_I^{\text{new}} > J_I^*$, then: 1) the follower flies to the leader's target, 2) the total mission information cost is updated:

$$J_I^* = J_I^{\text{new}}, \tag{4.61}$$

and 3) the optimal time schedules $\mathbf{t}_l^*$, $\mathbf{t}_f^*$ are updated by replacing the elements corresponding to the updated values from $\mathbf{t}_l^{\text{new}}$ and $\mathbf{t}_f^{\text{new}}$.

The algorithm to maximize information given a time constraint can be summarized by the following steps:

1. Solve the optimization problem in Equations (4.40)-(4.41) and (4.45)-(4.46) yielding the optimal time schedules for the vehicles $\mathbf{t}_l^*$, $\mathbf{t}_f^*$ and the associated mission information cost J_I^*, Equation (4.47).

2. If both vehicles finished collecting information about their targets then the mission is over. Else continue.

3. If the leader has identified an adversary, then the updated cost J_I^{new}, Equation (4.60), with cooperation is evaluated, Equations (4.51)-(4.52) and (4.57)-(4.58). Else go back to step 2.

4. If $J_I^{\text{new}} > J_I^*$, then let $J_I^* = J_I^{\text{new}}$ and update the optimal time schedules $\mathbf{t}_l^*$, $\mathbf{t}_f^*$ by replacing the elements corresponding to the updated values from $\mathbf{t}_l^{\text{new}}$ and $\mathbf{t}_f^{\text{new}}$. The follower cooperatively collects information about the leader's current target point. The vehicles then continue visiting their assigned targets with the new time schedule. Else the vehicles continue collecting information about their targets.

5. Go back to step 2.

4.3 The SeaScan UAV

SeaScan is an unmanned aerial vehicle platform developed by the Insitu Group and is now a key component in Boeing's UAV strategic plan [56]. The SeaScan was developed for a variety of applications that include fishing reconnaissance, coastal patrol, and search-and-rescue. It is a robust platform with over fifteen years of development and operations in weather reconnaissance [57], crossing the Atlantic Ocean [58], and deployment in Iraq [59].

4.3.1 Mode Perturbation Signatures

Consider a rectangular pulse composed of m_ρ points with amplitude, ρ^0, or ρ^1 corresponding to the 0 or 1 chip (or bit) respectively and let the sequence of such n_ρ nonoverlapping rectangular pulses for the i^{th} signature be defined as

$$p^i = \left[b_{i1}, b_{i2}, \ldots, b_{in_\rho}\right] \tag{4.62}$$

where $p^i \in \mathbb{R}^{u_t}$ and $b_{(\cdot)} \in \left[\rho^0, \rho^1\right]$. A chip is defined as the duration of a symbol or bit such as $b_{i,\{\cdot\}}$ in Equation (4.62). This investigation adopts bi-phase shift keying where the 0 chip (*off*) is represented by $\rho^0 = -1$, while the 1 bit (*on*) is $\rho^1 = 1$. The i^{th} mode perturbation signature at time k, z^i_{sig}, is formally defined as product of p^i and a sinusoid carrier:

$$z^i_{\text{sig},k} = p^i_k \cos\left[2\pi f_c t_k + \theta_k\right], \tag{4.63}$$

where f_c, the carrier frequency, and θ is the carrier phase. By combining n_ρ chips, a mode signature, z_{sig} is defined.

Pseudorandom noise (PRN) is a known sequence of bits that, when added to a base signal, results in a signal that has statistical properties similar to noise [35]. An observer could recover the base signal only through correlation with a known sequence which is an exact replica of the original PRN. Certain PRN sequences have desirable properties in terms of auto and cross-correlation. The discrete time cross-correlation function for two binary sequences d_s and e_s is defined as follows:

$$S\left[\tau_d\right] = \sum_{k=1}^{T_p} d_{s,k} e_{s,k}(\tau_d), \tag{4.64}$$

where T_p is the number of samples in a period of the sequences and τ_d is a delay. Maximal length sequences or *m*-sequences are a special kind of periodic PRN sequences whose properties are useful in communications [36]. In the late 1960's, Gold published a construction that takes two preferred pair of *m*-sequences yielding a family of sequences called Gold Codes, that have cross-correlation functions (or auto-correlation, $e_s = d_s$) that are three-valued [35]. Ref. [37] presents a thorough discussion on the special properties of PRN sequences such as *m*-sequences and Gold Codes. A summary of the implementation of PRN sequences in communications and navigation as well as a large bibliography is also provided.

Applying Equation (4.64) to two Gold Codes determines whether two signals are correlated and if there exists a delay between the signals. Because of their favorable

properties Gold codes are used in communications applications such as in Code Division Multiple Access (CDMA)[38, 36]. Gold Codes are also chosen to define the mode perturbation signatures in this paper because of their favorable correlation properties.

Because each mode perturbation signature z^i_{sig} is defined using the i^{th} observed vehicle's internal time clock, the observing vehicle also estimates this clock offset, τ, in order to synchronize its stored signature replica, $\tilde{z}_{\text{sig}}$, with z^i_{sig}. This problem is also encountered in the global positioning system (GPS) where the signal traveling time is determined by the time shift required for a match between the received code from the satellite and the receiver replica [38, 16]. To determine the clock offset, a correlation test is performed on z^i_{sig} and the expected signature replica time shifted by the clock offset, $\tilde{z}_{\text{sig}}(\tau)$. The correlation test consists of correlating $z^i_{\text{sig},k}$ and the stored signatured shifted by the clock offset $\tilde{z}^i_{\text{sig}}(\tau)$,

$$S[\tau] = \sum_{k=1}^{T_t} z^i_{\text{sig},k} \tilde{z}^i_{\text{sig},k}(\tau), \tag{4.65}$$

where T_t is the number of samples in the testing interval. To find the delay, τ is varied over a range, Γ, from 0 to twice the signature period, $\Gamma \in [0, \ldots, 2T_p]$. Γ is divided into $\overline{b}$ equally-sized intervals or cells. Each cell, $\tau(m) = m\frac{2T}{\overline{b}}$ for $m \in \{0, \ldots, \overline{b}-1\}$, is equally probable of being the correct delay. Under the assumption of the absence of noise, the value of m that maximizes $S(\tau[m])$, Equation (4.65), is the estimated clock offset or delay, $\hat{\tau}$.

4.3.2 Continuous and Discrete Time Modeling

The reconnaissance behavior of each vehicle is defined by a finite set of N reconnaissance operating modes. Using a hybrid automaton, the system is described in a hybrid framework as shown in Figure 4.3. Each node in the automaton, q_i, corresponds to one of the N operating modes. The vehicle dynamics and state evolution for the i^{th} mode are

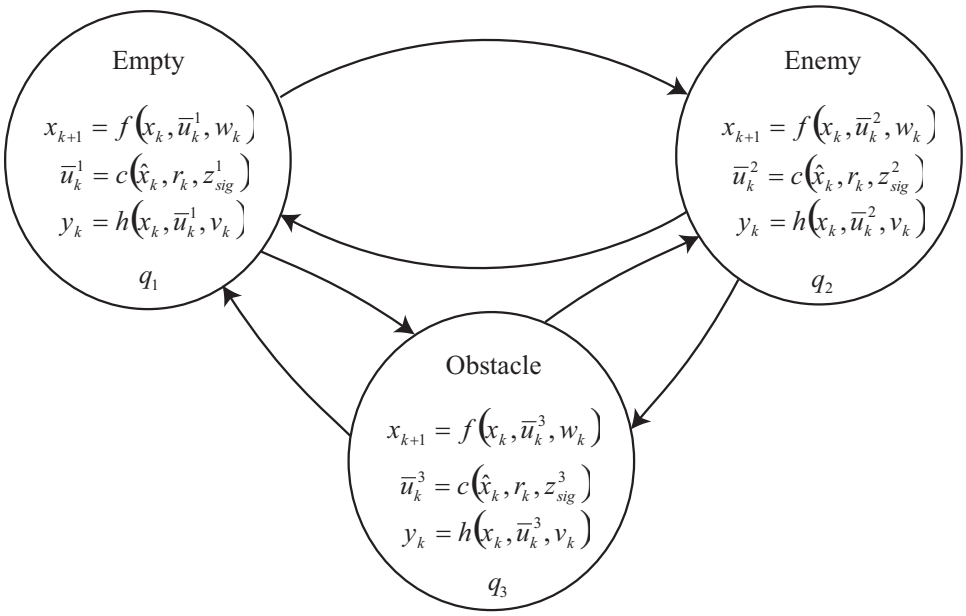

Figure 4.3: Hybrid automaton with 3 reconnaissance operating modes corresponding to: 1) an empty area, 2) an enemy, and 3) an obstacle.

governed by:

$$\mathbf{x}_{k+1} = f^i\left(\mathbf{x}_k, \mathbf{u}_k, z_k^i, \mathbf{w}_k\right) \tag{4.66}$$

$$\mathbf{y}_k = h^i\left(\mathbf{x}_k, \mathbf{u}_k, z_k^i, \mathbf{v}_k\right) \tag{4.67}$$

where at time k, $\mathbf{x}_k \in \mathbb{R}^{n_x}$ is the state, $\mathbf{y}_k \in \mathbb{R}^{n_y}$ the measurement, $\mathbf{u}_k \in \mathbb{R}^{n_u}$ the control input, and $z_{\text{sig},k}^i \in \mathbb{R}$ is a signature correlated to the i^{th} mode. In contrast to most hybrid system formulations, the state evolution while inside mode i is not only influenced by the model ($f^i(\mathbf{x},\mathbf{u})$), but also by a perturbation, z_{sig}^i, to the control input. The process noise $\mathbf{w}_k$ and sensor noise $\mathbf{v}_k$ are zero-mean white Guassian noise with covariance,

$$E\left[\mathbf{w}_k \mathbf{w}_k^T\right] = Q_k, \tag{4.68}$$

$$E\left[\mathbf{v}_k \mathbf{v}_k^T\right] = R_k. \tag{4.69}$$

A feedback controller is needed to assure that the nonlinear system in Equation (4.66) tracks a desired reference $\mathbf{r}_k$. The reference $\mathbf{r}_k$ is the necessary vehicle trajectory

to complete its task. A controller, $c(\cdot,\cdot)$, computes the nominal control input $\mathbf{u}_k$ given $\mathbf{x}_k$ such that $\mathbf{r}_k$ is tracked:

$$\mathbf{u}_k = c(\mathbf{x}_k, \mathbf{r}_k). \tag{4.70}$$

The controller in Equation (4.70) represents any linear or nonlinear controller that minimizes the tracking error, $||\mathbf{r}_k - \mathbf{x}_k||$, in the presence of disturbances.

Now consider a small reference perturbation, $\mathbf{r}^i_{\text{sig},k}$, to the nominal reference signal of the system, $\mathbf{r}_k$,

$$\bar{\mathbf{r}}^i_k = \mathbf{r}_k + \mathbf{r}^i_{\text{sig},k}, \tag{4.71}$$

where $\bar{\mathbf{r}}^i_k$ is the total reference to be tracked by the system. Let $t^r_z(\cdot)$ denote the mapping from the scalar signature to the reference:

$$\mathbf{r}^i_{\text{sig}} = a_{\text{sig}} t^r_z\left(z^i_{\text{sig}}\right), \tag{4.72}$$

where a_{sig} is the mode perturbation signature scaling factor. The function $t^r_z(\cdot)$ considers the element of the system that the mode perturbation signature will be embedded and builds the corresponding mode perturbation vector, $\mathbf{r}^i_{\text{sig}}$. If others elements in the reference vector have a differential relationship with the element in which the signature is embedded, $t^r_z(\cdot)$ preserves this relationship when building $\mathbf{r}^i_{\text{sig}}$. For example, if the reference vector is composed of position and its derivative and the perturbation signature is embedded in the position reference then the output of $t^r_z(\cdot)$ is:

$$\begin{aligned} \bar{\mathbf{r}}^i_k &= \mathbf{r}_k + a_{\text{sig}} t^r_z\left(z^i_{\text{sig}}\right), & (4.73)\\ &= \mathbf{r}_k + a_{\text{sig}} \begin{bmatrix} z^i_{\text{sig}} \\ \frac{d}{dt} z^i_{\text{sig}} \end{bmatrix}. & (4.74) \end{aligned}$$

The reference perturbation, $\mathbf{r}^i_{\text{sig}}$, must be small enough so that the performance of the vehicle is not compromised, yet large enough to be detected in the presence of process and measurement noise.

For the vehicle to follow the perturbed reference, $\mathbf{r}^i_{\text{sig}}$ is added to $\mathbf{r}_k$ such that the perturbed control input $\overline{\mathbf{u}}_k$ becomes:

$$\overline{\mathbf{u}}^i_k = c\left[\mathbf{x}_k, \mathbf{r}_k + a_{\text{sig}} t^r_z\left(z^i_{\text{sig}}\right)\right]. \tag{4.75}$$

4.3.3 Vehicle Dynamics and Control

The nonlinear equations of motion of the SeaScan are expressed in standard form:

$$\dot{\mathbf{x}} = f(\mathbf{x}, \mathbf{u}) + \mathbf{w} \tag{4.76}$$

where $\mathbf{x} \in \mathbb{R}^9$ is the SeaScan state vector, $\mathbf{u} \in \mathbb{R}^5$ is the control input state vector, and $\mathbf{w}$ is a process noise vector with covariance Q. The SeaScan state vector has nine states:

$$x = \begin{bmatrix} \phi & \theta & \psi & p & q & r & V & \alpha & \beta \end{bmatrix}^T \tag{4.77}$$

which includes the roll, pitch, yaw (rad) in reference from Earth to the aircraft-body-centered (ABC) coordinate frame, the roll, pitch, yaw rates (rad/sec) in ABC, the vehicle velocity (m/s) in the wind axis coordinate frame, the angle of attack (rad), and the sideslip angle (rad). The vector control input, $\mathbf{u}$, is composed of seven controls surfaces:

$$\mathbf{u} = \begin{bmatrix} \delta_{eis} & \delta_{eip} & \delta_{eos} & \delta_{eop} & \delta_{ws} & \delta_{wp} & F_T \end{bmatrix}^T, \tag{4.78}$$

which respectively are starboard and port inner elevons (rad), the starboard and port outer elevons (rad), the starboard and port winglets (rad), and the throttle (N). The seven control surface are shown in Figure 4.4. The nonlinear function, $f(\mathbf{x}, \mathbf{u})$, represents both the nonlinear kinematics and aerodynamics. A complete nonlinear aerodynamic simulation, $f(\mathbf{x}, \mathbf{u})$, was developed by The Insitu Group based on years of wind tunnel and flight tests of the SeaScan, and is used here for algorithm validation.

Although the SeaScan equations of motion are nonlinear, the system is stabilized about the r^{th} trim condition, $\tilde{x}$, using the linear quadratic regular (LQR). The linear trim model(s) $\Phi_{\tilde{x}^r} = (A, B, C, D)$ near $\tilde{x}^r$ are found using numerical methods.

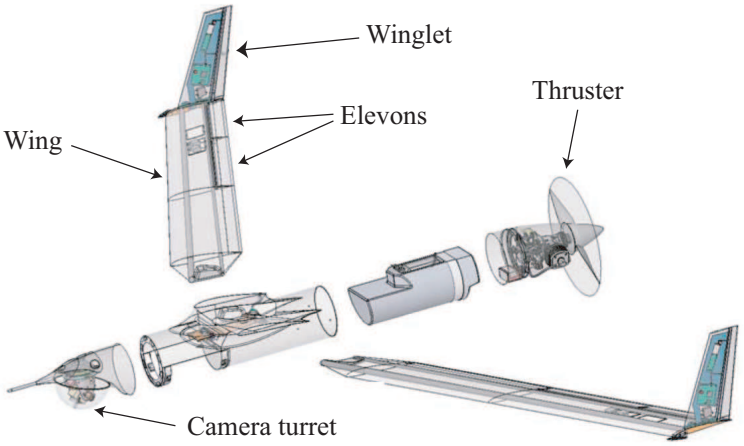

Figure 4.4: The SeaScan unmanned aerial vehicle is shown with its seven control surfaces (2 pair of inner and outer elevons, a pair of winglets, and thruster) and its camera turret (Courtesy of The Insitu Group).

4.3.4 Sensor Suite

The SeaScan is equipped with a digital color video camera with 25x zoom, 640x480 pixel sensor, and collecting 30 frames per second [56]. The video camera is attached to a turret gimbal, see Figures 4.4 and 4.5, and allows rotation in pan, $\lambda \in [0, 2\pi]$, tilt, $\mu \in \left[-\frac{\pi}{4}, \frac{\pi}{4}\right]$, and scan, $\nu \in [-0.12, +0.12]$ where all the units are in radians. Testing by The Insitu Group has shown that the camera is able to resolve objects such as small boats and logs from at least 8 kilometers away [59].

The object measurement uncertainty is a function light conditions, weather conditions, and distance. Although camera sensor uncertainty has been experimentally determined, it is not stated in this investigation due to International Traffic in Arms Regulations restrictions. In this study, the assumption is that measurements are independent of the distance to the object of interest, taken under ideal weather and lighting conditions, and have a standard deviation of ± 0.5 meter in the vertical and horizontal directions of the captured images.

Objects found in the images of the camera are described in a screen coordinate sys-

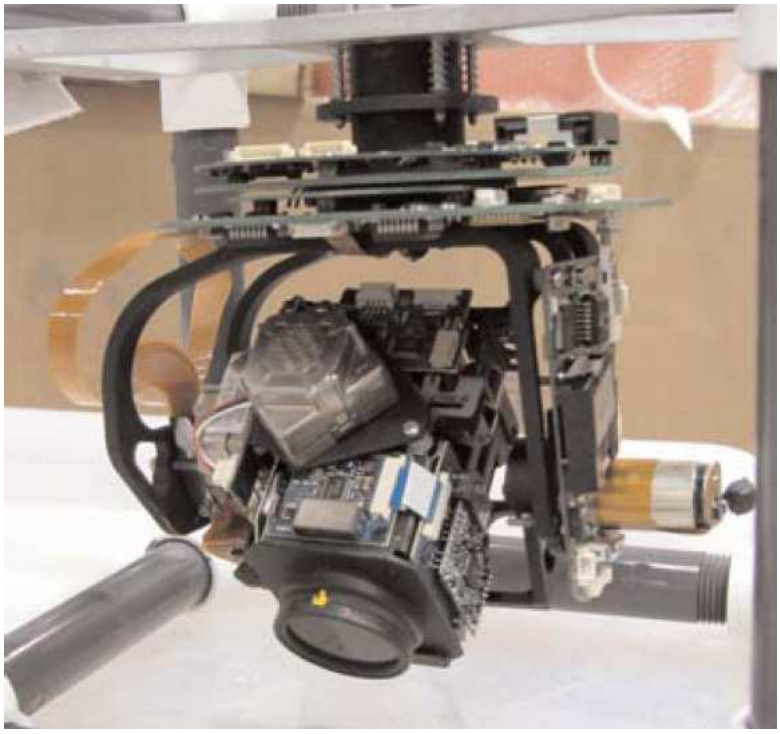

Figure 4.5: The SeaScan video digital camera and turret (Courtesy of The Insitu Group).

tem (SCR) fixed at the upper left hand side of the image where $(\cdot)^{SCR}$ denotes a vector in this coordinate system. To relate camera measurements, $\mathbf{y}^{SCR}$, must be converted to a camera-turret-centered coordinate system (CAM) to relate them to other state variables of the vehicles. The CAM coordinate system is centered on the camera's field of view and fixed to the camera with x-axis forward, y-axis right, z-axis down where $(\cdot)^{CAM}$ denotes a vector in CAM coordinates. The conversion from SCR to CAM is the following:

$$\mathbf{y}^{CAM} = \zeta \left[\mathbf{y}^{SCR} - \mathbf{C}^{SCR} \right], \tag{4.79}$$

where $\mathbf{C}^{SCR}$ is the location of the center of the screen axis in pixels and $\zeta = diag\left(\zeta_x, \zeta_y\right)$ is the pixel to length scaling factor matrix determined by the field of view angle,

$$\zeta_x = \frac{\tan\left(0.5\vartheta\right)}{P_{max_x}} \tag{4.80}$$

$$\zeta_y = \frac{\tan\left(0.5\vartheta\right)}{P_{max_y}}. \tag{4.81}$$

where υ is the field of view and P_{max_x}, P_{max_y} is the maximum pixels of the camera in the x and y directions [60].

The follower vehicle determines the leader's mode of operation by correlating camera measurements to expected behavior. Reconstructing the leader's state from camera measurements would be ideal, however it is an intractable problem due to observability. Instead, the follower uses a simplified model (lower order) to track the behavior of the vehicle. Since the camera is not able to accurately measure range, only the vertical and horizontal movements of the object of interest can be detected in the camera plane. Therefore, a simple kinematic model of the following form is used:

$$\mathbf{x}_{k+1}^{kin} = \mathbf{x}_k^{kin} + T \begin{bmatrix} V^{kin} \cos \psi^{kin} \\ V^{kin} \sin \psi^{kin} \\ \omega^{kin} \end{bmatrix} + \mathbf{w}_k^{kin}, \tag{4.82}$$

where $\mathbf{x}_k^{kin} = \begin{bmatrix} x_k^{kin} & y_k^{kin} & \psi_k^{kin} \end{bmatrix}^T$ and x_k^{kin} and y_k^{kin} are the position in the follower's camera plane (m), V^{kin} the speed (m/s), ψ^{kin} the heading (rad), ω^{kin} the heading rate of the vehicle (rad/sec), and $\mathbf{w}_k^{kin}$ is a zero mean process noise vector with covariance Q^{kin}. The output equations for the follower are:

$$\mathbf{y}_k^{SCR} = h\left(\mathbf{x}_k^{kin}\right) + \mathbf{v}_k^{kin}, \tag{4.83}$$

where $\mathbf{v}_k^{kin}$ is the measurement noise vector with covariance R^{kin}.

Although a video camera mounted on a UAV is used as the sensor to acquire information for mode detection, the formulation presented in [55] could be implemented with other sensor configurations or types of sensors. Instead of using one articulated video camera, the UAV could be equipped with an array of smaller, lighter, and cheaper cameras each aimed in different directions. Even though the camera array implementation would require sensor fusion, it would allow the reception of information from multiple vehicles, thus facilitating communication when more than two vehicles are present. A

Laser Imaging Detection and Raging (LIDAR) sensor could also be used. LIDAR sensors have been used in various applications that include seismology, forestry, and atmospheric physics. In autonomous navigation of uncertain environments, LIDAR sensors has been proven to be a robust solution and are experimentally tested in References [61] and [62]. A third option is to use to use passive devices such as infrared sensors (IRs) to reduce the chance of enemy detection. References [63] and [64] develop methods to acquire ship velocity information from IR sensors mounted on an autonomous flying vehicle.

4.3.5 Tracking and Estimation of the Mode Perturbation Signatures

It is important to show the proposed mode perturbation signatures can be tracked by the SeaScan and they do not compromise its ability to navigate. Figure 4.6 shows the trajectory of two SeaScan UAVS with and without a perturbation signatures in the pitch rate (ABC coordinates). In both trajectories, wind is modeled as a zero-mean Gaussian process noise with covariance $Q_{wind} = 0.1\ N/s^2$. As the figure shows, the perturbation signature does not significantly affect the trajectory of the vehicle. The normalized altitude plotted in Figure 4.7 shows that SeaScan tracking a perturbation signature has a larger peak-to-peak normalized altitude value compared to the other vehicle, but as expected the motion appears random.

Now consider how the follower estimates the trajectory of the leader using the lower order model in Equations (4.82) and (4.83). Since the simplified vehicle dynamics are nonlinear the sigma-point filter (SPF) is implemented. The estimator on the follower uses digital camera measurements with measurement noise covariance $R = diag\left(\left[0.1^2, 0.1^2\right]\right)$. Figure 4.8 shows the pitch rate of the leader SeaScan vehicle while tracking a perturbation signature in pitch rate.

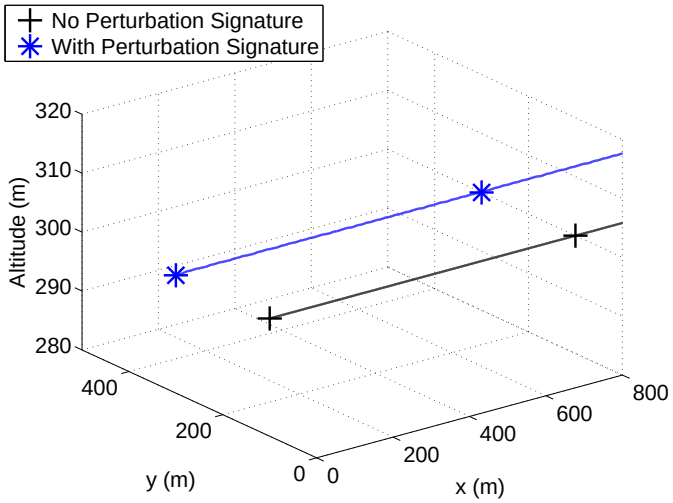

Figure 4.6: Two SeaScan vehicles travelling at a speed of 30 m/s and altitude of 100 m. One of the vehicles is tracking a perturbation signature while the other one is not in the pitch rate.

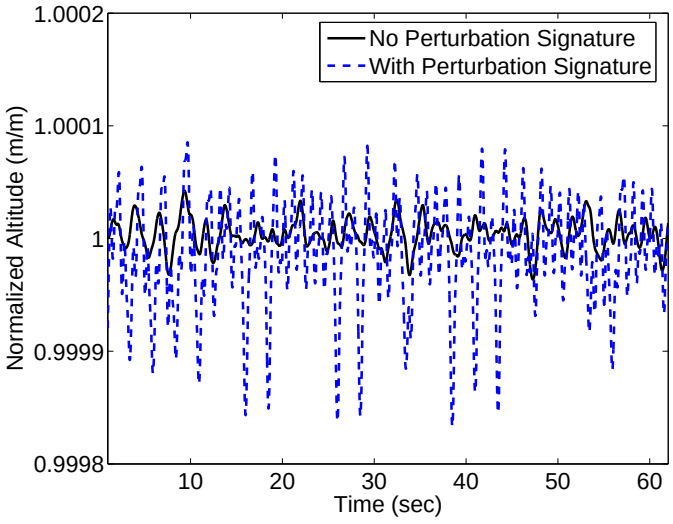

Figure 4.7: The normalized altitude (m/m) of two SeaScan vehicles traveling at a of 30 m/s and altitude of 100 m. The trajectory is shown with and without tracking a mode perturbation signature in the pitch rate.

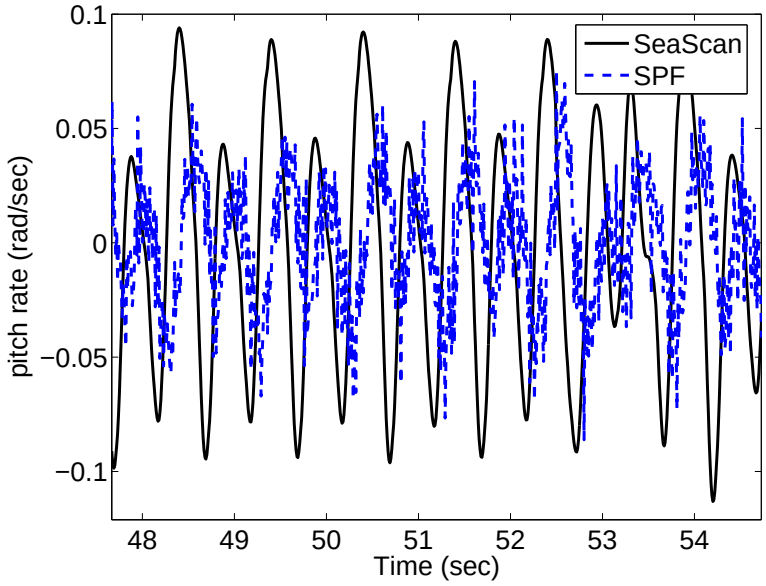

Figure 4.8: The pitch rate of the leader SeaScan vehicle while tracking a perturbation signature in pitch rate is shown. A nonlinear estimator on the follower uses digital camera measurements to estimate the signature using noisy data.

4.4 Mode Detection Methods

The purpose of assigning a unique signature to each of the modes q_i is to facilitate mode estimation. By knowing which mode a partner vehicle is operating, a higher quality of cooperation can be realized. Information in the form of encoded signatures is passed through the dynamics of the aircraft to be observed by a receiver vehicle. This process is shown in Figure 4.9. The trajectory of the leader which includes an embedded mode perturbation signature is measured by the follower using a digital camera. These noisy measurements along with the mode perturbation signature replicas are used to detect the leader's current mode. This mode estimate is then used to evaluate the mission cost, Section 4.2.1, and determine whether collecting information cooperatively would improve mission performance. In this section, the problem of transmitting a message through movements is considered from an estimation perspective. Estimation and detection theory are combined to derive an optimal mode detector as well as an approximation

that is more feasible for real-time implementation.

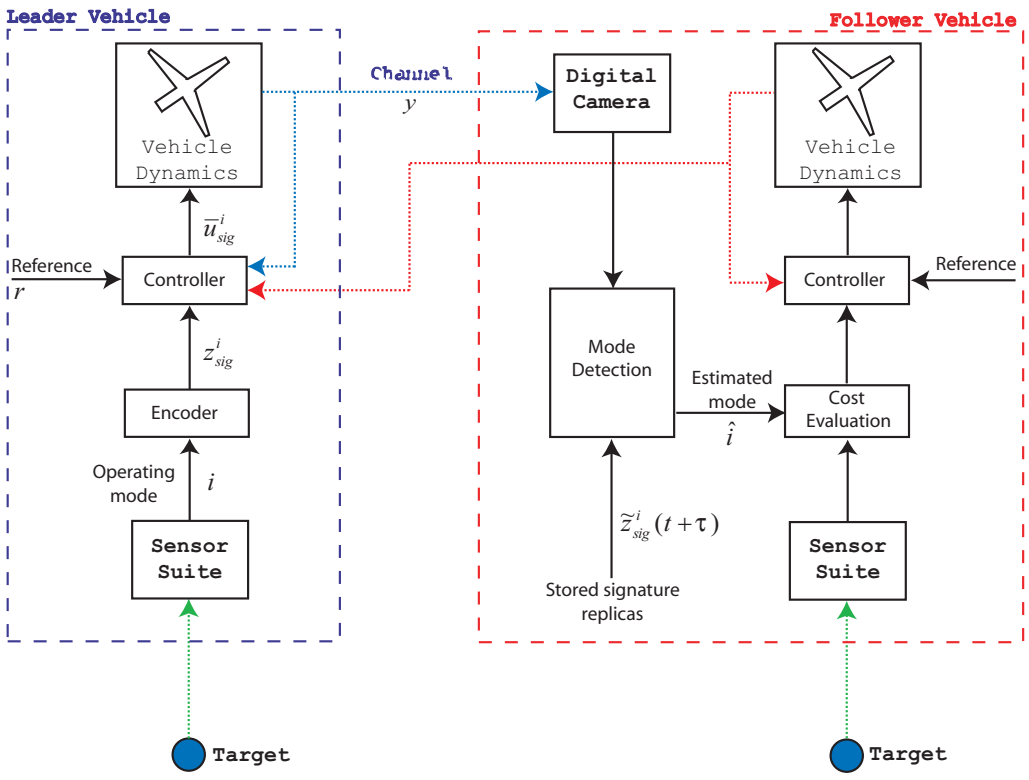

Figure 4.9: A block diagram of the leader/follower SeaScan configuration for cooperative reconnaissance in low communication environments.

4.4.1 The Locally Most Powerful Mode Detector

In this section, a summary of a locally most powerful (LMP) mode perturbation signature detector is presented. The detector consists on evaluation a test statistic as a function of the Kalman Filter (KF) innovations, denoted ν with covariance S, conditioned on hypotheses which are a function of the i^{th} mode, Gold Code phase τ, and carrier phase f_c.

In summary, the LMP test statistic is:

$$\hat{i},\hat{\tau},\hat{f}_c = \max_{i,\tau,f_c}\left\{ 2\cdot\left[\frac{1}{2}\sum_{j=0}^{k}\nu_j^T S_j^{-1}\nu_j\right]_{H_0} - \left[\frac{1}{2}\sum_{j=0}^{k}\nu_j^T S_j^{-1}\nu_j\right]_{H_{1,\cos}} - \left[\frac{1}{2}\sum_{j=0}^{k}\nu_j^T S_j^{-1}\nu_j\right]_{H_{1,\sin}}\right\}. \tag{4.84}$$

where for each i^{th} mode, τ Gold Code phase, and f_c carrier frequency, the locally most powerful detector requires the evaluation of:

1. A KF under hypothesis H_0 that assumes no perturbation signature is present.
2. A KF under the hypothesis, $H_{1,\cos}$, that there is a perturbation signature present, with an in-phase carrier, $\cos(\cdot)$, that has the form $t_z^r\left(z_{\cos}^{i,\tau,f_c}\right)$.
3. A KF under the hypothesis, $H_{1,\cos}$, that there is a perturbation signature present, with a quadrature carrier, $\sin(\cdot)$, that has the form $t_z^r\left(z_{\sin}^{i,\tau,f_c}\right)$.

The values of i, τ, and f_c which maximize the LMP test statistic, Equation (4.84), are declared under the LMP test as the detected parameters. As already mentioned a detailed derivation and explanation of the LMP detector is found in Chapter 3 of this dissertation.

4.4.2 Suboptimal Detector

Although the Neyman-Pearson Lemma guarantees the optimally of the LMP for linear systems [39], a suboptimal detector might be more feasible for real-time implementation by providing comparable performance with less computations. The suboptimal detector uses a model-based estimator to reconstruct, from noisy measurements, the full reference $\left(\bar{\mathbf{r}}^i = \mathbf{r} + a_{\text{sig}} t_z^r\left(z_{\text{sig}^i}\right)\right)$. The estimate is then correlated with replicas of the mode perturbation signatures, as a function of i, τ, f_c and f_d. If the total reference is a vector, then only the component in which the mode perturbation signature was embedded is correlated with the signature replica. This suboptimal method referred to in this

paper as the Suboptimal Cascading Approach (SCA), detects a particular mode based on correlation in contrast to the LMP which uses a test statistic as a function of the estimator's innovations.

Consider the linear discrete time system,

$$\mathbf{x}_{k+1} = A_k \mathbf{x}_k + B_u \mathbf{u}_k, \tag{4.85}$$

and the corresponding linear full state feedback controller, $\mathbf{u}_k^i = K\left(-\mathbf{x}_k + \overline{\mathbf{r}}_k^i\right)$. The variables $\mathbf{x}_k$ and $\overline{\mathbf{r}}_k^i$ are then stacked into a state vector yielding the following augmented state space model:

$$\begin{bmatrix} \mathbf{x}_{k+1} \\ \overline{\mathbf{r}}_{k+1}^i \end{bmatrix} = \begin{bmatrix} A_k - B_u K & B_u K \\ \mathbf{0} & \overline{A}_r \end{bmatrix} \begin{bmatrix} \mathbf{x}_k \\ \overline{\mathbf{r}}_k^i \end{bmatrix} + \overline{\mathbf{w}}_{\mathbf{k}}^{\mathbf{SCA}}, \tag{4.86}$$

where $\overline{\mathbf{w}}_k^{SCA} = \begin{bmatrix} \mathbf{w}_k^x & \mathbf{w}_k^{\overline{r},i} \end{bmatrix}^T$. The estimate of the total reference at time k is denoted as $\hat{\overline{\mathbf{r}}}_k^i$.

The test statistic for the SCA relies on calculating the correlation of one the components of the KF estimated total reference of the KF, $\hat{\overline{r}}^{i,j}$ and the mode perturbation signature. The term $\hat{\overline{r}}^{i,j}$ is defined to emphasize that if the total reference is a vector, only one of its components will be used in the test statistic. Define $\hat{\overline{\mathbf{r}}}^{i,j}$ as the stacked vector of n_m scalar $\hat{\overline{r}}^{i,j}$, or

$$\hat{\overline{\mathbf{r}}}^{i,j} = \begin{bmatrix} \hat{\overline{r}}_1^{i,j} \\ \hat{\overline{r}}_2^{i,j} \\ \vdots \\ \hat{\overline{r}}_{n_m}^{i,j} \end{bmatrix}. \tag{4.87}$$

Having calculated an estimate of the total reference, results for detection under carrier phase uncertainty or noncoherent detection are applied. The optimal noncoherent detector correlates a set of measurements with in-phase and quadrate Gold replicas [39], [40], [41]. For the SCA, the optimal noncoherent detector test statistic for the i^{th} mode replaces the measurements $\mathbf{y}_k$ with $\hat{\overline{\mathbf{r}}}^{i,j}$, and correlates them with the in-phase and quadra-

ture components of the perturbation signature replicas,

$$\lambda_{SCA} = \left(\left[\hat{\tilde{\mathbf{r}}}^{i,j} \right]^T P^{-1} \mathbf{z}_{\sin}^{i,\tau,f_c} \right)^2 + \left(\left[\hat{\tilde{\mathbf{r}}}^{i,j} \right]^T P^{-1} \mathbf{z}_{\cos}^{i,\tau,f_c} \right)^2. \tag{4.88}$$

In this application, the detector is used to optimize over the unknown i, τ, and f_c to find the optimal value of the SCA test statistic is then:

$$\hat{i}, \hat{\tau}, \hat{f}_c = \arg\max_{i,\tau,f_c} \lambda_{SCA}. \tag{4.89}$$

It should be noted that the SCA test statistic does not consider the optimality of the KF estimate.

A more detailed derivation of the SCA detector is found in Chapter 3 of this dissertation.

4.4.3 Real-Time Implementation on Nonlinear Systems

The motivation for the suboptimal detector is to reduce the complexity and the computational cost of the detector. The SCA simplifies the detector by relying on a lower order KF and relies on correlation calculations for detection. In general, the computational cost of the KF is approximately proportional to the cube of the larger dimension between the state vector or measurement vector, $\max(n_x, n_y)$[16]. Let n_{sig}, n_τ, and n_F denote the number mode signatures, mode signature phases, and sinusoid carrier frequency offsets that compose the detection search space. The LMP requires the KF to estimate an augmented vector, $\begin{bmatrix} \mathbf{x_k} & \mathbf{r_k} & a_{\text{sig}} \end{bmatrix}^T \in \mathbb{R}^{2n_x+1}$, which is composed of the state, reference, plus the mode signature amplitude. However, three KFs must be run for each condition in the search space. Therefore, the computational cost for the LMP is: $3n_{\text{sig}} \cdot n_\tau \cdot n_F \cdot (2n_x+1)^3$ which is roughly $n_{\text{sig}} \cdot n_\tau \cdot n_F \cdot n_x^3$. In contrast to the LMP, the SCA only requires one computation of the KF with an augmented state vector of dimension $\begin{bmatrix} \mathbf{x_k} & \mathbf{r_k} \end{bmatrix}^T \in \mathbb{R}^{2n_x}$ and $n_{\text{sig}} \cdot n_\tau \cdot n_F$ correlation computations. This analysis shows

that the computational cost reduction of the SCA is proportional to $n_{\text{sig}} \cdot n_{\tau} \cdot n_F$ and thus makes its implementation in real-time more feasible.

Monte Carlo simulations of linear and nonlinear systems in Chapter 3 showed that the detection performance of the SCA was comparable to the LMP. As described in Section 4.3.4, the output equations used by the follower for noisy camera measurements are nonlinear. Furthermore, it was observed that if the dependence of the SCA test statistic on the Gold Code phase can be removed by summing the energy detected at each Gold Code phase:

$$\overline{\lambda}_{SCA}^{i,f_c} = \max_{\tau} \sum_{\tau=0}^{N_\tau} \left[\left(\left[\hat{\tilde{\mathbf{r}}}^{i,j} \right]^T P^{-1} \mathbf{z}_{\text{sig}}^{\sin,\mathbf{i},\tau,\mathbf{f_c}} \right)^2 + \left(\left[\hat{\tilde{\mathbf{r}}}^{i,j} \right]^T P^{-1} \mathbf{z}_{\text{sig}}^{\cos,\mathbf{i},\tau,\mathbf{f_c}} \right)^2 \right], \tag{4.90}$$

the performance of the detector improves. The detector chooses the largest $\overline{\lambda}_{SCA}^{i,f_c}$ for all the i modes. However, another detector was studied, which chooses the mode perturbation signature corresponding to the largest correlation value for all mode signatures, Gold Code phases, and carrier frequencies, or:

$$\hat{i}, \hat{\tau}, \hat{f}_c = \arg\max_{\hat{i},\hat{\tau},\hat{f}_c} \lambda_{SCA}^{i,\tau,f_c}. \tag{4.91}$$

The detection is deemed correct if the detector chooses the correct mode perturbation even if the selected Gold Code phase is incorrect. For the nonlinear systems tested in Chapter 3 in which the estimation horizon is small (less than twice the period of the Gold Code) and the nominal reference was at least an order of magnitude less than the frequency of the mode perturbation, Equation (4.91) proved to perform better than $\overline{\lambda}_{SCA}^{i,f_c}$, Equation (4.90). As either the estimation horizon increases or the frequency of the reference increases the performance of both detectors become similar. It should be emphasized that reducing the estimation horizon is very important in this application as it is beneficial for the cost of the mission, Section 4.2.1, for the mode detection time to be as small as possible.

The modified SCA, Equation (4.91), is chosen as the preferred method for mode

detection for the SeaScan because: 1) it reduces the computational cost compared to the LMP, and 2) it provides acceptable detection performance for nonlinear systems.

4.5 Numerical Study

In this section the performance of two vehicles in terms of the cost functions described in Section 4.2.1 will be evaluated. Two vehicles are assigned the task of searching a grid of (4 x 2) target points. There are four obstacles or adversaries randomly distributed between each row of the grid. The leader and follower vehicles start their trajectories at $\mathbf{x}_0$ and $\mathbf{y}_0$ respectively. Each vehicle collects information about a target by circling it with radius R. The follower vehicle only flies to help the leader when the leader detects an adversary and the evaluated costs shows cooperation is beneficial.

In order to quantify the performance benefits of cooperation using mode perturbation signatures, two other communication scenarios are also considered. As a baseline, consider a fully decentralized vehicle strategy where each vehicle separately explores one side of the search area. In this scenario, there is no cooperation between the vehicles, thus no communication is required. Next consider a fully centralized solution where the leader has a continuous communication link to the follower. In this case, the follower will be receive immediate notification if the leader detects an enemy. This strategy reduces the total time required to complete the mission because of the improved utility through cooperation (Figure 4.2). Examples of trajectories for both decentralized and centralized strategies are shown in Figure 4.10. As shown in the figure, when the leader reaches its third target, the leader detects an adversary and communicates with the follower. The follower leaves its current target and circles the leader's third target. Once the information collected on the target is greater than the required threshold or a time limit has expired, the leader continues to its next target and the follower returns to its assigned targets.

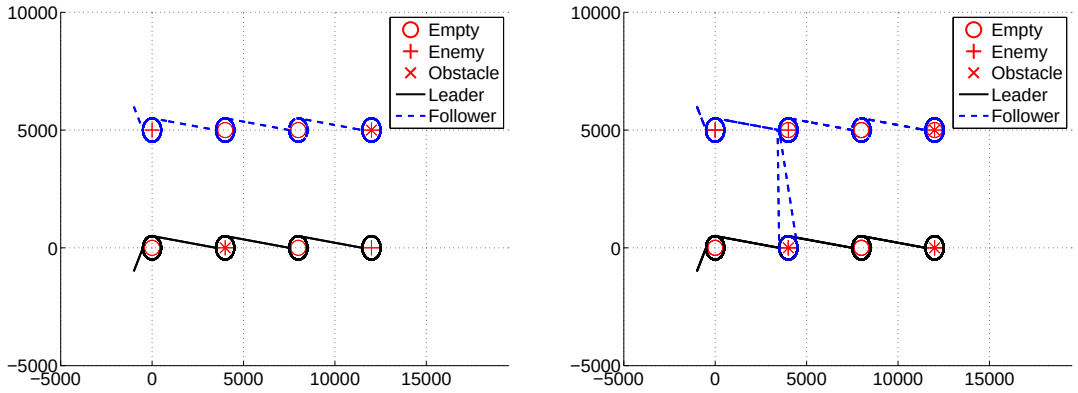

(a) Decentralized Strategy (no cooperation) (b) Centralized Strategy (cooperation)

Figure 4.10: Trajectories for the leader and follower with and without cooperation.

4.5.1 Estimator

The SCA mode detection algorithm proposed in Section 4.4.2 requires an estimator to reconstruct the state of the leader. The nonlinear model, Equation (4.82), based on camera measurements proposed in this investigation require the use of a nonlinear estimator. It is documented that the Sigma-point filter (SPF) in certain cases is better able to handle nonlinearities than the Extended Kalman Filter (EKF) [65, 66, 67]. It can be said that the EKF addresses nonlinearities with a first-order accuracy while the SPF achieves at least second-order accuracy [49]. Compared to the EKF, the SPF has similar computational complexity and does not require an analytic derivation of the Jacobian. For these reasons and for numerical stability, the square-root implementation of the SPF is chosen as the nonlinear estimator [47].

4.5.2 Discrete Modes

The mode perturbation signatures embedded in the trajectory of the leader are dependent on the target its encircling and are described by three operating modes: 1) sensing an empty target, 2) sensing an adversary in target, and 3) sensing a neutral target. These

Table 4.1: Operating modes and corresponding mode signatures.

Mode	Behavior	Signature
1	Empty	[11000010101110010110110000011011]
2	Enemy	[11001000010111011101110011101100]
3	Obstacle	[10101101101100101111011101010010]

modes are defined with the corresponding Gold Codes shown in Table 4.1.

4.5.3 Algorithm Implementation

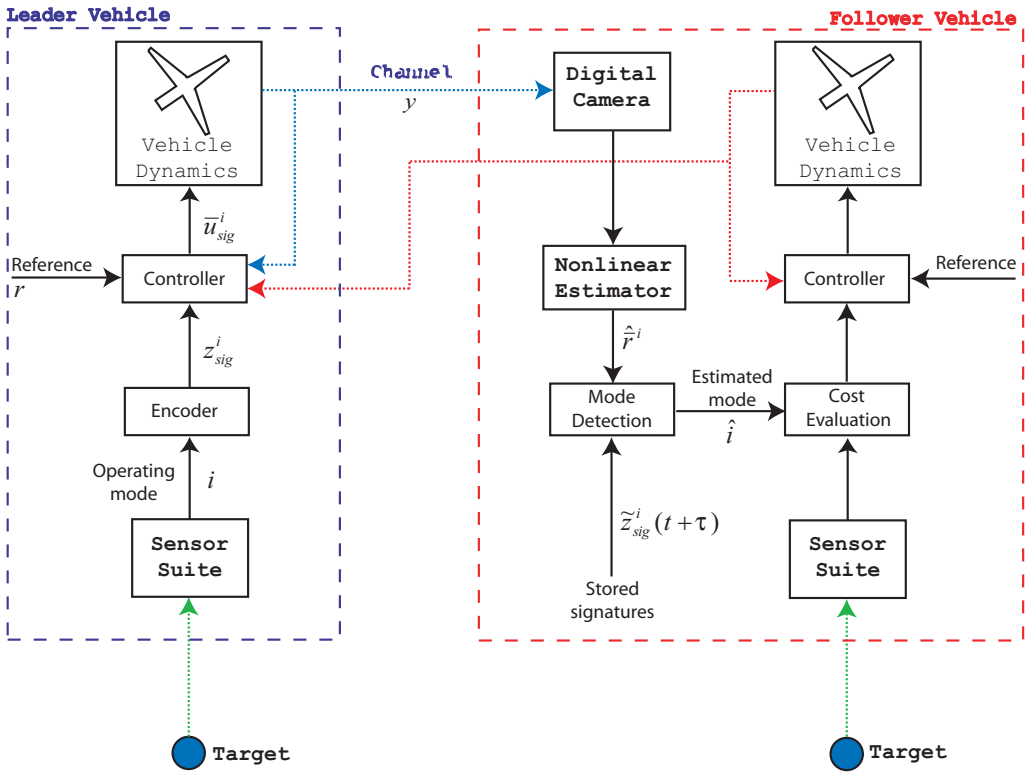

Figure 4.11: A block diagram of the leader/follower SeaScan configuration for cooperative reconnaissance in low communication environments.

The motivation for embedding mode perturbation signatures on the trajectory of an aircraft is to enable the exchange of low-level information in order to more efficiently gather information about an area. As shown in Figure 4.11, the first vehicle associates a target with one of the operating modes, i, listed in Table 4.1. The vehicle's encoder converts the sequence of bits into a continuous mode perturbation signature, $\mathbf{z}^i_{\text{sig}}$ that is sent to the controller. The controller then computes a control sequence, $\overline{\mathbf{u}}^{\mathbf{i}}_{\text{sig}}$, based on the reference $\mathbf{r}$, and the current state of the vehicle $\mathbf{y}$. Figure 4.12 shows the desired trajectory of the vehicle with the mode perturbation, $\bar{\mathbf{r}}^{\mathbf{i}}$, and the SeaScan response. Although tracking error with an LQR controller is not zero, the frequency content of the mode perturbation signature is preserved as at $t \approx 5$ a change of bit $(1 \rightarrow -1)$ occurs. The mode perturbation algorithm is robust to tracking error (which could be considered process noise) and it is not essential to eliminate the tracking error by the use of integrators or other control techniques. The movements of the first vehicle, $\mathbf{y}$, are then captured by the digital camera of the second vehicle as shown in Figure 4.13. Along with the low-order kinematic model, Equation (4.82), the SPF uses the camera measurements, $\mathbf{y}$, to estimate ω^{kin}, which is the signal that includes the perturbation signature. Figure 4.14 shows the pitch angular rate of the first vehicle and the SPF estimate. It is noted that the process noise covariance of the SPF requires tuning as the second vehicle's SPF uses a simpler model for estimation. The mode perturbation signature estimate, $\hat{\mathbf{r}}^{\mathbf{i}}_{\text{sig}}$, of the SPF is then used by the mode detection block to estimate the operating mode of the first vehicle.

A limitation on the performance of using mode perturbation signatures is the estimation horizon or detection time needed for the follower to detect information from the movements of the leader. As shown in Section 4.2.1, the detection time, t_{det}, is the main difference between a centralized system where the vehicles have direct communication and cooperation using mode perturbation signatures. As shown in Figure 4.10,

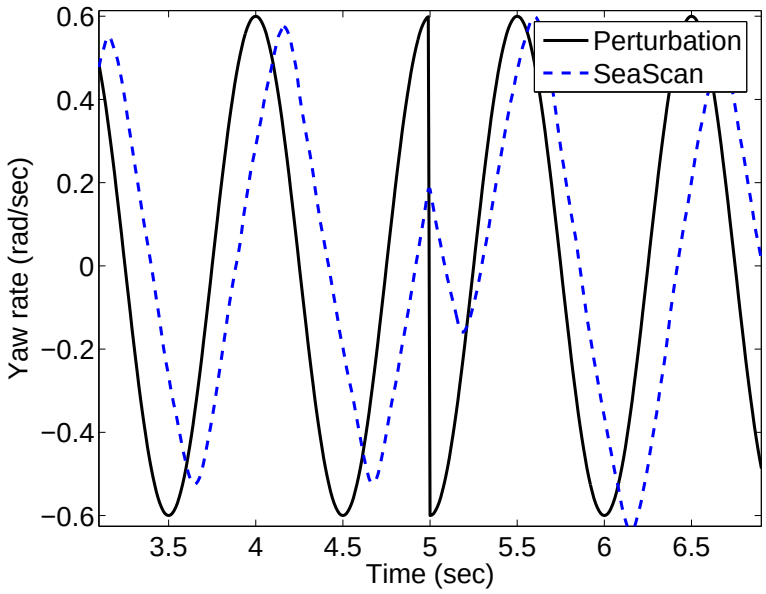

Figure 4.12: The desired trajectory of the vehicle with the mode perturbation, $\bar{\mathbf{r}}^{\mathbf{i}} = \mathbf{r} + \mathbf{r}^{\mathbf{i}}_{\text{sig}}$, and the SeaScan response.

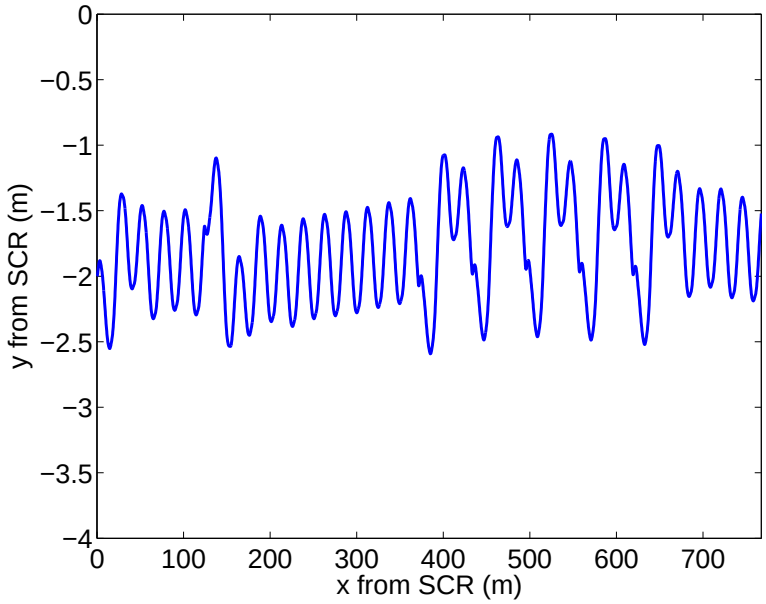

Figure 4.13: The movements of the first vehicle as seen by the digital camera of the second vehicle.

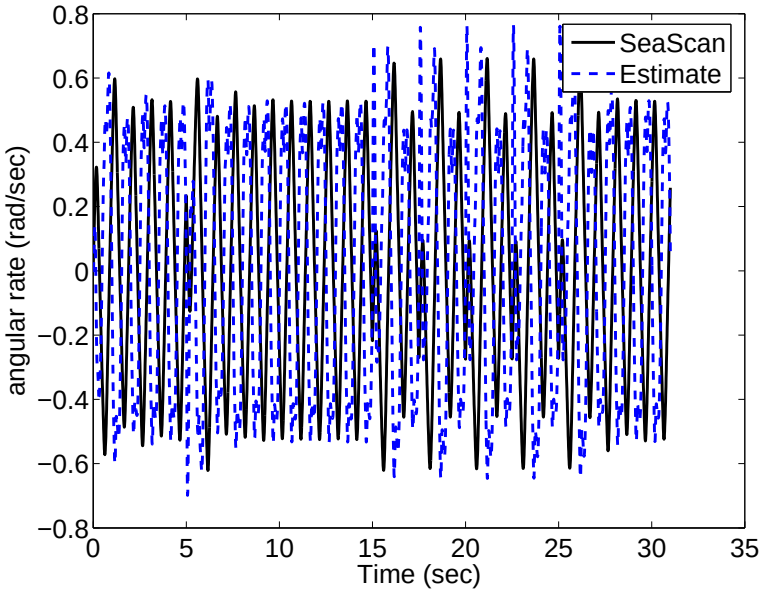

Figure 4.14: Comparison of the first vehicle's pitch angular rate and the SPF estimate.

the vehicles will fly in parallel collecting information about a (4x2) grid of targets. For this target configuration, the observability of the mode perturbation signatures is maximized by embedding the signatures in the leader's pitch rate (the response is similar to the one shown in Figure 4.14). The camera can only measure movements that have non-zero projections onto the camera plane. In other words, the distance to an object is an observable measurement for a digital camera. For implementation, it is necessary to determine what is the detection time and amplitude-to-noise ratio (ANR) needed to achieve an acceptable detection performance. The ANR is defined as:

$$\text{ANR} = \frac{a_{\text{sig}}^2}{2R_{\text{cam}}}, \tag{4.92}$$

where a_{sig} is the amplitude of the perturbation signature and $R_{\text{cam}} = 0.5^2$ is the noise covariance for the camera for both the horizontal and vertical directions. The performance of the detector was measured by calculating the percentage of times the correct mode was detected using Equation (4.91). Figure shows the detection percentage as a function of ANR in decibels and the estimation horizon or t_{det}. Since a detection percentage

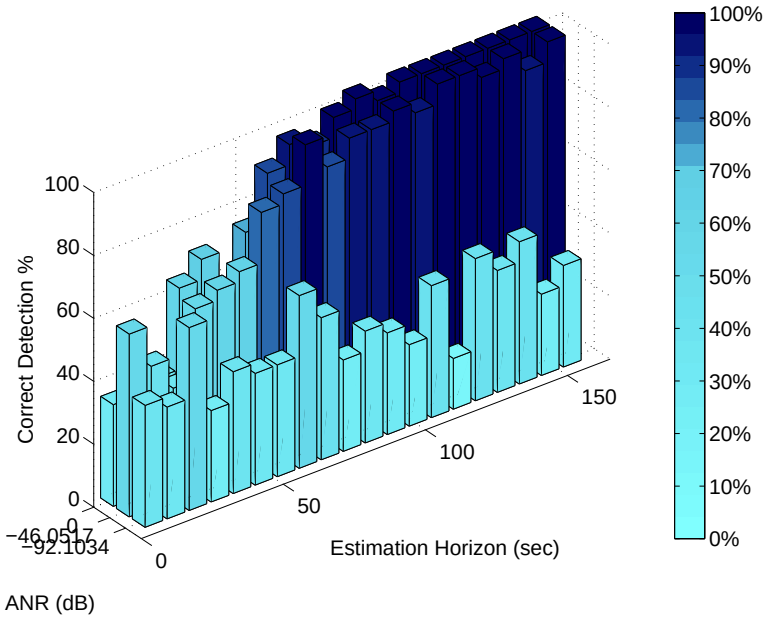

Figure 4.15: The correct detection percentage using the detector in Equation (4.91) for the SeaScan with the mode perturbation signature embedded in the rate of change of pitch. The vehicle is flying at an altitude around 300 meters and moving at a speed of 25 meters per second.

of above 95% is desired, a ANR of 0 (which corresponds to $a_{\text{sig}} = 1$) and an estimation horizon of $t_{\text{det}} = 75$ seconds were chosen. Although a shorter estimation horizon could have been chosen, $t_{\text{det}} = 75$ was selected in order for the detector to have greater robustness for unaccounted disturbances.

4.5.4 Monte Carlo Simulations

Monte Carlo simulations are used to gauge the performance of the vehicles in collecting information about the targets. The mission performance was measured based on minimizing mission time (Section 4.2.2) or maximizing information (Section 4.2.3). The centralized, decentralized, and mode perturbation signature communication scenarios were also tested. Each scenario was simulated 50 times in order to compute

Table 4.2: Simulation parameters for the Monte Carlo runs.

Parameter	Value
a_{sig}	1.00 meter
t_{det}	75 seconds
ω	$\frac{1}{2\pi}$ rad/sec
v_{AUV}	30 meters per second
R	500 meters
M	4
N	3
Q_{SPF}	diag(0.01^2,0.01^2,0.01^2,0.01^2,0.01^2,0.01^2)
R_{SPF}	diag(0.1^2,0.05^2)
λ	10^{-3}
λ^c	1.73×10^{-3}
$\zeta_x = \zeta_y$	1.0
I_{empty}	70
I_{enemy}	70
I_{obstacle}	70
T_{max}	9000 seconds

significant statistics. The simulation parameters used in the simulations are shown in Table 4.2 where depending on whether the target is identified as empty, an adversary, or an obstacle, different thresholds of information must be collected: I_{empty}, I_{enemy}, I_{obstacle} respectively. In the scenario in which information is maximized, the time constraint is T_{max}. The speed at which the UAV travels, v_{AUV}, is constant throughout the simulation.

Table 4.3 compares the decentralized and the average mission time results (Section 4.2.2) for the mode perturbation strategies for the 25 cases, where the results are normalized by the minimum time (with full communication) required by the best decentralized strategy. Also shown is the 95% confidence boundary. As shown in Table 4.3, the mode estimation strategy performs better than the centralized strategy.

Table 4.4 compares the decentralized and the average information collected (Section 4.2.3) for the mode perturbation strategies for the Monte Carlo simulations, where the results are normalized by the maximum information (with full communication) col-

Table 4.3: Normalized time average results.

Strategy	Average Normalized Time	Communication
Decentralized	1.00 $\pm$0.01	None
Centralized	0.86 $\pm$0.01	Full
Mode Signature	0.88 $\pm$0.01	None

Table 4.4: Normalized average information results.

Strategy	Average Normalized Information	Communication
Decentralized	0.96 $\pm$0.01	None
Centralized	1.00 $\pm$0.01	Full
Mode Signature	0.99 $\pm$0.01	None

lected by the best centralized strategy. The 95% confidence boundary is also shown. The simulation results presented in Table 4.4 show that the mode perturbation strategy performs better than the decentralized strategy.

The performance results for this example (Tables 4.3 and 4.4) show that implementing mode perturbation signatures allow the vehicles to approach the performance of a centralized strategy without the use of direct communication (as in the decentralized strategy). The performance of the mode perturbation signature strategy is limited by various variables that include the distance between the leader and follower targets, and the information collection curves for the vehicles. These variables determine whether cooperation significantly improves performance. However, the simulations show that in certain cases mode perturbation signatures can effectively be used to transfer information between vehicles, thus enabling cooperation without the need of direct communication.

4.6 Summary and Conclusion

A strategy using hybrid mode estimation has been developed and integrated into a UAV leader/follower cooperative reconnaissance problem in order to minimize communication between vehicles. The behavior of the leader was modelled as a hybrid system. Each node of the hybrid system was defined by the vehicle's dynamics as well as a mode perturbation signature. Truth-model simulations showed that the SeaScan's performance is not significantly affected by the addition of mode perturbation signatures. The cooperative performance of the system was defined by one of two metrics: 1) the length of time required by the two vehicles to collect a level of information, and 2) the total information collected in a fixed time interval. As the follower traverses the target random environment, it evaluates a performance metric to decide whether cooperation is beneficial. The results of Monte Carlo simulations showed that the performance of the system was better than the performance of a decentralized system with no cooperation, where both cases (time or information) required no communication. Although the necessary detection time makes exchanging target information slower than direct radio communication, most of the benefits of cooperation are recovered. The performance in terms of the time and information metrics of the system that cooperated using mode perturbation is close to the performance of the system with full communication.

APPENDIX A

PROOFS FOR CHAPTER 2

Showing that the state ellipsoid and the estimation error are bounded follows from nonlinear observability. This derivation is similar to stability analysis of the EKF in Ref. [68] and the error dynamics analysis in Ref. [69]. Consider the nonlinear systems of Equations (2.1-2.2), the following two definitions are made.

Definition 1 *The nonlinear observability test is satisfied if the following matrix has rank n:*

$$O\left(\overline{\mathbf{x}}_{(\cdot),\mathbf{k}}\right) = \begin{pmatrix} \frac{\partial h}{\partial \mathbf{x}}\left(\overline{\mathbf{x}}_{(\cdot),\mathbf{k}}\right) \\ \frac{\partial h}{\partial \mathbf{x}}\left(\overline{\mathbf{x}}_{(\cdot),\mathbf{k+1}}\right)\frac{\partial f}{\partial \mathbf{x}}\left(\overline{\mathbf{x}}_{(\cdot),\mathbf{k}}\right) \\ \vdots \\ \frac{\partial h}{\partial \mathbf{x}}\left(\overline{\mathbf{x}}_{(\cdot),\mathbf{k+n-1}}\right)\frac{\partial f}{\partial \mathbf{x}}\left(\overline{\mathbf{x}}_{(\cdot),\mathbf{k+n-2}}\right)\cdots\frac{\partial f}{\partial \mathbf{x}}\left(\overline{\mathbf{x}}_{(\cdot),\mathbf{k}}\right) \end{pmatrix}, \tag{A.1}$$

where $\overline{\mathbf{x}}_{(\cdot),\mathbf{k}} \in \overline{\mathbf{x}}_{\mathbf{i},\mathbf{k}}$, $\mathbf{i} \in [1,\ldots,N]$ *can take on values of any of the operating points.*

Lemma 1 *If the nonlinear system, Equations (2.1-2.2), satisfies nonlinear observability on a compact subset* $\mathbb{K} \subset \mathbb{R}^n$, *then* $\exists\ \underline{m}$, $\overline{m}$, $0 < \underline{m} \leq \overline{m} < \infty$ *and* $\mu_1 > 0$ *such that,* $\underline{m} \cdot I \leq O\left(\overline{\mathbf{x}}_{(\cdot),\mathbf{k}}\right)^T O\left(\overline{\mathbf{x}}_{(\cdot),\mathbf{k}}\right) \leq \overline{m} \cdot I$, *for all* μ_1 *such that* $\|\mathbf{x_k} - \overline{\mathbf{x}}_{(\cdot),\mathbf{k}}\| \leq \mu_1$.

Proof 1 *See Ref. [70].*

Definition 2 *For the nonlinear system, Equations (2.1-2.2), the observability Grammian is defined as*

$$M_{k+q,k} = \sum_{j=k}^{k+q} \Phi_{j,k}^T C_j C_j^T \Phi_{j,k} \tag{A.2}$$

where $\Phi_{j,k} = \Pi_{q=j-1}^{k} A_q$ *and* $\Phi_{k,k} = I$ *and* $A_q = \frac{\partial f}{\partial \mathbf{x}}\left(\overline{\mathbf{x}}_{\mathbf{i},\mathbf{q}}\right)$ *and* $C_q = \frac{\partial h}{\partial \mathbf{x}}\left(\overline{\mathbf{x}}_{\mathbf{i},\mathbf{q}}\right)$. *Then the pair* (A_k, C_k) *is uniformly observable if there exists* $\underline{m}$ *and* $\overline{m} > 0$ *such that* $\underline{m} \cdot I \leq M_{k+i,k} \leq \overline{m} \cdot I$ *[69].*

Lemma 2 *Consider the nonlinear system, Equations (2.1-2.2), without process noise. Let* $\mathbb{K}$ *be a compact subset of* $\mathbb{R}^n$ *and assume the nonlinear system is observable in the nonlinear sense* $\forall \mathbf{x_k} \in \mathbb{K}$. *Then* $\exists \mu_2 > 0$ *such that*

$$A_k = \frac{\partial f}{\partial \mathbf{x}}(\hat{\mathbf{x}}_\mathbf{k}), \;\; C_k = \frac{\partial h}{\partial \mathbf{x}}(\hat{\mathbf{x}}_\mathbf{k}) \tag{A.3}$$

satisfy the uniform observability test if $\|\mathbf{x_k} - \hat{\mathbf{x}}_\mathbf{k}\| \leq \mu_2$.

Proof 2 *See Reference [70].*

When *noise* is present (as it is in the switched estimator case since the combined noise terms, $\hat{\mathbf{w}}_\mathbf{k}$, $\hat{\mathbf{v}}_\mathbf{k}$, must be used) Lemma 2 holds if the combined process noise is small enough. If $\|\bar{\mathbf{x}}_\mathbf{k} - \mathbf{x_k}\| \leq \mu_w$ and $\mu_w > 0$, where $\bar{\mathbf{x}}_\mathbf{k}$ is the solution for the system without the combined process noise, then the following must be satisfied: $\|\mathbf{x_k} - \hat{\mathbf{x}}_\mathbf{k}\| \leq \|\mathbf{x_k} - \bar{\mathbf{x}}_\mathbf{k}\| + \|\bar{\mathbf{x}}_\mathbf{k} - \hat{\mathbf{x}}_\mathbf{k}\|$ [69].

Theorem 1 *When*

1. $q \leq \|Q_k\|$, $\underline{r} \leq \|R_k\|$
2. *the pair* (A_k, C_k) *is uniformly observable*
3. Σ_0 *is a positive definite matrix*

then there are real numbers $\bar{s}$ *and* $\underline{s}$ *such that,* $\underline{s} \cdot I \leq \Sigma_k \leq \bar{s} \cdot I$, *for all* $k \geq 0$.

Proof 3 *See Reference [71].*

Hence, the state ellipsoid $\Sigma\left(\hat{\mathbf{x}}_\mathbf{k}, \Sigma_{k,k}\right)$ is bounded if the nonlinear observability condition is satisfied for all (combinations of) operating points. Under the assumptions of the existence of a bound on the process and measurement noise ellipsoids, it can be shown that the nonlinear switched SMF gives an ellipsoidal estimate where the error dynamics are bounded [69].

APPENDIX B

NOMENCLATURE FOR CHAPTER 3

i	Operating mode
z^i_{sig}	i^{th} mode perturbation signature
$\mathbf{r}^i_{\text{sig}}$	Vehicle perturbed reference
$\mathbf{r}$	Nominal vehicle reference
$\overline{\mathbf{r}}^i$	Total vehicle reference, $\mathbf{r} + a_{\text{sig}} t_z^r \left(z^i_{\text{sig}} \right)$
$\overline{\mathbf{u}}^i_{\text{sig}}$	Perturbed control input
$\overline{\mathbf{y}}$	First vehicle's output
$\mathbf{y}$	Second vehicle's sensor measurements of the first vehicle
$\tilde{z}^{i,\tau,f_c}_{\text{sig}}$	Store mode perturbation signature replicas as function of τ and f_c
m_ρ	Number of points in the rectangular pulses, ρ^0 or ρ^1
T_c	Chip duration
ρ^0	0 (*off*) bit
ρ^1	1 (*on*) bit
n_ρ	Number of nonoverlapping rectangular chips in the p^i sequence
p^i	Sequence of nonoverlapping rectangular pulses for the i^{th} mode perturbation signature
f_c	Carrier frequency, Hz
θ	Carrier phase in radians
N	Number of operating modes
a_{sig}	Amplitude of the mode perturbation signature
$\hat{(\cdot)}$	Estimate of $(\cdot)$
$S(\cdot)$	Continuous time correlation function

τ_d	Time delay, seconds
$\hat{z}^i_{\text{sig}}$	Estimate of the i^{th} mode perturbation signature
e	Estimation error
τ	Sequence time offset expressed as number of bits
Γ	Range of time over which sequence time offsets are tested
τ_m	Sequence time offset in seconds
f_d	Carrier frequency offset
k	Discrete time index
$t^r_z(\cdot)$	Mapping from the scalar signature to the reference
q_i	Node in the hybrid automaton corresponding to the i^{th} mode
$\mathbf{x}_k$	State vector of the system at time k
n_x	Dimension of $\mathbf{x}_k$
n_y	Dimension of $\mathbf{y}_k$
n_u	Dimension of the $\mathbf{u}_k$
$\mathbf{w}_k$	Zero-mean Gaussian process noise with covariance Q_k
$\mathbf{v}_k$	Zero-mean Gaussian measurement noise with covariance R_k
H_0	Hypothesis that the signal (mode perturbation signature) is absent or $a_{\text{sig}} = 0$
n_m	Number of measurements used for detection
H_1	Hypothesis that the signal (mode perturbation signature) was present
$\mathbf{z}^{i,\tau,\theta,f_c}_{\text{sig}}$	Stacked vector of the scalar mode perturbation signatures, $z^{i,\tau,\theta,f_c}_{\text{sig}}$
$p(\mathbf{y}\|H_0)$	Measurement probability density function, or likelihood, under hypothesis H_0
$p(\mathbf{y}\|H_1)$	Measurement probability density function, or likelihood, under hypothesis H_1

λ_{thresh}	Threshold to accept hypothesis H_1
LMP	Locally most powerful test
$z_{\cos,k}^{i,\tau,f_c}$	Mode perturbation signature with an in-phase carrier (cos) as function of i, τ, and f_c
$z_{\sin,k}^{i,\tau,f_c}$	Mode perturbation signature with a quadrature carrier (sin) as function of i, τ, and f_c
$\overline{\lambda}_{\text{LMP}}(\mathbf{y})$	Test statistic for the LMP derived around $a_{\text{sig}} = 0$
$H_{1,\cos}$	Hypothesis that the signal with an in-phase (cos) mode perturbation signature was present
$p(\mathbf{y}\|H_{1,\cos})$	Measurement probability density function, or likelihood, under hypothesis $H_{1,\cos}$
$H_{1,\sin}$	Hypothesis that the signal with a quadrature (sin) mode perturbation signature was present
$p(\mathbf{y}\|H_{1,\sin})$	Measurement probability density function, or likelihood, under hypothesis $H_{1,\sin}$
K	Full-state feedback control gain
Y^k	Sequence of measurements from $[1,\ldots,k]$
KF	Kalman Filter
ν_{k+1}	KF innovation at time $k+1$
$\mathcal{L}^{KF}(\cdot)$	Log likelihood function of the KF
SCA	Suboptimal Cascading Approach
$\overline{r}^{i,j}$	Component of the total reference, $\hat{\overline{\mathbf{r}}}^i$, that is used to compute the SCA test statistic
λ_{SCA}	Test statistic for the SCA
a_r	Sinusoid amplitude of the reference

f_r	Sinusoid reference frequency in Hz
$\hat{\bar{\mathbf{r}}}_k^i$	Estimate of the total reference, $\bar{\mathbf{r}}^i$
SPF	Sigma Point Filter
β_{cos}	Correlation of the measurements and the in-phase component of the carrier
β_{sin}	Correlation of the measurements and the quadrature component of the carrier

APPENDIX C

STATISTICS OF THE SIMULATION RESULTS FOR CHAPTER 3

The simulation results in Chapter 3 calculated the percentage of times the algorithm was able to detect the correct mode perturbation signature parameters. The results presented in the form of bar graphs in Chapter 3 showed the average correct detection performance. In this appendix, standard deviation of the simulation results are presented. In the figures the results are also presented as bar graphs. However, the average correct detection performance percentage corresponds to the middle of the bar while the lower and upper values correspond to the average correct detection performance percentage plus and minus one standard deviation respectively.

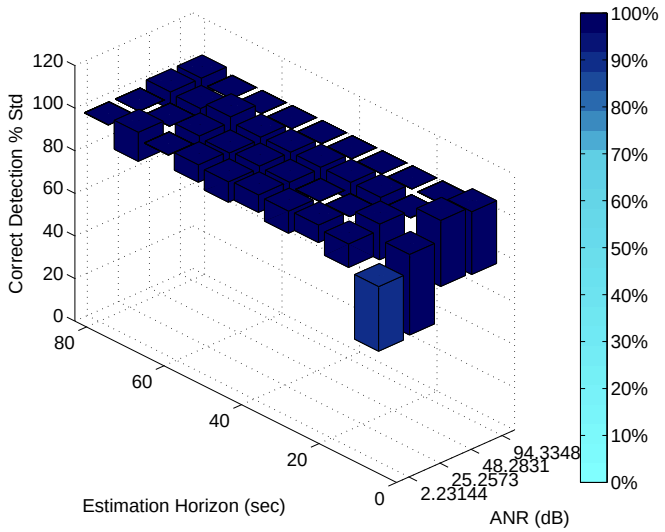

Figure C.1: The correct mode detection percentage shown with error bars for the LMP detector, Equation (3.109), with a mode perturbation signature amplitude of $a_{\text{sig}} = 0.5$ tracking a reference with frequency of 0.01 Hz. The results correspond to the bar graph in Figure 3.15.

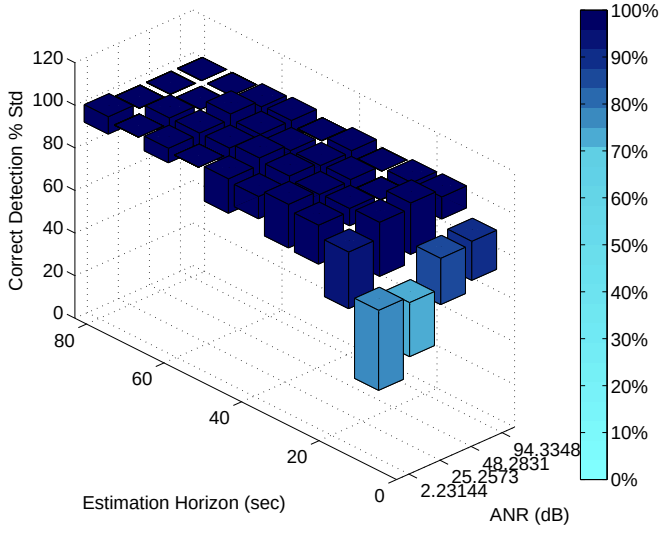

Figure C.2: The correct mode detection percentage shown with error bars for the LMP detector, Equation (3.109), with a mode perturbation signature amplitude of $a_{\text{sig}} = 0.5$ tracking a reference with frequency of 0.10 Hz. The results correspond to the bar graph in Figure 3.16.

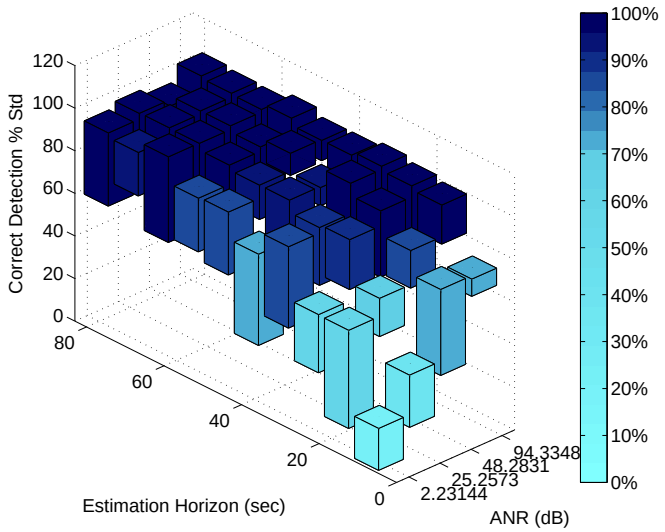

Figure C.3: The correct mode detection percentage shown with error bars for the LMP detector, Equation (3.109), with a mode perturbation signature amplitude of $a_{\text{sig}} = 0.5$ tracking a reference with frequency of 1.00 Hz. The results correspond to the bar graph in Figure 3.17.

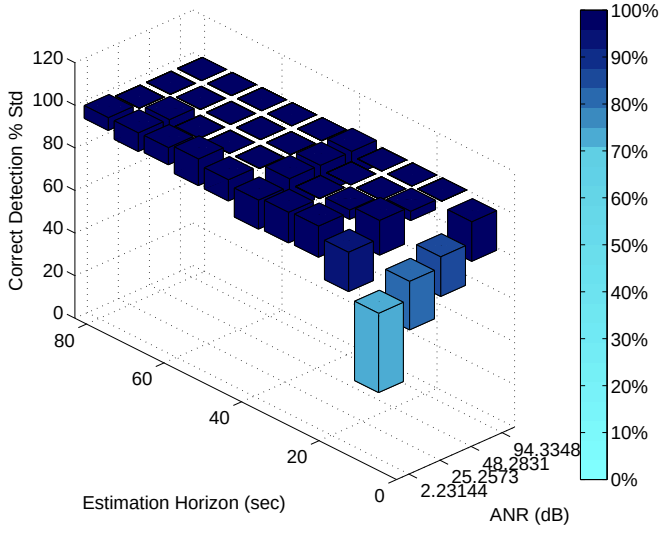

Figure C.4: The correct mode detection percentage shown with error bars for the SCA detector, Equation (3.113), with a mode perturbation signature amplitude of $a_{\text{sig}} = 0.5$ tracking a reference with frequency of 0.01 Hz. The results correspond to the bar graph in Figure 3.18.

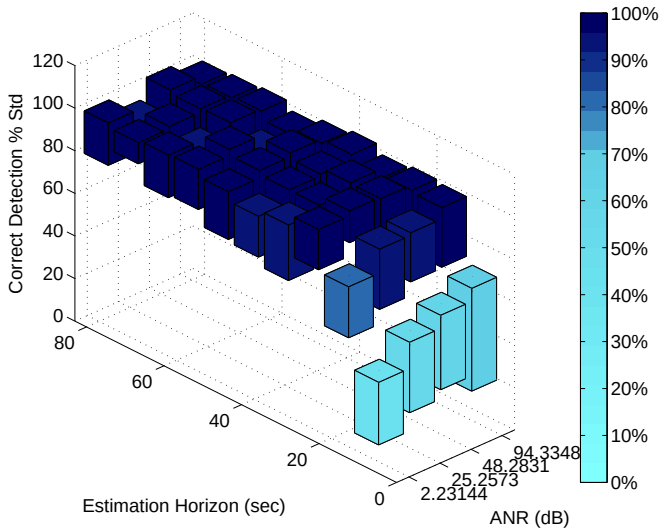

Figure C.5: The correct mode detection percentage shown with error bars for the SCA detector, Equation (3.113), with a mode perturbation signature amplitude of $a_{\text{sig}} = 0.5$ tracking a reference with frequency of 0.10 Hz. The results correspond to the bar graph in Figure 3.19.

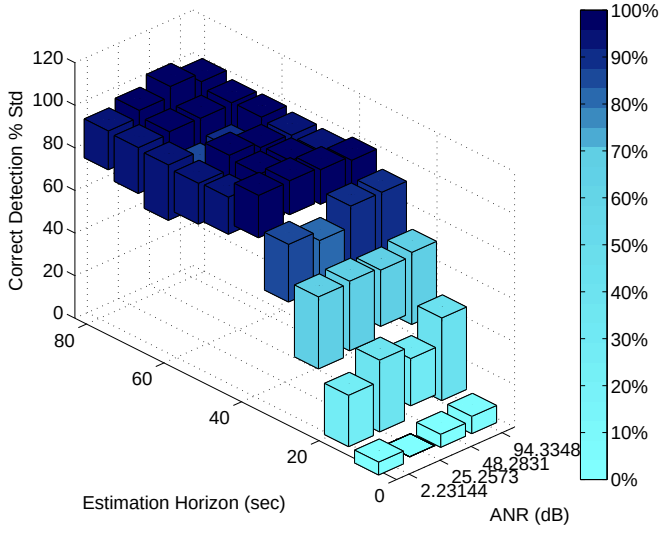

Figure C.6: The correct mode detection percentage shown with error bars for the SCA detector, Equation (3.113), with a mode perturbation signature amplitude of $a_{\text{sig}} = 0.5$ tracking a reference with frequency of 1.00 Hz. The results correspond to the bar graph in Figure 3.20.

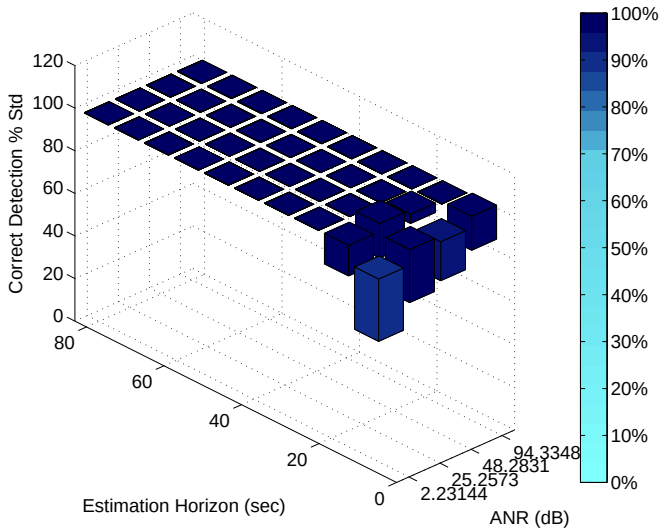

Figure C.7: The correct mode detection percentage shown with error bars for the modified SCA test statistic, Equation (3.160), with a mode perturbation signature amplitude of $a_{\text{sig}} = 0.5$ tracking a reference with frequency of 0.01 Hz. The results correspond to the bar graph in Figure 3.22.

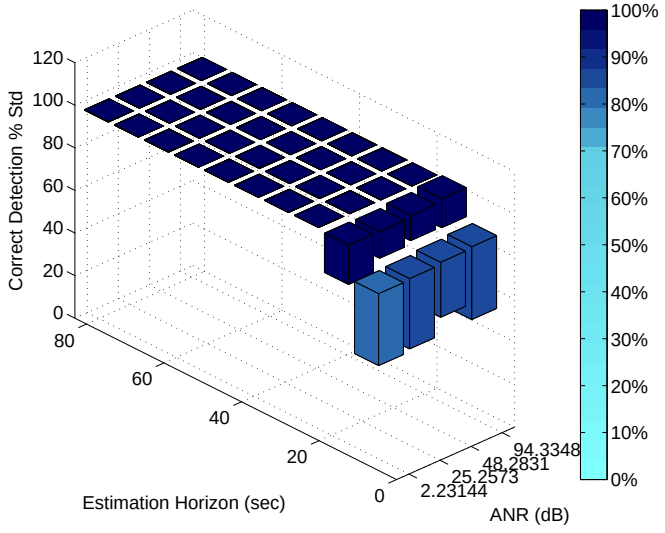

Figure C.8: The correct mode detection percentage shown with error bars for the modified SCA test statistic, Equation (3.160), with a mode perturbation signature amplitude of $a_{\text{sig}} = 0.5$ tracking a reference with frequency of 0.10 Hz. The results correspond to the bar graph in Figure 3.23.

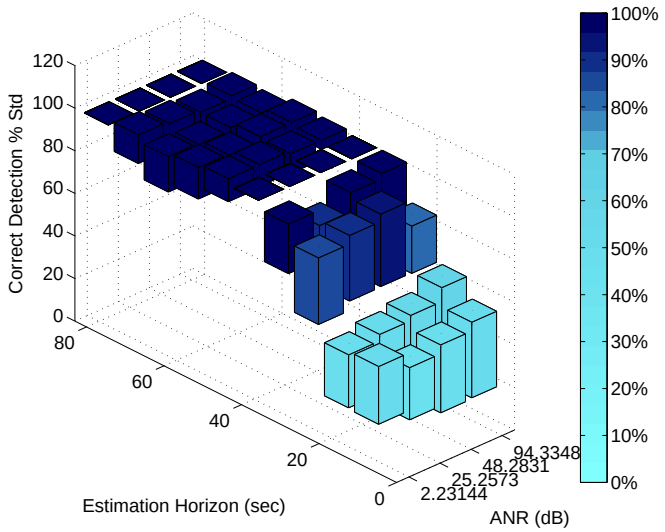

Figure C.9: The correct mode detection percentage shown with error bars for the modified SCA test statistic, Equation (3.160), with a mode perturbation signature amplitude of $a_{\text{sig}} = 0.5$ tracking a reference with frequency of 1.00 Hz. The results correspond to the bar graph in Figure 3.24.

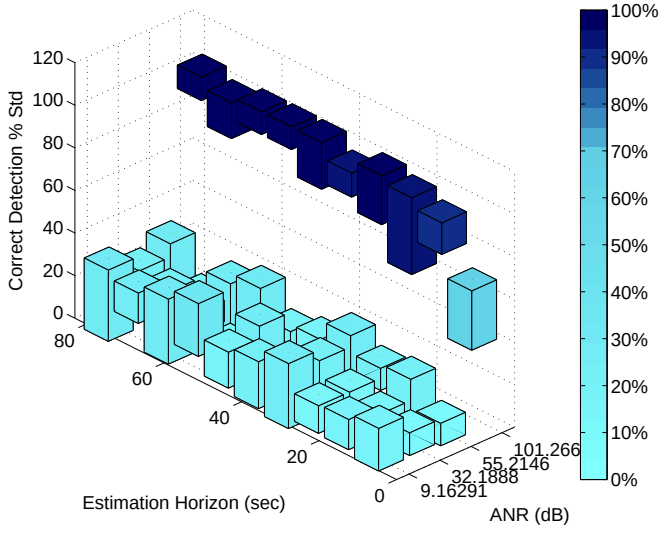

Figure C.10: The correct mode detection percentage shown with error bars for the LMP detector for the nonlinear simulation example with a mode perturbation signature amplitude of $a_{\text{sig}} = 0.5$ tracking a reference with frequency of 0.01 Hz. The results correspond to the bar graph in Figure 3.27.

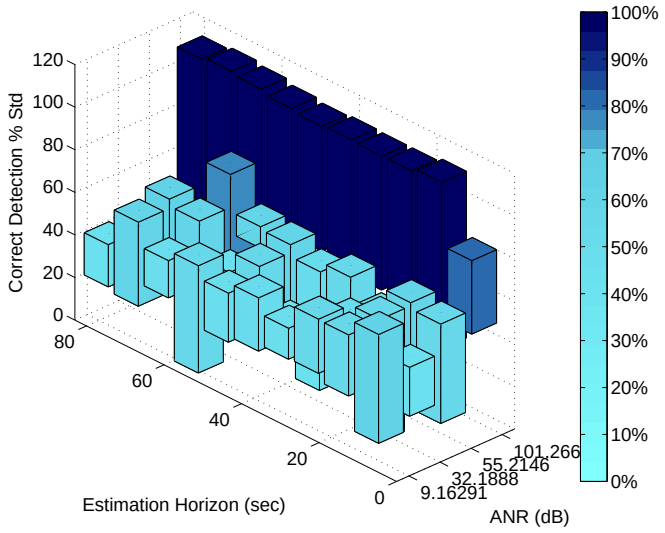

Figure C.11: The correct mode detection percentage shown with error bars for the modified LMP detector, Equation (3.177), for the nonlinear simulation example with a mode perturbation signature amplitude of $a_{\text{sig}} = 0.5$ tracking a reference with frequency of 0.01 Hz. The results correspond to the bar graph in Figure 3.29.

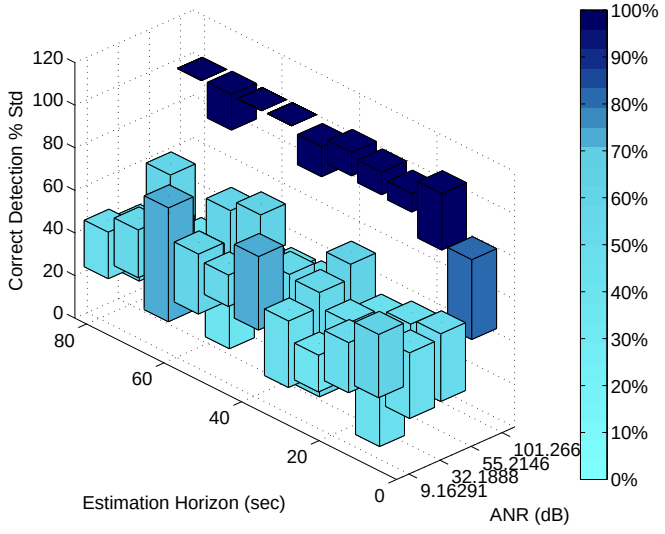

Figure C.12: The correct mode detection percentage shown with error bars for the modified LMP detector based on only estimating i, Equation (3.178), for the nonlinear simulation example with a mode perturbation signature amplitude of $a_{\text{sig}} = 0.5$ tracking a reference with frequency of 0.01 Hz. The results correspond to the bar graph in Figure 3.30.

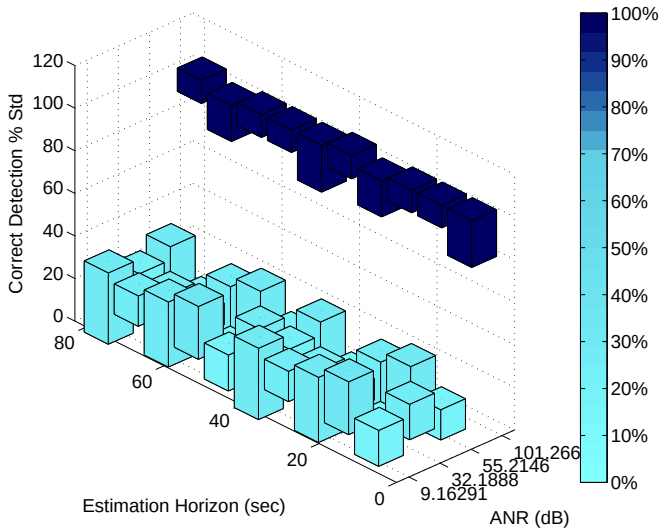

Figure C.13: The correct mode detection percentage shown with error bars for the LMP test statistic for the nonlinear simulation example with a mode perturbation signature amplitude of $a_{\text{sig}} = 0.5$ tracking a reference with frequency of 0.10 Hz. The results correspond to the bar graph in Figure 3.31.

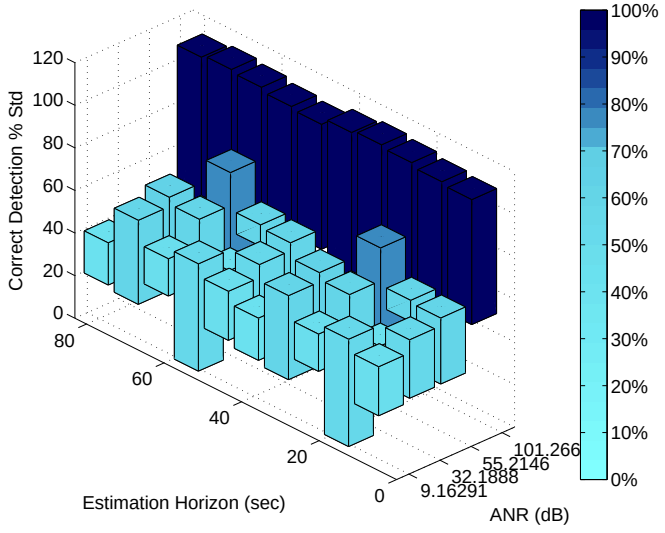

Figure C.14: The correct mode detection percentage shown with error bars for the modified LMP detector, Equation (3.177), for the nonlinear simulation example with a mode perturbation signature amplitude of $a_{\text{sig}} = 0.5$ tracking a reference with frequency of 0.10 Hz. The results correspond to the bar graph in Figure 3.32.

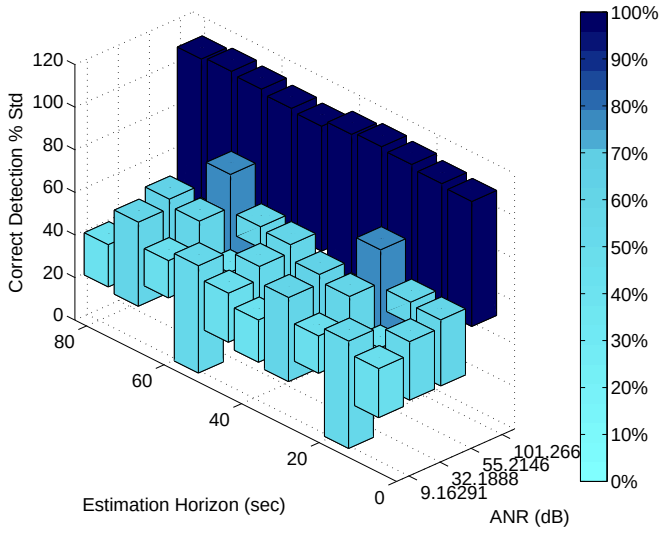

Figure C.15: The correct mode detection percentage shown with error bars for the modified LMP detector based on only estimating i, Equation (3.178), for the nonlinear simulation example with a mode perturbation signature amplitude of $a_{\text{sig}} = 0.5$ tracking a reference with frequency of 0.10 Hz. The results correspond to the bar graph in Figure 3.33.

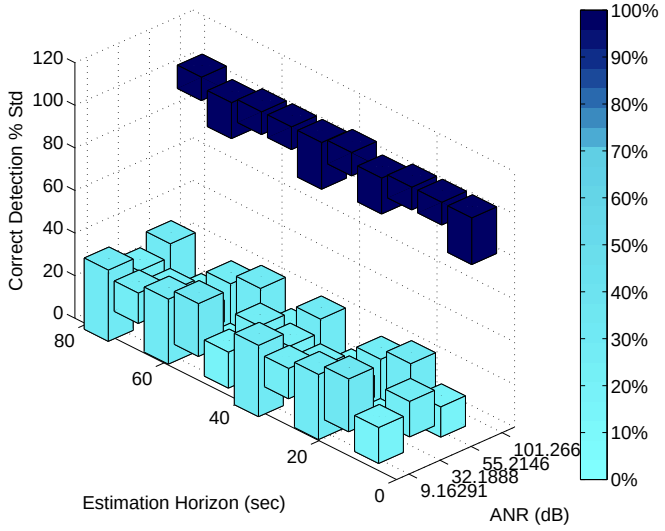

Figure C.16: The correct mode detection percentage shown with error bars for the LMP detector for the nonlinear simulation example with a mode perturbation signature amplitude of $a_{\text{sig}} = 0.5$ tracking a reference with frequency of 1.00 Hz. The results correspond to the bar graph in Figure 3.34.

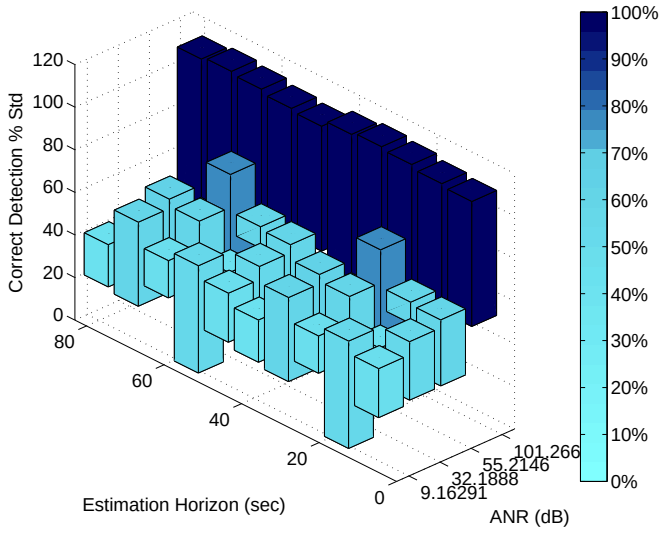

Figure C.17: The correct mode detection percentage shown with error bars for the modified LMP detector, Equation (3.177), for the nonlinear simulation example with a mode perturbation signature amplitude of $a_{\text{sig}} = 0.5$ tracking a reference with frequency of 1.00 Hz. The results correspond to the bar graph in Figure 3.35.

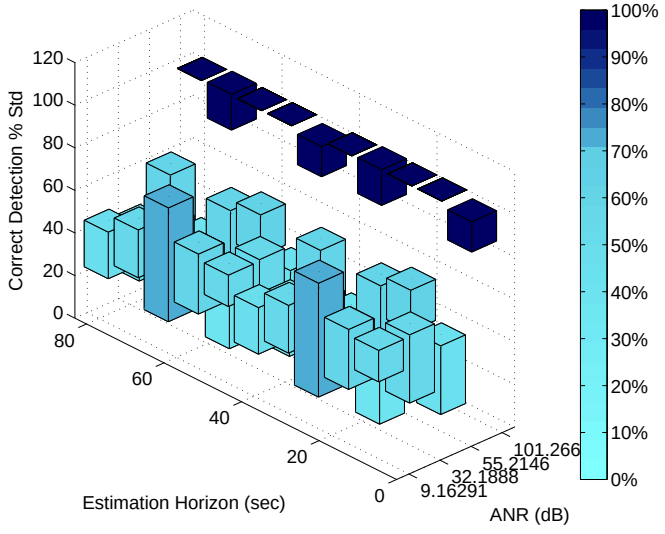

Figure C.18: The correct mode detection percentage shown with error bars for the modified LMP detector based on only estimating i, Equation (3.178), for the nonlinear simulation example with a mode perturbation signature amplitude of $a_{\text{sig}} = 0.5$ tracking a reference with frequency of 1.00 Hz. The results correspond to the bar graph in Figure 3.36.

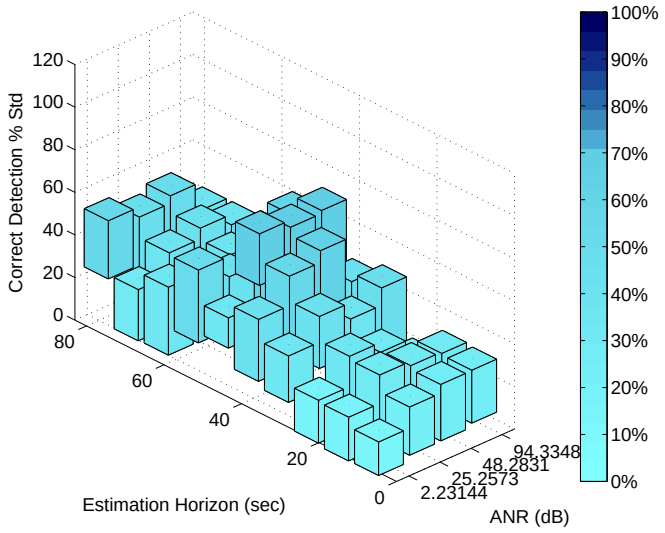

Figure C.19: The correct mode detection percentage shown with error bars for the modified SCA detector, Equation (3.160), for the nonlinear simulation example with a mode perturbation signature amplitude of $a_{\text{sig}} = 0.5$ and tracking a reference with frequency of 0.01 Hz. The results correspond to the bar graph in Figure 3.37.

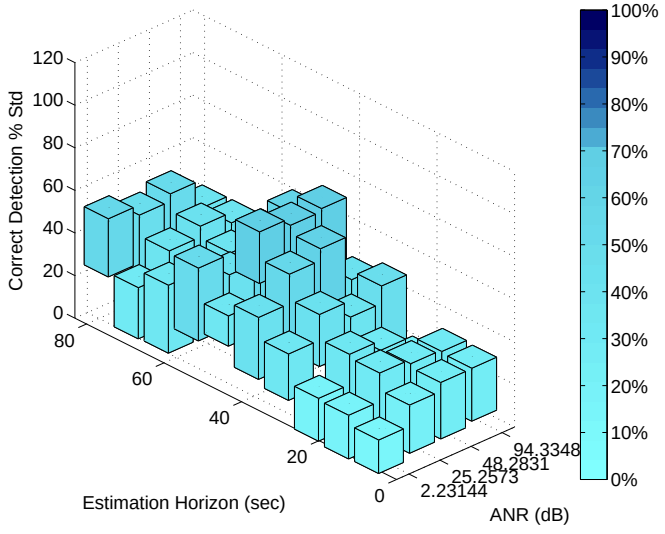

Figure C.20: The correct mode detection percentage shown with error bars for the modified SCA detector based on only estimating $\hat{\imath}$, Equation (3.179), for the nonlinear simulation example with a mode perturbation signature amplitude of $a_{\text{sig}} = 0.5$ and tracking a reference with frequency of 0.01 Hz. The results correspond to the bar graph in Figure 3.38.

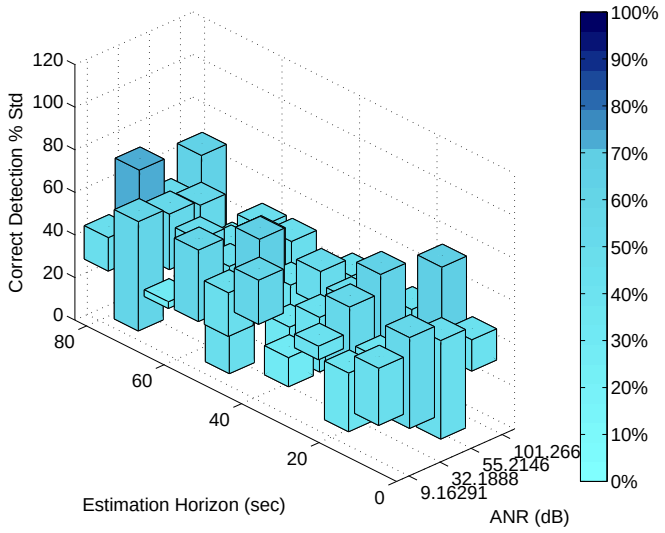

Figure C.21: The correct mode detection percentage shown with error bars for the modified SCA detector, Equation (3.160), for the nonlinear simulation example with a mode perturbation signature amplitude of $a_{\text{sig}} = 0.5$ tracking a reference with frequency of 0.10 Hz. The results correspond to the bar graph in Figure 3.39.

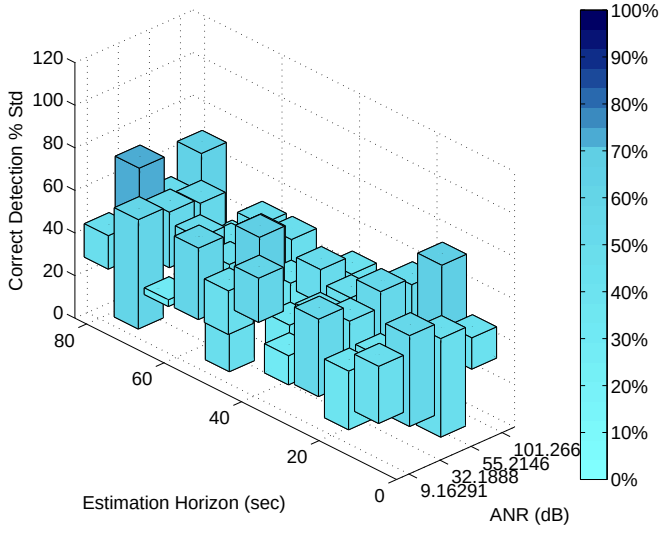

Figure C.22: The correct mode detection percentage shown with error bars for the modified SCA detector based on only estimating $\hat{\imath}$, Equation (3.179), for the nonlinear simulation example with a mode perturbation signature amplitude of $a_{\text{sig}} = 0.5$ and tracking a reference with frequency of 0.10 Hz. The results correspond to the bar graph in Figure 3.40.

BIBLIOGRAPHY

[1] F. C. Schweppe, "Recursive state estimation: Unknown but bounded error and system inputs," *IEEE Transactions on Automatic Control*, vol. 13, pp. 22–28, February 1968.

[2] E. Scholte and M. Campbell, "A nonlinear set-membership filter for on-line applications," *International Journal of Robust and Nonlinear Control*, vol. 13, pp. 1337–1358, October 2003.

[3] A. Balluchi, L. Benvenuti, and M. D. Benedetto, "Hybrid systems and the design of embedded controllers for automotive engine management," in *Proc. of the 37th IEEE Conference on Decision and Control*, (Tampa, FL), 1998.

[4] J. Lygeros, D. Godbole, and S. Sastry, "Verified hybrid controllers for automated vehicles," *IEEE T. on Auto. Cont.*, vol. 43, no. 4, pp. 522–539, 1998.

[5] C. Tomlin, G. Pappas, and S. Sastry, "Conflict resolution for air traffic management: A study in multiagent hybrid systems," *IEEE Transactions on Automatic Control*, vol. 43, pp. 509–521, April 1998.

[6] A. Savkin and R. Evans, *Hybrid Dynamical Systems*. Birkhauser, 2002.

[7] H. Blom and Y. Bar-Shalom, "The interacting multiple model algorithm for systems with markov switching coefficients," *IEEE Transactions on Automatic Control*, vol. 3, no. 8, pp. 780–783, 1988.

[8] J. Evans and R. Evans, "Image-enhanced multiple model tracking," *Automatica*, vol. 35, no. 11, pp. 1769–1786, 1999.

[9] C. Chang and M. Athans, "State estimation for discrete systems with switching paramters," *IEEE Trans. on Aerospace and Electronic Systems*, vol. AES-14, pp. 418–425, May 1978.

[10] G. A. Ackerson and K. Fu, "On state estimation in switching environments," *IEEE Trans. on Automatic Control*, vol. AC-15, pp. 10–17, February 1970.

[11] D. Sworder and J. Boyd, *Estimation Problems in Hybrid Systems*. Cambridge Univ. Press, 1999.

[12] D. D. Sworder, J. Boyd, and R. Elliott, "Modal estimation in hybrid systems," *Journal of Mathematical Analysis and Applications*, vol. 245, pp. 225–247, 2000.

[13] Y. Liu, "Switching observer design for uncertain nonlinear systems," *IEEE Trans. on Automatic Control*, vol. 42, pp. 1699–1703, December 1997.

[14] M. Campbell and S. Brunke, "Nonlinear estimation of aircraft models for on-line controls customization," in *Proc. of the IEEE Aerospace Conference*, vol. 2, (Big Sky, MT), pp. 621 – 628, 2001.

[15] S. de Oliveira Kothare and M. Morari, "Contractive model predictive control for constrained nonlinear systems," *Transactions on Automatic Control*, vol. 45, pp. 1053–1071, June 2000.

[16] Y. Bar-Shalom, X. R. Li, and T. Kirubarajan, *Estimation with Applications to Tracking and Navigation*. John Wiley and Sons, Inc., 2001.

[17] F. Schweppe, *Uncertain Dynamic Systems*. Prentice Hall, 1973.

[18] E. Hansen, *Global Optimization Using Interval Analysis*. Marcel Dekker, Inc., 1992.

[19] F. Chernousko, *State Estimation for Dynamic Systems*. CRC Press, 1994.

[20] D. Bertsekas, *Dynamic Programming and Optimal Control*. Athena Scientific, 2000.

[21] J. Nocedal and S. Wright, *Numerical Optimization*. Springer-Verlag, New York, Inc., 1999.

[22] B. Stevens and F. Lewis, *Aircraft Control and Simulation*. John Wiley and Sons, 1992.

[23] M. Campbell, R. D'Andrea, J. Lee, and E. Scholte, "Experimental demonstrations of semi-autonomous control," in *Proc. of the American Control Conference*, (Boston, MA), July 2004.

[24] J. Yan, A. Minai, and M. Polycarpou, "Balancing search and target response in cooperative unmanned aerial vehicle (UAUV) teams," *IEEE Transactions Systems, Man and Cybernetics, Part B*, vol. 36, pp. 571–587, June 2006.

[25] N. Leonard, D. Paley, F. Lekien, R. Sepulchre, D. Fratantoni, and R. Davis, "Collective motion, sensor networks and ocean sampling," *Proceedings of the IEEE*, To appear 2006.

[26] Y. Liu, K. Passino, and M. Polycarpou, "Stability analysis of M-dimensional swarms with a fixed communication topology," *IEEE Transactions on Automatic Control*, vol. 48, pp. 76–95, January 2003.

[27] Y. Liu, K. Passino, and M. Polycarpou, "Stability analysis of one-dimensional asynchronous swarms," *IEEE Transactions on Automatic Control*, vol. 48, pp. 1848–1854, October 2003.

[28] V. Gazi and K. Passino, "Stability analysis of swarms," *IEEE Transactions on Automatic Control*, vol. 48, pp. 692–697, April 2003.

[29] J. Fax and R. M. Murray, "Information flow and cooperative control of vehicle formations," *IEEE Transactions on Automatic Control*, vol. 49, pp. 1465–1476, September 2004.

[30] A. Richards, J. Bellingham, M. Tillerson, and J. How, "Co-ordination and control of multiple UAV's," in *Proc. of the AIAA Guidance, Navigation, and Control Conference*, August 2002.

[31] J. Ousingsawat and M. Campbell, "Multiple team tasking for cooperative estimation," in *Proc. of the AIAA Guidance, Navigation, and Control Conference*, August 2004.

[32] C. J. Tomlin, J. Lygeros, and S. S. Sastry, "A game theoretic approach to controller design for hybrid systems," *Proceedings of the IEEE*, 2000.

[33] P. Otanez and M. Campbell, "Bounded switched linear estimator for smooth nonlinear systems," *IEEE Transactions on Control Systems Technology*, vol. 15, pp. 358–368, March 2007.

[34] F. Ferrari-Trecate, D. Mignone, and M. Morari, "Moving horizon estimation for hybrid systems," *IEEE Transactions on Automatic Control*, vol. 47, pp. 1663–1676, October 2002.

[35] R. Gold, "Optimal binary sequences for spread spectrum multiplexing," *IEEE Transactions on Information Theory*, vol. 13, no. 4, pp. 619–621, 1967.

[36] R. L. Peterson, R. E. Ziemer, and D. E. Borth, *Introduction to Spread Spectrum Communications*. Prentice Hall, 1995.

[37] D. V. Sarwate and M. B. Pursley, "Crosscorrelation properties of pseudorandom and related sequences," *Proceedings of the IEEE*, vol. 68, pp. 593–619, May 1980.

[38] E. Kaplan, ed., *Understanding GPS Principles and Applications*. Artech House Publishers, 1996.

[39] H. V. Poor, *An Introduction to Signal Detection and Estimation*. Springer-Verlag, 1994.

[40] D. Torrieri, *Principles of Spread-Spectrum Communication Systems*. Springer, 2005.

[41] V. P. Ipatov, *Spread Spectrum and CDMA, principles and applications*. Wiley, 2005.

[42] A. Papoulis, *Probability, Random Variables and Stochastic Processes*. McGraw Hill, 2001.

[43] R. Kalman, "A new approach to linear filtering and prediction problems," *Transactions of the ASME, Journal of Basic Engineering*, vol. 82, pp. 35–45, March 1960.

[44] R. Brown and P. Hwang, *Introduction to Random Signals and Applied Kalman Filtering*. John Wiley and Sons, Inc., 1992.

[45] R. F. Stengel, *Optimal Control and Estimation*. Dover Publications, 1994.

[46] B. Ekstrand, "Poles and zeros of $\alpha - \beta$ and $\alpha - \beta - \gamma$ tracking filters," *IEE Proceedings of Control Theory Applications*, vol. 148, pp. 370–376, September 2001.

[47] S. Brunke and M. Campbell, "Square root sigma point filtering for real-time, nonlinear estimation," *Journal of Guidance, Control, and Dynamics*, vol. 27, no. 2, pp. 314–317, 2004.

[48] S. Julier, J. Uhlmann, and H. F. Durrant-Whyte, "A new method for the nonlinear transformation of means and covariances in filters and estimators," *IEEE Transactions on Automatic Control*, vol. 45, no. 3, pp. 477–482, 2000.

[49] R. van der Merwe and E. Wan, "Sigma-point kalman filters for nonlinear estimation and sensor-fusion - applications to integrated navigation," in *Proc. of the AIAA Guidance, Navigation, and Control Conference*, August 2004.

[50] S. Haykin, ed., *Kalman Filtering and Neural Networks*. Wiley, 2001.

[51] D. Weatherington, "Unmanned aerial vehicle (UAV) roadmap report," tech. rep., Department of Defense, 2003.

[52] J. Ousingsawat and M. Campbell, "Establishing trajectories for multi-vehicle reconnaissance," in *Proc. of the AIAA Guidance, Navigation, and Control Conference and Exhibit*, (Providence, RI), August 2004.

[53] E. Frazzoli, M. A. Dahleh, and E. Feron, "Maneuver-based motion planning for nonlinear systems with symmetries," *IEEE Transactions on Robotics and Automation*, vol. 21, pp. 1077–1091, December 2004.

[54] P. Otanez and M. Campbell, "Bounded model switching in uncertain hybrid systems," in *Proc. of the American Control Conference*, (Boston, MA), June 2004.

[55] P. Otanez and M. Campbell, "Mode estimation switching using perburation signatures for hybrid multi-vehicle systems," in *Proc. of the AIAA Guidance, Navigation, and Control Conference*, August 2005.

[56] The Insitu Group, "The SeaScan UAV." www.insitu.com.

[57] G. Holland, T. McGeer, and H. Youngren, "Autonomous aersondes for economical atmospheric soundings anywhere on the globe," *Bulletin of the American Metereological Society*, no. 32, 1992.

[58] T. McGeer and J. Vagners, "Historic crossing: an unmanned aircraft's atlantic flight," *GPS World*, vol. 10, pp. 24–30, February 1999.

[59] M. E. Campbell and M. Wheeler, "A vision based geolocation tracking system for UAV's," in *Proc. of the AIAA Guidance, Navigation and Control Conference*, (Keystone, CO), August 2006.

[60] M. Campbell and W. Whitacre, "Cooperative tracking using vision measurements on SeaScan UAV's," *IEEE Transactions on Control Systems Technology*, Accepted 2006.

[61] I. Miller, S. Lupashin, N. Zych, P. Moran, B. Schimpf, A. Nathan, and E. Garcia, "Cornell University's 2005 DARPA Grand Challenge entry," *Journal of Field Robotics*, vol. 23, pp. 625–652, August 2006.

[62] I. Miller and M. Campbell, "A mixture-model based based algorithm for real-time terrain estimation," *Journal of Field Robotics*, vol. 23, pp. 755–775, September 2006.

[63] I. Kaminer, W. Kang, O. Yakimenko, and A. Pascoal, "Application of nonlinear filtering to navigation system design using passive sensors," *IEEE Transactions on Aerospace and Electronic Systems*, vol. 37, pp. 158–172, January 2001.

[64] J. Hespanha, O. Yakimenko, I. Kaminer, and A. Pascoal, "Linear parametrically varying systems with brief instabilities: An application to vision/inertial navigation," *IEEE Transactions on Aerospace and Electronic Systems*, vol. 40, pp. 889–902, July 2004.

[65] S. Brunke and M. Campbell, "Estimation architecture for future autonomous vehicles," in *Proc. of the American Control Conference*, vol. 2, pp. 1108–1114, June 2002.

[66] Y. Chen, T. Huang, and Y. Rui, "Parametric contour tracking using the unscented kalman filter," in *Proc. of the International Conference on Image Processing*, vol. 3, pp. 613–616, June 2002.

[67] M. Andersen, R. Andersen, and K. Wheeler, "Filtering in hybrid dynamic bayesian networks," in *Proc. of the IEEE International Conference on Acoustics, Speech, and Signal Processing*, vol. 5, pp. 773–776, May 2002.

[68] K. Reif and R. Unbehausen, "The EKF as an exponential observer for nonln. systems," *IEEE Trans. on Signal Processing*, vol. 47, no. 8, pp. 2324–2328, 1999.

[69] E. Scholte and M. Campbell, "A nonlinear set-membership filter for on-line applications," *Int. J. of Robust and Nonlinear Cont.*, vol. 13, no. 15, pp. 1337–1358, 2003.

[70] Y. Song and J. Grizzle, "The extended kalman filter as a local asymptotic observer for nonlinear discrete-time systems," *J. of Math. Sys., Esti., and Cont.*, vol. 5, no. 1, pp. 59–78, 1995.

[71] B. Anderson and J. Moore, "Detectability and stabilizability of time-varying discrete-time linear systems," *SIAM Journal of Control and Optimization*, vol. 19, no. 1, pp. 395–404, 1981.